



FACULTY OF SCIENCES
Department of Chemistry

Theoretical Physical Chemistry
Prof. Françoise Remacle

**Steering chemical reactions with mechanical forces and
attosecond optical pulses.**

Dissertation presented by

Academic year 2024-2025

Manuel Cardoso-Gutierrez

to obtain the grade of
Doctor of Sciences

Jury

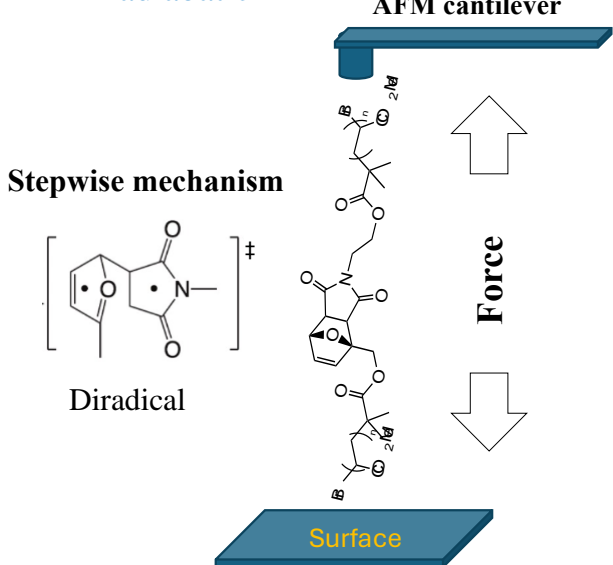
Supervisor	Prof. Françoise Remacle	<i>Université de Liège</i>
President	Prof. Anne-Sophie Duwez	<i>Université de Liège</i>
Secretary	Prof. Bernard Leyh	<i>Université de Liège</i>
Members	Prof. Guillaume De Bo	<i>University of Manchester</i>
	Prof. Jeremy Harvey	<i>KU Leuven</i>
	Prof. Ludovic Noels	<i>Université de Liège</i>

Steering chemical reactions with mechanical forces and attosecond optical pulses

Abstract

External mechanical forces and ultrashort optical pulses can be used to steer and control chemical reactions. We demonstrate that an external mechanical force can not only enhance or inhibit the [4+2] cycloreversion of furan/maleimide Diels-Alder adducts, but also shift its mechanism from concerted to stepwise, mediated by diradical species. To better understand how attosecond light pulses can control photochemical reactions, we derived an expression for the force exerted on the nuclei by the electronic coherences created through interaction with the light and show that they can be used to steer nuclear motion. We propose a computational scheme based on singular value decomposition to simplify the simulation of an ensemble of molecules with random initial orientations interacting with an attopulse. We show that a few principal orientations only suffice to describe the ensemble dynamics and that electronic coherences are robust with respect to the ensemble averaging. We also show that conical intersections control the relaxation of the excited ethylene cation, shaping the yields of fragments after dissociation. Our findings contribute to a better understanding of control mechanisms in the fields of mechanochemistry and attochemistry.

Mechanochemistry adiabatic



Attochemistry ultrafast

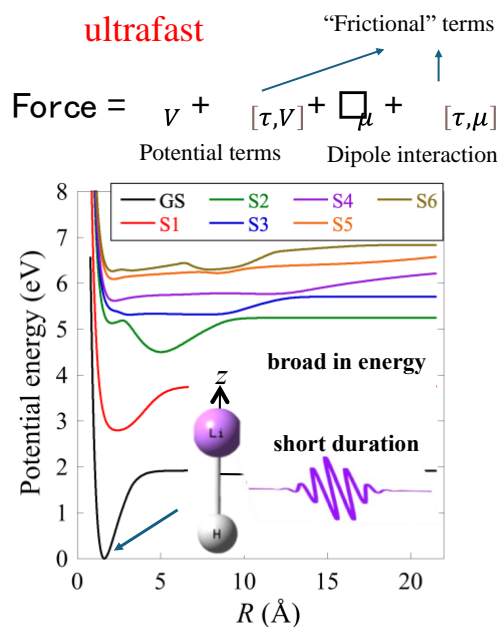


Table of Contents

List of Publications	1
List of Acronyms.....	2
Chapter 1 Introduction.....	4
1.1 Overview of chemical reactivity.....	4
1.2 Mechanical activation of polymers.....	9
1.2.1 Experimental methods for the mechanical activation of polymers.....	9
1.2.1.1 Ultrasound sonication	9
1.2.1.2 Single-molecule spectroscopy	10
1.2.2 From mechanical activation to chemical reactivity	11
1.2.3 Role of theoretical calculations in mechanochemistry	12
1.2.4 The furan/maleimide retro Diels Alder reaction	15
1.3 Steering chemical reactivity with ultrashort light pulses.....	17
1.3.1 Attochemistry.....	17
1.3.2 Femtochemistry: Photoinduced control with femtosecond pulses.....	18
1.3.3 Control with attopulses	19
1.3.4 High harmonic generation of attosecond pulses	21
1.4 Outline.....	22
1.5 References.....	25
Chapter 2. Electronic Structure and Molecular Dynamics Methods	34
2.1 Electronic Structure Methodologies	34
2.1.1. Introduction to quantum chemistry.....	34
Approximate solution of the SE equation.....	38
2.1.2. Density Functional Theory	39
2.1.3. Modeling systems with strong correlation.....	42
Unrestricted HF and DFT	42
2.1.4. The multireference CASSCF approach	43
Describing excited states: the state-averaged algorithm in CASSCF.....	46
2.2 Modeling molecular dynamics.....	46
2.2.1. Introduction.....	46
Choice of initial conditions.....	47
2.2.2. Ab initio molecular dynamics.....	48

Sampling initial velocities from thermal distribution	49
2.2.3. Photoinduced coupled electron-nuclei quantum dynamics.....	51
2.2.3.1 Introduction on quantum dynamics	51
2.2.3.2 Modeling light-matter interaction within the dipole approximation.....	51
2.2.3.3 The Franck-Condon Principle.....	57
2.2.4. Quantum mechanical description of the molecular system interacting with the pulse.	58
2.2.4.1 Solving the TDSE	59
2.2.4.2 Discretization of the nuclear wavefunctions and of the Hamiltonian operator	64
2.2.5. Hamiltonian in the linear diatomic molecule LiH.	65
2.2.6. Numerical integration of the TDSE	68
2.3 Modeling ultrafast excited-state processes in large molecular systems.....	69
2.3.1. Surface hopping dynamics using the SHARC method.....	70
2.3.2. Sampling of initial conditions from the Wigner distribution	73
2.4 References.....	75
Chapter 3 Ab initio modeling of the molecular response to an external mechanical force.....	78
3.1 Theoretical methods to simulate the response to an external force	78
3.1.1 Free energies and rate constants from ab initio computations.....	80
3.2 Summary of key findings.....	81
3.3 Summary of contributions.....	83
3.4 References.....	83
3.5 Publication: “Bond breaking of furan–maleimide adducts via a diradical sequential mechanism under an external mechanical force”	84
Chapter 4. Isotope effects in the ultrafast excited state photodissociation of the ethylene cation.	85
4.1. Overview of photorelaxation of ethylene cation in pump-probe experiments	85
4.2. Modeling the non-adiabatic dynamics in the four lowest electronic states of the ethylene cation	87
4.3. Explanation of the isotope effect on the oscillations of the experimental yields.....	91
4.4. Summary of contributions.....	95
4.5. References.....	96
4.6. Publication: “Isotope effect on the few-femtosecond relaxation dynamics of the ethylene cation”	97
Chapter 5. Control of the chemical reactivity by leveraging the electronic coherences built with an attopulse	98
5.1 Quantum description of the intramolecular forces in a coherent vibronic wavepacket	98

5.2	Steering reactivity in LiH with an attopulse: role of the electronic coherences in the control of the force on the nuclei	101
5.3	Summary of contributions.....	102
5.4	References.....	103
5.5	Publication: “Electronic coherences built by an attopulse control the forces on the nuclei”	104
Chapter 6	Efficient simulation of an ensemble of photoexcited randomly oriented molecules	105
6.1	Stereochemical effects in the photodynamics of an ensemble of LiH molecules.....	105
6.1.1	Introduction to the singular value decomposition (SVD) of a matrix	107
6.1.2	SVD of the density matrix in an ensemble of photoexcited randomly oriented molecules	109
6.2	Summary of contributions.....	112
6.3	References.....	113
6.4	Publication: “Electronic Coherences Excited by an UltraShort Pulse Are Robust with Respect to Averaging over Randomly Oriented Molecules as Shown by Singular Value Decomposition”	113
Chapter 7	Perspectives.....	114
7.1	Perspectives on the modeling of mechanochemistry	114
7.2	Perspectives on modeling attochemistry.....	120
7.2.1	Forces arising in an ensemble of initially randomly oriented photoexcited molecules.	121
7.2.2	Forces mediating the ultrafast stereo dynamics in the Jahn-Teller rearrangement of CD ₄ ⁺	124
7.3	References.....	130
Chapter 8	Conclusions.....	132
	References.....	135

List of Publications

1. M. Cardosa-Gutierrez, G. De Bo, A.-S. Duwez, F. Remacle, [Bond breaking of furan–maleimide adducts via a diradical sequential mechanism under an external mechanical force](#). *Chemical Science* **14**, 1263-1271 (2023).
2. M. Cardosa-Gutierrez, R. D. Levine, F. Remacle, [Electronic coherences built by an attopulse control the forces on the nuclei](#). *J. Phys. B: At. Mol. Opt. Phys.*, (2024).
3. M. Cardosa-Gutierrez, R. D. Levine, F. Remacle, [Electronic Coherences Excited by an Ultra Short Pulse Are Robust with Respect to Averaging over Randomly Oriented Molecules as Shown by Singular Value Decomposition](#). *J. Phys. Chem. A* **128**, 2937-2947 (2024).
4. M. Lucchini, M. Cardosa-Gutierrez, M. Murari, F. Frassetto, L. Poletto, M. Nisoli, F. Remacle, [Isotope effect on the few-femtosecond relaxation dynamics of the ethylene cation](#). *J. Phys. Chem. Lett.*, (submitted)

List of Acronyms

- BO: Born-Oppenheimer
- BOMD: Born-Oppenheimer Molecular Dynamics
- MD: Molecular Dynamics
- EUV, XUV: extreme ultraviolet
- HHG: high harmonic generation
- CEP: carrier-envelope phase
- DA: Diels Alder
- rDA: retro Diels Alder
- SMFS: single-molecule force spectroscopy
- AFM: atomic force microscopy
- MO: molecular orbital
- HOMO: highest occupied molecular orbital
- LUMO: lowest unoccupied molecular orbital
- IR: infrared
- NIR: near infrared
- CoGEF: constrained geometry optimization simulate the external force
- PMA: poly-methyl acrylate
- SCF: self-consistent field
- EFEI: external force is explicitly included
- EGO: enforced geometry optimization
- AISMD: ab-initio steered molecular dynamics
- DFT: density functional theory
- UDFT: unrestricted DFT
- CASSCF: complete active space self-consistent field
- PES: potential energy surface
- FMPES: force-modified potential energy surface
- CSF: configuration state function
- MCSCF: multiconfiguration self-consistent field
- CAS: complete active space
- HF: Hartree Fock
- SS-CASSCF: state-specific CASSCF
- SA-CASSCF: state-averaged CASSCF
- Ensemble NVT: fixed N: number of particles, V: volume, T: temperature
- TS: transition state
- DFTB: density functional tight binding
- xTB: extended tight binding
- AMBER: Assisted Model Building with Energy Refinement
- CHARMM: Chemistry at HARvard Macromolecular Mechanics
- GROMOS: GRoningen MOlecular Simulation
- DNA: deoxyribonucleic acid

- GPU: graphics processing unit
- MPI: message passing interface
- SMD: steered molecular dynamics
- QM/MM: quantum mechanics/molecular mechanics
- FWHM: full width at the half maximum
- FT: Fourier transform
- FC: Franck-Condon
- JT: Jahn-Teller
- WP: wave packet
- CI: conical intersection
- SE: Schrödinger equation
- TDSE: time-dependent Schrödinger equation
- BH: Born-Huang
- NAC: non-adiabatic derivative coupling
- MECI: minimum energy conical intersection
- DVR: discrete variable representation
- DFT, IDFT: discrete Fourier transform, inverse discrete Fourier transform
- RK4: Runge Kutta 4th order
- CSR: compressed sparse representation
- LAPACK: Linear Algebra PACKage
- MKL: Math Kernel Library
- SHARC: Surface Hopping with Arbitrary Couplings
- SH: surface hopping
- SOC: spin-orbit coupling
- MCH: molecular Coulomb Hamiltonian
- FSSH: Fewest Switches Surface Hopping
- SVD: singular value decomposition
- GS: ground state
- PMF: potential of mean force
- NDE: nonstatistical dynamic effects
- CW (laser): continuous wave (laser)
- gDCC: gem-dichlorocyclopropane
- WHD: Woodward-Hoffmann-DePuy

Chapter 1 Introduction

Table of Contents

Chapter 1	Introduction	4
1.1	<i>Overview of chemical reactivity</i>	4
1.2	<i>Mechanical activation of polymers</i>	9
1.2.1	Experimental methods for the mechanical activation of polymers	9
1.2.2	From mechanical activation to chemical reactivity	11
1.2.3	Role of theoretical calculations in mechanochemistry	12
1.2.4	The furan/maleimide retro Diels Alder reaction	15
1.3	<i>Steering chemical reactivity with ultrashort light pulses</i>	17
1.3.1	Attochemistry	17
1.3.2	Femtochemistry: Photoinduced control with femtosecond pulses	18
1.3.3	Control with attopulses	19
1.3.4	High harmonic generation of attosecond pulses	21
1.4	<i>Outline</i>	22
1.5	<i>References</i>	25

1.1 Overview of chemical reactivity

Chemistry studies matter and the changes it undergoes.⁽¹⁾ In a chemical reaction, one or more reactants are converted to one or more products with different structural and physical properties. A change in energy and entropy also accompanies this change of matter. Reactions such as combustion, fermentation, and the reduction of ores to metals have been known since antiquity. Others, more complex, were already used by alchemists in the Middle Ages. But it wasn't until the 19th century, with the development of thermodynamics, that scientists developed a rigorous interpretation of chemical reactions regarding the underlying physical laws of nature. Groundbreaking discoveries such as the first and second laws of thermodynamics, which introduced the fundamental principles governing energy conservation and entropy, provided chemists with a conceptual, quantitative framework to analyze and predict the outcome of chemical reactions. However, this also posed a challenge, as it quickly became apparent that processes forbidden by the laws of thermodynamics cannot be practically achieved without external intervention. In other words, we need to supply energy or employ spontaneous reactions to drive non-spontaneous processes forward.

A key area of interest is understanding how reactions proceed from the initial state of reactants to the final product state. Although thermodynamics in the long-term dictates to which product configuration the system will evolve, the time scale for this to occur could be remarkably long, sometimes surpassing the human lifespan. In this situation, a product can adopt a more unstable configuration that is formed faster and still lasts a long period of time. Then, the kinetics of the reaction is what dictates the configuration of the product. Chemical kinetics studies how

experimental conditions influence the speed of a reaction and yield information about its mechanism and transition states. By discretizing the whole chemical reaction process into elementary steps, it is possible not only to understand and characterize the reaction better but also it allows to control it better. Within the transition state theory, each of the elementary steps of a reaction involves the conversion between two distinct configurations of the molecular system, mediated by an activated transition state complex. For a reaction that consists of one elementary step, the two configurations are the reactants and the products, but for multi-step reactions, the system can visit several intermediate configurations on the way to the products. Intermediates can be consumed rather quickly, or in some cases, they can last long enough to be captured experimentally. This suggests that the process of transition from the reactants to the products is not direct and can be rather complex. The path followed by the system is particularly sensitive to experimental conditions and to external interferences such as external forces, electric fields, or other substances like catalysts. To determine experimentally the path followed by the system from its initial state, in the reactant form, toward the products is not easy. However, certain techniques like spectroscopy can provide valuable information. There is a great interest in the scientific community to develop light attosecond pulses ($1 \text{ as} = 10^{-18} \text{ s}$) that can be used to address the electrons directly to steer nuclear motion and to probe phenomena in molecules occurring at time scales as fast as the electronic motion. This would extend the amazing capabilities in the lab to track chemical reactions and understand their mechanisms in detail. Theoretically, the evolution of a molecular system from reactants to products can be modeled using molecular dynamics techniques, and great accuracy and agreement with experiments can be achieved using ab initio quantum chemistry methodologies. Molecular dynamics simulations can be used to study multiple aspects of kinetics, particularly the time-dependent behavior of molecular systems, which includes reaction dynamics, diffusion processes, and the rate of molecular transformations. It can explore reaction mechanisms by simulating how atoms and molecules interact during a transformation.

With advancements in industry, medicine, and engineering, the search for novel compounds with properties valuable to these fields has become a central goal of modern chemistry. Achieving this requires the exploration of new chemical pathways, which involves discovering innovative combinations of reactants and designing experimental setups that enhance the synthesis of desired products. Optimizing yields, product selectivity, and stereoselectivity is crucial for the successful application of chemical reactions and the resulting compounds. Traditional approaches to improving chemical reactions in both laboratory and industrial settings often involve controlling temperature and pressure, selecting appropriate solvents, or employing catalysts. However, the use of external agents to guide or influence chemical reactions has also become well-established. For instance, electrical currents are widely used to drive key technological processes, such as electroplating, electrolysis, electrochemical synthesis, and electrophoresis.

Mechanical activation of chemical bonds is another method to trigger the reactivity of a system. Strained molecular architectures govern many physiological processes, including enzyme activities, motion of molecular motors, division of cells, or muscle contraction.⁽²⁾ Given the vector character of the force, mechanochemical reactions can follow specific pathways, yielding products that may differ from those of non-directional classical activation in solution (like thermal activation). A mechanical force modifies the free-energy surface of chemical reactions, enabling thermodynamically unfavored reaction pathways and yielding products that are either prohibited or too slow to be obtained under thermodynamic control. ⁽³⁻⁸⁾ Exploiting the coupling between

mechanical loads acting on a polymer and the propensity of its monomers to undergo chemical reactions offers the attractive potential to create new stress-responsive and energy-transducing materials.

Because the force is applied to the nuclei on a millisecond-to-second time scale, which is much slower than the intrinsic time scale of the electronic and internal vibrational motions, the mechanochemical reaction is governed by the ground electronic state of the system, and the interaction with the force follows an adiabatic Born-Oppenheimer regime.

A much different situation arises when the chemical reaction is initiated by the absorption of energy in the form of light. This process creates transient excited states of the reactants. The excited molecule then evolves to equilibrium, releasing the excess of energy by emitting light quanta or through the rupture/creation of chemical bonds, the transfer of charge or atoms, or simply via collisions with surrounding molecules. Photochemical reactions power photosynthesis, from which almost all life forms on Earth depend. They are also critical in commercial processes and devices, including photography and the manufacture of semiconductor chips. (9) Like the case of mechanical activation, the excitation with light drives the reactants into a nonstatistical distribution, where vibrational modes on different electronic states are preferentially activated. These sources of excitation contrast with thermal excitation, where the energy added to the molecular system is equally distributed among all the vibrational, translational, and rotational degrees of freedom, according to the Boltzmann distribution. This is an example of an incoherent source of molecular excitation. (10) However, the time scale for reaching this equilibrium distribution depends on factors such as the spacing between quantum levels, the coupling of the system to its environment, and the dynamics of energy exchanges within the system. The energy is generally redistributed through collisions and transferred from translational motion to rotational and vibrational modes. This leads to an equilibrium distribution of velocities. While the transfer of energy from translation to overall rotations often happens relatively quickly, the transfer of kinetic energy from the center-of-mass motion to internal vibrational modes is much slower, as vibrational excitation typically requires larger energy quanta.

An important point is that thermal activation uniquely involves the energy transfer to nuclear degrees of freedom in the molecule. This process occurs so slowly compared to the time scale of the motion of the electrons, which are ≈ 2000 lighter, that the latter can adjust almost instantaneously to the deformation of the nuclei. Therefore, it is generally assumed that when the molecule moves, rotates, or vibrates, the motion of the electrons instantaneously adjusts to the new configuration of the nuclei. This assumption forms the basis of the Born-Oppenheimer (BO) approximation, which is used in quantum mechanics to simplify the solution of the Schrödinger equation for a molecular system, as discussed in Chapter 3. The BO approximation relies on the large difference between the electron mass and the masses of atomic nuclei, which determines the time scales of their motion. In the simplest atom, hydrogen, the electron mass is nearly 2000 times smaller than the nucleus and even smaller in heavier atoms. As a result, electrons move much faster than the nuclei on timescales of attoseconds (10^{-18} s). During this brief timescale, the nuclei can be considered effectively frozen since their motion occurs on much longer timescales, ranging from femtoseconds (10^{-15} s) to picoseconds (10^{-12} s).

A coherent excitation of the molecular energy states can be induced with coherent light. Specifically, high-intensity lasers can trigger selective bond activation or cleavage reactions if the wavelength of the light is in resonance with the vibrational energy of a particular chemical bond and when the quanta deposited reach the appropriate barrier height or the dissociation limit. (11) In practice, one needs to use ultrafast laser pulses, which will act in the time frame of the photochemical reaction and will maintain the energy localized within a single vibrational mode. In that way, the intramolecular energy redistribution, induced by the coupling within the molecular modes, and taking place on hundreds of ps time scale, will not have time to occur.

Femtosecond ($\sim 10^{-15}$ s) pulses can be used to follow the motion and reorganization of the nuclei upon electronic excitation because they are shorter than the typical ps time scale of significant nuclear motion. (11) A vibrational wave packet can be created on this time scale, and its coherent evolution can be probed. The introduction of these pulses by Zewail and coworkers paved the way for impressive applications in industry and medicine. (12-17) However, we need even shorter pulses, of attosecond duration, to explore faster processes occurring inside a molecule, such as the motion of the electrons and their reorganization. Since the ultimate limit in pulse duration is set by the wavelength of light, sub-femtosecond pulses require the generation of short-wavelength radiation in the extreme ultraviolet (XUV) or soft-X ray spectral region. High-order harmonic generation (HHG) is the technique typically used for the generation of XUV radiation, which is based on nonlinear processes in gas or plasma excited by high-peak-power, femtosecond laser pulses. (18-23) The 2023 Nobel Prize in Physics was awarded to Pierre Agostini, Ferenc Krausz, and Anne L'Huillier for the engineering of attopulses.

Attosecond ($\sim 10^{-18}$) pulses (24-27) can excite a molecule in the time scale of the electronic motion, driving the electrons in a non-equilibrium state with respect to the nuclei. According to the energy-time uncertainty principle, the shorter the pulse time duration, the broader its energy bandwidth will be in the Fourier transform domain. Broad-in-energy attosecond pulses allow exciting coherently several electronic states in molecules, leading to a breakdown of the BO approximation at the excitation step and the formation of a nonequilibrium electronic density. The electronic coherences built by the attopulse drive the motion of the non-equilibrium electronic density on a purely electronic time scale before a significant onset of the nuclear motion. (28-31) They induce ultrafast charge migration between different parts of the molecule, during which one could implement charge-directed reactivity. (32-36) In molecules excited by attopulses, the vibronic dynamics therefore occur in a post-Born-Oppenheimer regime. (11) The electronic state is not in equilibrium with the instantaneous position of the nuclei and so can be exploited to control chemical reactivity. (31, 37-40) Tuning the parameters of the pulse, such as its carrier frequency, envelope duration, polarization, and carrier-envelope phase (CEP), provides control of the electronic motion in the initially pumped state and of the entanglement between the electronic and nuclear motions. (41-43) Such control opens the way to developing robust and efficient schemes to steer chemical reactivity by targeting electronic motion, with direct implications in materials science, medicine, and modern information technology. (19, 23, 44-46)

This thesis summarizes our efforts in the study of the response of molecular systems subjected to external mechanical forces or attosecond pulses. This work is part of the MECHANOCHEM project, where our Theoretical Physical Chemistry lab, led by Prof Françoise Remacle, joined forces with the experimental group "NanoChem" of Prof Anne-Sophie Duwez, to design control

schemes based on the selective application of external perturbations to steer the electron-nuclei quantum dynamics of a molecule to specific reaction products. We report on the mechanical stability of furan/maleimide mechanophores and the switch of the mechanism of their [4+2] cycloreversion reaction from a typical thermal concerted pathway to a diradical sequential pathway in the presence of an asymmetric external force.⁽⁴⁷⁾ In qualitative agreement with sonication experiments ⁽⁴⁸⁾, we show that the *endo* stereoisomer is more labile as it will dissociate for lower values of the force. Our theoretical computations support and explain these facts. These findings open the way for the rational design of mechanophores that exploit the stereo and regio control provided by the reversible Diels-Alder reaction of furan/maleimide adducts. And we propose their utilization for the generation of a new generation of intelligent materials and logic devices driven by mechanical forces. In addition, we worked in the emerging attochemistry field and investigated the role of electronic response in the force exerted on the nuclei by a vibronic wave packet created by excitation of the molecule with an atto or a few fs pulse. In the literature, there is evidence of the regulation of photochemical reactions by the application of external forces ^(49, 50) and of the utilization of light pulses to generate mechanical molecular work and to control the mechanical properties of materials. ⁽⁵¹⁻⁵³⁾

Towards the control of chemical reactivity by attopulses, we derive the quantum mechanical expression for the force exerted by the vibronic wave packet on the nuclei. The force arises from the interaction between the electric field of the exciting pulse and the charge distribution of the molecule, which indirectly controls the motion of the nuclei. This contrasts with the work in mechanochemistry, where the force is directly applied to specific nuclei. Because the electrons are much lighter than the nuclei, they primarily respond to the electric field on an attosecond timescale, which allows an ultrafast control. We demonstrate how tuning the pulse parameters allows exciting specific electronic coherences that will determine the force strength and direction during and after the pulse. After the pulse, the component of the force due to the non-adiabatic interactions accelerates or slows down the motion of the vibronic wave packet on the excited electronic states, and its sign controls the direction of population transfer. In this thesis, we discuss proof-of-principle computational results for the LiH and LiT molecules, but the methods developed here can be applied to larger molecules, which is a goal for future research in our group.

In the following sections of this introduction, we provide a more technical introduction to the two fields we have worked in: mechanochemistry and attochemistry. First, we discuss the mechanical activation of polymers, achieved in single-molecule force spectroscopy (SMFS) experiments and in ultrasound sonication experiments. Our experimental partners from the group of Anne-Sophie Duwez at the University of Liège have extensive experience in developing SMFS experiments, and we provide an overview of the technique. We also emphasize the importance of theoretical modeling in understanding the chemical phenomena underlying force-induced reactivity. Our work in mechanochemistry, concerning the bond breaking of furan/maleimide adducts under force, is discussed in Chapter 3. Next, we explore the generation of ultrashort, attosecond, pulses and their applications in steering and controlling photochemical reactions. We have worked extensively in attochemistry in collaboration with the group of Mauro Nisoli (Politecnico di Milano), who conducted pump-probe experiments in ethylene (Chapter 4), and with Raphael Levine (Hebrew University) on a theoretical work, where we uncovered the role of electronic coherences built with an attopulse in controlling the vibronic forces acting on the nuclei (Chapter 5). Chapter 2 provides an overview of the theoretical methodologies used in our work.

1.2 Mechanical activation of polymers

Polymers are ubiquitous in the industry of synthetic materials and play a major role in all biological processes. They are the functional materials of choice for applications such as organic electronics, biological scaffolds, and drug-delivery coatings.⁽⁵⁴⁾ Mechanical properties such as high strength, toughness, and elasticity, together with their processability, and low cost justify their broad range of applications. By incorporating additional chemical functionality, certain polymers can be stimuli-responsive, providing a desired behavior when subjected to a specific chemical or physical perturbation.^(54, 55) Particularly, mechanoresponsive polymers are good candidates for designing smart materials that could find applications as force sensors or in self-healing systems,⁽⁵⁶⁾ because they allow using mechanical energy to drive chemical transformations. However, there is a link missing between the detailed molecular design and the control of mechanical forces applied during scalable processing techniques.⁽⁵⁴⁾ For that reason, there is ongoing research on the behavior of polymers under the influence of external mechanical stress. In terms of mechanophore design and understanding, it is important to know how the force affects an individual mechanophore and how the surrounding structure and connectivity affect its activation.⁽⁵⁴⁾ This requires a mechanistic understanding of the chemistry driven by the external force, and especially from a dynamical point of view. Time scales are essential to assess the response to the force.

Polymer mechanochemistry aims to understand and exploit macromolecular chains' reactivity in highly non-equilibrium stretched geometries resulting from interactions between the chains and their surroundings.⁽⁵⁷⁾ The current techniques for supplying mechanical force range from solution-based studies to bulk activation in the solid state, and they cover a wide range of strain rates and applied forces.⁽⁵⁶⁾ The examination of mechanoresponsive materials in the bulk is imperative as most polymeric materials find applications in the solid state. This can be done by applying forces to polymers through elongation, compression, or extrusion. Solution-based methods encompass the application of strong hydrodynamic forces with flow fields, ultrasound sonication, and single-molecule force spectroscopy (SMFS). ^(54, 56)

In this thesis, we study the behavior of furan/maleimide mechanophores at the molecular scale in the presence of external forces such as the ones applied in SMFS or sonication experiments.

1.2.1 Experimental methods for the mechanical activation of polymers

1.2.1.1 Ultrasound sonication

Ultrasound generates mechanical stress on a polymer in solution. The high-frequency sound waves pass through the liquid and create cavitation, which is the generation, growth, and violent collapse of solvent microbubbles. After the collapse, the void space left induces a high-velocity solvent flow that drags the polymers' segments near the cavitation site. The flow velocities decrease rapidly away from the edge of the collapsing bubble, creating a velocity gradient along the polymer backbone. This causes the elongation of the chain by tensile forces of enough strength to break covalent bonds.⁽⁵⁶⁻⁵⁹⁾

Figure 1.1 shows a cartoon representation of the activation of a bulk of polymers with an ultrasound wave.

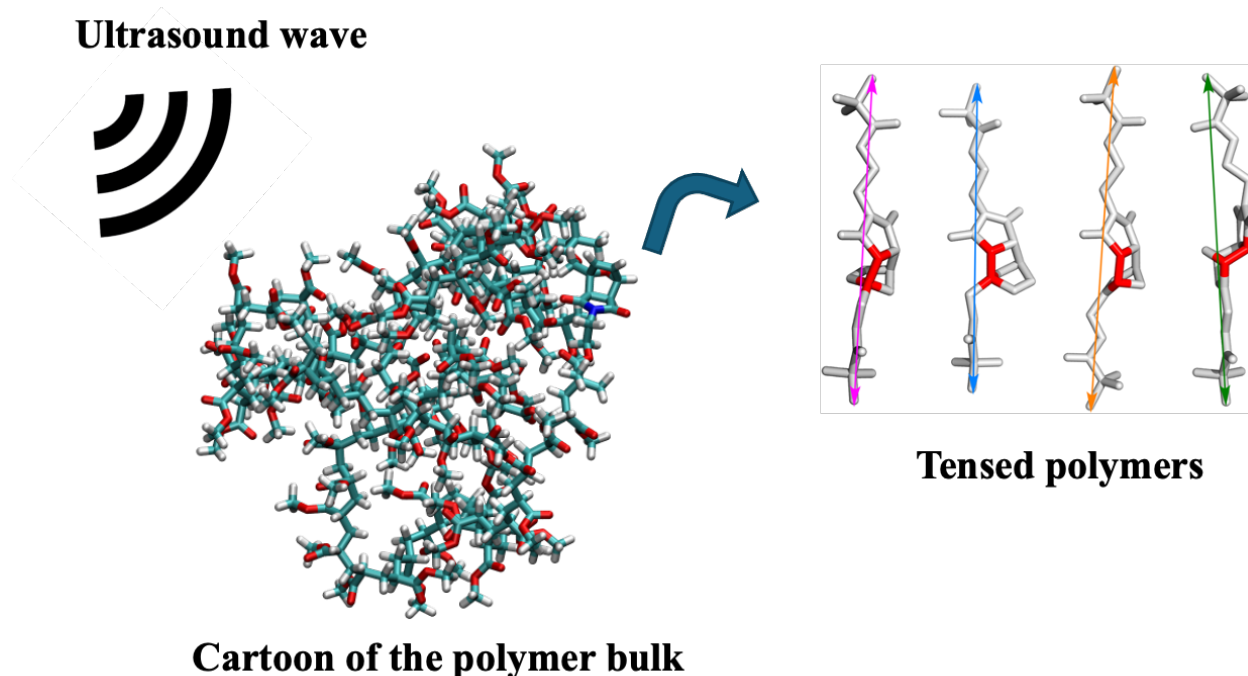


Figure 1.1: Mechanical activation of a bulk polymer system in solution using an ultrasound wave directed towards it. A mechanical force is collectively applied to the bulk system in an isotropic, non-directional way.

1.2.1.2 Single-molecule spectroscopy

Single-molecule force spectroscopy (SMFS) employs single-molecule manipulation techniques such as optical tweezers, magnetic tweezers, or atomic force microscopy (AFM) to examine mechanochemistry at the single-molecule level. Typically, one end of the molecule under study is attached to a surface, and the free end is attached to a probe: an optically trapped bead, magnetic bead, or AFM tip through which the force is applied.⁽⁶⁰⁾ Ideally, the bonds linking the molecule to the surface and to the probe would not break under stress and would not affect the mechanical or biological properties of the target molecule. For optical tweezers and the AFM, the magnitude of the force is calculated from the deviation of the probe from its equilibrium position. Therefore, the measurements' precision and accuracy depend critically on the ability to measure the position of the probe.⁽⁶⁰⁾

Our experimental partners from the NanoChem group have developed strategies and methods to graft molecules of interest onto AFM tips or surfaces and manipulate them at the single-molecule level. Such tools have been used to probe, trigger and control chemical processes and to detect the induced mechanical response *in situ* and in real-time. They have applied them to the investigation of molecular recognition processes and the detection of inter- and intra-molecular forces in biological systems (proteins, antigens, antibodies) or synthetic systems (receptors, polymers) and for the measurement of interaction forces of (macro)molecules on surfaces.⁽⁶¹⁻⁶⁵⁾ The group has shown that when combining mechanical forces and chemical interactions at the single molecule level and dealing with forces of single bonds, it was possible to selectively break covalent bonds and deliver single molecules on a target surface.⁽⁶¹⁾ This study was a landmark in single-molecule covalent mechanochemistry. Recently, the group applied SMFS to measure the force response of

synthetic small-molecule trefoil knots (66): structures with a knot-like topology (67), where a flexible chain of atoms is twisted into a three-looped configuration.

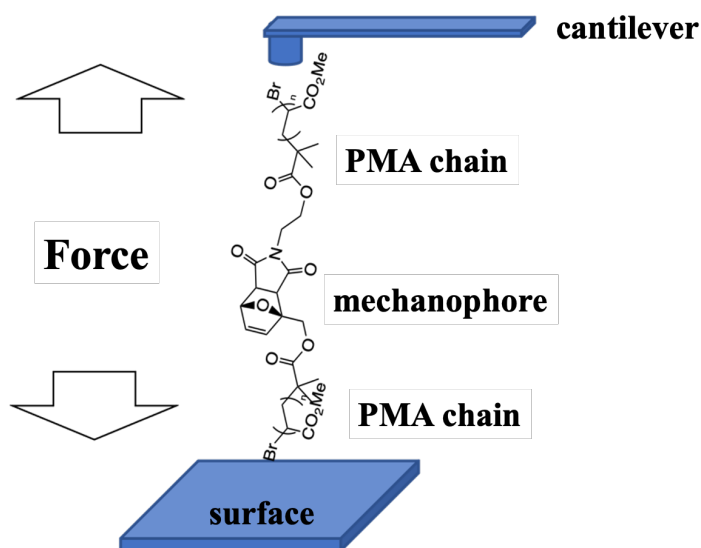


Figure 1.2: Experimental setup used in SMFS experiments. The PMA polymers with the mechanophore at the center are attached to the surface. The tip of the cantilever of an AFM is used to grab a single polymer and then stretch it until it breaks by exerting a mechanical force.

1.2.2 From mechanical activation to chemical reactivity

Mechanophores are the force-sensitive units present in the polymer that respond to external mechanical fields by undergoing predictable chemical transformations. (55) These include covalent bond-breaking reactions like selective cycloreversion and ring-opening reactions, and non-scissile events such as conformational changes, the (de)construction of aggregates, and the disruption of Coulombic and hydrogen bonding non-covalent interactions. (56, 68) These mechanically induced transformations occur when the mechanophores are appropriately positioned within the polymer chains to experience the applied forces. (56, 69) In SMFS/AFM experiments, the mechanophores are embedded in the middle of the chain, where the strain created by the pulling of both ends of the polymer has the highest intensity.

Bond rupture has been shown to occur in the nanonewton regime. (54, 70) However, SMFS has a resolution in the piconewton regime, allowing investigation into how changes in structure and conformation of the mechanophore itself affect the force required for mechanical activation. (54)

Wang et al. reported that the force required to open an E-alkene-substituted gem-dichlorocyclopropane (gDCC) mechanophore was 0.4 nN lower than that required for the corresponding Z-alkene-substituted mechanophore at ~ 800 pN. (71) Wang et al. have also used SMFS to observe several ring-opening reactions that are “forbidden” by the Woodward-Hoffmann rules, which describe the direction of concerted nuclear motion in electrocyclic reactions (8, 72). They found that it was possible to use SMFS to pull a gem-chlorofluorocyclopropane species outward in a disrotatory fashion along the anti-Woodward-Hoffmann-DePuy (WHD) pathway. Pill

et al. used SMFS to show the cycloreversion of cyclobutane with attached ethylene glycol chains of specific lengths to give a defined increase in polymer contour length within the experimentally accessible regime.(54, 73) Hickenboth *et al.* reported the mechanochemical ring-opening reaction of benzocyclobutane mechanophore to produce ortho-quinodimethide as the reactive intermediate.(4, 54)

Depending on how well the force is transduced to the reactive bond(s) of a particular functional group, mechanical activation can lead to an enhancement(74) or a reduction in reactivity.(75-79) For instance, it has been shown that the reactivity of a mechanophore is affected by stereo-,(8, 72, 80-84) regio-,(85-87) and even topological isomerism,(88) as well as by the nature of the linker joining the mechanophore to the force-transducing polymer.(71, 89-92)

External forces can induce nonstatistical dynamic effects (NDEs) resulting in product selectivities that differ from those achieved under thermal equilibration. They can also stabilize intermediate structures (83) and even shift the reaction mechanism. For instance, Liu et al. (93) demonstrated that an external force activates intramolecular motions in the cyclobutane ring-opening reaction, bypassing isomerization and resulting in high stereoselectivity. Tian et al. (94) showed that an external force can shift the rate-determining step in the reduction of organic disulfides by phosphines in water, which proceeds via a thiophosphonium zwitterionic intermediate. At low forces, the rate-determining step is the hydrolysis of the intermediate, but at higher forces, it shifts to the formation of the intermediate. In another study, Kean et al. (95) explored the mechanism of [2 + 2] cycloreversion in cyclobutane-based mechanophores, specifically bicyclo[4.2.0]octane (BCO) units, revealing that the ring-opening proceeds via a 1,4-diradical intermediate rather than a concerted mechanism.

The mechanical reversibility of the furane/maleimide DA reaction has been demonstrated through sonication. The group of De Bo at the University of Manchester synthesized both proximal and distal exo and endo adducts and studied the mechanical reactivity under sonication. (96) They found that proximal adducts tend to be more labile than their distal counterparts. In particular, the thermally active distal-exo adduct was inert under tension due to ineffective mechanochemical coupling arising from the misalignment of the scissile bonds with the force vector. In a recent study, the group showed the force-controlled release of furan molecules via a force-promoted double retro-[4+2][3+2] cycloaddition in oxanorbornane-triazoline-based mechanophores.(97)

The Craig group observed stereochemical effects in the furan–maleimide rDA reaction, where the endo adducts are more labile than the exo adducts (48). Our theoretical study (47) corroborates this result.

1.2.3 Role of theoretical calculations in mechanochemistry

Experimental studies in mechanochemistry are essential to understanding reactivity and the mechanical response of molecules under stress. However, their capabilities of observation are limited by the resolution of the instruments and by the challenging experimental conditions under which the instruments operate. SMFS is a sophisticated technique available only to a handful of laboratories worldwide. Carrying out SMFS measurements demands thorough planning and design of the experiments as well as expertise in the synthesis of the polymers, embedding the

mechanophore, and attaching the ends of the polymer to the tip of the AFM cantilever and to the surface. Moreover, to determine the magnitude of the forces in a bond-breaking event, the same experiment with the same pulling velocity must be realized thousands of times. This is necessary because the rupture forces are distributed over a wide range. (98) Hence, neither a single rupture event nor the average rupture force at any fixed pulling velocity can meaningfully characterize the strength of the chemical bond.(98)

Theoretical studies offer a comprehensive understanding of the mechanical response of molecular systems mimicking experimental conditions, thereby streamlining laboratory procedures and expediting the exploration and investigation of mechanophores. Additionally, they are a crucial tool for validating observations made through SMFS, particularly in instances where experimental analysis falls short. Theoretical studies are essential for analyzing processes inaccessible through experimentation alone, such as the internal relaxation of mechanophores upon force activation, the reactivity and mechanisms involving short-lived intermediates, and the dynamics of the bond breaking and possibly reformation.

Quantum-chemical calculations can quantify the restoring forces of all internal molecular coordinates and calculate geometries, energies, reaction rates, and other properties of mechanically deformed molecules.(99) Molecular dynamics can simulate the stretching of the polymers in solution in the presence of the external force, allowing us to study the effect on the reactivity of the mechanophore and discern the possible pathways that the force inhibits or activates. Dynamical methods(7) have the advantage that the multidimensional nature of the nuclear motion and temperature effects are inherently included. However, the computational cost limits the application of the simulation of mechanochemical processes from the theoretical point of view. As a result, the model systems used in calculations of mechanochemical processes generally employ truncated or coarse-grained representations of the external groups used to apply the force or even exclude these groups entirely.(2) In addition, modeling the force exerted by the external device (such as the AFM cantilever in our case) on the molecule is very challenging. It has been approached so far using either a classical interpretation of the force (isotensional approaches(100-102)) or indirectly measuring its effect (isometric approach(103)). Steered dynamics approaches (93, 104) allow us to explore dynamically the potential energy surfaces distorted by the external force using an ensemble of steered trajectories with initial thermal conditions. Typically, the reaction under force is found to proceed in a nonstatistical manner that depends on the strength and directionality of the external force applied to the system.

The response to the molecular strain induced by the external mechanical force is intrinsically multidimensional. The reason is that the direction of the external force that pulls the polymers can have components along several internal degrees of freedom, which may or may not participate in the bond rearrangement. Accordingly, the strain energy in the deformed structures is redistributed in a nonstatistical manner among the internal molecular degrees of freedom. Because of the intrinsic multidimensional character of the molecular response, as well as of the nN strength of the force involved in breaking and making covalent bonds, the reaction path can be significantly modified so that the simple one-dimensional Bell model(105) and its extensions(106) that provide valuable insights in the case of noncovalent mechanochemistry are usually not applicable in the case of covalent mechanochemistry. To break a covalent bond, what matters is not the nominal value of the force but instead the amount of energy or work that can be transferred to the bond. In

other words, it depends on how well the force projects on the target bond since the work is defined as $W = \vec{F} \cdot \vec{d} = F d \cos(\theta)$, where θ is the angle between the direction of the force and the bond.

In our investigation of furan/maleimide adducts under external mechanical force, such as the one exerted in SMFS or sonication experiments, we employed state-of-the-art methodologies to model the system itself and the interaction with the force. We used static methods to identify the reactants, transition states, products, and minimum energy reaction paths on the force-modified potential energy surfaces. Additionally, we examined the relevant thermodynamic and kinetic factors governing the reaction under mechanical stress, as well as the impact of the force on the electronic structure. Dynamical methods were then employed to study the effect of a constant velocity pulling of the system in solution, enabling us to relate the mechanochemical response to the rate of stretching.

The response of the mechanophore in SMFS occurs in an adiabatic regime of force applied to the nuclei in the ground electronic state of the system, where the electrons rearrange to equilibrium for every change in geometry of the nuclei induced by the external force. We also studied another kind of force that is established in the time scale comparable to the motion of the electrons. This force is exerted on the electrons and/or on the nuclei by the electric field of an attosecond pulse when it interacts with the charge distribution of the molecule, so its nature is electrostatic and not mechanical as in the case of SMFS. This electrostatic force is transduced into internal nuclear forces that determine the motion of the nuclei and the way the molecule relaxes in a more complex way compared to the mechanical force. This is because the electrons can be taken out of equilibrium and the molecule is driven into a quantum superposition of several electronic states. We advanced in the understanding of these internal forces that arise from the interaction with the pulse and during the motion of the superposition wavepacket, using a purely quantum approach. We developed a theoretical method, that relies on the integration of the time-dependent Schrödinger equation and the Ehrenfest theorem, to assess both the magnitude and direction of the force in molecular systems where the BO approximation is not valid and thus the force experienced by the nuclei is more complex than the classical definition $F = -\nabla V$ where V is a single potential energy surface. This includes strongly correlated systems like diradicals or transition metal complexes. Details on this approach are given in Chapter 5.

Attosecond pulse set-ups are now reaching a mature stage and becoming more compact and versatile. Attosecond and short fs pulses could be used to probe the progress of electronic and nuclear rearrangements of the mechanophore in SMFS upon force activation. On the other hand, longer laser pulses or CW lasers have been used to photoexcite the molecule that is subject to an external force. (49) Although quantum dynamics is currently applicable mainly to small molecules due to computational constraints, ongoing efforts, including our proposal (107) of a new efficient methodology for quantum dynamics in an ensemble of randomly oriented molecules, aim to extend its applicability to larger systems, to demonstrate control with attopulses in molecular systems of larger sizes.

1.2.4 The furan/maleimide retro Diels Alder reaction

Furan/maleimide adduct generically refers to bicyclic compounds synthesized by the [4+2] Diels-Alder (DA) cycloaddition of a derivative of furan (a conjugated diene, the donor) and a derivative of maleimide (a dienophile, the acceptor). In a DA reaction, partial charge transfer occurs from the diene to the dienophile, with electrostatic and dispersion interactions contributing to the stabilization of the adduct.^(108, 109) Figure 1.3 shows the furan/maleimide DA reaction object of this study.

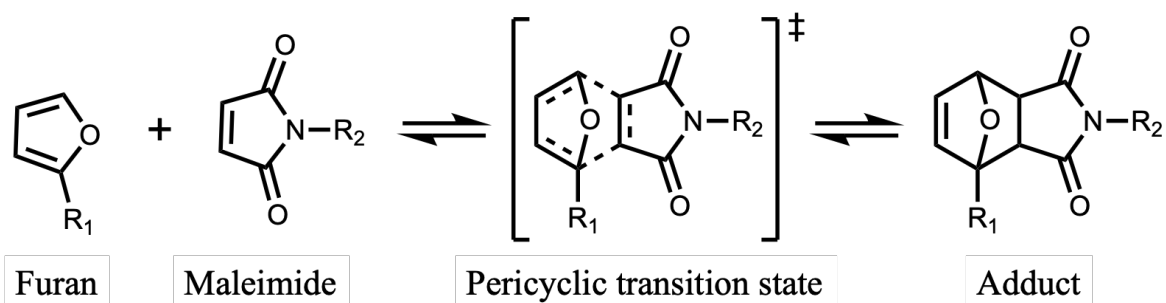


Figure 1.3 The furan/maleimide reaction. The transition state represented corresponds to the concerted reaction. R_1 and R_2 represent the attachments to the polymer chains when the adduct is used as a mechanophore.

Two stereoisomers can be formed depending on the orientation of the furan and maleimide parts. The *exo* stereoisomer adopts a Z-shape characterized by a minimal overlap between the two moieties. In contrast, in the *endo* stereoisomer, the two moieties approach each other with maximum overlap between their faces, resulting in a kind of C-shape. See Figure 1.4.

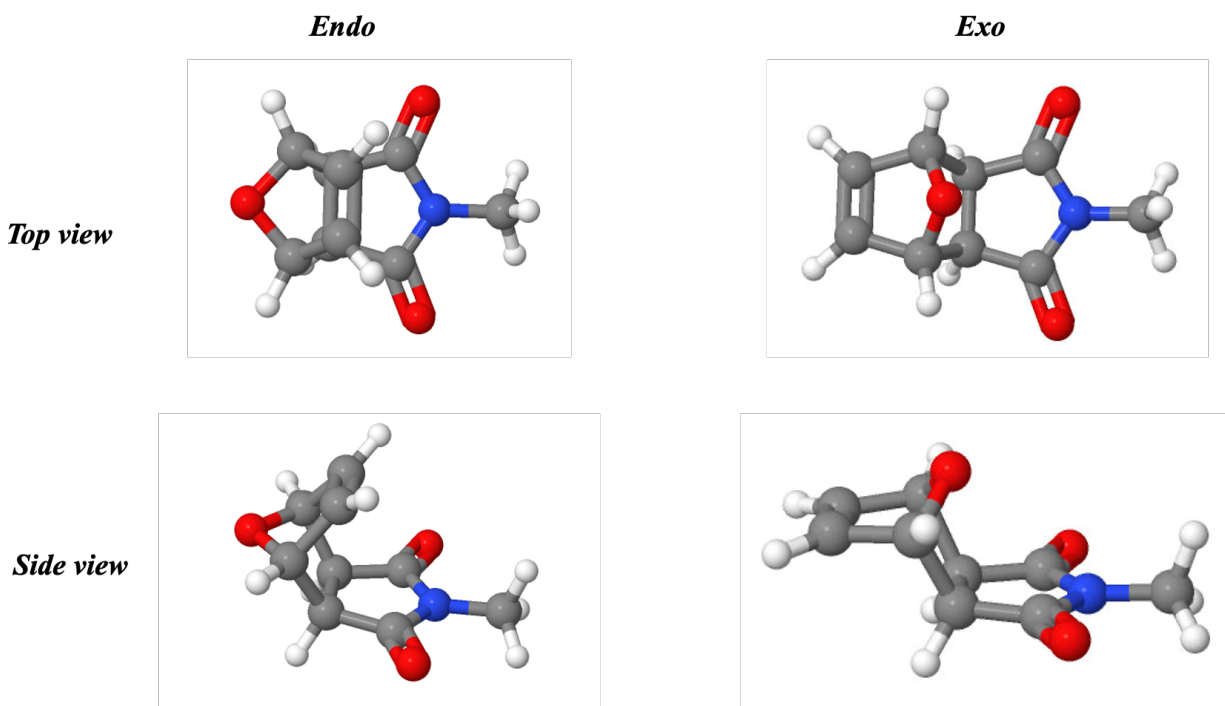


Figure 1.4: Stereoisomers *endo* and *exo* shown in 3D with different perspective. The C-shape of the *endo* stereoisomer, as opposed to the Z-shape of the *exo*, can be well appreciated.

In addition, according to the position of the substituent R1 in the furan moiety (see Figure 1.5), two regioisomers are possible: one proximal, where R1 is close to the furan/maleimide junction, and the other distal, where R1 is positioned farther away. In summary, four different isomers must be considered, and they are sketched in Figure 1.5.

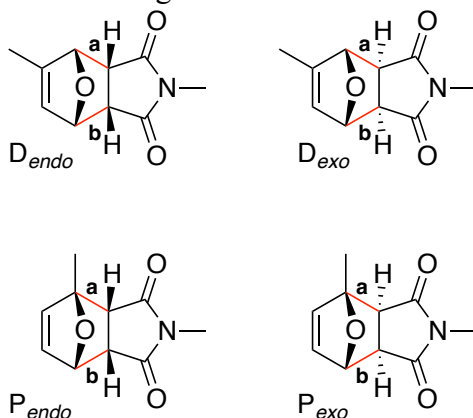


Figure 1.5 : The four furan/maleimide adducts investigated. They differ by their stereo (*endo* and *exo*) and regio (Distal and Proximal) character. The putative scissile bonds are shown in red and labeled 'a' and 'b'. 'a' is the bond along the shortest distance between the two methyl groups to which the pulling force is applied.

The furan/maleimide DA reaction has a low energetic barrier, allowing the reverse reaction also to take place under appropriate conditions. For example, the adducts which are stable at room temperature, break open after heating at elevated temperature. (110, 111) The mechanical reversibility has been demonstrated as well in sonication experiments.(96)

The interplay between attractive and repulsive interactions in the pericyclic transition state determines the stereoselectivity in Diels Alder reactions. The *endo* transition state is stabilized by secondary orbital and electrostatic interactions (112, 113) between the partially positively charged diene (furan) and the partially negative dienophile (maleimide). (108) The steric hindrance (114, 115) has the opposite effect, as it destabilizes the *endo* configuration in favor of the *exo* one. Substituents on the dienophile can change the charge distribution and alter this selectivity.(108, 116) In the furan/maleimide case, the *endo* transition state has a lower activation barrier, which kinetically favors the *endo* product. However, asymptotically, the *exo* adduct is thermodynamically favored, which can be explained by the lower steric hindrance in that configuration.

Concerning the role of substituents, the reaction is facilitated if the diene and the dienophile contain groups of opposite electrostatic character. Thus, electron-rich furan derivatives react quickly with electron-poor maleimide derivatives. For example, furans bearing electron-donating groups (e.g. H, Me, OMe, CH₂OH, etc.) display good kinetics, while electron-poor furans (e.g. with CH=O or COOR) are inactive substrates. (117) π -accepting groups conjugated to the dienophile's π -bond are activating because they lower the energy of the lowest unoccupied molecular orbital (LUMO) and enhance the mixing with the highest occupied MO of the diene. This results in a transfer of charge from the diene to the π -accepting groups conjugated to the dienophile's π -bond. Hence,

heteroatoms in those groups can form stronger hydrogen bonds with hydrogen-bond-donating solvent molecules, which contributes to stabilizing the pericyclic transition state. (118) Both forward and reverse reactions are accelerated in aqueous solution due to the hydrogen-bonding catalysis. (118, 119) Hydrocarbon and fluoruous solvents can also accelerate the reaction, although the increase in the rate is more modest relative to the one observed in water. (118)

There is a consensus that thermal DA and retro-DA reactions proceed in one step, but molecular dynamics studies have shown that there is some time lag (or time interval) between forming the first and second bonds. This time separation (~ 100 fs) is much shorter than the lifetime of a detectable intermediate (108), thereby supporting the idea of an asynchronous concerted mechanism. The stepwise mechanism, however, cannot be discarded. Experiments and theoretical results revealed an electric field-catalyzed mechanism with a zwitterionic intermediate for the furan/maleimide DA reaction at high temperatures in a high voltage. (119, 120) A shift to a stepwise zwitterionic mechanism was also proposed for the hetero-DA reaction of ketones with electron-rich dienes, and it was induced using chloroform as a solvent. (119, 121, 122) Zewail (1999), studying the femtosecond reaction dynamics of the retro-Diels-Alder reactions of norbornene and norbornadiene, concluded that both concerted and stepwise mechanisms are possible and that the asymmetry of the adduct, the barrier height, and the available energy are the controlling factors for the formation of nonconcerted trajectories involving a diradicaloid transition state. (123)

Thus, furan–maleimide adducts are characterized by dynamic (weak) covalent bonds (‘a’ and ‘b’ in Figure 1.5) that are more labile and slightly longer than typical carbon-carbon covalent bonds. They are susceptible to clean cycloreversion under relatively mild conditions, which makes them attractive mechanophores when embedded in polymers and networks.(2, 48, 96, 124-127) However, although their retro-DA reaction has been studied at room temperature under ultrasound sonication (57, 96, 124), before our work, (47) there was not a detailed understanding of the rupture mechanism of these adducts under tension, in particular on the concerted or sequential nature of the reaction path.(57) Our study (47), discussed in Chapter 3, showed that the rDA reaction can follow a sequential mechanism when the adducts are pulled by asymmetric forces of strength larger than 1 nN. We provided evidence that the reaction pathway has an intermediate diradical state, which is more stable in the exo configuration, thereby explaining its lower lability as reported by recent sonication experiments. (48) The external force inhibits the concerted mechanism but enhances the sequential pathway, favoring the dissociation through diradical intermediates.

1.3 Steering chemical reactivity with ultrashort light pulses

1.3.1 Attochemistry

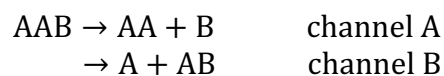
The time scale of electronic motion in a molecule is of the order of an attosecond: it takes 150 as for an electron to orbit around the nucleus in the hydrogen atom.(31, 128) This is orders of magnitude faster than the motion of the nuclei. This implies that by manipulating the electronic density, we can steer the nuclear motion and control the reactivity in a molecule. Attosecond pulses provide a means to do so because the electrical field of the pulse interacts with the molecular system on the natural time scale of the electronic motion, producing a non-equilibrium electronic state of the molecule that can be exploited to control the motion of the nuclei, thereby directing the way the molecule chemically reacts or relaxes. This paves the way for a new branch of chemistry, known as attochemistry, whose aim is to directly influence the electronic motion with

attopulses to cleave or form chemical bonds in molecules selectively or to vary the branching ratios of a photoinduced reaction.

When an attosecond pulse interacts with a molecule, because its duration is so short, the nuclei can be considered frozen, and only the electrons move. Therefore, the response of the molecule to the absorption of a photon from the light is a charge migration process (31, 129) that causes the redistribution of the electronic density. As the electrons migrate along the molecular backbone, the electron density increases in certain locations, and it is depleted in others, which ultimately causes the weakening or strengthening of covalent or non-covalent bonds once the nuclei begin to move. It is worth noting that as this process occurs so fast, the energy that can be transferred to the reactive modes as the nuclei begin to move is not redistributed to other modes in a statistical fashion as would be the case when exciting the molecule with longer pulses or with thermal excitation. This suggests the selectivity that can be achieved via excitation in the attosecond timescale.

1.3.2 Femtochemistry: Photoinduced control with femtosecond pulses

Before the development of attopulses at the turn of the XXI century, several experimental methods were proposed to exploit the quantum nature of light-matter interaction to design suitably tailored light fields capable of steering the molecule towards desired photoproducts. Using longer pulses, of a duration of dozens of femtoseconds or longer, whose energy is narrower so that typically a single electronic state is selectively excited. The Tannor-Rice-Kosloff scheme (130) proposes to control the time delay between the incidence of two femtosecond laser pulses directed towards a molecule to assist the synthesis of different products on the ground state potential energy surface. The first “pump” pulse creates a localized nonstationary wavepacket on a single bound excited state, which then evolves freely until the “dump” strong pulse brings it down to the ground state along the desired reaction channel, allowing the wave packet to “jump” any barrier obstructing that channel.(131) By controlling the delay, it is possible to control the propagation time on the excited state potential energy surface and dump a specific wave packet on the ground state at a specific time so that it evolves to the targeted product. This methodology exploits the coherent nature of the exciting and stimulating pulses and the vibrational wave packet evolution dynamics during the time delay on a single excited electronic state. The pulse shapes, durations, and separations required to achieve selectivity of product formation depend on the properties of the singly excited state potential energy surface and of the ground state. (130) However, the applicability of the pump-dump approach was limited by the difficulty in determining the pulses needed to steer the reactants into a given reaction channel. A solution to this problem came from optimal control theory. (132-135) The idea is to find the optimum laser pulse, specifically designed for the molecule, to enhance a given reaction channel while suppressing the others (131). Theoretically, given a wavefunction $\Psi(t_0)$ at a time t_0 the goal is to produce a wavefunction Φ at a later time t_f concentrated in one of the exit channels of a bifurcating chemical reaction (136) such as



The objective is then to maximize the functional $J = \langle \Psi(t_f) | P | \Psi(t_f) \rangle$, where $P \equiv |\Phi\rangle\langle\Phi|$ is the projection operator onto the state of interest, subject to physical and practical constraints such as fixing the total energy of the laser pulse.

Brumer and Schapiro developed an alternative approach (136). It uses two monochromatic laser fields with commensurate frequencies to drive an initially pure molecular state through two or more independent coherent optical excitation routes. The resultant product probability displays quantum-mechanical constructive and destructive interferences between these two routes, whose magnitude and sign depend upon laboratory parameters. Properly controlling the fields' amplitudes and phases makes it possible to enhance one reaction channel while suppressing the others selectively. (131)

The previous approaches relied on the ability to control experimental parameters of the laser pulses, such as the phase difference or the time delay. But recently, with the development of attosecond pulses (23, 27, 137), which allow the coherent excitation of several electronic states in molecules and the creation of electronic coherences in the Franck–Condon region, other degrees of freedom can be explored. For example, it has been shown that tuning parameters of the pulse, such as its carrier frequency, envelope duration, polarization, and carrier-envelope phase (CEP), provides control of the electronic motion in the initially pumped state and of the entanglement between the electronic and nuclear motions (38, 41-43)

1.3.3 Control with attopulses

In the literature, several reports of both experimental and theoretical works show examples of the application of attosecond pulses to steer chemical processes by exploiting the electronic coherences in the initial superposition state.

Kling (2006) (138) reported the first example of femtosecond control of the motion of the electrons in a molecule driven by light. They studied the dissociative ionization of the deuterium molecule ($D_2 \rightarrow D^+ + D$) triggered by few-cycle near-infrared laser pulses and showed that it is possible to control the localization of the electrons on the D^+ ions before the dissociation takes place. Sansone (2010) (139) extended this work by designing a pump-probe experiment where they measured the localization of the electronic charge distribution within the D_2 and H_2 molecules with an attosecond time resolution. They employed an attosecond ultraviolet laser as a pump to ionize D_2 and an intense few-cycle infrared pulse to probe the dissociation of the D^{2+} ion. The electronic localization is a consequence of the influence of the infrared laser on both the photoionization, by changing the wavefunction of the continuum electron, and the dissociation, by changing the wavefunction of the molecular ion.

Znakovskaya (2009) (140) described experiments and full quantum calculations that achieved control over the electron dynamics in carbon monoxide (CO) by manipulating the CEP of phase-stabilized 4 fs strong IR laser pulses. These pulses were utilized to dissociatively ionize the CO molecule, and the study highlighted a CEP dependence in the direction of the emitted ionic fragments. The experimental results revealed how varying the CEP affected the ionization process and the subsequent dynamics of the system, while the quantum mechanical calculations provided a mechanistic interpretation and understanding of the observed control.

Ranitovic (2013) (141), in a groundbreaking study, introduced a method for coherently exciting and controlling the outcome of a simple chemical reaction in a deuterium (D_2) molecule. They demonstrated that it is possible to precisely control molecular dynamics on both nuclear (femtosecond) and electronic (attosecond) timescales. Additionally, they showed that the population of electronic excited states in a neutral molecule can be switched, enabling the coherent steering of excitation and ionization along specific pathways. To achieve this, they employed trains of attosecond vacuum ultraviolet pulses, which are tunable across the frequency domain. Selective bond-breaking was accomplished by manipulating both the excitation wavelength and the time delay between the pump and probe pulses

Kraus (2015) (29) resolved spatially and temporally the charge migration of an electron hole right after the ionization of iodoacetylene (HCCI) with an intense IR laser field using High Harmonic Spectroscopy which allows for reconstructing both the amplitude and phase of the superposition of electronic states produced by strong-field ionization with a resolution of approximately 100 as. They also demonstrated extensive control over charge migration on a purely electronic time scale by controlling the direction of polarization of the IR pulse for exciting oriented molecules. The use of different driving wavelengths also provided the ability to tune the electron dynamics, revealing how the spatial configuration and laser parameters influence charge migration. An ultrashort period of about 2 fs was reported for the charge migration, showing that it takes place before a significant onset of nuclear motion, in agreement with the theoretical prediction for charge migration in short oligo-peptide cation previously reported (31).

Li (2015) (30) reported the experimental control of the spatial localization of the out-of-equilibrium electronic excitation in the C_{60} fullerene using an intense few-cycle IR CEP-controlled 4 fs pulse. The control is achieved by tailoring the CEP and the polarization direction of the pulse. For CEP = 0, the electron density is localized. Charge migration between the top and the bottom of the C_{60} cage takes place on a period of 3.5 fs, faster than typical vibrational periods of the cage.

Nikodem (2017) (37) investigated theoretically the nonequilibrium electronic dynamics in LiH induced by the interaction with strong ultrashort optical pulses coupled to nuclear motion including nonadiabatic effects. They show that switching the CEP from 0 to π controls the fragmentation yields of the different dissociation asymptotes. By changing the CEP, the electric field at its maximum can either point to the Li or to the H atom, which allows the selection of excited states with different polarities. This results in a different ionic character ($Li^{\delta+}H^{\delta-}$ vs $Li^{\delta-}H^{\delta+}$) in the nonstationary electronic wavepacket built at the end of the pulse, which in turn steers the nuclear dynamics to different dissociation products. The authors also demonstrated that the electronic coherences built with the pulse can be spectroscopically monitored by transient absorption, resulting from the interaction of the total molecular dipole with the electric field. This can be used as a probe of the phase of electronic coherences and the charge migration.

In the thesis, we report our efforts to advance the understanding of molecular phenomena triggered by the interaction with ultrafast lasers in the attosecond time scale and how to exploit them to steer and control certain chemical reactions. We introduce a theoretical scheme (142) (Chapter 5, Section 5.1) that aims to measure the effects of the electronic coherences built with an ultrashort pulse by determining and analyzing the forces experienced by the nuclei as they move in coupled potential energy surfaces. In addition, we propose a numerical scheme (107) that we discussed in

detail in Chapter 5, Section 5.2. It is based on the singular value decomposition of the density matrix of an ensemble of randomly oriented molecules to compute and interpret the non-adiabatic dynamics in a much less time-consuming and memory-efficient way than the approaches utilized so far.

We also studied the nonadiabatic dynamics of the ethylene cation following the sudden ionization and further excitation of a sample of the neutral molecule, using EUV pump pulses synthesized by HHG as the 9th, 11th, and 13th harmonics of IR pulses. It is reported in Chapter 4 and a recent publication submitted to *J. Phys. Chem. Lett.* Using a semiclassical surface hopping approach, we modeled the nonadiabatic dynamics of the cation and addressed important experimental questions such as why there is a strong isotope effect in the dissociation yields after H₂/D₂-loss and H/D-loss. We found that the slower motion of the wavepacket in the deuterated cation favors the relaxation to the ground state D₀ through a planar conical intersection that constrains the distribution of geometries, enhancing the three-photon resonant photoionization to D₃ that is induced by the IR probe in the experiments. Our theoretical computations found a period of ~ 50 fs in the oscillations of the yields, which agrees with the experiments carried out on the deuterated molecule.

1.3.4 High harmonic generation of attosecond pulses

When an intense laser pulse is directed towards a gas, plasma, solid, or liquid sample, it can induce multiphoton ionization, which is the source of several phenomena such as high harmonic generation, multiphoton two-electron ejection, and very high energy above-threshold-ionization electrons. They all arise from the interaction between the ejected electrons and ion parents since once the ionization takes place, there is a significant probability of finding the electron in the vicinity of the parent ion for one or more laser periods. (143) So strictly speaking, even though the photon beam can remove the weakest bounded electrons from the material, they can be accelerated back and forth by the oscillatory field of the pulse and follow trajectories around the ion that can lead to recollision and recombination events. This recombination process releases energy in the form of photons.

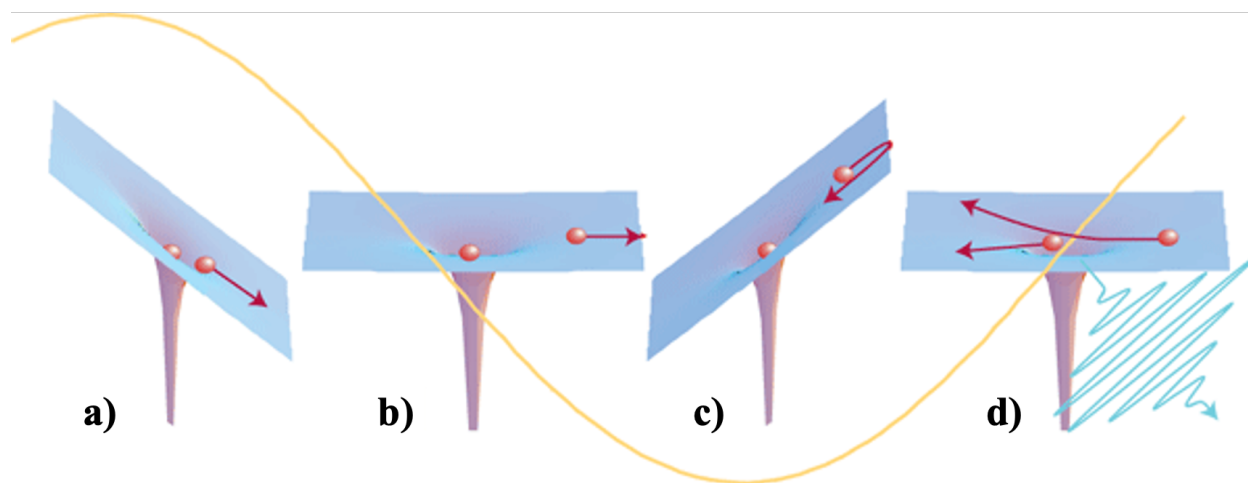


Figure 1.6. Illustration of the high harmonic generation process that allows the synthesis of XUV/soft X-ray attosecond pulses from an intense IR laser source. The IR in yellow causes strong field ionization of the atoms in the target sample, which leads to the ejection of the photoelectron

(a). The electron is then accelerated forward (b) and backward (c) in the field, moving around the parent ion. Due to the recombination of the electrons, carrying already kinetic energy from the field, with the parent ions, the excess energy is released as a photon with a higher frequency corresponding to harmonics of the IR driving pulse (d). This figure has been adapted from ref (25).

The attopulses that are used in the experiments to steer chemical reactions with light coherently are typically produced from the high harmonic generation (HHG) process driven by an intense near-IR femtosecond laser. This non-linear process leads to the emission of XUV or soft X-ray photons whose frequency is a high harmonic of the driver laser frequency. The formation of an attosecond pulse occurs during every optical half-cycle of the driver laser when the probability of electron ejection is sufficiently high, and the femtosecond laser is linearly polarized. (144) In practice, this produces a train of XUV/soft X-ray pulses (145) with a duration that is a small fraction of the optical cycle of the driver laser. In rare gas atoms, due to spherical symmetry, the harmonics are odd multiples of the frequency of the driver laser. (144)

But in the context of pump-probe experiments, a train of pulses is not ideal; instead, a single attosecond pulse must be isolated. This can be achieved by restricting the number of cycles in the driver NIR laser, which ensures that the ejection of electrons occurs during the most intense part of the laser pulse (temporal selection). (144) By further selecting only the highest-energy XUV photons produced during this phase (spectral selection), an isolated attosecond pulse can be generated. Krausz and others (146) reported for the first time the generation of an isolated attosecond pulse employing extremely short, few-cycle lasers. They demonstrated its application in tracing the electronic dynamics with a time resolution of ≤ 150 attoseconds.

1.4 Outline

Chapter 2 introduces the electronic structure and molecular dynamics methods used in our work in mechanochemistry and attochemistry. Special attention is given to the description with multireference quantum chemistry calculations of the open-shell diradical species that are intermediates in the furan/maleimide cycloreversion, and that require more careful treatment of the electronic structure than the adducts or the furan and maleimide species. We explain how to model molecules photoexcited by ultrashort attosecond laser pulses, typically synthesized via high harmonic generation (HHG) from a plasma gas. This mode of excitation differs from mechanochemistry in that instead of using an external mechanical force acting directly on the nuclei to steer chemical reactions, optical pulses are used where the electric field is the force acting on both negatively charged electrons and positively charged nuclei in the molecule. Attopulses are short enough to address selectively electrons in molecules. Because of their small mass, the electrons are set in motion by the electric field in an ultrafast timescale and the nonstationary electronic density can be used to steer the motion of the nuclei. In contrast, the external mechanical force acts only on the nuclei on a much slower timescale. In Chapter 2, we describe the quantum mechanical treatment of the molecule and the semiclassical treatment of its interaction with the electric field of the pulse. The attopulses are modeled with a Gaussian envelope applied to a sinusoidal carrier wave. Their properties are highly controllable in the experiments, offering great potential for exploring and steering reactivity in molecules. We provide the formalism for the time propagation of the time-dependent Schrödinger equation (TDSE) on a grid of nuclear coordinates, where the electronic potential energies, non-adiabatic couplings, and transition dipoles are precomputed to construct the matrix of the Hamiltonian. This method allows us to study the

interaction of the LiH/LiT molecules with attosecond pulses (Chapters 5 and 6) and the ultrafast relaxation of the CD_4^+ cation following sudden ionization of the neutral molecule (Chapter 7). In addition to analyzing the discretization of the wavefunction and the process of constructing the matrix of the Hamiltonian, accounting for nonadiabatic couplings and light-matter interactions, we also describe the computational implementation. For example, we discuss the Runge-Kutta method used to solve the TDSE numerically. Finally, we explore methodologies for studying the nonadiabatic dynamics of larger molecules. In particular, we describe the surface hopping (SH) method, which treats the nuclei classically while treating the electrons quantum mechanically. We applied this method to the study of the ethylene cation presented in Chapter 4, using the SHARC program. We highlight crucial aspects of the SH method, particularly the importance of generating a correct sample of initial conditions from the Wigner distribution, which enables accurate characterization of the molecule in its ground electronic and vibrational state before sudden excitation by the pulse. The sudden ionization process is described using the Franck-Condon principle for the ethylene and the methane cation.

Chapter 3 discusses the mechanical activation of proximal endo and exo furan/maleimide adducts under external forces, such as those exerted on both ends of a single polymer chain by an atomic force microscopy (AFM) cantilever. The polymers studied are made of polymethyl acrylate units with a furan/maleimide mechanophore located in the center. We model the retro-Diels-Alder (rDA) reaction responsible for the rupture of two bonds in the furan/maleimide adducts, forming the stable molecules furan and maleimide, which we call scissile bonds. We present state-of-the-art computational methodologies used to simulate the stretching of the mechanophore under external force. Additionally, we analyze the approach employed to estimate free energies and rates from ab initio computations. Switching of the mechanism under force has been reported for another type of pericyclic reaction forbidden by the Woodward-Hoffmann rules on the ground electronic state. (8, 72) Here, we report a switch in the mechanism of the furan/maleimide rDA reaction, a [4+2] reaction that is allowed by WH rules on the ground electronic state, under external force, from the typical concerted mechanism, where both bond ruptures occur simultaneously, to a sequential mechanism. This mechanism is mediated by a diradical intermediate, with the two bond ruptures occurring at different times. These findings have been published in (47).

Chapter 4 presents our study on the nonadiabatic dynamics of deuterated and hydrogenated ethylene cations triggered by excitation with the 13th, 11th, and 9th EUV harmonics synthesized from an IR driver pulse. This work was carried out in collaboration with the group of Mauro Nisoli (Politecnico di Milano). We describe in detail the motivation for this study and present our theoretical results, which help explain the experimental observations. In the experiments, the pump few-fs EUV pulses are broad-in-energy, meaning that when they interact with the neutral ethylene molecule, they ionize the molecule and create the cation in a superposition of several electronic states. Due to the complexity of this phenomenon, we do not strictly model it in our computations. Instead, we approximate the process by considering a sudden ionization of the neutral ground state to the four lowest excited states of the cation: D_0 , D_1 , D_2 , and D_3 . Using experimentally measured photoionization cross-sections, we extrapolate our insights from the dynamics to provide a relevant interpretation of the physics and chemistry underlying the experimental observations. Particularly, we explain the mechanism by which the isotopic substitution stabilizes the oscillations in the dissociation yields of the cation. We corroborate the mechanism of three-photon resonant excitation from the ground state D_0 of the cation to the excited state D_3 , as discussed in ref (147),

which leads to higher differential dissociation yields. In addition, we discuss that the isotope effect originates from the dynamics of the excited wavepacket through the network of conical intersections. As shown in the chapter, one of the main planar conical intersections between D_0 and D_1 is favored due to the slower motion of the deuterated wavepacket compared to the hydrogenated one. The passage through this conical intersection constrains the distribution of geometries that reach the ground state to have an elongated CC bond and activated torsional motion. These geometries favor the re-excitation to D_3 due to a large transition dipole D_0/D_3 . Additionally, the activated torsional motion has a period of ~ 70 fs in the hydrogenated ethylene cation, while in the deuterated case, it is ~ 100 fs. This means the molecule is planar every 50 fs, explaining the period found in the experiments, particularly noticeable in the deuterated molecule. This work has been submitted for publication and is under revision.

Chapters 5 and 6 summarize our work in attochemistry that contributed to advancing the attosecond science field to achieve the goal of steering and controlling chemical reactivity by exploiting the electronic coherences induced by attopulses. In Chapter 5, we present a theoretical formalism we developed and published (*142*) to compute the forces exerted by the vibronic wavepacket on the nuclei during and after the interaction of the molecule with the electric field of the pulse, using the dipole approximation. This method, derived from the Ehrenfest theorem in quantum mechanics, provides a theoretical framework to monitor the force on the nuclei exerted by the vibronic wave packet to changes in the parameters of the pulse. Specifically, we investigate how altering the carrier-envelope phase (CEP) of the pulse can tune the composition of the wavepacket, which is built as a superposition of several electronic states. This, in turn, affects the forces acting on the nuclei during the dynamics, thereby influencing the nuclear motion and reactivity. We present numerically converged results for the wave packet dynamics of LiH and LiT molecules excited by broad-in-energy CEP-controlled NIR pulses and a VIS pulse.

In Chapter 6, we discuss a method for simplifying the treatment of an ensemble of randomly oriented molecules interacting with an electric field, a more realistic scenario in the experiments compared to assuming a specific molecular orientation with respect to the polarization direction of the field. In the molecular frame, this can be achieved by sampling many orientations of the pulse polarization with respect to the molecule from the unit sphere, integrating the TDSE for each orientation, and then averaging the resulting dynamics over the pulse polarization direction. However, this approach proved computationally expensive. To address this, we developed and published a computational scheme (*107*), based on singular value decomposition (SVD) of the matrix of the wavefunctions for all the sampled orientations at the end of the pulse. We explain this method in the chapter and demonstrate its application to the efficient modeling of the dynamics in an ensemble of randomly oriented LiH molecules. After the pulse, only a few principal orientations remain, and we can explore how these principal orientations influence the quantum dynamics, providing insights into the stereodynamics of the ensemble. We demonstrate the method's efficiency, as it leads to massive data compaction and saves computational time and resources.

Chapter 7 discusses perspectives and ongoing efforts that advance the research presented in the thesis in both mechanochemistry and attochemistry fields. Concerning mechanochemistry, we discuss future work, including the modeling of the stretching of the furan/maleimide adducts with additional PMA units and the inclusion of solvent effects. Based on the literature analysis and

preliminary studies presented in this chapter, we propose two methodologies to describe the combined effects of the external force on the polymer and mechanophore. The first, Ab-initio Steered Molecular Dynamics (AISMD), is well-suited for studying polymers with a few PMA units, allowing observation of the dynamics of the bond breaking at a fixed external force. The second approach, classical Steered Molecular Dynamics (SMD), is suitable for modeling constant-velocity pulling experiments done in the single-molecule force spectroscopy (SMFS) field. While less accurate due to the use of force fields like Amber to model the potential of the ground electronic state of the molecule, SMD is computationally more efficient and enables the modeling of complex systems, such as large polymer chains surrounded by thousands of solvent molecules. SMD can also be combined with a QM/MM method to treat quantum-mechanically the mechanophore, enabling the description of bond-breaking events while the polymer chains are treated classically. In attochemistry, we discuss our current efforts to extend the method introduced in Chapter 5, which computes the force of the wave packet on the nuclei. We show preliminary results related to the analysis of the forces in the system studied in Chapter 6, which corresponds to an ensemble of randomly oriented LiH molecules interacting with the electric field of an attopulse. We examined the components of the force arising for each of the principal orientations of the electric field, determined by SVD. We also apply the methodology of the vibronic force to study a system with more than one nuclear degree of freedom such as the CD_4^+ cation using the potential energy surfaces and electronic structure data of a previous work. (148)

Finally, in Chapter 8, we revisit the key results presented in this thesis and discuss their broader impact and significance for both mechanochemistry and attochemistry. We emphasize the understanding gained throughout this research, aiming to advance the control of chemical reactivity using external perturbations, such as mechanical forces or light pulses.

1.5 References

1. R. Chang, *Chemistry*. (McGraw-Hill, Boston, ed. 10th, 2010), pp. 1.
2. R. Boulatov, Ed., *Polymer Mechanochemistry*, (Springer, 2015), vol. 369, pp. 1-377.
3. S. Garcia-Manyes, A. E. M. Beedle, Steering chemical reactions with force. *Nat Rev Chem* **1**, 1-16 (2017).
4. C. R. Hickenboth *et al.*, Biasing reaction pathways with mechanical force. *Nature* **446**, 423-427 (2007).
5. F. R. Kersey, W. C. Yount, S. L. Craig, Single-Molecule Force Spectroscopy of Bimolecular Reactions: System Homology in the Mechanical Activation of Ligand Substitution Reactions. *J. Am. Chem. Soc.* **128**, 3886-3887 (2006).
6. J. N. Ladenthin *et al.*, Force-induced tautomerization in a single molecule. *Nature Chem* **8**, 935-940 (2016).
7. J. Ribas-Arino, D. Marx, Covalent Mechanochemistry: Theoretical Concepts and Computational Tools with Applications to Molecular Nanomechanics. *Chem. Rev.* **112**, 5412-5487 (2012).
8. J. Wang *et al.*, Inducing and quantifying forbidden reactivity with single-molecule polymer mechanochemistry. *Nature Chem* **7**, 323-327 (2015).
9. J. Longworth, B. P. Krueger, G. R. Fleming, E. Britannica., Ed. (2023).

10. N. E. Henriksen, Laser control of chemical reactions. *Chemical Society Reviews* **31**, 37-42 (2002).
11. A. H. Zewail, Femtochemistry: Atomic-Scale Dynamics of the Chemical Bond. *J. Phys. Chem. A* **104**, 5660-5694 (2000).
12. C. E. Ascheron, H. J. Kölsch, W. Skolaut, Eds., *Femtosecond Technology for Technical and Medical Applications*, (Springer Berlin Heidelberg, Berlin, Heidelberg, 2004), vol. 96.
13. S. H. Chung, E. Mazur, Surgical applications of femtosecond lasers. *Journal of Biophotonics* **2**, 557-572 (2009).
14. Y. Han *et al.*, Generation, optimization, and application of ultrashort femtosecond pulse in mode-locked fiber lasers. *Progress in Quantum Electronics* **71**, 100264 (2020).
15. I. V. Ilina *et al.*, Application of femtosecond laser pulses in biomedical cell technologies. *High Temp* **51**, 173-178 (2013).
16. S. Lei *et al.*, Ultrafast Laser Applications in Manufacturing Processes: A State-of-the-Art Review. *Journal of Manufacturing Science and Engineering* **142**, 031005 (2020).
17. X. Liu, in *Lasers and Applications in Science and Engineering*, J. Fieret *et al.*, Eds. (2005), pp. 372.
18. G. Farkas, C. Tóth, Proposal for attosecond light pulse generation using laser induced multiple-harmonic conversion processes in rare gases. *Physics Letters A* **168**, 447-450 (1992).
19. M. Nisoli, Attosecond science the art of making electron movies. *Europhysics News* **55**, 22-25 (2024).
20. M. Nisoli, G. Sansone, New frontiers in attosecond science. *Progress in Quantum Electronics* **33**, 17-59 (2009).
21. P. Agostini, L. F. DiMauro, The physics of attosecond light pulses. *Rep. Prog. Phys.* **67**, 813 (2004).
22. D. M. Villeneuve, Attosecond science. *Contemporary Physics* **59**, 47-61 (2018).
23. M. Nisoli, P. Decleva, F. Calegari, A. Palacios, F. Martín, Attosecond Electron Dynamics in Molecules. *Chem. Rev.* **117**, 10760-10825 (2017).
24. P. H. Bucksbaum, The future of attosecond spectroscopy. *Science* **317**, 766-769 (2007).
25. P. B. Corkum, F. Krausz, Attosecond science. *Nature Phys* **3**, 381-387 (2007).
26. H. Kapteyn, O. Cohen, I. Christov, M. Murnane, Harnessing Attosecond Science in the Quest for Coherent X-rays. *Science* **317**, 775-778 (2007).
27. F. Krausz, M. Ivanov, Attosecond physics. *Rev. Mod. Phys.* **81**, 163-234 (2009).
28. F. Calegari *et al.*, Ultrafast electron dynamics in phenylalanine initiated by attosecond pulses. *Science* **346**, 336-339 (2014).
29. P. M. Kraus *et al.*, Measurement and laser control of attosecond charge migration in ionized iodoacetylene. *Science* **350**, 790-795 (2015).
30. H. Li *et al.*, Coherent Electronic Wave Packet Motion in C₆₀ Controlled by the Waveform and Polarization of Few-Cycle Laser Fields. *Phys. Rev. Lett.* **114**, 123004 (2015).

31. F. Remacle, R. D. Levine, An electronic time scale in chemistry. *Proc. Natl. Acad. Sci. U.S.A.* **103**, 6793-6798 (2006).
32. J. Breidbach, L. S. Cederbaum, Migration of holes: Formalism, mechanisms, and illustrative applications. *The Journal of Chemical Physics* **118**, 3983-3996 (2003).
33. L. S. Cederbaum, J. Zobeley, Ultrafast charge migration by electron correlation. *Chemical Physics Letters* **307**, 205-210 (1999).
34. A. I. Kuleff, L. S. Cederbaum, Charge migration in different conformers of glycine: The role of nuclear geometry. *Chemical Physics* **338**, 320-328 (2007).
35. F. Remacle, R. D. Levine, M. A. Ratner, Charge directed reactivity: a simple electronic model, exhibiting site selectivity, for the dissociation of ions. *Chemical Physics Letters* **285**, 25-33 (1998).
36. F. Remacle, R. D. Levine, E. W. Schlag, R. Weinkauff, Electronic Control of Site Selective Reactivity: A Model Combining Charge Migration and Dissociation. *J. Phys. Chem. A* **103**, 10149-10158 (1999).
37. A. Nikodem, R. D. Levine, F. Remacle, Spatial and temporal control of populations, branching ratios, and electronic coherences in LiH by a single one-cycle infrared pulse. *Phys. Rev. A* **95**, 053404 (2017).
38. F. Remacle, M. Nest, R. D. Levine, Laser Steered Ultrafast Quantum Dynamics of Electrons in LiH. *Phys. Rev. Lett.* **99**, 183902 (2007).
39. A. Valentini, S. v. d. Wildenberg, F. Remacle, Selective bond formation triggered by short optical pulses: quantum dynamics of a four-center ring closure. *Phys. Chem. Chem. Phys.* **22**, 22302-22313 (2020).
40. S. van den Wildenberg, B. Mignolet, R. D. Levine, F. Remacle, Temporal and spatially resolved imaging of the correlated nuclear-electronic dynamics and of the ionized photoelectron in a coherently electronically highly excited vibrating LiH molecule. *The Journal of Chemical Physics* **151**, 134310 (2019).
41. M. Blavier, R. D. Levine, F. Remacle, Time evolution of entanglement of electrons and nuclei and partial traces in ultrafast photochemistry. *Phys. Chem. Chem. Phys.* **24**, 17516-17525 (2022).
42. L.-M. Koll, L. Maikowski, L. Drescher, T. Witting, M. J. J. Vrakking, Experimental Control of Quantum-Mechanical Entanglement in an Attosecond Pump-Probe Experiment. *Phys. Rev. Lett.* **128**, 043201 (2022).
43. Y. Nabekawa, K. Midorikawa, Analysis of attosecond entanglement and coherence using feasible formulae. *Phys. Rev. Res.* **5**, 033083 (2023).
44. F. Calegari, G. Sansone, S. Stagira, C. Vozzi, M. Nisoli, Advances in attosecond science. *J. Phys. B: At. Mol. Opt. Phys.* **49**, 062001 (2016).
45. L. Gallmann, C. Cirelli, U. Keller, Attosecond Science: Recent Highlights and Future Trends. *Annu. Rev. Phys. Chem.* **63**, 447-469 (2012).
46. X. Shi *et al.*, Attosecond light science and its application for probing quantum materials. *J. Phys. B: At. Mol. Opt. Phys.* **53**, 184008 (2020).
47. M. Cardosa-Gutierrez, G. De Bo, A.-S. Duwez, F. Remacle, Bond breaking of furan-maleimide adducts *via* a diradical sequential mechanism under an external mechanical force. *Chemical Science* **14**, 1263-1271 (2023).

48. Z. Wang, S. L. Craig, Stereochemical effects on the mechanochemical scission of furan–maleimide Diels–Alder adducts. *Chemical Communications* **55**, 12263-12266 (2019).
49. X. Hu, M. E. McFadden, R. W. Barber, M. J. Robb, Mechanochemical Regulation of a Photochemical Reaction. *J. Am. Chem. Soc.* **140**, 14073-14077 (2018).
50. D. Rivero *et al.*, Mechanical Forces Alter Conical Intersections Topology. *J. Chem. Theory Comput.* **11**, 3740-3745 (2015).
51. T. Kim, L. Zhu, R. O. Al-Kaysi, C. J. Bardeen, Organic Photomechanical Materials. *ChemPhysChem* **15**, 400-414 (2014).
52. K. M. Lee *et al.*, Enhancement of Photogenerated Mechanical Force in Azobenzene-Functionalized Polyimides. *Angewandte Chemie* **124**, 4193-4197 (2012).
53. M. H. Tong *et al.*, Multiphoton photochemical crosslinking-based fabrication of protein micropatterns with controllable mechanical properties for single cell traction force measurements. *Sci Rep* **6**, 20063 (2016).
54. N. Willis-Fox, E. Rognin, T. A. Aljohani, R. Daly, Polymer Mechanochemistry: Manufacturing Is Now a Force to Be Reckoned With. *Chem* **4**, 2499-2537 (2018).
55. J. Li, C. Nagamani, J. S. Moore, Polymer Mechanochemistry: From Destructive to Productive. *Acc. Chem. Res.* **48**, 2181-2190 (2015).
56. K. M. Wiggins, J. N. Brantley, C. W. Bielawski, Methods for activating and characterizing mechanically responsive polymers. *Chemical Society Reviews* **42**, 7130-7147 (2013).
57. S. Akbulatov, R. Boulatov, Experimental Polymer Mechanochemistry and its Interpretational Frameworks. *ChemPhysChem* **18**, 1422-1450 (2017).
58. T. G. McKenzie, F. Karimi, M. Ashokkumar, G. G. Qiao, Ultrasound and Sonochemistry for Radical Polymerization: Sound Synthesis. *Chemistry A European J* **25**, 5372-5388 (2019).
59. T. J. Mason, J. P. Lorimer, *Applied Sonochemistry: Uses of Power Ultrasound in Chemistry and Processing*. (Wiley, ed. 1, 2002).
60. K. C. Neuman, A. Nagy, Single-molecule force spectroscopy: optical tweezers, magnetic tweezers and atomic force microscopy. *Nat Methods* **5**, 491-505 (2008).
61. A.-S. Duwez *et al.*, Mechanochemistry: targeted delivery of single molecules. *Nature Nanotech* **1**, 122-125 (2006).
62. P. Lussis *et al.*, A single synthetic small molecule that generates force against a load. *Nature Nanotech* **6**, 553-557 (2011).
63. D. Sluysmans, F. Devaux, C. J. Bruns, J. F. Stoddart, A.-S. Duwez, Dynamic force spectroscopy of synthetic oligorotaxane foldamers. *Proc. Natl. Acad. Sci. U.S.A.* **115**, 9362-9366 (2018).
64. D. Sluysmans *et al.*, Synthetic oligorotaxanes exert high forces when folding under mechanical load. *Nature Nanotech* **13**, 209-213 (2018).
65. A. Van Quaethem, P. Lussis, D. A. Leigh, A.-S. Duwez, C.-A. Fustin, Probing the mobility of catenane rings in single molecules. *Chemical Science* **5**, 1449 (2014).
66. M. Calvaresi *et al.*, Mechanical tightening of a synthetic molecular knot. *Chem* **9**, 65-75 (2023).

67. S. D. P. Fielden, D. A. Leigh, S. L. Woltering, Molecular Knots. *Angew Chem Int Ed* **56**, 11166-11194 (2017).
68. M. M. Caruso *et al.*, Mechanically-Induced Chemical Changes in Polymeric Materials. *Chem. Rev.* **109**, 5755-5798 (2009).
69. J. N. Brantley, K. M. Wiggins, C. W. Bielawski, Polymer mechanochemistry: the design and study of mechanophores. *Polymer International* **62**, 2-12 (2013).
70. J. M. Lenhardt, A. L. Black Ramirez, B. Lee, T. B. Kouznetsova, S. L. Craig, Mechanistic Insights into the Sonochemical Activation of Multimechanophore Cyclopropanated Polybutadiene Polymers. *Macromolecules* **48**, 6396-6403 (2015).
71. J. Wang *et al.*, A Remote Stereochemical Lever Arm Effect in Polymer Mechanochemistry. *J. Am. Chem. Soc.* **136**, 15162-15165 (2014).
72. J. Wang, T. B. Kouznetsova, S. L. Craig, Reactivity and Mechanism of a Mechanically Activated anti-Woodward–Hoffmann–DePuy Reaction. *J. Am. Chem. Soc.* **137**, 11554-11557 (2015).
73. M. F. Pill *et al.*, Mechanochemical Cycloreversion of Cyclobutane Observed at the Single Molecule Level. *Chemistry A European J* **22**, 12034-12039 (2016).
74. M. K. Beyer, H. Clausen-Schaumann, Mechanochemistry: The Mechanical Activation of Covalent Bonds. *Chem. Rev.* **105**, 2921-2948 (2005).
75. S. Akbulatov *et al.*, Experimentally realized mechanochemistry distinct from force-accelerated scission of loaded bonds. *Science* **357**, 299-303 (2017).
76. S. Akbulatov, Y. Tian, E. Kapustin, R. Boulatov, Model Studies of the Kinetics of Ester Hydrolysis under Stretching Force. *Angew Chem Int Ed* **52**, 6992-6995 (2013).
77. S. Garcia-Manyes, J. Liang, R. Szoszkiewicz, T.-L. Kuo, J. M. Fernández, Force-activated reactivity switch in a bimolecular chemical reaction. *Nature Chem* **1**, 236-242 (2009).
78. M. Krupička, W. Sander, D. Marx, Mechanical Manipulation of Chemical Reactions: Reactivity Switching of Bergman Cyclizations. *J. Phys. Chem. Lett.* **5**, 905-909 (2014).
79. B. Lee, Z. Niu, J. Wang, C. Slebodnick, S. L. Craig, Relative Mechanical Strengths of Weak Bonds in Sonochemical Polymer Mechanochemistry. *J. Am. Chem. Soc.* **137**, 10826-10832 (2015).
80. R. Groote *et al.*, Strain-Induced Strengthening of the Weakest Link: The Importance of Intermediate Geometry for the Outcome of Mechanochemical Reactions. *Macromolecules* **47**, 1187-1192 (2014).
81. M. J. Kryger, A. M. Munaretto, J. S. Moore, Structure–Mechanochemical Activity Relationships for Cyclobutane Mechanophores. *J. Am. Chem. Soc.* **133**, 18992-18998 (2011).
82. J. M. Lenhardt *et al.*, Reactive Cross-Talk between Adjacent Tension-Trapped Transition States. *J. Am. Chem. Soc.* **133**, 3222-3225 (2011).
83. J. M. Lenhardt *et al.*, Trapping a Diradical Transition State by Mechanochemical Polymer Extension. *Science* **329**, 1057-1060 (2010).
84. J. Wang, T. B. Kouznetsova, S. L. Craig, Single-Molecule Observation of a Mechanically Activated *Cis*-to-*Trans* Cyclopropane Isomerization. *J. Am. Chem. Soc.* **138**, 10410-10412 (2016).

85. G. R. Gossweiler, T. B. Kouznetsova, S. L. Craig, Force-Rate Characterization of Two Spiropyran-Based Molecular Force Probes. *J. Am. Chem. Soc.* **137**, 6148-6151 (2015).
86. S. S. M. Konda *et al.*, Molecular Catch Bonds and the Anti-Hammond Effect in Polymer Mechanochemistry. *J. Am. Chem. Soc.* **135**, 12722-12729 (2013).
87. M. J. Robb *et al.*, Regioisomer-Specific Mechanochromism of Naphthopyran in Polymeric Materials. *J. Am. Chem. Soc.* **138**, 12328-12331 (2016).
88. B. Lee, Z. Niu, S. L. Craig, The Mechanical Strength of a Mechanical Bond: Sonochemical Polymer Mechanochemistry of Poly(catenane) Copolymers. *Angew Chem Int Ed* **55**, 13086-13089 (2016).
89. H. M. Klukovich *et al.*, Tension Trapping of Carbonyl Ylides Facilitated by a Change in Polymer Backbone. *J. Am. Chem. Soc.* **134**, 9577-9580 (2012).
90. H. M. Klukovich, T. B. Kouznetsova, Z. S. Kean, J. M. Lenhardt, S. L. Craig, A backbone lever-arm effect enhances polymer mechanochemistry. *Nature Chem* **5**, 110-114 (2013).
91. J. Ribas-Arino, M. Shiga, D. Marx, Mechanochemical Transduction of Externally Applied Forces to Mechanophores. *J. Am. Chem. Soc.* **132**, 10609-10614 (2010).
92. Y. Tian, R. Boulatov, Quantum-Chemical Validation of the Local Assumption of Chemomechanics for a Unimolecular Reaction. *ChemPhysChem* **13**, 2277-2281 (2012).
93. Y. Liu *et al.*, Flyby reaction trajectories: Chemical dynamics under extrinsic force. *Science* **373**, 208-212 (2021).
94. Y. Tian, T. J. Kucharski, Q.-Z. Yang, R. Boulatov, Model studies of force-dependent kinetics of multi-barrier reactions. *Nat Commun* **4**, 2538 (2013).
95. Z. S. Kean, Z. Niu, G. B. Hewage, A. L. Rheingold, S. L. Craig, Stress-Responsive Polymers Containing Cyclobutane Core Mechanophores: Reactivity and Mechanistic Insights. *J. Am. Chem. Soc.* **135**, 13598-13604 (2013).
96. R. Stevenson, G. De Bo, Controlling Reactivity by Geometry in Retro-Diels–Alder Reactions under Tension. *J. Am. Chem. Soc.* **139**, 16768-16771 (2017).
97. K. Suwada, A. W. Jeong, H. L. H. Lo, G. De Bo, Furan Release via Force-Promoted Retro-[4+2][3+2] Cycloaddition. *J. Am. Chem. Soc.* **145**, 20782-20785 (2023).
98. S. Getfert, M. Evstigneev, P. Reimann, Single-molecule force spectroscopy: Practical limitations beyond Bell's model. *Physica A: Statistical Mechanics and its Applications* **388**, 1120-1132 (2009).
99. T. Stauch, A. Dreuw, Advances in Quantum Mechanochemistry: Electronic Structure Methods and Force Analysis. *Chem. Rev.* **116**, 14137-14180 (2016).
100. M. T. Ong, J. Leiding, H. Tao, A. M. Virshup, T. J. Martínez, First Principles Dynamics and Minimum Energy Pathways for Mechanochemical Ring Opening of Cyclobutene. *J. Am. Chem. Soc.* **131**, 6377-6379 (2009).
101. J. Ribas-Arino, M. Shiga, D. Marx, Understanding Covalent Mechanochemistry. *Angew Chem Int Ed* **48**, 4190-4193 (2009).
102. K. Wolinski, J. Baker, Geometry optimization in the presence of external forces: a theoretical model for enforced structural changes in molecules. *Molecular Physics* **108**, 1845-1856 (2010).

103. M. K. Beyer, The mechanical strength of a covalent bond calculated by density functional theory. *The Journal of Chemical Physics* **112**, 7307-7312 (2000).
104. Z. Chen *et al.*, The cascade unzipping of ladderane reveals dynamic effects in mechanochemistry. *Nature Chem* **12**, 302-309 (2020).
105. G. I. Bell, Models for the Specific Adhesion of Cells to Cells: A theoretical framework for adhesion mediated by reversible bonds between cell surface molecules. *Science* **200**, 618-627 (1978).
106. S. S. M. Konda, J. N. Brantley, C. W. Bielawski, D. E. Makarov, Chemical reactions modulated by mechanical stress: Extended Bell theory. *The Journal of Chemical Physics* **135**, 164103 (2011).
107. M. Cardoso-Gutierrez, R. D. Levine, F. Remacle, Electronic Coherences Excited by an Ultra Short Pulse Are Robust with Respect to Averaging over Randomly Oriented Molecules as Shown by Singular Value Decomposition. *J. Phys. Chem. A* **128**, 2937-2947 (2024).
108. K. N. Houk, F. Liu, Z. Yang, J. I. Seeman, Evolution of the Diels–Alder Reaction Mechanism since the 1930s: Woodward, Houk with Woodward, and the Influence of Computational Chemistry on Understanding Cycloadditions. *Angew Chem Int Ed* **60**, 12660-12681 (2021).
109. V. D. Kiselev, J. G. Miller, Experimental proof that the Diels–Alder reaction of tetracyanoethylene with 9,10-dimethylantracene passes through formation of a complex between the reactants. *J. Am. Chem. Soc.* **97**, 4036-4039 (1975).
110. A. Gandini, The furan/maleimide Diels–Alder reaction: A versatile click–unclick tool in macromolecular synthesis. *Progress in Polymer Science* **38**, 1-29 (2013).
111. S. Kotha, S. Banerjee, Recent developments in the retro-Diels–Alder reaction. *RSC Adv.* **3**, 7642 (2013).
112. Y. Apeloig, E. Matzner, Evidence for the Dominant Role of Secondary Orbital Interactions in Determining the Stereochemistry of the Diels–Alder Reaction: The Case of Cyclopropene. *J. Am. Chem. Soc.* **117**, 5375-5376 (1995).
113. R. Hoffmann, R. B. Woodward, Orbital Symmetries and endo–exo Relationships in Concerted Cycloaddition Reactions. *J. Am. Chem. Soc.* **87**, 4388-4389 (1965).
114. J. I. García, J. A. Mayoral, L. Salvatella, Do Secondary Orbital Interactions Really Exist? *Acc. Chem. Res.* **33**, 658-664 (2000).
115. J. D. Xidos, T. L. Gosse, E. D. Burke, R. A. Poirier, D. J. Burnell, Endo–Exo and Facial Stereoselectivity in the Diels–Alder Reactions of 3-Substituted Cyclopropenes with Butadiene. *J. Am. Chem. Soc.* **123**, 5482-5488 (2001).
116. B. J. Levandowski, K. N. Houk, Hyperconjugative, Secondary Orbital, Electrostatic, and Steric Effects on the Reactivities and Endo and Exo Stereoselectivities of Cyclopropene Diels–Alder Reactions. *J. Am. Chem. Soc.* **138**, 16731-16736 (2016).
117. R. C. Cioc *et al.*, Direct Diels–Alder reactions of furfural derivatives with maleimides. *Green Chem.* **23**, 367-373 (2021).
118. J. Chandrasekhar, S. Shariffskul, W. L. Jorgensen, QM/MM Simulations for Diels–Alder Reactions in Water: Contribution of Enhanced Hydrogen Bonding at the Transition State to the Solvent Effect. *J. Phys. Chem. B* **106**, 8078-8085 (2002).

119. R. Meir, H. Chen, W. Lai, S. Shaik, Oriented Electric Fields Accelerate Diels–Alder Reactions and Control the *endo/exo* Selectivity. *ChemPhysChem* **11**, 301-310 (2010).
120. C. Yang *et al.*, Electric field–catalyzed single-molecule Diels–Alder reaction dynamics. *Sci. Adv.* **7**, eabf0689 (2021).
121. L. R. Domingo, J. Andrés, Enhancing Reactivity of Carbonyl Compounds via Hydrogen-Bond Formation. A DFT Study of the Hetero-Diels–Alder Reaction between Butadiene Derivative and Acetone in Chloroform. *J. Org. Chem.* **68**, 8662-8668 (2003).
122. V. Polo, L. R. Domingo, J. Andrés, Toward an Understanding of the Catalytic Role of Hydrogen-Bond Donor Solvents in the Hetero-Diels–Alder Reaction between Acetone and Butadiene Derivative. *J. Phys. Chem. A* **109**, 10438-10444 (2005).
123. B. A. Horn, J. L. Herek, A. H. Zewail, Retro-Diels–Alder Femtosecond Reaction Dynamics. *J. Am. Chem. Soc.* **118**, 8755-8756 (1996).
124. H.-Y. Duan *et al.*, An Investigation of the Selective Chain Scission at Centered Diels–Alder Mechanophore under Ultrasonication. *Macromolecules* **50**, 1353-1361 (2017).
125. J. Kida *et al.*, The photoregulation of a mechanochemical polymer scission. *Nat Commun* **9**, 3504 (2018).
126. B. Lyu *et al.*, Surface Confined Retro Diels–Alder Reaction Driven by the Swelling of Weak Polyelectrolytes. *ACS Appl. Mater. Interfaces* **7**, 6254-6259 (2015).
127. Y. Min *et al.*, Sonochemical Transformation of Epoxy–Amine Thermoset into Soluble and Reusable Polymers. *Macromolecules* **48**, 316-322 (2015).
128. F. Calegari, F. Martin, Open questions in attochemistry. *Commun Chem* **6**, 184 (2023).
129. J. Biegert, F. Calegari, N. Dudovich, F. Quéré, M. Vrakking, Attosecond technology(ies) and science. *J. Phys. B: At. Mol. Opt. Phys.* **54**, 070201 (2021).
130. D. J. Tannor, R. Kosloff, S. A. Rice, Coherent pulse sequence induced control of selectivity of reactions: Exact quantum mechanical calculations. *The Journal of Chemical Physics* **85**, 5805-5820 (1986).
131. G. Cerullo, C. Vozzi, Coherent Control of Chemical Reactions on the Attosecond Time Scale. *Physics* **5**, 138 (2012).
132. R. S. Judson, H. Rabitz, Teaching lasers to control molecules. *Phys. Rev. Lett.* **68**, 1500-1503 (1992).
133. C. P. Koch, Controlling open quantum systems: tools, achievements, and limitations. *J. Phys.: Condens. Matter* **28**, 213001 (2016).
134. P. Nuernberger, G. Vogt, T. Brixner, G. Gerber, Femtosecond quantum control of molecular dynamics in the condensed phase. *Phys. Chem. Chem. Phys.* **9**, 2470 (2007).
135. C. Winterfeldt, C. Spielmann, G. Gerber, *Colloquium*: Optimal control of high-harmonic generation. *Rev. Mod. Phys.* **80**, 117-140 (2008).
136. P. Brumer, M. Shapiro, Laser Control of Molecular Processes. *Annu. Rev. Phys. Chem.* **43**, 257-282 (1992).
137. R. Borrego-Varillas, M. Lucchini, M. Nisoli, Attosecond spectroscopy for the investigation of ultrafast dynamics in atomic, molecular and solid-state physics. *Rep. Prog. Phys.* **85**, 066401 (2022).
138. M. F. Kling *et al.*, Control of Electron Localization in Molecular Dissociation. *Science* **312**, 246-248 (2006).

139. G. Sansone *et al.*, Electron localization following attosecond molecular photoionization. *Nature* **465**, 763-766 (2010).
140. I. Znakovskaya *et al.*, Attosecond Control of Electron Dynamics in Carbon Monoxide. *Phys. Rev. Lett.* **103**, 103002 (2009).
141. P. Ranitovic *et al.*, Attosecond vacuum UV coherent control of molecular dynamics. *Proc. Natl. Acad. Sci. U.S.A.* **111**, 912-917 (2014).
142. M. Cardoso-Gutierrez, R. D. Levine, F. Remacle, Electronic coherences built by an attopulse control the forces on the nuclei. *J. Phys. B: At. Mol. Opt. Phys.*, (2024).
143. P. B. Corkum, Plasma perspective on strong field multiphoton ionization. *Phys. Rev. Lett.* **71**, 1994-1997 (1993).
144. M. F. Kling, M. J. J. Vrakking, Attosecond Electron Dynamics. *Annu. Rev. Phys. Chem.* **59**, 463-492 (2008).
145. P. M. Paul *et al.*, Observation of a Train of Attosecond Pulses from High Harmonic Generation. *Science* **292**, 1689-1692 (2001).
146. M. Hentschel *et al.*, Attosecond metrology. *Nature* **414**, 509-513 (2001).
147. M. Lucchini *et al.*, Few-Femtosecond $C_2H_4^+$ Internal Relaxation Dynamics Accessed by Selective Excitation. *J. Phys. Chem. Lett.* **13**, 11169-11175 (2022).
148. C. E. M. Gonçalves, R. D. Levine, F. Remacle, Ultrafast geometrical reorganization of a methane cation upon sudden ionization: an isotope effect on electronic non-equilibrium quantum dynamics. *Phys. Chem. Chem. Phys.* **23**, 12051-12059 (2021).

Chapter 2. Electronic Structure and Molecular Dynamics Methods

Table of Contents

Chapter 2. Electronic Structure and Molecular Dynamics Methods	34
2.1 <i>Electronic Structure Methodologies</i>	<i>34</i>
2.1.1. Introduction to quantum chemistry	34
2.1.2. Density Functional Theory.....	39
2.1.3. Modeling systems with strong correlation	42
2.1.4. The multireference CASSCF approach.....	43
2.2 <i>Modeling molecular dynamics</i>	<i>46</i>
2.2.1. Introduction	46
2.2.2. Ab initio molecular dynamics	48
2.2.3. Photoinduced coupled electron-nuclei quantum dynamics.....	51
2.2.4. Quantum mechanical description of the molecular system interacting with the pulse.....	58
2.2.5. Hamiltonian in the linear diatomic molecule LiH.....	65
2.2.6. Numerical integration of the TDSE	68
2.3 <i>Modeling ultrafast excited-state processes in large molecular systems</i>	<i>69</i>
2.3.1. Surface hopping dynamics using the SHARC method	70
2.3.2. Sampling of initial conditions from the Wigner distribution	73
2.4 <i>References</i>	<i>75</i>

2.1 Electronic Structure Methodologies

2.1.1. Introduction to quantum chemistry

Atoms and molecules are among the most complex physical systems exhibiting quantum behavior because they are many-body correlated systems with a large number of interacting particles. Therefore, an accurate description of the molecular properties and phenomena that determine chemical reactivity and properties must satisfy the rules of quantum mechanics. The application of quantum mechanics to chemistry dates from the very beginning with the development of valence bond theory and shortly after molecular orbital theory, both aiming to explain the nature of a chemical bond. Since then, the field of quantum chemistry has grown robust with a series of developments of more sophisticated theoretical methods capable of describing more complex molecules, whether due to their size or due to the complexity of their electronic structure.

Molecules are composed by positive nuclei and negative electrons interacting by pairs through Coulomb interactions, and all the physical properties and reactivity are determined by the interplay between those constituent particles. The geometry of a molecule is determined by the positions adopted by the nuclei, which remain bound thanks to favorable electronic localization. From a quantum mechanical point of view, the state of the molecule can be expressed by a wavefunction $\Psi(\mathbf{r}, \mathbf{R}, t)$ that depends on the Cartesian coordinates of all nuclei (\mathbf{R}) and electrons (\mathbf{r}) and on time. The wavefunction is a mathematical construction that aims to represent the quantum mechanical

nature of a molecular system. For a wavefunction to have physical meaning, it must be single-valued, continuous, and quadratically integrable. These conditions ensure that its square modulus $|\Psi(\mathbf{r}, \mathbf{R}, t)|^2$ can represent the probability density of the system. (1)

The time evolution of the wavefunction is dictated by the time-dependent Schrodinger (TDSE) equation:

$$i\hbar \frac{\partial}{\partial t} \Psi(r, R, t) = \hat{H} \Psi(r, R, t) \quad (2.1)$$

Where $i = \sqrt{-1}$ is the imaginary unit, $\Psi(r, R, t)$ is the wavefunction, and \hat{H} is the Hamiltonian operator. The Hamiltonian determines the total energy of the molecule, including both kinetic energy and potential energy. The kinetic energy measures the interactive motion of electrons and nuclei of the molecule. The potential energy accounts for the interactions between the particles.

For a polyatomic molecule with K nuclei and N electrons, the Hamiltonian can be expressed as follows:

$$\hat{H} = \hat{T} + \hat{V} = \hat{T}_N + \hat{T}_e + \hat{V}_{NN} + \hat{V}_{Ne} + \hat{V}_{ee} \quad (2.2)$$

where \hat{T}_N is the kinetic energy operator of the nuclei and \hat{T}_e that of the electrons. The potential energy operator has three contributions: \hat{V}_{NN} which arises from the electrostatic repulsion between the positively charged nuclei, \hat{V}_{ee} which comes from the electrostatic repulsion between the negatively charged electrons, and finally, \hat{V}_{Ne} is due to the electrostatic attraction between the electrons and the nuclei, as they have opposite charges. Each term can be expressed in atomic units, as shown in Equations 2.3a to 2.3e.

$$\hat{T}_N = -\frac{1}{2} \sum_A^K \frac{\nabla_{\mathbf{R}_A}^2}{M_A} \quad (2.3a)$$

$$\hat{T}_e = -\frac{1}{2} \sum_i^N \nabla_{\mathbf{r}_i}^2 \quad (2.3b)$$

$$\hat{V}_{NN} = \sum_A^K \sum_{B>A}^K \frac{Z_A Z_B}{|\mathbf{R}_A - \mathbf{R}_B|} \quad (2.3c)$$

$$\hat{V}_{Ne} = -\sum_A^K \sum_i^N \frac{Z_A}{|\mathbf{R}_A - \mathbf{r}_i|} \quad (2.3d)$$

$$\hat{V}_{ee} = \sum_i^N \sum_{j>i}^N \frac{1}{|\mathbf{r}_i - \mathbf{r}_j|} \quad (2.3e)$$

where A and B indices designate nuclei, i and j electrons, \mathbf{R}_A , M_A , and Z_A stand for the position, the mass and the charge of the nucleus A , while \mathbf{r}_i indicates the position of the electron i . In atomic units, the mass of the electron, its charge, the reduced Planck constant \hbar , and $4\pi\epsilon_0$ (with ϵ_0 being the vacuum permittivity constant) are all set to 1.

For a molecule that experiences no time-dependent external forces, the potential energy depends only on nuclear and electron coordinates but not on time. When the system is in an eigenstate of the time independent molecular Hamiltonian, \hat{H} (Eq. 2.2), the temporal and spatial dependences of the wavefunction can be separated as shown in Equation 2.4:

$$\Psi(\mathbf{r}, \mathbf{R}, t) = \psi(\mathbf{r}, \mathbf{R})e^{-iEt/\hbar} \quad (2.4)$$

Where $\Psi(\mathbf{r}, \mathbf{R}, t)$ is the total time-dependent wavefunction, $\psi(\mathbf{r}, \mathbf{R})$ is the spatial wavefunction which depend only on the position of the electrons and nuclei, and is in an eigenstate of the stationary Hamiltonian, \hat{H} with energy E (Eq. 2.5) and $e^{-iEt/\hbar}$ is the corresponding time-dependent phase factor.

The eigenvalue equation

$$\hat{H}|\psi\rangle = E|\psi\rangle \quad (2.5)$$

is the time-independent Schrödinger equation (TISE) where $|\psi\rangle \equiv \psi(\mathbf{r}, \mathbf{R})$ is the spatial wavefunction. Using the spectral theorem, we can expand a given state wavefunction into a complete orthonormal system of energy eigenstates $|n\rangle$ with coefficients c_n , as shown in Equation 2.6.

$$|\psi\rangle = \sum_n c_n |n\rangle, \quad c_n = \langle n|\psi\rangle \quad (2.6)$$

In the TISE, the wavefunction is typically expressed as a function of spatial coordinates and solving it for larger systems becomes increasingly computationally challenging due to the high dimensionality involved. The molecular wavefunction $\psi(\mathbf{r}, \mathbf{R})$ depends on $6M$ degrees of freedom, where M is the total number of particles in the system, including both nuclei and electrons. Consequently, the dimensionality of the wavefunction increases rapidly with the size of the molecule.

The main difficulty in solving the TISE for interacting systems arises from the inability to fully separate the nuclear and electronic coordinates. The motion of all the particles is coupled through the terms \hat{V}_{NN} , \hat{V}_{Ne} , \hat{V}_{ee} in the Hamiltonian (Eq. 2.2), which represents nucleus-nucleus, nucleus-electron, and electron-electron interactions. This coupling makes the TISE Schrödinger equation unsolvable exactly for all but the simplest systems.

The first approximation that is made to simplify the solution of the TISE Schrödinger equation is the Born-Oppenheimer (BO) approximation, in which the total wavefunction at every fixed position of the nuclei can be written approximately as the product of an electronic wavefunction ($\phi^{el}(\mathbf{r}; \mathbf{R})$), parametrically depending on \mathbf{R} , and a nuclear wavefunction $\chi(\mathbf{R})$.

$$\psi(\mathbf{r}, \mathbf{R}) \approx \phi^{el}(\mathbf{r}; \mathbf{R})\chi(\mathbf{R}) \quad (2.7)$$

The BO approximation is based on the fact that the ≈ 2000 larger mass of the nuclei compared to that of the electrons causes the nuclear motion to be much slower than the electronic motion. This means that the electrons, moving quickly, have enough time to adjust to every nuclear configuration. In other words, the BO approximation implies that the electrons are in equilibrium with the nuclei for each new position of the nuclei. This allows us to simplify the solution of the TISE by finding the electronic configuration that is in equilibrium with fixed nuclear positions, effectively treating the nuclear repulsion term \hat{V}_{NN} as a constant and the term \hat{V}_{Ne} at a fixed position of the nuclei, thereby depending only on the electronic coordinates, \mathbf{r} . The stationary Schrödinger Equation for the electrons, SE, then becomes a variational problem, expressed by the eigenvalue equation:

$$\hat{H}^{el}\phi^{el}(\mathbf{r}; \mathbf{R}) = E^{el}\phi^{el}(\mathbf{r}; \mathbf{R}) \quad (2.8)$$

Where

$$\hat{H}^{el} = \hat{T}_e + \hat{V}_{Ne} + \hat{V}_{ee} = -\frac{1}{2}\sum_{i=1}^N \nabla_i^2 + \sum_{i=1}^N v(\mathbf{r}_i) + \sum_j \sum_{i>j} \frac{1}{r_{ij}} \quad (2.9)$$

is the electronic Hamiltonian operator, in atomic units, that acts solely on the electronic coordinates \mathbf{r} at each fixed position of the nuclei. The first term, $\hat{T}_e = -\frac{1}{2}\sum_{i=1}^N \nabla_i^2$, (Eq. 2.3b) represents the electronic kinetic energy. The second term, $\hat{V}_{Ne} = \sum_{i=1}^N v(r_i)$, corresponds to the attractive potential energy due to the interaction between the electrons and the static nuclei (Eq. 2.3d). The third term, $\hat{V}_{ee} = \sum_j \sum_{i>j} \frac{1}{r_{ij}}$ (Eq. 2.3e) describes the electron-electron repulsion, where r_{ij} is the distance between electrons i and j .

The second term in Equation 2.9, involves the potential $v(\mathbf{r}_i)$, which accounts for the interaction between electron i and the static nuclei. It is defined as:

$$v(r_i) = -\sum_A \frac{Z_A}{r_{Ai}} \quad (2.10)$$

Here, Z_A is the charge of nucleus A and $r_{Ai} = |\mathbf{R}_A - \mathbf{r}_i|$ is the distance between electron i and nucleus A . Since the nuclei are external to electron system, $v(\mathbf{r}_i)$ is referred to as the external potential. The external potential varies for each geometry of the molecule because it is determined by the positions and composition of the nuclei.

Solving the eigenvalue equation, Equation 2.8, yields a set of orthonormal eigenfunctions representing the "adiabatic" electronic states $\phi^{el}(\mathbf{r}; \mathbf{R})$, with the eigenvalues $E^{el}(\mathbf{R})$ corresponding to the electronic energies and defines the V_{NN} term, the potential in which the nuclei are moving. The term "adiabatic" emphasizes the uncoupled nature of the nuclear and electronic motion in the BO framework.

Approximate solution of the SE equation

Most quantum chemistry methods rely on the variational principle and perturbation theory to solve the SE. The variational principle applied to the SE states that for any trial wavefunction ψ_{trial} , the expectation value of the electronic Hamiltonian gives an upper bound to the true ground state energy. The energy associated with the trial wavefunction is given by:

$$E_{trial}^{el} = \frac{\langle \phi_{trial}^{el} | \hat{H}^{el} | \phi_{trial}^{el} \rangle}{\langle \phi_{trial}^{el} | \phi_{trial}^{el} \rangle} \quad (2.11)$$

The goal of the variational procedure is to minimize the energy E_{trial}^{el} with respect to the parameters of the trial electronic wavefunction. Two of the most important variational methods include the Hartree Fock (HF) method which is solved for the exact electronic Hamiltonian (Eq. 2.9) and Density Functional Theory (DFT) where the electronic Hamiltonian is parametrized via a functional describing the electronic correlation and exchange interactions. Although the Hartree Fock method may not provide sufficient accuracy for many molecular systems, it serves as the foundation for more advanced electronic structure methods, such as Møller-Plesset perturbation theory and Complete Active Space Self-Consistent Field (CASSCF). We use the CASSCF methodology in this thesis to model the molecular systems studied in mechanochemistry and attochemistry. The CASSCF method is described in detail in Section 2.1.

In the HF method, the ground state wavefunction of a system of N electrons is approximated as a single Slater determinant, ensuring the antisymmetry required by the Pauli exclusion principle

$$\Psi_{HF} \equiv \phi^{el}(\mathbf{r}_1, \mathbf{r}_2, \dots, \mathbf{r}_N) = \frac{1}{\sqrt{N!}} \begin{vmatrix} \varphi_1(1)\alpha(1) & \varphi_1(1)\beta(1) & \cdots & \varphi_{N/2}(1)\beta(1) \\ \varphi_1(2)\alpha(2) & \varphi_1(2)\beta(2) & \cdots & \varphi_{N/2}(2)\beta(2) \\ \vdots & \vdots & \ddots & \vdots \\ \varphi_1(N)\alpha(N) & \varphi_1(N)\beta(N) & \cdots & \varphi_{N/2}(N)\beta(N) \end{vmatrix} \quad (2.12)$$

Where φ_i represents a single-particle spatial orbital, the molecular orbitals (MOs), and α and β are spin functions, corresponding to the two possible spin states: up and down. The spatial orbitals φ_i are expressed as linear combinations of atomic orbitals (LCAO):

$$\varphi_i = \sum_b c_{ib} \gamma_b \quad (2.13)$$

where γ_b are the basis functions, and c_{ib} are the coefficients to be optimized, known as LCAO coefficients. The choice of the basis set of atomic orbitals is a critical aspect of any quantum chemistry method, as it determines the accuracy and efficiency of the calculation. A larger basis set provides a more accurate description of the molecular orbitals and thus the electronic structure, but at the cost of higher computational resources. Conversely, a smaller basis set reduces computational demand but sacrifices accuracy.

The spin orbitals, denoted by $\phi_i(\mathbf{r})$, are formed combining the spatial orbitals with the spin functions:

$$\phi_i(\mathbf{r}) = \varphi_i(\mathbf{r})\zeta_{\alpha/\beta} \quad (2.14)$$

Where $\varphi_i(\mathbf{r})$ is the spatial part of the orbital, and $\zeta_{\alpha/\beta}$ is the spin part, with α and β representing the spin-up and spin-down states, respectively.

The HF wavefunction Ψ_{HF} , built as an antisymmetrized Slater determinant (as shown in Equation 2.12), serves as a trial wavefunction in the variational procedure. The HF method iteratively minimizes the energy by varying the orbitals. This leads to the one-electron Fock equations (Eq. 2.15), which leads to one-electron spatial wave functions, the MOs.

$$\hat{F}\varphi_i = \epsilon_i\varphi_i \quad (2.15)$$

Where \hat{F} is the Fock operator, φ_i are the spatial orbitals, and ϵ_i are the corresponding energies. The Fock equations given in Eq 2.15, are applicable to closed-shell molecules, since only the spatial part of the spin orbitals is varied. In Section 2.1 we discuss how HF theory can be extended to model open-shell species. Fock operator is constructed as:

$$\hat{F}(\mathbf{r}) = \hat{h}(\mathbf{r}) + \sum_j^{K/2} 2\hat{J}_j(\mathbf{r}) - \hat{K}_j(\mathbf{r}) \quad (2.16)$$

Where $\hat{h}(\mathbf{r})$ is the core Hamiltonian defined by:

$$\hat{h}(\mathbf{r}) = -\frac{1}{2}\hat{\nabla}^2 + v(\mathbf{r}) \quad (2.17)$$

Where $v(\mathbf{r}) = -\sum_A \frac{Z_A}{|\mathbf{R}_A - \mathbf{r}|}$ is the nuclear attraction potential, defined in Eq. 2.10 above. $\hat{J}_j(\mathbf{r})$ is the Coulomb operator, and $\hat{K}_j(\mathbf{r})$ is the exchange operator, most easily defined via their action on the spatial orbitals φ_i , as shown below:

$$\hat{J}_j(\mathbf{r})\varphi_i(\mathbf{r}) = \left[\int \phi_j^*(\mathbf{r}') \frac{1}{|\mathbf{r} - \mathbf{r}'|} \phi_j(\mathbf{r}') d\mathbf{r}' \right] \phi_i(\mathbf{r}) \quad (2.18)$$

$$\hat{K}_j(\mathbf{r})\varphi_i(\mathbf{r}) = \left[\int \phi_j^*(\mathbf{r}') \frac{1}{|\mathbf{r} - \mathbf{r}'|} \phi_i(\mathbf{r}') d\mathbf{r}' \right] \phi_j(\mathbf{r}) \quad (2.19)$$

To obtain a solution of the Fock equations, one expands the spatial orbitals $\varphi_i(\mathbf{r})$ in a basis of atomic orbitals (Eq. 2.13) and varies the coefficients self-consistently, since the Fock operator depends on its own solutions because of the two electron integrals $\hat{J}_j(\mathbf{r})$ and $\hat{K}_j(\mathbf{r})$. This leads to the Hall-Roothaan equations.

2.1.2. Density Functional Theory

Density functional theory (DFT) is a powerful and widely used method for calculating the ground state energy (E_0) of a molecular system, along with other related properties derived from the ground-state one electron density $\rho_0(\mathbf{r})$. DFT emerged from decades of research aimed at finding a simpler alternative to the electronic wavefunction for describing and calculating the quantum state of a molecule. For a system of N electrons, the electronic wavefunction depends on $3N$ spatial

and N spin coordinates, meaning it contains much more information than what is typically needed for calculating the observables of the system, which are averaged over the wave function. For instance, the matrix of the electronic Hamiltonian operator can be expressed in terms of one- and two-electron integrals, which only involve six spatial coordinates. (1)

A breakthrough in this regard came from Hohenberg and Kohn, who demonstrated that for molecules with a non-degenerate ground state, the ground-state energy, wavefunction, and all other molecular electronic properties are uniquely determined by the ground-state one electron density, $\rho(x, y, z)$. This result forms the foundation of the famous Hohenberg-Kohn Theorem, which marked the beginning of DFT's development and has since made it one of the most valuable tools in quantum chemistry for studying both molecular and solid-state systems.

The Hohenberg-Kohn theorem implies the existence of a functional that relates the ground-state energy to the one electron density (see Equation 2.20).

$$E_0 = E_0[\rho_0] \quad (2.20)$$

Where E_0 is the ground state energy, $E_0[\cdot]$ is a functional of ρ_0 , and ρ_0 is the ground state electronic density.

Every term in the purely electronic Hamiltonian (Eq. 2.9) is related to a molecular property determined by the ground-state electronic wavefunction, which, in turn, is determined by $\rho_0(\mathbf{r})$. This leads to the expression of the density functional shown below:

$$E_0[\rho_0] = \bar{T}_e[\rho_0] + \bar{V}_{Ne}[\rho_0] + \bar{V}_{ee}[\rho_0] \quad (2.21)$$

Where the notation $\bar{X} = \langle \phi_0^{el} | \hat{X} | \phi_0^{el} \rangle$, represents the energy contribution from each operator in the electronic Hamiltonian ($\hat{X} = \hat{T}_e, \hat{V}_{Ne}, \hat{V}_{ee}$). In particular, the term $\bar{V}_{Ne}[\rho_0] = \int \rho_0(\mathbf{r})v(\mathbf{r})d\mathbf{r}$ (Eq. 2.3d) is the known external potential energy, which depends directly on the external potential $v(\mathbf{r})$, Eq. 2.10, and thus on the positions of the nuclei. However, the functionals $\bar{T}_e[\rho_0]$ and $\bar{V}_{ee}[\rho_0]$ are unknown, which limits the direct application of DFT to compute the electronic structure. These unknown functionals encapsulate the complex many-body interactions between electrons, electronic correlation and exchange terms.

To overcome this challenge, Kohn and Sham devised a practical method for obtaining ρ_0 and for calculating E_0 from ρ_0 . They proposed mapping the intractable many-body problem of interacting electrons in the static external potential of the nuclei to a much simpler problem of non-interacting electrons moving in an effective potential. This approach follows a similar iterative process to the Hartree-Fock method, which also employs self-consistent field equations to determine molecular orbitals and ground state energies. The Kohn-Sham method considers a reference system of noninteracting electrons whose external potential energy function $v_{ref}(\mathbf{r}_i)$ is chosen so that the reference ground-state electron probability density equals the exact ground-state density of the molecule of interest; i.e., $\rho_{ref}(\mathbf{r}) = \rho_0(\mathbf{r})$.

The expression of the total energy in Kohn-Sham density functional theory is given by:

$$E_0[\rho_0] = \int \rho_0(\mathbf{r})v(\mathbf{r})d\mathbf{r} + \bar{T}_e^{ref}[\rho_0] + \frac{1}{2} \int \int \frac{\rho_0(\mathbf{r}_1)\rho_0(\mathbf{r}_2)}{r_{12}} d\mathbf{r}_1 d\mathbf{r}_2 + E_{xc}[\rho_0] \quad (2.22)$$

Where \bar{T}_e^{ref} represents the kinetic energy of the reference non-interacting system. The first term, $\int \rho_0(\mathbf{r})v(\mathbf{r})d\mathbf{r}$, accounts for electron-nucleus attractive interactions, while the third term, $\frac{1}{2} \int \int \frac{\rho_0(\mathbf{r}_1)\rho_0(\mathbf{r}_2)}{r_{12}} d\mathbf{r}_1 d\mathbf{r}_2$, quantifies the classical Coulomb electron-electron repulsion. In contrast, the exact form of the exchange-correlation energy functional $E_{xc}[\rho_0]$ is unknown and must, therefore, be approximated. Many exchange-correlation functionals have been developed, each optimized for modeling different molecular properties. Therefore, selecting the appropriate exchange-correlation functional in DFT calculations is crucial, as much as selecting the atomic orbital basis set. For example, in our work in mechanochemistry, we use a ω B97XD functional which is well-suited for modeling long-range interactions critical to stabilizing the diradical species formed when the furan/maleimide molecule breaks in a single bond.

The Kohn-Sham wavefunction is a single Slater determinant constructed from a set of orbitals obtained by solving the eigenvalue Kohn-Sham equation:

$$\left(-\frac{1}{2}\nabla^2 + v_{eff}(\mathbf{r})\right)\theta_i^{KS}(\mathbf{r}) = \epsilon_i\theta_i^{KS}(\mathbf{r}) \quad (2.23)$$

Where ϵ_i is the orbital energy corresponding to the Kohn-Sham orbital θ_i^{KS} , a set of single-particle orbitals resembling the Hartree-Fock orbitals. The term $v_{eff}(\mathbf{r})$ is the effective potential defined as:

$$v_{eff}(\mathbf{r}) = v(\mathbf{r}) + \int \frac{\rho_0(\mathbf{r}')}{|\mathbf{r}-\mathbf{r}'|} d\mathbf{r}' + \frac{\delta E_{xc}[\rho_0]}{\delta \rho_0(\mathbf{r})} \quad (2.24)$$

Here, $v(\mathbf{r})$ is the external potential from the fixed nuclei, $\int \frac{\rho_0(\mathbf{r}')}{|\mathbf{r}-\mathbf{r}'|} d\mathbf{r}'$ is the Hartree potential, which represents the electrostatic repulsion interaction between the electrons, and $\frac{\delta E_{xc}[\rho_0]}{\delta \rho_0(\mathbf{r})}$ is the exchange correlation potential.

The density is obtained from the Kohn-Sham orbitals as follows:

$$\rho_0(\mathbf{r}) = \sum_i^N |\theta_i^{(KS)}(\mathbf{r})|^2 \quad (2.25)$$

The Kohn-Sham method is variational in nature but applied to a parametrized electronic Hamiltonian because of the parametrization of the functional. Initially, a guess for the density $\rho_0(\mathbf{r})$ is used to construct an effective potential $v_{eff}(\mathbf{r})$. This potential is then used to solve the Kohn-Sham equations for the single-particle orbitals $\theta_i^{KS}(\mathbf{r})$, which are developed in an atomic basis set. These orbitals are optimized by varying the LCAO coefficients similar to the Hartree-Fock method (Eq. 2.13). From the resulting orbitals, a new density is computed, which is used to

calculate a new effective potential and solve the Kohn-Sham equations again. This process is repeated until the energy is minimized, and the density converges to a self-consistent value.

2.1.3. Modeling systems with strong correlation

Unrestricted HF and DFT

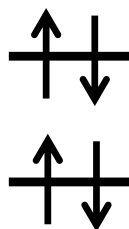
To describe species exhibiting strong correlation, such as systems with a degenerate ground state, more than a single Slater determinant must be used. In HF or DFT, this can be addressed using an unrestricted formalism, where the α and β spin orbitals are treated independently, allowing each electron to occupy a different spatial orbital (see Figure 2.3).(2) This means that in both unrestricted HF (UHF) and unrestricted DFT (UDFT), the spin-orbitals are not restricted to having the same spatial orbital for electrons with different spins, which allows to describe well diradical species and homolytic bond rupture.

Restricted formalism

$$\phi_i(\mathbf{x}) = \begin{cases} \varphi_j(\mathbf{r})\alpha(\omega) \\ \varphi_j(\mathbf{r})\beta(\omega) \end{cases}$$

Spatial function Spin functions

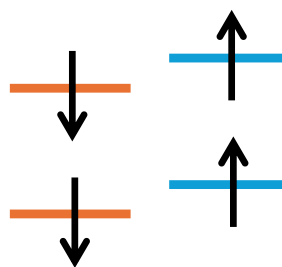
Spin orbital



φ_j

Unrestricted formalism

$$\phi_i(\mathbf{x}) = \begin{cases} \varphi_j^\alpha(\mathbf{r})\alpha(\omega) \\ \varphi_j^\beta(\mathbf{r})\beta(\omega) \end{cases}$$



φ_j^α

φ_j^β

Figure 2.1 Contrary to the restricted formalism where spatial function representing electrons with different spin in an orbital is the same, in the unrestricted formalism the two electrons are treated independently.

In the case of systems with an even number of electrons, such as the furan/maleimide compounds, when computing the singlet ground electronic state, we need to ensure that the spin symmetry of the initial guess orbitals is broken, (3) otherwise, the algorithm used to solve the one electron electronic eigenstate equation (2.15 for HF and 2.23 for DFT) would not converge to the correct open-shell solution. This can be done by mixing the HOMO and LUMO orbitals of the guess and performing a stability analysis to ensure that the solution wavefunction is a minimum and it does not suffer from spin-contamination. We utilized the internal stability analysis tool available Q-Chem(4) which will automatically displace the MOs and redo the calculation if an unstable wavefunction is obtained. Although, the UDFT methodology can describe correctly the geometries of the diradical species as well as the sequential reaction pathway under force, a more robust multi-reference method is needed to better characterize the electronic structure of the furan/maleimide diradicals, enabling the assessment of phenomena such as the singlet/triplet degeneracy and charge

delocalization. For this purpose, we selected the CASSCF formalism, which gives a good compromise between accuracy and computational cost, to model the furan/maleimide mechanophores under force.

2.1.4. The multireference CASSCF approach

In multiconfigurational self-consistent field (MCSCF) theory (5-7) the many N -electron wavefunction is expressed as a linear combination of Slater determinants or configuration state functions (CSF), (Equation 2.20 below).

$$|\Psi_{\text{MCSCF}}\rangle = \sum_i c_i |\Phi_i\rangle \quad (2.26)$$

A CSF, $|\Phi_i\rangle$, is a linear combination of Slater determinants that form a spin-adapted many electron wavefunction that is an eigenfunction of both the total spin operator (\hat{S}^2) and the spin projection operator (\hat{S}_z). The CSFs provide a more compact basis set of the multi determinantal electronic wave function of the system, with fewer terms than in an expansion in Slater determinants, and with the correct spin symmetry imposed. (8)

The MC-SCF energy is written as follows:

$$E^{\text{MCSCF}} = \langle \Psi_{\text{MCSCF}} | \hat{H}^{\text{elec}} | \Psi_{\text{MCSCF}} \rangle = \sum_{ij} \langle \varphi_i | \hat{h} | \varphi_j \rangle \gamma_{ij} + \frac{1}{2} \sum_{ijkl} [\varphi_i \varphi_j | \varphi_k \varphi_l] \Gamma_{ijkl} \quad (2.27)$$

$$\langle \varphi_i | \hat{h} | \varphi_j \rangle = \int d\mathbf{r}_1 \varphi_i^*(\mathbf{r}_1) \hat{h} \varphi_j(\mathbf{r}_1)$$

$$[\varphi_i \varphi_j | \varphi_k \varphi_l] = \int \int d\mathbf{r}_1 d\mathbf{r}_2 \varphi_i^*(\mathbf{r}_1) \varphi_k^*(\mathbf{r}_2) \frac{1}{|\mathbf{r}_1 - \mathbf{r}_2|} \varphi_j(\mathbf{r}_1) \varphi_l(\mathbf{r}_2)$$

where E^{MCSCF} denotes the MC-SCF energy and \hat{H}^{elec} the electronic Hamiltonian which has been expressed in terms of the one-electron integral $\langle \varphi_i | \hat{h} | \varphi_j \rangle$, \hat{h} is the one-electron Hamiltonian, and the two-electron integral $[\varphi_i \varphi_j | \varphi_k \varphi_l]$. The γ_{ij} and Γ_{ijkl} , are the reduced one- and two-electron transition density matrices, defined from the CI coefficients and the generators of the Lie Algebra of the unitary group $U(n)$, where n is the number of orbitals.(5)

During a MC-SCF calculation both the expansion coefficients c_i and the orthonormal orbitals φ_i contained in the CSF $|\Phi_i\rangle$ are simultaneously self-consistently optimized. They are expressed as a linear combination of atomic orbitals with LCAO coefficients. This optimization is a very difficult computational variational problem since the MC-SCF energy function (Equation 2.27) is highly nonlinear, with potentially many local solutions.

This means, in practice, that even for small molecules it is not feasible to include all possible configurations $|\Phi_i\rangle$ that can be generated from the full orbital Hilbert space of the molecule. Instead, a select a subset of configurations relevant to the chemical problem being modeled must be selected. These determinants can either be chosen manually, based on intuition or prior knowledge of the system, or systematically by selecting all possible determinants formed within a specific set of "active" molecular orbitals. The latter approach is known as the complete-active-space self-consistent-field (CASSCF) method(6). CASSCF streamlines the configuration selection process, by focusing only on the molecular orbitals that significantly contribute to the chemical process. In this method, the orbital space is divided into a set of "active" orbitals, while

the remaining orbitals have fixed electron occupations or are not optimized, thereby reducing computational complexity. We used for CASSCF calculations, the program Multi(9-12) available in the Molpro (13, 14) quantum chemistry package. In Multi, the orbital space can be partitioned into four subgroups: (Figure 2.2)

- 1) a set of *frozen orbitals* which are doubly occupied in all configurations, and that are not optimized,
- 2) a set of *closed orbitals* which are also doubly occupied but their coefficients are optimized during the MC-SCF procedure,
- 3) a set of *active orbitals* with no restriction on their occupations and that are optimized, and
- 4) a set of *virtual orbitals*, which remain unoccupied in all configurations and their coefficients are not optimized.

Along with the number of active orbitals, a set of 'active' electrons must be specified in order to build all possible configurations within the active space. Both the c_i coefficients and the molecular orbital LCAO coefficients are variationally optimized using the configurations generated under the complete active space (CAS) restrictions. This approach allows moderately sized systems to be studied when the active space is relatively small. On modern computing architectures, active spaces up to approximately 18 electrons in 18 orbitals ($\sim 2 \times 10^9$ determinants) can be handled.

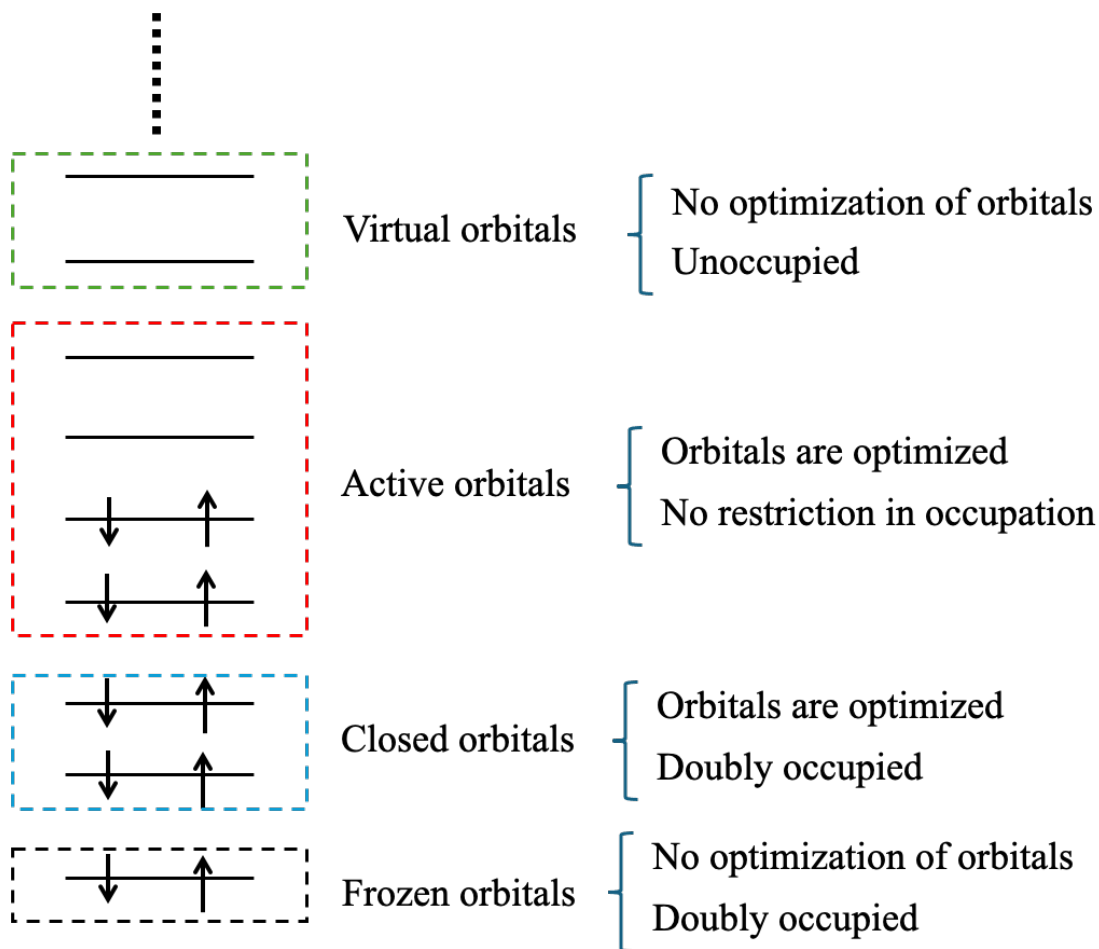


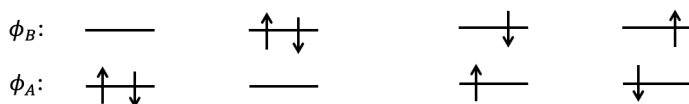
Figure 2.2. Partition of the total orbital space in the CASSCF methodology.

The small number of active orbitals that can be treated in MCSCF theory usually makes it impossible to treat dynamical correlation. Therefore, only a qualitatively correct description of the electronic system can be expected. (8) Nevertheless, CASSCF excels at treating the static electronic correlation present in open-shell systems like diradicals due to its inherent multideterminantal character. To describe correctly an open-shell singlet, two Slater determinants are needed. An illustration of the multiconfigurational structure of the singlet open-shell wavefunctions in diradicals is shown in Figure 2.3.

The singlet ground state wavefunction is a superposition of two configurations

$$|\Psi\rangle^{\text{Singlet}} = \frac{1}{\sqrt{2}} (|\Phi_+\rangle - |\Phi_-\rangle)$$

$$|\Phi_+\rangle = [(\phi_A(1)\phi_A(2) + \phi_B(1)\phi_B(2)) + (\phi_A(1)\phi_B(2) + \phi_B(1)\phi_A(2))]/(2 + 2S_{AB})$$



$$|\Phi_-\rangle = [(\phi_A(1)\phi_A(2) + \phi_B(1)\phi_B(2)) - (\phi_A(1)\phi_B(2) + \phi_B(1)\phi_A(2))]/(2 - 2S_{AB})$$

Covalent terms

Ionic terms

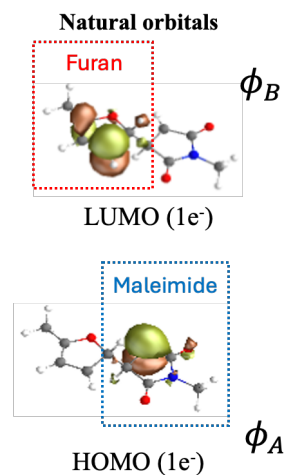


Figure 2.3. The singlet open-shell wavefunction is given by a linear combination of the two configurations $|\Phi_+\rangle$ and $|\Phi_-\rangle$, in which the ionic terms cancel, resulting in a covalent state: the singlet diradical. The natural orbitals show the localization of the HOMO and LUMO on different parts of the molecule, and they are occupied by 1e⁻, which are manifestations of the diradical state.

In CASSCF, various types of molecular orbitals can be used to construct an initial guess for the wavefunction in the variational procedure, with converged Hartree-Fock canonical orbitals being a popular choice. Unlike in HF and most wavefunction-based methods, the orbitals obtained in CASSCF are not ranked by energy but by occupation. These orbitals, called *natural (localized) orbitals* (15), diagonalize the one-electron density matrix. Canonical orbitals are not reported because the CASSCF wavefunction is invariant to unitary transformations, such as rotations within the active space (6), meaning no unique set of orbitals emerges from the energy minimization procedure. Natural orbitals provide a more intuitive representation of the electron distribution within the active space, where strong electron correlation effects are significant. Diagonalizing the one-electron density matrix yields natural orbitals and their occupation numbers, which are real numbers. They reflect the degree of electron correlation: values near 0, 1, or 2 suggest weak correlation, while intermediate real values indicate strong correlation in the multideterminantal wave function.

The CASSCF formalism can be applied to describe the electronic structure of furan/maleimide mechanophores (see Chapter 3) due to the moderate size of those molecules (25 atoms). It was also used to solve the electronic structure of the LiH molecule, of the methane cation and of the ethylene cation discussed in Chapters 4, 5, and 6.

Describing excited states: the state-averaged algorithm in CASSCF

We have mentioned that the rDA reactions of the furan/maleimide mechanophores under force proceed entirely on the ground electronic state surface. However, CASSCF can also be applied to studying several electronic states. This is particularly the case of our work in attochemistry; see Chapters 5 and 6, where we have more than one electronic state present in the wavefunction of the superposition state created by the ultrashort attosecond pulse.

There are two ways of computing several electronic states in MC-SCF theory. The first, known as *state-specific CASSCF* (SS-CASSCF), involves the independent optimization of each electronic state of interest, for which a specific wavefunction is calculated. A downside of this method is that the wavefunctions of different electronic states optimized separately are not orthogonal, which can lead to difficulties in accurately describing transitions between states or calculating transition properties such as dipole moments or non-adiabatic couplings. Non-orthogonality can also complicate the interpretation of excited-state dynamics, as the overlap between wave functions might introduce errors or inconsistencies in the computed energies and transition probabilities. The second approach, called *state-averaged CASSCF*, treats all the electronic states in a common orbital basis and simultaneously implements the MC-SCF optimization. The energy to be optimized is a linear combination of the energies of the individual electronic states E_I (see Equation 2.28). So, in SA-CASSCF, the orbitals are not optimized for a particular state, as in the case of SS-CASSCF. Instead, they are the ones that minimize the weighted average energy of all the states.(8)

$$E^{\text{SA-CASSCF}} = \sum_I w_I E_I \quad (2.28)$$

The weights w_I in Equation 2.28 are usually the same for each electronic state, although they can be fixed to other values according to the problem at hand.

SA-CASSCF is not recommended when the goal is to accurately describe a particular electronic state, whether it be the ground state or an excited state; for this purpose, SS-CASSCF is preferred. However, SA-CASSCF provides a consistent set of orthonormal electronic states, which is particularly important when studying conical intersections or systems with near-degenerate states. Moreover, the method simplifies the subsequent treatment of the electronic states through post-MC-SCF approaches, which aim to include dynamical correlation.

2.2 Modeling molecular dynamics

2.2.1. Introduction

Molecular dynamics (MD) is a computational method used to simulate the motion of atoms and molecules over time by solving equations of motion, which can be classical, quantum, or hybrid classical-quantum in nature.

In *ab initio* molecular dynamics (AIMD), also called BOMD, the nuclear motion is treated classically, while the electronic structure is solved quantum mechanically, typically using methods like density functional theory (DFT) or Hartree-Fock. The forces on the nuclei are computed *ab initio*, using an electronic structure computation at each position of the nuclei for determining the gradient of the potential. AIMD relies on classical equations of motion for the nuclei, assuming

the separation of electronic and nuclear dynamics via the Born-Oppenheimer approximation and motion of the nuclei on a single electronic state. Classical molecular dynamics employs empirical parametrized force fields to simulate the behavior of large molecular systems. This approach is well-suited for systems where quantum effects are less significant or very large. For large systems, it becomes prohibitive to compute the forces *ab initio* for each new position of the nuclei.

In contrast, quantum dynamics involves a full quantum mechanical treatment of both the nuclei and electrons, capturing their coupled evolution. This approach requires solving the Time-Dependent Schrödinger Equation (TDSE) for the entire system, accounting for both the electronic and nuclear wavefunctions. Meanwhile, surface hopping and other quantum-classical hybrid methods focus on modeling non-adiabatic transitions between electronic states within a quantum framework, while treating the nuclei classically.

The QM/MM (Quantum Mechanics/Molecular Mechanics) method is a hybrid approach in which quantum mechanics is applied to a small, critical part of the system, typically the region of interest, such as the active site of a chemical reaction, while the surrounding environment is treated classically using force fields. This method allows for computationally feasible simulations of large systems where a full quantum mechanical treatment would be prohibitively expensive.

Choice of initial conditions

The selection of initial conditions is a crucial aspect of any MD simulation. These conditions must be chosen carefully, as the equations of motion are solved numerically, and the algorithms employed are often sensitive to the starting point. Whether in classical or quantum MD, well-defined initial conditions can significantly enhance both the accuracy and efficiency of the simulation. The choice of appropriate initial conditions depends on the specific molecular system and the physical context being simulated. A thoughtful selection of these conditions ensures that the system begins in a physically realistic configuration, which is essential for obtaining accurate results in its time evolution.

In classical and *ab initio* MD, the initial conditions consist of the positions and velocities of all the nuclei in the system. These are typically obtained from experimental data, previous simulations, or by assigning random velocities that satisfy the desired temperature of the system. The latter approach, known as thermal sampling, involves drawing velocities from the Maxwell-Boltzmann distribution and is a common method, as experiments are typically conducted at a given temperature. Consequently, the appropriate initial state is often taken to be an ensemble at thermal equilibrium. The initial atomic positions are usually taken from an idealized or equilibrated structure, such as a crystal lattice or a minimized conformation for a molecular system. In the *ab initio* and classical steered molecular dynamics (AISMD) simulations, that we performed in our mechanochemistry work, the external force, both magnitude and direction, is also an initial condition, and greatly influences the course of the dynamics.

In quantum dynamics, the initial state must accurately reflect the quantum description of the molecular system. A pure quantum state is typically represented by a wavefunction, such as the wave function of the molecule in its equilibrium ground electronic. Unlike classical MD, where initial conditions are set by sampling coordinates and velocities, there is no general recipe for selecting the initial wavefunction in quantum dynamics, as it depends on the specific quantum

behavior of the system. For instance, in our work on the quantum dynamics of LiH, described in Chapters 5 and 6, the initial state was chosen as the ground electronic and vibrational state of the molecular Hamiltonian. In the case of CD_4^+ , the initial state reflects the wavepacket composition of the cation after the sudden photoionization of the ground electronic and vibrational state of the neutral molecule. On the other hand, a mixed quantum state cannot be described by a single wavefunction; instead, a density matrix is used. Mixed states arise when all the molecules in the ensemble are not in the same initial state, like in our work dealing with an ensemble of molecules with initial random orientations with respect to the polarization direction of the laser pulse discussed in Chapter 6. Environmental effects, such as solvent interactions, or higher temperatures, also lead to initial states that are mixed states.

In surface hopping dynamics, see 2.3 below, which is a semiclassical theory, a pure quantum state is represented by an ensemble of positions and velocities, which are sampled from the ground-state (electronic and vibrational) quantum Wigner distribution. This distribution maps the stationary ground vibrational states of the nuclei in each normal nuclear coordinate in the ground electronic state to a probability distribution in the phase space of the molecule. Additionally, it is essential to specify the initial electronic state from which the trajectories are initiated since the photoexcitation or photoionization process is described in the sudden approximation. This step is crucial, as the potential energies and nonadiabatic couplings, which are computed on the fly at each time step, are determined by the electronic state in which the trajectory is localized. A detailed description of sampling from the Wigner distribution can be found in Section 2.3.2 devoted to the surface hopping semi-classical method.

2.2.2. Ab initio molecular dynamics

Ab initio MD, also referred as Born-Oppenheimer MD (BOMD), incorporates electronic structure calculations into molecular dynamics simulations by solving the static electronic structure problem in each time step given the set of fixed nuclear positions to compute the force on the nuclei. At each time step, the time-independent, stationary Schrödinger equation (SE), Eq. 2.8, is solved concurrently to propagating the nuclei according to classical mechanics.

Formally, the equations of motion in AIMD can be written as:

$$M_\alpha \ddot{\mathbf{R}}_\alpha(t) = -\nabla_\alpha \min_{\phi_0^{\text{el}}} \{ \langle \phi_0^{\text{el}} | \hat{H}^{\text{el}} | \phi_0^{\text{el}} \rangle \} \quad (2.29)$$

Where M_α is the mass of nucleus α , $\ddot{\mathbf{R}}_\alpha(t)$ is the acceleration, \hat{H}^{el} is the electronic Hamiltonian (Eq. 2.9) and ϕ_0^{el} is the ground-state electronic wavefunction. Thus, the electronic energy is minimized with respect to the electronic wavefunction at the geometry of the nuclei reached at time t .

AIMD allows to model molecular dynamics at a high level of accuracy computing accurate forces ab initio. However, the method is computationally expensive, as it requires solving the SE at each time step, making it typically feasible only for relatively small systems or short simulation times.

To propagate the nuclear positions in AIMD simulations, classical integration algorithms, such as the velocity Verlet algorithm or the Leapfrog method, are commonly used to update the positions and velocities of the nuclei at each time step. These methods are efficient and widely employed

for integrating the classical equations of motion. For longer simulations or to improve thermodynamic accuracy, more sophisticated algorithms, such as those based on Hamiltonian dynamics or canonical ensemble methods, can be used to conserve energy or temperature. However, the primary computational challenge in AIMD arises from the need to solve the electronic structure problem, using methods like density functional theory (DFT), at each time step.

Throughout our research, we employed AIMD to model the relaxation of ethylene cation on the ground state potential energy surface, after the surface hopping trajectories spent more than 10 fs in the ground state. In this context, the initial conditions were taken from the final iteration of the surface hopping propagation scheme (see section 2.3 below). Additionally, the ab initio steered molecular dynamics simulations performed to model the response of furan/maleimide adducts to an external force can be considered a special case of AIMD, where a term due to the external force is added to the ab initio energy at each time step. For further details, see Chapter 3.

Sampling initial velocities from thermal distribution

The Maxwell-Boltzmann distribution describes the statistical distribution of velocities of particles in a system at thermal equilibrium. For ab initio steered molecular dynamics simulations performed on furan/maleimide adducts, the initial coordinates correspond to the equilibrium geometry of the molecule, previously optimized at a given value of the force. The velocities are drawn randomly from the Maxwell-Boltzmann distribution, allowing the generation of a set of different initial conditions. This randomness provides a way to create an ensemble of trajectories with statistical significance, which is crucial for simulating the system's dynamics under force.

The Maxwell-Boltzmann distribution for the velocities of particles in a system at temperature T is given by:

$$f(\mathbf{v}) = \left(\frac{m}{2\pi k_B T}\right)^{3/2} \exp\left(-\frac{mv^2}{2k_B T}\right) \quad (2.30)$$

Where $f(\mathbf{v})$ is the probability density function for the velocity vector $\mathbf{v} = [v_x, v_y, v_z]$, m is the particle mass, k_B is the Boltzmann constant, T is the temperature and $v = \|\mathbf{v}\| = \sqrt{v_x^2 + v_y^2 + v_z^2}$ is the magnitude of the velocity.

The distribution for the magnitude of the velocity or speed is deduced from the distribution of the velocity vector, Equation 2.31 and is illustrated in the graph of Figure 2.4.

$$f(v) = \sqrt{\frac{2}{\pi}} \left(\frac{m}{2\pi k_B T}\right)^{3/2} v^2 \exp\left(-\frac{mv^2}{2k_B T}\right) \quad (2.31)$$

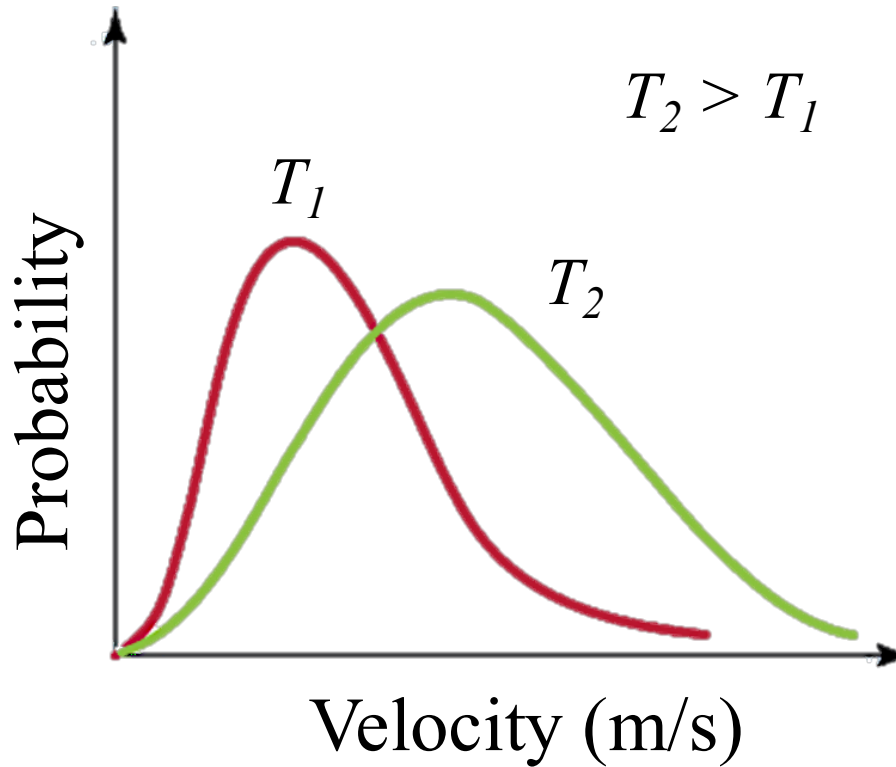


Figure 2.4: Maxwell-Boltzmann distribution of speed at two temperatures. At lower temperatures, the molecules have less kinetic energy, resulting in lower speeds and narrower distribution. At higher temperatures, molecules move faster, leading to a broader distribution.

The velocity vector distribution (Equation 2.30) is the product of the three distributions for each velocity component in the x , y , and z directions: $f(\mathbf{v}) = f(v_x)f(v_y)f(v_z)$. This implies that each component has a normal distribution with mean $\mu_{v_x} = \mu_{v_y} = \mu_{v_z} = 0$ and standard deviation $\sigma_{v_x} = \sigma_{v_y} = \sigma_{v_z} = \sqrt{k_B T/m}$, as shown in Equation 2.32.

$$f(v_i) = \sqrt{\frac{m}{2\pi k_B T}} \exp\left(-\frac{mv_i^2}{2k_B T}\right), \quad i = x, y, z \quad (2.32)$$

This allows us to obtain the velocity vector for atom by sampling its components v_x , v_y , and v_z independently from a normal distribution with mean 0 and standard deviation $\sigma = \sqrt{k_B T/m}$. This ensures that the system is initialized in thermal equilibrium at temperature T , where m is the mass of each atom.

2.2.3. Photoinduced coupled electron-nuclei quantum dynamics

2.2.3.1 Introduction on quantum dynamics

Quantum dynamics studies how quantum systems evolve over time, governed by the principles of quantum mechanics. Unlike classical dynamics, which describe systems via deterministic trajectories, quantum dynamics takes into account the probabilistic nature of the behavior of atoms and molecules. This involves the time evolution of wavefunctions, which describe the quantum state of a system, by integrating the TDSE (see Equation 2.1). Quantum dynamics is essential for modeling systems where quantum effects, such as superposition, entanglement, coherence phenomena, branching at conical intersections, tunneling, and the interaction with light play, a significant role, particularly in areas like molecular reactions, electron transfer, and excited-state dynamics. In the next section, we describe in detail how can we model the dynamics of molecular systems photoexcited by ultrashort laser pulses. Setting up quantum dynamics simulations is often limited to systems with a small number of nuclear degrees of freedom because of the exponential raise in the number of complex coefficients of the wavefunction when the size of the molecule increases. In our work in attochemistry we proposed methodologies that aim to reduce the computational complexity associated with solving the TDSE in a quantum dynamics simulation, without compromising the accuracy. This is discussed in Chapter 6.

2.2.3.2 Modeling light-matter interaction within the dipole approximation

Light pulses constitute a ubiquitous tool for studying ultrafast chemical processes. These include charge relocalization and transfer phenomena, such as those observed in photosynthesis, exciton dynamics in semiconductors, and electron transfer in metal complexes, as well as photoinduced chemical reactions, including those mediated by radicals and excited electronic states. The wide range of applications of optical pulses leverage key properties such as coherence, higher and selective excitation energy, and ultrafast timescales.

Few-femtosecond (10^{-15} s) and attosecond (10^{-18} s) pulses can be used to photoexcite molecules from their ground electronic state into a superposition of several excited electronic states. This excitation creates a molecular vibronic wavepacket on several electronic states that moves in phase from the Franck Condon region defined by the ground state into more complex regions of the configurational space, accessing reaction pathways and geometries that are otherwise inaccessible in the ground state. The potential energy surfaces of each electronic state often exhibit complex landscapes that affect the motion of the wavepacket in different ways, leading to intramolecular dephasing and the dispersion of the coherent motion on a picosecond or even femtosecond time scale. Dephasing can also arise from interactions with the environment, such as collisions with solvent molecules.

A time-evolving molecular system in a superposition state has both electrons and nuclei out of equilibrium, with their motions entangled, giving rise to novel interactions that have no classical counterpart. Studying the motion of the molecular wavepacket in these conditions is essential to understanding the subsequent photorelaxation processes and the chemical reactions they induce. From a theoretical perspective simulating such phenomena demands a fully quantum mechanical description of at least the molecular system. In a fully quantum mechanical treatment, energy conservation dictates that a change in the state of the molecular system shall be accompanied by the annihilation of a photon from the optical pulse. This way the Hamiltonian \hat{H} has three terms,

$$\hat{H} = \hat{H}_M + \hat{H}_L + \hat{H}_{LM} \quad (2.33)$$

where \hat{H}_M , \hat{H}_L , and \hat{H}_{LM} represent the Hamiltonians for the molecule, the optical pulse, and for the light-molecule interaction.

However, we are interested in the effect that the light has on the matter, so we neglect the term \hat{H}_L in Equation 2.33, leading to the two terms of Equation 2.34, where $\hat{H}_{LM}(t)$ is treated semiclassically, as we now detail. The Hamiltonian for the molecular system is generally time-independent, whereas the one that describes how the light pulse influences the matter is time-dependent.

$$\hat{H} \approx \hat{H}_M + \hat{H}_{LM}(t) \quad (2.34)$$

The effect of the exciting pulse can be described by a classical electromagnetic field, with real electric and magnetic vectors obeying Maxwell's equations. This approach of simulating light-matter interaction is semiclassical as the molecule is treated quantum mechanically, but the light classically. The Hamiltonian \hat{H}_{LM} has off-diagonal matrix elements between two electronic states which induce transitions between them.

Light pulses applied in attochemistry typically have low intensity and wavelengths much larger than the molecular dimensions. This means that the amplitude of the electromagnetic field can be assumed to be practically constant over the spatial extent of the molecule, so we focus exclusively on the time dependence, which can then be evaluated conveniently at the center of charge of the molecule \mathbf{r}_0 . This approximation is known as the *long-wavelength approximation*. In these circumstances, the Hamiltonian \hat{H}_{LM} has the form of the interaction energy arising from a classical electric dipole localized at \mathbf{r}_0 in a field with intensity $\mathbf{E}(\mathbf{r}_0, t)$.

$$\hat{H}_{LM} = -\hat{\mu} \cdot \mathbf{E}(\mathbf{r}_0, t) \quad (2.35)$$

The electric molecular dipole $\hat{\mu}$ is determined by the arrangement of electrons and nuclei in the molecule, so it has contributions from both. The nuclear dipole moment (first term in Equation 2.36) arises from the positions of the positively charged atomic nuclei in the molecule.

$$\hat{\mu} = \sum_{\substack{A \\ \text{Nuclei}}} eZ_A \mathbf{R}_A - \sum_{\substack{i \\ \text{Electrons}}} e\mathbf{r}_i \quad (2.36)$$

In Equation 2.36, e is the elemental constant charge of the electron, Z_A , \mathbf{R}_A are the number of protons, and the position, respectively, of the nuclei A , while \mathbf{r}_i is the position vector of the electron i .

If the positions of the nuclei in the molecule are asymmetric, it will result in an unequal distribution of positive charge, creating a permanent dipole moment. The electronic term accounts for the distribution of negative charge in the molecule due to the electron cloud within the molecule. This distribution can be calculated using ab initio methods. When multiple electronic states are involved

simultaneously, such as in the superposition wavepacket, the electronic term can be written as a matrix with elements $\mu_{ij}(\mathbf{R}) = \langle \psi_i | (e\mathbf{r}) | \psi_j \rangle$, where ψ_i and ψ_j represent two electronic states, and the integration is over electronic coordinates.

- Diagonal elements μ_{ii} represent the dipole within the same electronic state and contribute to the *permanent dipole* of the molecule, along with the nuclear contribution.
- Off-diagonal elements μ_{ij} (where $i \neq j$) correspond to the dipole moments between two different electronic states and are known as *transition dipole vectors*. The magnitude and direction of the transition dipole determine the magnitude and polarization of photon absorption or emission, as they quantify the probability of a molecule transitioning from one electronic state to another when interacting with the electromagnetic field of light.

From the two Maxwell equations $\nabla \cdot \mathbf{B} = 0$, which implies the non-existence of sources for the magnetic field, and $\nabla \times \mathbf{E}(\mathbf{r}, t) = -\partial \mathbf{B}(\mathbf{r}, t) / \partial t$, we deduce expressions for the magnetic and electric fields that depend on two potential functions, the vector potential $\mathbf{A}(\mathbf{r}, t)$ and the scalar potential $U(\mathbf{r}, t)$,

$$\begin{cases} \mathbf{B}(\mathbf{r}, t) = \nabla \times \mathbf{A}(\mathbf{r}, t) \\ \mathbf{E}(\mathbf{r}, t) = -\frac{\partial}{\partial t} \mathbf{A}(\mathbf{r}, t) - \nabla U(\mathbf{r}, t) \end{cases} \quad (2.37)$$

where $\mathbf{B}(\mathbf{r}, t)$, and $\mathbf{E}(\mathbf{r}, t)$ represent the magnetic and electric field vectors, respectively, and $\mathbf{A}(\mathbf{r}, t)$, and $U(\mathbf{r}, t)$ are the vector and scalar potentials, which characterize completely the fields. Notice the electric field $\mathbf{E}(\mathbf{r}, t)$ depends on an electrostatic term $-\nabla U(\mathbf{r}, t)$, and electrodynamic term $-\frac{\partial}{\partial t} \mathbf{A}(\mathbf{r}, t)$.

This ansatz, however, implies the existence of an infinite number of valid definitions of the potentials $U(\mathbf{r}, t)$ and $\mathbf{A}(\mathbf{r}, t)$, since they can be transformed without altering the physical electromagnetic field ($\mathbf{E}(\mathbf{r}, t)$ and $\mathbf{B}(\mathbf{r}, t)$). These transformations of the potentials that leave the fields intact are known as *gauge transformations*. The gauge freedom reflects the fact that, unlike the fields, the potentials are not directly observable.

To get rid of the ambiguity in the definition of the electromagnetic potentials and to have a consistent definition of the interaction Hamiltonian, we must select a particular gauge. A common choice in quantum optics is the Coulomb gauge, which is defined by the condition,

$$\nabla \cdot \mathbf{A}(\mathbf{r}, t) = 0 \quad (2.38)$$

which restricts the choice of vector potential $\mathbf{A}(\mathbf{r}, t)$ to a solenoidal or divergence-free vector field, much like the magnetic field.

The Coulomb gauge allows for a clear distinction between the static electric field generated by the nuclei (electrostatic term) and the externally applied electromagnetic radiation. (16) In other words, in the Coulomb gauge, the electric field due to the pulse is source-free, leading to the

vanishing of the scalar potential term $\nabla U(\mathbf{r}, t)$ in Equation 2.37. As a result, the electric field of the pulse can be derived entirely from the time-derivative of the vector potential,

$$\mathbf{E}(\mathbf{r}, t) = -\frac{\partial}{\partial t}\mathbf{A}(\mathbf{r}, t) \quad (2.39)$$

The vector potential satisfies a homogeneous wave equation whose solution can be written as a set of plane waves:

$$\mathbf{A}(\mathbf{r}, t) = A_0\hat{\varepsilon}e^{i(\mathbf{k}\cdot\mathbf{r} - \omega t + \phi_0)} + A_0^*\hat{\varepsilon}e^{-i(\mathbf{k}\cdot\mathbf{r} - \omega t + \phi_0)} \quad (2.40)$$

Using only real components, as both the electric and magnetic fields are real, and employing Euler's formula $e^{i\theta} = \cos(\theta) + i\sin(\theta)$, the vector potential can be expressed as

$$\mathbf{A}(\mathbf{r}, t) = A_0\hat{\varepsilon}\cos(\mathbf{k}\cdot\mathbf{r} - \omega t + \phi_0) \quad (2.41)$$

which describes the free electromagnetic wave oscillating in time at an angular frequency ω , and propagating in space in the direction along the wavevector \mathbf{k} . It has an amplitude A_0 directed along the polarization unit vector $\hat{\varepsilon}$, and ϕ_0 is the initial phase. Notice that since the sine and cosine functions differ just by a phase shift of $\pi/2$, that is to say $\sin(\theta) = \cos\left(\theta + \frac{\pi}{2}\right)$, the above equation can be written as well as

$$\mathbf{A}(\mathbf{r}, t) = A_0\hat{\varepsilon}\sin(\mathbf{k}\cdot\mathbf{r} - \omega t + \phi_0) \quad (2.42)$$

where the $\pi/2$ shift has been absorbed in the phase.

To represent the vector potential of an ultrashort light pulse, we can apply to Equation 2.42 a Gaussian filter, centered at a time t_0 and with a duration determined by the standard deviation σ . This leads to Equation 2.43, where we have also neglected the spatial dependence, in line with the long-wavelength approximation.

$$\mathbf{A}(t) = A_0\hat{\varepsilon}\exp\left(-\frac{(t - t_0)^2}{2\sigma^2}\right)\sin(\omega(t - t_0) + CEP) \quad (2.43)$$

The phase term *CEP* (stands for carrier-envelope phase) is an important parameter of the pulse. It is determined by the phase difference between the *carrier* electromagnetic wave and the Gaussian *envelope*. Different CEPs will select different features of the electromagnetic carrier wave, which in turn will influence the interaction with the molecule. For example, by appropriately selecting the CEP and the duration of the pulse, a positive or negative component of the carrier wave can be isolated and directed to a molecule, triggering remarkably different relaxation dynamics and chemical events. We took advantage of this feature in our work, ref (17).

Substituting Eq 2.43 in Eq 2.39, we arrive at the expression of the electric field of the optical pulses utilized in our work of attochemistry.

$$\mathbf{E}(t) = \hat{\mathbf{e}}E_0 \exp\left[\frac{-(t-t_0)^2}{2\sigma^2}\right] \left(\cos(\omega(t-t_0) + CEP) - \frac{\sin(\omega(t-t_0) + CEP)(t-t_0)}{\omega\sigma^2} \right) \quad (2.44)$$

where ω is the carrier frequency, E_0 is the field strength, σ is the pulse duration, $\hat{\mathbf{e}}$ is a unit polarization vector, and CEP the carrier-envelope phase. The duration is related to the Full-Width at the Half Maximum (FWHM) of the Gaussian envelope by the expression $FWHM = 2.35\sigma$.

The Fourier transform (FT) of a pulse oscillating in time gives its spectral representation in the frequency domain (see Eq 2.45a and Eq 2.45b).

$$\text{direct FT} \quad \mathcal{F}[E(t)] = X(\omega) = \int_{-\infty}^{\infty} E(t)e^{-i\omega t} dt \quad (2.45a)$$

$$\text{inverse FT} \quad \mathcal{F}^{-1}[X(\omega)] = E(t) = \int_{-\infty}^{\infty} X(\omega)e^{i\omega t} d\omega \quad (2.45b)$$

The frequency of a pulse is essentially its carrier frequency, which determines the photon energy ($E = h\omega$) responsible for inducing a transition between two electronic states. However, the shorter the pulse duration, the wider the spectral bandwidth, and vice versa. The finite energy bandwidth means there are photons of different energies in the pulse, which is used to excite several electronic states with atto and few femtosecond pulses. This relationship between the pulse duration (Δt) and the spectral bandwidth ($\Delta\omega$) is formally expressed in Equation 2.46,

$$\Delta t \cdot \Delta\omega \geq \frac{1}{4\pi} \quad (2.46)$$

If the pulse satisfies the equality relation $\Delta t \cdot \Delta\omega = 1/4\pi$, then it is said that the pulse is *Fourier transform limited*, or *bandwidth limited*. A Fourier-limited pulse has the smallest possible duration over the set of pulses that have an identical power spectrum $|X(\omega)|^2$. Therefore, the envelope in time of Fourier limited pulses must contain at least one oscillation of the electric field. Note that we define pulse by their peak power (Eq 2.47).

$$P_p = f_p \left(\frac{E_p}{FWHM} \right) \quad (2.47)$$

Where P_p is the peak power in Watts, E_p is the energy of the pulse and $FWHM$ gives the duration of the pulse. The constant factor f_p is related to the shape of the pulse and accounts for its temporal profile. For Gaussian pulses is ≈ 0.94 . Equation 2.47 is valid only when nonlinear effects are negligible. When strong nonlinear distortions are present, a significant amount of the pulse energy may reside in the regions of the pulse that extend beyond the main peak, where the energy decreases. This redistribution of energy can lead to substantial modifications in the relationship between peak power and pulse energy.

Having resolved the expression of the electric field and considering that the evaluation of the dipole moment matrix can be done by ab initio calculations, the time-dependent Hamiltonian $-\hat{\mu} \cdot \mathbf{E}(t)$, which describes the interaction of the light with the molecule, can be evaluated as well.

In the following, we describe in more detail the optical pulses used in attochemistry. The scheme in Figure 2.5 shows the two types of few cycles Gaussian pulses of different energy as indicated by the different wavelengths of the carriers, a deep UV pulse and a \approx one cycle IR pulse. They can be used to model the pulses engineered in optics. While the IR pulses of this type can be intense ($\sim 10^{13} \text{ W/cm}^2$ or more (18)) and induce multiphoton transitions, the deep UV pulses (19, 20) remain up to now weak ($< 10^{12} \text{ W/cm}^2$) and induce one photon or two photon transitions.

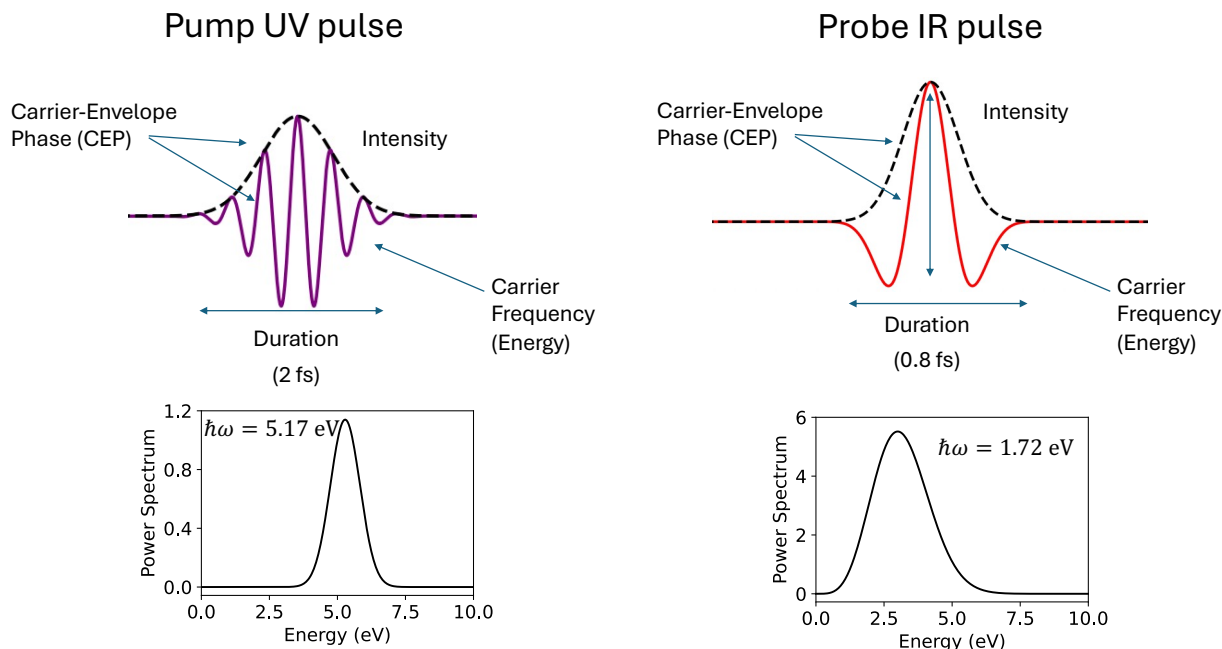


Figure 2.5: Illustration of the Gaussian pulses used to simulate optical pulses in attochemistry, highlighting the control parameters. The pulse on the left has a carrier frequency in the UV range and thus is more energetic; it also has several full oscillations inside the envelope, so it can excite or ionize a molecule by absorbing a very energetic photon. The pulse on the right contains an IR carrier, so it is less energetic, and it has a single full oscillation inside the envelope, but it is more intense, so it can be used to induce multi-photon excitations.

In the context of pump-probe experiments in attochemistry, a high-energy pulse, such as an XUV pulse, can be used to "pump" a wavepacket from a lower to a higher energy state. This process involves exciting a vibrational distribution of molecules from their electronic ground state to a superposition of the ground state and excited states. If the pump pulse has sufficient energy to exceed the ionization potential, it can ionize the molecules by removing an electron. Low energy pulses, such as IR pulses, can then be used to "probe" or monitor the motion of the excited wavepacket along its relaxation pathways. When they are sufficiently intense, they can also be used to excite neutral molecules and/or to induce multiphoton ionization.

In Chapter 4, we discuss a pump-probe scheme that uses few-femtosecond tunable EUV radiation in combination with few-femtosecond IR pulses to study the photodissociation of hydrogenated and deuterated ethylene cations. We explain the more pronounced oscillations observed in the relative fragmentation yields of C_2D_4^+ compared to the hydrogenated case, where such oscillations are less discernible.

2.2.3.3 *The Franck-Condon Principle*

For our studies on ethylene (Chapter 4) and methane (Chapter 7) cations, we assume sudden photoionization of the neutral molecule, meaning the ionizing pulse is not included in the dynamics. Under these conditions, we apply the Franck-Condon (FC) principle to describe the photoionization process

The FC principle assumes that the electronic transitions occurs almost instantaneously compared to the time scale of nuclear motion. It relies on the Born-Oppenheimer approximation, which neglects nuclear motion on the timescale of electronic motion due to the much heavier mass of the nuclei and the Condon principle, which assumes that during light absorption, the electrons move, while the nuclei do not have enough time to adjust their positions to the new electronic density and only relax after the electronic transition is complete. As a result, the nuclear wavefunctions do not change significantly during the electronic transition.

After the transition, however, the molecule moves to an excited electronic state, where the potential energy surface (PES) is very different from that of the initial state (typically the ground electronic state). This difference in PESs leads to vibrational excitation in the excited state. The reason is that the nuclear wavefunction that describes the vibrational state in the initial electronic state is not well suited to describe the vibrational state in the final electronic state, which has a different PES and a different equilibrium geometry. This means that the vibrational motion is nonstationary in the excited electronic state. Figure 2.6 illustrates this process in a cartoon.

The overlap integral between the vibrational wavefunctions of the initial and final states largely determines the transition probability between the two electronic states. The region of maximum overlap corresponds to the Franck-Condon region, where the intensity of the transition is largest.

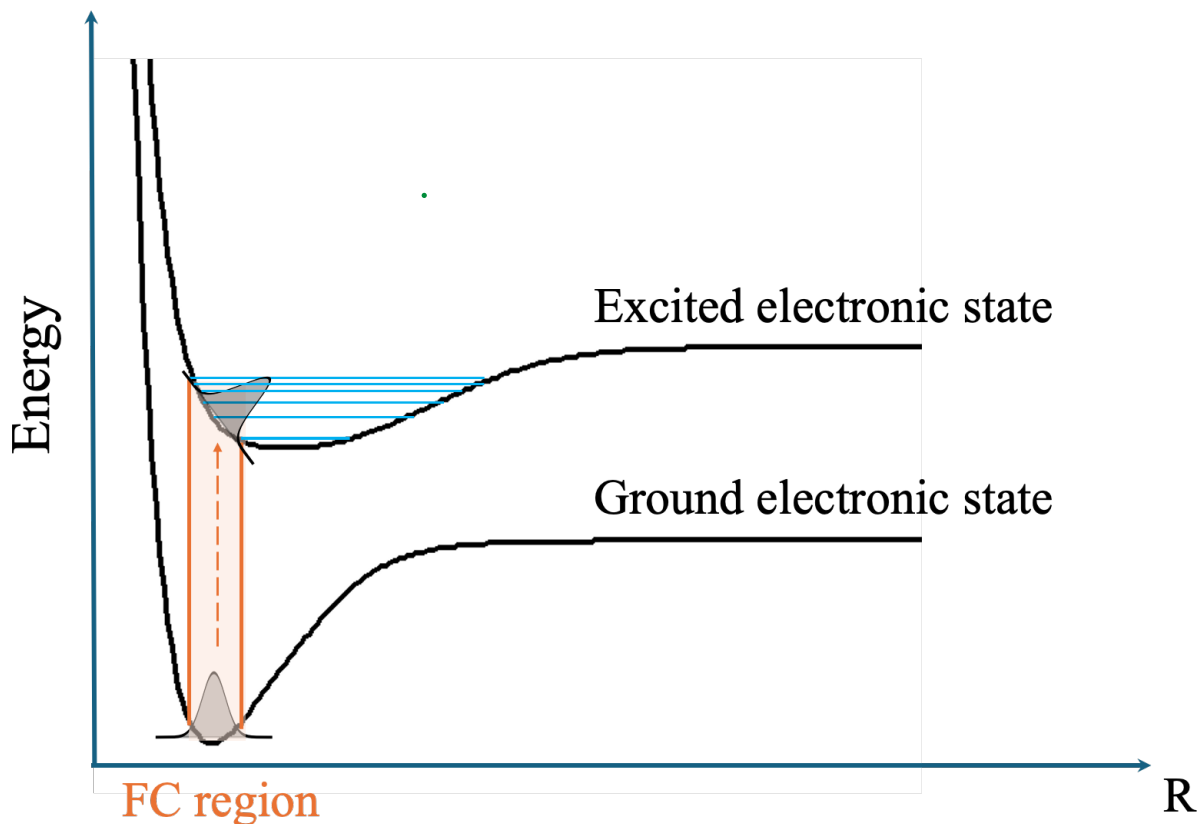


Figure 2.6: Vertical electronic transitions according to the Franck-Condon principle. Because the nuclei do not have time to adjust to the change in electronic configuration, the initial vibrational wavepacket in the ground electronic state is projected onto the vibrational states of the excited electronic state within the FC region. This results in a superposition of vibrational states in the excited electronic state, which is thus nonstationary.

2.2.4. Quantum mechanical description of the molecular system interacting with the pulse.

Having resolved the time-dependent interaction Hamiltonian (\hat{H}_{LM}) that couples the electromagnetic field of the light to the molecule and induces transitions between electronic or vibrational states, we will now discuss the quantum mechanical description of the molecular system. The molecular Hamiltonian (\hat{H}_M) is the time-independent Hamiltonian representing the energy of the electrons and nuclei in the molecule. See Eq. 2.2.

According to the postulates of quantum mechanics(21), once the Hamiltonian \hat{H} for the molecular system is defined, including the light-matter interaction term, the state of the system (i.e., the wavefunction) at any given time can be determined by solving the time-dependent Schrödinger (TDSE) equation.

$$-\frac{1}{i} \frac{\partial \Psi(\mathbf{r}, \mathbf{R}, t)}{\partial t} = \left(\hat{H}_M - \mathbf{E}(t) \cdot \hat{\mu}(\mathbf{R}) \right) \Psi(\mathbf{r}, \mathbf{R}, t) \quad (2.48)$$

Here, the wavefunction $\Psi(\mathbf{r}, \mathbf{R}, t)$, which depends on the electronic coordinates \mathbf{r} , the nuclear coordinates \mathbf{R} , and time, contains all the information that can be determined about the system. It describes its behavior and response during and after interaction with the electric field of the pulse

The BO treatment of the wavefunction, presented in Section 2.1.1, has been successfully employed to study molecules as they evolve in their ground electronic state. This covers a wide range of applications. However, when a molecule is excited with an ultrashort pulse, the wave packet comprises several coupled electronic states that have different potentials, and the electrons are out of equilibrium. We need a formalism that accounts for the coupling between electrons and nuclei for simulating the dynamics of a wavepacket described by a superposition of several electronic states.

The Born-Huang (BH) approach is an extension of the BO approximation that addresses these effects by expanding the total molecular wavefunction as a sum over adiabatic electronic states, each weighted by a corresponding nuclear wavefunction:

$$\Psi(\mathbf{r}, \mathbf{R}, t) = \sum_n^{\infty} \phi_n^{el}(\mathbf{r}; \mathbf{R}) \chi_n(\mathbf{R}, t) \quad (2.49)$$

The adiabatic electronic states $\phi_n^{el}(\mathbf{r}; \mathbf{R})$ form an infinite basis for the Hilbert space of the molecular wavefunction, while the time-dependent nuclear wavefunctions $\chi_n(\mathbf{R}, t)$ serve as coefficients for this expansion.

In practice, we must truncate the BH expansion, as dealing with an infinite set of adiabatic electronic states is computationally unfeasible. By considering only a set of N electronic states, which could be the ones that are accessed by excitation with the ultrashort pulse, we obtain the truncated version of the BH expansion:

$$\Psi(\mathbf{r}, \mathbf{R}, t) \approx \sum_n^N \phi_n^{el}(\mathbf{r}; \mathbf{R}) \chi_n(\mathbf{R}, t) \quad (2.50)$$

The time-dependent Schrödinger equation, despite its mathematical simplicity, can be solved analytically only for very simple two-body interacting systems, such as the hydrogen atom or other systems with a single electron. For more complex systems, this equation typically must be solved numerically, as analytical solutions become impractical. In many cases, we do not know the eigenstates of the Hamiltonian, which makes it challenging to employ methods based on these eigenstates for time evolution.

2.2.4.1 Solving the TDSE

In the Born-Huang (BH) approach, the nuclei and electrons are treated separately, each with its own wavefunction. However, the nuclear kinetic energy term \hat{T}_N introduces couplings between the particles, as the Laplacian operator involves derivatives with respect to the nuclear coordinates R . It is important to note that both the nuclear and electronic wavefunctions depend on R , although in the electronic wavefunction, the nuclear coordinates are considered fixed parameters.

The complete Hamiltonian can be expressed as:

$$\hat{H} = \hat{T}_N + \hat{H}^{el} + \hat{V}_{NN} - \mathbf{E} \cdot \hat{\mu} \quad (2.51)$$

where the electronic terms have been concentrated in the electronic Hamiltonian \hat{H}^{el} which satisfies the eigenvalue equation from Eq 2.8: $\hat{H}^{el} \phi^{el}(\mathbf{r}; \mathbf{R}) = E^{el} \phi^{el}(\mathbf{r}; \mathbf{R})$, yielding the adiabatic basis for the molecular wavefunction.

Substituting the Hamiltonian (Equation 2.51) and the Born-Huang expansion (Eq 2.50) in the TDSE (Eq 2.48), projecting onto the set of adiabatic electronic wave functions and integrating over electronic coordinates, we obtain a set of coupled Hamiltonian equations for the nuclei. These equations describe the motion of the nuclei on the coupled electronic adiabatic potential energy surfaces. The derivation is provided below.

1. Substitute \hat{H} and $\Psi(\mathbf{r}, \mathbf{R}, t)$ in the TDSE.

$$\begin{aligned} -\frac{1}{i} \frac{\partial \Psi(\mathbf{r}, \mathbf{R}, t)}{\partial t} &= (\hat{T}_N + \hat{H}^{el} + \hat{V}_{NN} - \mathbf{E}(t) \cdot \hat{\mu}(\mathbf{R})) \Psi(\mathbf{r}, \mathbf{R}, t) \\ &= -\frac{1}{i} \frac{\partial}{\partial t} \left[\sum_n^N \phi_n^{el}(\mathbf{r}; \mathbf{R}) \chi_n(\mathbf{R}, t) \right] = \\ &= (\hat{T}_N + \hat{H}^{el} + \hat{V}_{NN} - \mathbf{E}(t) \cdot \hat{\mu}(\mathbf{R})) \left[\sum_n^N \phi_n^{el}(\mathbf{r}; \mathbf{R}) \chi_n(\mathbf{R}, t) \right] \end{aligned} \quad (2.52a)$$

Projecting onto the orthonormal set of adiabatic electronic eigenfunctions $\{\phi_m^{el}(\mathbf{r}; \mathbf{R})\}$ the left-hand side resolves as follows:

$$\begin{aligned} &\left\langle \phi_m^{el}(\mathbf{r}; \mathbf{R}) \left| -\frac{1}{i} \frac{\partial}{\partial t} \left[\sum_n^N \phi_n^{el}(\mathbf{r}; \mathbf{R}) \chi_n(\mathbf{R}, t) \right] \right. \right\rangle \\ &= \sum_n^N \left(\left\langle \phi_m^{el}(\mathbf{r}; \mathbf{R}) \left| \phi_n^{el}(\mathbf{r}; \mathbf{R}) \right. \right\rangle \left(-\frac{1}{i} \frac{\partial}{\partial t} \chi_n(\mathbf{R}, t) \right) \right) \\ &= -\frac{1}{i} \frac{\partial}{\partial t} \chi_m(\mathbf{R}, t) \end{aligned} \quad (2.52b)$$

The right-hand side becomes:

$$\begin{aligned} &\left\langle \phi_m^{el}(\mathbf{r}; \mathbf{R}) \left| \hat{T}_N + \hat{H}^{el} + \hat{V}_{NN} - \mathbf{E}(t) \cdot \hat{\mu}(\mathbf{R}) \right| \Psi(\mathbf{r}, \mathbf{R}, t) \right\rangle \\ &= \left\langle \phi_m^{el}(\mathbf{r}; \mathbf{R}) \left| \hat{T}_N \right| \Psi(\mathbf{r}, \mathbf{R}, t) \right\rangle + \left\langle \phi_m^{el}(\mathbf{r}; \mathbf{R}) \left| \hat{H}^{el} \right| \Psi(\mathbf{r}, \mathbf{R}, t) \right\rangle \\ &+ \left\langle \phi_m^{el}(\mathbf{r}; \mathbf{R}) \left| \hat{V}_{NN} \right| \Psi(\mathbf{r}, \mathbf{R}, t) \right\rangle - \mathbf{E} \cdot \left\langle \phi_m^{el}(\mathbf{r}; \mathbf{R}) \left| \hat{\mu} \right| \Psi(\mathbf{r}, \mathbf{R}, t) \right\rangle \end{aligned} \quad (2.52c)$$

Each term can be evaluated independently, as described below:

2. Evaluate the nuclear kinetic energy operator $\hat{T}_N = -\frac{1}{2}\sum_A \frac{\nabla_{\mathbf{R}_A}^2}{M_A}$ using the Born Huang expansion of the total wavefunction

$$\langle \phi_m^{el}(\mathbf{r}; \mathbf{R}) | \hat{T}_N | \Psi(\mathbf{r}, \mathbf{R}, t) \rangle = -\frac{1}{2} \sum_A \frac{1}{M_A} \langle \phi_m^{el}(\mathbf{r}; \mathbf{R}) | \nabla_{\mathbf{R}_A}^2 | (\sum_n^N \phi_n^{el}(\mathbf{r}; \mathbf{R}) \chi_n(\mathbf{R}, t)) \rangle \quad (2.52d)$$

Distributing the Laplacian operator over the sum and differentiating on the product of electronic and nuclear wavefunctions we obtain:

$$\begin{aligned} & \nabla_{\mathbf{R}_A}^2 \left(\sum_n \phi_n^{el}(\mathbf{r}; \mathbf{R}) \chi_n(\mathbf{R}, t) \right) = \\ & \sum_n \phi_n^{el}(\mathbf{r}; \mathbf{R}) \nabla_{\mathbf{R}_A}^2 \chi_n(\mathbf{R}, t) + 2 \nabla_{\mathbf{R}_A} \phi_n^{el}(\mathbf{r}; \mathbf{R}) \cdot \nabla_{\mathbf{R}_A} \chi_n(\mathbf{R}, t) + (\nabla_{\mathbf{R}_A}^2 \phi_n^{el}(\mathbf{r}; \mathbf{R})) \chi_n(\mathbf{R}, t) \end{aligned} \quad (2.52e)$$

Substituting this result back into Eq 2.52d leads to three terms that can be evaluated separately. The first term represent the nuclear kinetic energy on each adiabatic electronic state. It is diagonal as $\langle \phi_m^{el}(\mathbf{r}; \mathbf{R}) | \phi_n^{el}(\mathbf{r}; \mathbf{R}) \rangle = \delta_{mn}$

$$-\frac{1}{2} \sum_A \frac{1}{M_A} \sum_n \langle \phi_m^{el}(\mathbf{r}; \mathbf{R}) | \phi_n^{el}(\mathbf{r}; \mathbf{R}) \rangle \nabla_{\mathbf{R}_A}^2 \chi_n(\mathbf{R}, t) = -\frac{1}{2} \sum_A \frac{1}{M_A} \nabla_{\mathbf{R}_A}^2 \chi_m(\mathbf{R}, t) \quad (2.52f)$$

The second and third terms contain the first-order and second-order non-adiabatic couplings that couple nuclear and electronic motion. They are by convention designated τ_{mn} , and G_{mn} , respectively. The first-order coupling τ_{mn} couples the nuclear gradient to electronic transitions. The second-order coupling G_{mn} represent more complex transitions between nuclear and electronic motion.

$$\begin{aligned} & -\frac{1}{2} \sum_A \frac{1}{M_A} \sum_n 2 \langle \phi_m^{el}(\mathbf{r}; \mathbf{R}) | \nabla_{\mathbf{R}_A} \phi_n^{el}(\mathbf{r}; \mathbf{R}) \rangle \cdot \nabla_{\mathbf{R}_A} \chi_n(\mathbf{R}, t) \\ & = -\sum_A \frac{1}{M_A} \sum_n \tau_{mn}(\mathbf{R}) \cdot \nabla_{\mathbf{R}_A} \chi_n(\mathbf{R}, t) \end{aligned} \quad (2.52g)$$

$$-\frac{1}{2} \sum_A \frac{1}{M_A} \sum_m \langle \phi_m^{el}(\mathbf{r}; \mathbf{R}) | \nabla_{\mathbf{R}_A}^2 \phi_n^{el}(\mathbf{r}; \mathbf{R}) \rangle \chi_n(\mathbf{R}, t) = -\frac{1}{2} \sum_A \frac{1}{M_A} \sum_n G_{mn}(\mathbf{R}) \chi_n(\mathbf{R}, t) \quad (2.52h)$$

Notice that by definition:

$$\tau_{nm} = \langle \phi_m^{el}(\mathbf{r}; \mathbf{R}) | \nabla_{\mathbf{R}_A} \phi_n^{el}(\mathbf{r}; \mathbf{R}) \rangle \quad (2.52i)$$

$$G_{nm} = \langle \phi_m^{el}(\mathbf{r}; \mathbf{R}) | \nabla_{\mathbf{R}_A}^2 \phi_n^{el}(\mathbf{r}; \mathbf{R}) \rangle \quad (2.52j)$$

3. Evaluate the electronic Hamiltonian operator \hat{H}^{el} . Due to the choice of the adiabatic basis, this Hamiltonian is diagonal in that representation, so it can be easily resolved considering the orthonormality of its eigenstates $\phi_n^{el}(\mathbf{r}; \mathbf{R})$.

$$\begin{aligned} \langle \phi_m^{el}(\mathbf{r}; \mathbf{R}) | \hat{H}^{el} | (\sum_n^N \phi_n^{el}(\mathbf{r}; \mathbf{R}) \chi_n(\mathbf{R}, t)) \rangle &= \sum_n \langle \phi_m^{el}(\mathbf{r}; \mathbf{R}) | \hat{H}^{el} | \phi_n^{el}(\mathbf{r}; \mathbf{R}) \rangle \chi_n(\mathbf{R}, t) \\ &= E_m^{el}(\mathbf{R}) \chi_m(\mathbf{R}, t) \end{aligned} \quad (2.53)$$

4. Evaluate the nuclear potential \hat{V}_{NN} . This operator acts as a multiplicative constant since the positions of the nuclei are fixed.

$$\begin{aligned} \langle \phi_m^{el}(\mathbf{r}; \mathbf{R}) | \hat{V}_{NN} | (\sum_n^N \phi_n^{el}(\mathbf{r}; \mathbf{R}) \chi_n(\mathbf{R}, t)) \rangle &= \sum_n \langle \phi_m^{el}(\mathbf{r}; \mathbf{R}) | \phi_n^{el}(\mathbf{r}; \mathbf{R}) \rangle \hat{V}_{NN} \chi_n(\mathbf{R}, t) \\ &= V_{NN}(\mathbf{R}) \chi_m(\mathbf{R}, t) \end{aligned} \quad (2.54)$$

5. Evaluate the electric dipole Hamiltonian which carries the interaction with the electric field of the pulse. Remembering that the dipole operator has an electronic and a nuclear term $\hat{\mu} = \hat{\mu}^{el} + \hat{\mu}^{nuc}$, and that the nuclear dipole is diagonal as it acts only within the same electronic state, we obtain:

$$\begin{aligned} \langle \phi_m^{el}(\mathbf{r}; \mathbf{R}) | -\mathbf{E}(t) \cdot \hat{\mu} | (\sum_n^N \phi_n^{el}(\mathbf{r}; \mathbf{R}) \chi_n(\mathbf{R}, t)) \rangle &= \\ -\mathbf{E}(t) \cdot \sum_n \langle \phi_m^{el}(\mathbf{r}; \mathbf{R}) | \hat{\mu}^{el} | \phi_n^{el}(\mathbf{r}; \mathbf{R}) \rangle \chi_n(\mathbf{R}, t) & \\ -\mathbf{E}(t) \cdot \sum_n \langle \phi_m^{el}(\mathbf{r}; \mathbf{R}) | \hat{\mu}^{nuc} | \phi_n^{el}(\mathbf{r}; \mathbf{R}) \rangle \chi_n(\mathbf{R}, t) &= \\ -\mathbf{E}(t) \cdot \sum_n \mu_{mn}^{el}(\mathbf{R}) \chi_n(\mathbf{R}, t) - \mathbf{E}(t) \cdot \mu^{nuc}(\mathbf{R}) \chi_m(\mathbf{R}, t) & \end{aligned} \quad (2.55)$$

6. Gathering all the terms we get the expression of the nuclear TDSE with a coupled Hamiltonian,

$$\begin{aligned} -\frac{1}{i} \frac{\partial}{\partial t} \chi_m(\mathbf{R}, t) &= -\frac{1}{2} \sum_A \frac{1}{M_A} \nabla_{\mathbf{R}_A}^2 \chi_m(\mathbf{R}, t) - \sum_A \frac{1}{M_A} \sum_n \tau_{mn}(\mathbf{R}) \cdot \nabla_{\mathbf{R}_A} \chi_n(\mathbf{R}, t) \\ &- \frac{1}{2} \sum_A \frac{1}{M_A} \sum_n G_{mn}(\mathbf{R}) \chi_n(\mathbf{R}, t) + \left(E_m^{el}(\mathbf{R}) + V_{NN}(\mathbf{R}) \right) \chi_m(\mathbf{R}, t) \\ &- \mathbf{E}(t) \cdot \sum_n \mu_{mn}^{el}(\mathbf{R}) \chi_n(\mathbf{R}, t) - \mathbf{E} \cdot \mu_m^{el}(\mathbf{R}) \chi_m(\mathbf{R}, t) \end{aligned} \quad (2.56)$$

This equation can be written in a more compact matrix form notation, using mass-scaled coordinates:

$$-\frac{1}{i} \frac{\partial \Psi(t)}{\partial t} = \left(-\frac{1}{2M} (\nabla^2 + 2\boldsymbol{\tau} \cdot \nabla + G) + V - \mathbf{E}(t) \cdot \boldsymbol{\mu} \right) \Psi(t) \quad (2.57)$$

where $\Psi(t)$ is a column vector with components $\chi_m(\mathbf{R}, t)$, m runs over electronic states, M is the mass of the system, V contains the effective potentials $(E_m^{el}(\mathbf{R}) + V_{NN}(\mathbf{R}))$ governing the nuclear motion on each electronic state, the so-called Potential Energy Surfaces (PESs).

The dipole matrix contains both electronic and nuclear components of the permanent dipole in the diagonal, and off-diagonal entries represent the transition dipole between two electronic states. If the transition dipole moment between two electronic states is large, then the electric field of a resonant pulse induces a transition between these two states, leading to entanglement of the nuclear and electronic motion.

The nonadiabatic coupling matrix τ couples the motion of the wavepacket between two different electronic states. It is an intrinsic property of the system and does not depend on external factors, such as the interaction with the light. It modulates the initial entanglement created with the pulse and it is responsible for the occurrence of nonradiative process through conical intersections or avoided crossings.

A conical intersection (CI) is a geometry in n -dimensional configuration space for the nuclear coordinates where two (or more) electronic states become degenerate. CIs form a $(n-2)$ -dimensional subspace known as the seam for a given pair of degenerate electronic states. Near the seam, the potential energy surfaces behave linearly, within a first-order approximation, such that the intersection between the two electronic states resembles the crossing of two planes in 3D space, forming a cone. This is why these degeneracy points are referred to as (points of) *conical intersection*, or simply CIs.(22) The lowest-energy CI in the seam is called the minimum energy conical intersection (MECI) and it can be located with geometry optimization techniques. The two-dimensional space orthogonal to the seam is known as the branching space.(23) In the vicinity of the MECI, it can be spanned by two vectors: one corresponding to the non-adiabatic derivative coupling and the other to the energy gradient difference.

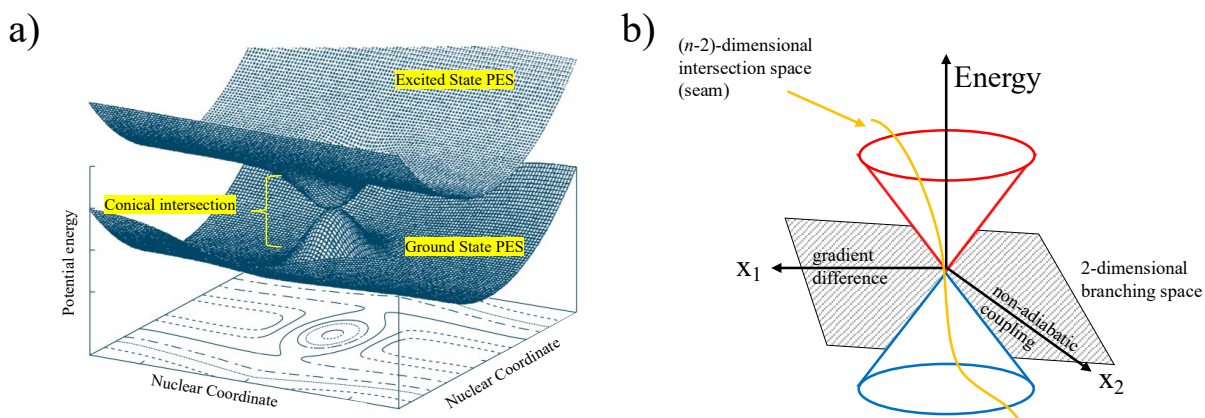


Figure 2.7: a) Cartoon representing a conical intersection between two electronic states, which become degenerate. Adapted from ref. (22). b) In the vicinity of the conical intersection, the nonadiabatic coupling vectors and the gradient difference form a plane that lifts the degeneracy between the two states. The points of intersection, represented by the yellow line, form a $(N-2)$ -dimensional space known as the seam.

Loosely speaking, we call a conical interaction a region of the configurational space traversed by the nuclear wavepacket where two or more electronic states become very close in energy. In such regions, the non-adiabatic coupling induces transitions from one electronic state to another without emitting a photon (nonradiative decay). The electronic energy is converted to nuclear kinetic energy thanks to the couplings between the electronic and nuclear motion in the vicinity of an MECI. Conical intersections act as funnels or geometrical filters in the configurational space as the wavepacket, driven by the non-adiabatic coupling vector, tends to adopt a particular geometry. For example, in our work on photorelaxation of ethylene cation (submitted to *J. Phys. Chem. Lett.*), the wavepacket relaxes to the ground state mainly through a planar conical intersection, which constrains the molecule to be planar and with a CC bond compressed. The non-adiabatic coupling vector $\tau_{mn}(\mathbf{R})$ activates the twisting of the molecule and the CC bond, which in turn modulates the fragmentation yields due to higher probability of re-excitation with an IR pulse: a three-photon resonance mechanism identified previously for this molecule. (24) More details are given in Chapter 4.

The second-order nonadiabatic coupling term G is crucial to maintain the hermiticity of the Hamiltonian, and this guarantees it has real eigenvalues and orthogonal eigenfunctions, which is critical for a correct description of the dynamics of the system. However, evaluating the G term in the computer is very costly as it involves second derivatives of the electronic wavefunction with respect to the nuclear coordinates (Eq 2.52j). It is the case that for a group of electronic states that form a Hilbert subspace (N states in the BH expansion), the $\boldsymbol{\tau}$ matrix satisfies the divergence condition and G can be written in terms of $\boldsymbol{\tau}$ (22, 25, 26) as indicated below:

$$\mathbf{G} = \boldsymbol{\tau} \cdot \boldsymbol{\tau} + \nabla \cdot \boldsymbol{\tau} \quad (2.58)$$

Then the coupling of electronic and nuclear motion can be expressed entirely in terms of the nonadiabatic coupling matrix $\boldsymbol{\tau}$ (Eq 2.52i), which can be computed either by finite difference or analytically in state-average CASSCF using Molpro (13, 14) or any other multireference quantum chemistry code.

$$\boldsymbol{\Lambda} = 2\boldsymbol{\tau} \cdot \nabla + \boldsymbol{\tau} \cdot \boldsymbol{\tau} + \nabla \cdot \boldsymbol{\tau} \quad (2.59)$$

where $\boldsymbol{\Lambda}$ represents the full nonadiabatic coupling term. We used this approach in our work defining an exact quantum mechanical expression of the force exerted on the nuclei (Chapter 5 and ref (17)).

2.2.4.2 Discretization of the nuclear wavefunctions and of the Hamiltonian operator

In theory, the nuclear wavefunctions $\{\chi_m(\mathbf{R}, t), m = 1, 2, \dots, N\}$ are continuous functions that do not have a general analytical form. To represent them in the computer we need to discretize the nuclear motion using a finite basis set. We use a discrete variable representation (DVR) of the nuclear coordinates \mathbf{R} in a local basis based on a grid of points, with each point corresponding to a specific geometry. An alternative DVR basis employs delocalized nuclear functions, typically harmonic oscillator functions, which provide a more accurate description of nuclear behavior around equilibrium positions but are more computationally expensive.

Orthogonal door functions centered at every geometry sampled from the configurational space are commonly used in a grid-based DVR. The grid of geometries is made by partitioning all the nuclear degrees of freedom and taking steps along each dimension. A door function is a step function that is 1 over a certain interval or n -dimensional box, and 0 elsewhere.

$$|\theta_{\mathbf{A}}(\mathbf{R})\rangle = \begin{cases} 1, & \mathbf{x} \in \mathbf{A}, \\ 0, & \text{otherwise} \end{cases} \quad (2.60)$$

Which guarantees their orthogonality. \mathbf{A} in Equation 2.60 represents a multidimensional box centered at the geometry \mathbf{R} . It can be written as a Cartesian product of intervals across all N nuclear dimensions.

$$\mathbf{A} = \prod_g^N [x_g, x_{g+1}] \quad (2.61)$$

where g is an index over each nuclear coordinate, x_g and x_{g+1} defined an interval of length Δx that comprises the geometry \mathbf{R} along the coordinate g .

Because in the frame of the center of mass, for a non-rotating isolated molecule, the number of nuclear degrees of freedom is $3 * N - 6$ (where N is the number of nuclei in the molecule), the number of points that need to be sampled to completely specify the nuclear wavefunctions grows exponentially with the size of the molecule. This makes it impractical to treat the quantum dynamics of polyatomic molecules using all the nuclear degrees of freedom. Instead, a reduced number of coordinates must be selected, and this requires a thorough understanding of the chemical process to be able to choose among the whole set of nuclear degrees of freedom, those that are critical. This is why a crucial step when setting up a quantum dynamics simulation is the selection of optimal coordinates for constructing the nuclear grid. Having identified adequate coordinates guarantee a correct sampling of the geometries and pathways of interest from the configurational space, during the nuclear dynamics.

Once the nuclear grid is defined, for each geometry all the electronic properties and couplings are evaluated from ab initio computations. This includes the potential energies, the nonadiabatic couplings and the dipole moments. The wavefunction of the molecule, containing both electronic and nuclear parts, can be written in discrete form as:

$$|\psi(t)\rangle = \sum_{g=1}^{N_g} \sum_{i=1}^{N_e} c_{gi}(t) |gi\rangle \quad (2.62)$$

Where the indices g and i run over nuclear and electronic coordinates, respectively. $|gi\rangle = |g\rangle \otimes |i\rangle$ is the vibronic basis and $c_{gi}(t)$, the time-dependent coefficients of wavefunction in the linear combination of basis functions $|gi\rangle$.

2.2.5. Hamiltonian in the linear diatomic molecule LiH.

LiH is a simple diatomic polar molecule, commonly used for proving novel quantum dynamics methods. We used it as toy model to show as proof of principle the derivation of the expression of the force exerted by the vibronic wavepacket on the nuclei, considering all the nonadiabatic couplings and the interaction with the pulse in the dipole approximation. (17) For this purpose, we

had to simulate the coupled electron-nuclei dynamics of the molecule of LiH within 7 adiabatic electronic states S_0 to S_7 . The molecule LiH has a single nuclear degree of freedom as we can specify completely the molecular geometry by just giving the distance between the two atoms. This makes much simpler the expression of the Hamiltonian and easier to solve the TDSE. Partitioning uniformly the internuclear distance of LiH yields a one-dimensional grid of geometries where the potential energies, dipole and nonadiabatic couplings are evaluated. (27)

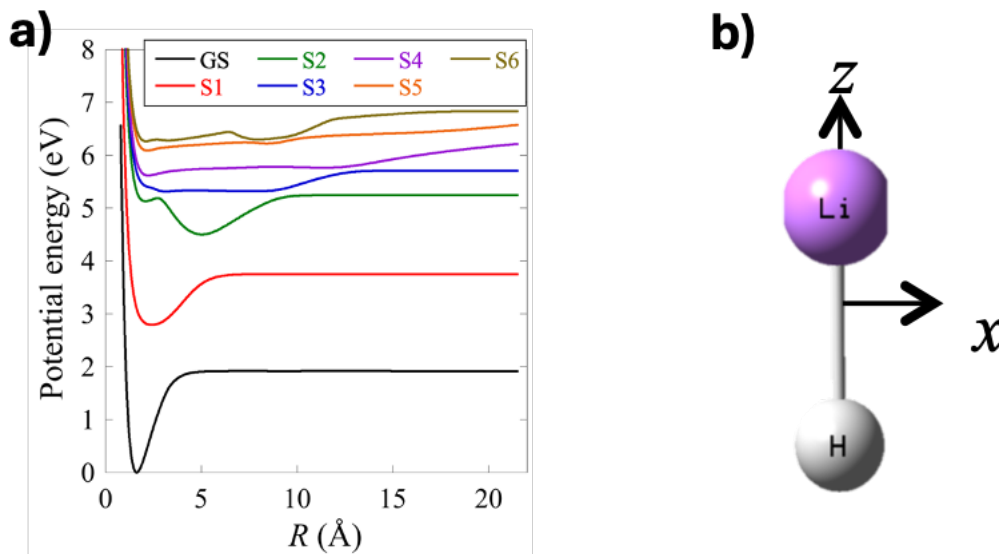


Figure 2.8: a) Potential energy surfaces of the 7 lowest singlet electronic states computed for each geometry in the grid of LiH. b) Geometry of LiH with the origin at the center of mass and oriented along the Z axis.

The Hamiltonian in LiH has the form

$$\mathbf{H} = -\frac{1}{2\mu}(\nabla_R^2 + 2\tau(R) \cdot \nabla_R + \nabla_R \tau(R) + \tau(R) \cdot \tau(R)) + V(R) - \mathbf{E}(t) \cdot \boldsymbol{\mu}(R) \quad (2.63)$$

where R is a scalar variable representing the internuclear distance, $\mu = \frac{m(\text{Li})m(\text{H})}{m(\text{Li}) + m(\text{H})}$ is the reduced mass, $V(R)$ is a diagonal matrix of potential energies of the adiabatic electronic states. The dipole matrix $\boldsymbol{\mu}(R) = \boldsymbol{\mu}^{nuc}(R) + \boldsymbol{\mu}^{el}(R)$ is diagonal in grid points, while $\tau(R)$, the matrix of nonadiabatic couplings (NAC) between all pairs of electronic states, has only off-diagonal entries with respect to the electronic states, and it is also diagonal on grid points. The nuclear kinetic energy given by ∇_R^2 is diagonal on both electronic and nuclear states.

All the terms of the Hamiltonian can be precomputed as the time dependence lies strictly in the electric field $\mathbf{E}(t)$ of the pulse and in the coefficients of the wavefunction. In a grid representation, the potential energies $V(R)$, nonadiabatic couplings $\tau(R)$, and dipole $\boldsymbol{\mu}(R)$ are local on the grid, so their matrix elements can be evaluated at each geometry of the grid, using state-averaged CASSCF in Molpro (7, 11, 13, 14), for example. The nuclear kinetic energy $T^{(R)} = -\frac{1}{2\mu} \nabla_R^2$ and momentum $p^{(R)} = -i\nabla_R$ are both nonlocal in the grid coordinate representation (R), but they are

local in the momentum representation (p), and act as a multiplicative term. The momentum becomes $p^{(p)} = \hbar k$ (simply $p^{(p)} = k$ in atomic units) with k being the wavenumber. The kinetic energy becomes $T^{(R)} = -\frac{1}{2\mu}k^2$. Using the Fourier transform and its inverse we can transform the wavefunction from position to momentum space and vice versa, respectively. Then, in the momentum representation, we can apply the kinetic energy operator by multiplying the $c(t)$ wavevector by $-k^2$. Finally, we transform back to the position representation. The next scheme describes the sequence of operations needed to evaluate the kinetic (and momentum) operators using the Fourier transform method. (28, 29) (30)

$$-\frac{1}{2\mu}\nabla_R^2 c(t)|_x \xrightarrow{DFT} -\frac{1}{2\mu}k^2 \cdot c(t)|_p = c'(t)|_p \xrightarrow{IDFT} c'(t)|_x$$

where DFT and IDFT are the discrete direct and inverse Fourier transforms, respectively.

However, utilizing the Fourier method to evaluate the nonlocal kinetic energy and momentum operators in the grid, makes the integration of the TDSE more complex as we now need to perform more complex operations every time step such as taking the two Fourier transforms. This is why in our work we decided not to follow such approach and instead we evaluated the operators in position space but using finite difference. This approach is accurate and has the advantage that the kinetic energy operators can now be written as matrices in the same way as the potential energy, NAC and dipole. This simplifies a lot the implementation in the computer as we integrate fully in the coordinate space and all the operators are applied as matrix-vector operations. (31) The action of the kinetic energy operator, using the 5 points central finite difference, and the momentum, using the 4 points central finite difference, with accuracy $O(h^4)$ are shown below:

$$\begin{aligned} \frac{dc_u}{du} &= \frac{c_{u-2} - 8c_{u-1} + 8c_{u+1} - c_{u+2}}{12h^2} + O(h^4) \\ \frac{d^2c_u}{du^2} &= \frac{-c_{u-2} + 16c_{u-1} - 30c_u + 16c_{u+1} - c_{u+2}}{12h^2} + O(h^4) \end{aligned} \tag{2.64}$$

where h represents the equal spacing of the intervals in the grid (~ 0.08 Bohr). c_u represents the component of the wavevector \mathbf{c} at the grid point u . Notice that because in LiH we deal with a single nuclear coordinate, the Laplacian and the gradient operators coincide with just the second and first derivative, respectively, with respect to the internuclear distance symbolized by the index u .

We can write the above operations in matrix form as we show below

with initial conditions $\mathbf{c}(t_0) = \mathbf{c}_0$. In the case of LiH, the initial state \mathbf{c}_0 is the lowest-energy eigenvector of the Hamiltonian \mathbf{H} , obtained by diagonalization with a Lanczos algorithm (36). The Hamiltonian matrix is inherently very sparse, so we allocate it in memory in compressed sparse form (CSR) during the propagation for better performance. This allowed us to leverage a variety of numerical algorithms optimized for sparse matrix-vector operations and to employ highly optimized linear algebra subroutines such as the ones provided by LAPACK and MKL libraries with intel C and Fortran compilers.

In the RK4 scheme, the coefficients at the time step $n + 1$ is obtained from the previous step as given in the next equation:

$$\begin{aligned} \mathbf{c}_{n+1} &= \mathbf{c}_n + \frac{1}{6}(k_1 + 2k_2 + 2k_3 + k_4)\Delta t \\ k_1 &= -i\mathbf{H}(t_n)\mathbf{c}_n \\ k_2 &= -i\mathbf{H}(t_n + \frac{\Delta t}{2})(\mathbf{c}_n + \frac{1}{2}k_1\Delta t) \\ k_3 &= -i\mathbf{H}(t_n + \frac{\Delta t}{2})(\mathbf{c}_n + \frac{1}{2}k_2\Delta t) \\ k_4 &= -i\mathbf{H}(t_n + \Delta t)(\mathbf{c}_n + k_3\Delta t) \end{aligned} \tag{2.67}$$

where Δt is the time step of the dynamics and the iteration is carried for a certain number of steps spanning the time range where the evolution of the wavepacket dynamics is followed and ensuring good accuracy so the norm of the wavefunction is kept within acceptable values, with a deviation from 1 of typically $< 10^{-11}$.

For the vibronic dynamics, the motion of the wavepacket can be followed accurately as soon as rotational and roto vibrational effects do not come into place, which occur in the order of picoseconds. In the study of LiH, the propagation was carried out up to 400 fs at most, where the norm of the wavefunction was still well preserved. When rotational and roto-vibrational effects come into play, one must solve the time-dependent Schrödinger equation in 2 or 3 dimensions depending on the symmetry of the molecule.

2.3 Modeling ultrafast excited-state processes in large molecular systems

Solving the Schrödinger Equation (SE) exactly becomes impractical for large molecules because as the number of degrees of freedom increases, the number of variables in the wavefunction grows exponentially, making direct solutions increasingly challenging and necessitating the use of advanced techniques and approximations to handle the complexity. This is known as the “curse” or the bottleneck of the dimensionality.

Previously, we discussed how, once a Hamiltonian is defined on a nuclear grid, the TDSE can be propagated to obtain the vibronic wavefunction and describe the molecular process in detail. However, for large systems with many degrees of freedom, creating an N-dimensional grid and evaluating the electronic potential energies, nonadiabatic couplings and dipoles to construct a Hamiltonian becomes unfeasible. The computational demands, such as the enormous storage

requirements for disk and memory, far exceed current capabilities. Additionally, numerical algorithms become increasingly inefficient when performing linear algebra operations on large matrices and vectors. In these circumstances, two alternatives can be explored. The first involves reducing the dimensionality of the vibronic wavefunction and Hamiltonian by selecting a subset of nuclear coordinates that can reproduce accurately the dynamics. This selection process can be guided by chemical intuition and prior knowledge of the system. For instance, in our study of the CD_4^+ cation, discussed in Chapter 7, we reduced the system to two nuclear coordinates, transforming the wavefunction and operators necessary for propagation to this simplified coordinate system. The wave packet dynamics were then propagated in a similar manner to the case of LiH but with a 2D grid instead of a 1D grid.

This dimensionality reduction approach allows quantum dynamics to be applied to studying small polyatomic molecules. However, as the size of the molecule increases, it becomes more challenging to identify which coordinates are most relevant for the calculations. Multiple modes may be involved in larger systems, and it may not be straightforward to select the coordinates that best represent the system's dynamics.

We must rely on approximations in modeling the nuclear motion for medium- and large-sized molecules, sacrificing some chemical accuracy to obtain results within a reasonable computational time. Nevertheless, these approximate methods can still provide valuable insights into photochemical processes triggered by ultrafast light pulses. In the next subsection, we describe in more detail the surface hopping method, which is widely used for such purposes.

2.3.1. Surface hopping dynamics using the SHARC method

The study of the photodynamics of medium-sized molecules requires a semi-classical approach in which the treatment of nuclear motion is done classically, while the electrons remain treated quantum-mechanically. The surface hopping (SH) method (37) is a popular approach that falls in this range of semiclassical algorithms. It excels due to its simplicity which makes it easy to interpret, its potential on-the-fly implementations and parallelization, and because it allows to treat all the nuclear degrees of freedom at reasonable computational cost. (38, 39) Nevertheless, SH cannot reproduce truly quantum effects like the zero-point energy, tunneling or electronic and nuclear interferences. (38, 39)

In the study of photorelaxation of ethylene cation, we have employed a variant of SH developed by the group of Leticia Gonzalez (38), which is able to account for spin-orbit coupling effects, as well as for the nonadiabatic nuclear-electronic couplings. The method is implemented in the program SHARC, maintained by the same group, and which is available free of cost. The SHARC acronym stands for *Surface Hopping including Arbitrary Couplings*, a reference to both the algorithm and the program. SHARC can be used to study many excited state processes in large molecules, such as intersystem crossing dynamics, relaxation throughout a network of conical intersections, and photoelectron spectroscopy. Another code that is used extensively is Newton-X, developed by Mario Barbatti's group. (40) In SH the quantum electronic part is represented by the electronic wavefunction $|\Phi^{el}(t)\rangle$ defined on an electronic basis. (37) (38)

$$|\Phi^{el}(t)\rangle = \sum_n c_n(t) |\Psi_n(t)\rangle \quad (2.68)$$

Where n runs over all the electronic basis states, $c_n(t)$ are the time-dependent coefficients, and $|\Psi_n(t)\rangle$ are the electronic basis states.

In SHARC, $(|\Psi_n(t)\rangle)$ represents the adiabatic basis that diagonalizes the electronic Hamiltonian at time t , corresponding to the geometry of the classically moving nuclei at that instance. Strictly speaking, it should be written as $|\Psi_n(\mathbf{r}; R(t))\rangle$, where \mathbf{r} represents the electronic coordinates and $R(t)$ the time-dependent nuclear positions. Alternatively, the method allows for the inclusion of states with different multiplicities in the simulation, which may be coupled through relativistic spin-orbit coupling (SOC) interactions. If that is the case, the electronic Hamiltonian contains a term composed of the kinetic energy and Coulombic terms of the molecular system, which is the molecular Coulomb Hamiltonian (MCH), and a second term that contains the SOC Hamiltonian with off-diagonal terms that couple electronic states of different spin multiplicity.

$$H^{el} = H^{MCH} + H^{SOC} \quad (2.69)$$

We employed the SHARC method to simulate the ultrafast photorelaxation of ethylene cation following the sudden ionization of a sample of ethylene with an XUV pump pulse. We modeled the coupled excited state dynamics of the doublet cation throughout a network of critical conical intersections. So, spin-orbit couplings were not considered, and the states have all the same spin multiplicity: doublet in this case. This means that our electronic Hamiltonian is the MCH, Equation 2.8.

The electronic time-dependent Schrödinger equation is then solved for the electronic Hamiltonian $H^{el} = H^{MCH}$ and with the electronic wavefunction $|\Phi^{el}(t)\rangle$

$$\hat{H}^{el}|\Phi^{el}(t)\rangle = i \frac{\partial}{\partial t} |\Phi^{el}(t)\rangle \quad (2.70)$$

After substituting the electronic wavefunction from Equation 2.68, projecting on the electronic state $\langle\Psi_m(t)|$, and using the orthonormality property of the adiabatic electronic basis $\delta_{mn} = \langle\Psi_m|\Psi_n\rangle$, we obtain a set of coupled differential equations for the coefficients $c_n(t)$:

$$\begin{aligned} \langle\Psi_m(t)|H^{el} \sum_n c_n(t) |\Psi_n(t)\rangle &= i \langle\Psi_m(t)| \frac{\partial}{\partial t} \sum_n c_n(t) |\Psi_n(t)\rangle \\ \sum_n c_n(t) \langle\Psi_m(t)|H^{el}|\Psi_n(t)\rangle &= i \sum_n [c_n(t) \langle\Psi_m(t)| \frac{\partial}{\partial t} |\Psi_n(t)\rangle + \frac{\partial c_n(t)}{\partial t} \langle\Psi_m(t)|\Psi_n(t)\rangle] \\ \sum_n c_n(t) \langle\Psi_m(t)|H^{el}|\Psi_n(t)\rangle - i \sum_n c_n(t) \langle\Psi_m(t)| \frac{\partial}{\partial t} |\Psi_n(t)\rangle &= i \sum_n \frac{\partial c_n(t)}{\partial t} \langle\Psi_m(t)|\Psi_n(t)\rangle \\ \sum_n c_n(t) V_{mn} - i \sum_n c_n(t) T_{mn} &= i \frac{\partial c_m(t)}{\partial t} \\ \frac{\partial}{\partial t} c_m(t) &= - \sum_n [iV_{mn} + T_{mn}]c_n(t) \end{aligned} \quad (2.71)$$

Where $V_{mn} = \langle \Psi_m | H^{el} | \Psi_n \rangle$ represent the off-diagonal elements of the electronic Hamiltonian and $T_{mn} = \langle \Psi_m | \partial / \partial t | \Psi_n \rangle$ the nonadiabatic derivative coupling term. Both terms can promote transitions between electronic states. V_{mn} vanish in the adiabatic representation because the electronic Hamiltonian is diagonal, which leads to the simpler Equation 2.72:

$$\frac{\partial}{\partial t} c_m(t) = - \sum_n T_{mn} c_n(t) \quad (2.72)$$

Remembering that the adiabatic function Ψ_n depends parametrically on the nuclear coordinates, and using the chain rule, the time-derivative coupling T_{mn} can be expanded further as the dot product of the nuclear velocity vector \mathbf{v} (since the nuclei are treated classically) and the nonadiabatic derivative coupling vector ($\boldsymbol{\tau}_{mn}$) as shown in Equation 2.73.

$$T_{mn} = \left\langle \Psi_m(\mathbf{r}; \mathbf{R}) \left| \dot{\mathbf{R}} \cdot \frac{\partial}{\partial \mathbf{R}} \right| \Psi_n(\mathbf{r}; \mathbf{R}) \right\rangle = \dot{\mathbf{R}} \cdot \left(\left\langle \Psi_m(\mathbf{r}; \mathbf{R}) \left| \frac{\partial}{\partial \mathbf{R}} \right| \Psi_n(\mathbf{r}; \mathbf{R}) \right\rangle \right)$$

$$T_{mn} = \mathbf{v} \cdot \boldsymbol{\tau}_{mn} \quad (2.73)$$

where $\mathbf{v} = \frac{d\mathbf{R}}{dt}$ and \mathbf{R} is the vector of nuclear positions.

The temporal evolution of the electronic wavefunction is then conditioned by the classical nuclear coordinates $\mathbf{R}(t)$, while the nuclei follow classical trajectories in which the state of each nucleus: its position and velocity at each time ($\mathbf{R}(t), \mathbf{v}(t)$), is determined by integrating the Newton equation of motion

$$M_A \frac{\partial^2 \mathbf{R}_A}{\partial t^2} = \vec{F}_A \equiv - \frac{\partial E^{el}}{\partial \mathbf{R}_A} \quad (2.74)$$

Notice from Equation 2.74 that the classical forces on each atom \vec{F}_A are defined from the gradient of the electronic adiabatic potential on which the nuclei move. In contrast to a wavepacket, which can experience multiple potential gradients simultaneously if it corresponds to a superposition of electronic states, see Chapter 5 Section 5.1, the classical nuclei in each trajectory follow a single force at any given time as they evolve on one specific potential energy surface called the “active” electronic state. Nevertheless, at any time, the nuclei can move or “hop” probabilistically to a different electronic state due to the nonadiabatic coupling effects, which leads to a branching of the population at the level of the ensemble. To determine the active space at every time, SHARC uses the “fewest switches” stochastic algorithm from Tully *et al.* (37) In *Fewest Switching Surface Hopping* (FSSH), the decision of whether to switch or not electronic states is made at each integration time step by generating a uniform random number ζ between 0 and 1 to compute the hopping probability from the following condition:

$$\text{If } \frac{\Delta t b_{mn}}{a_{nn}} > \zeta \text{ then a switch from state } m \text{ to state } n \text{ will be invoked} \quad (2.75)$$

Here, $a_{nn} = c_n^* c_n$ represents the population of the electronic state n . The quantity b_{mn} depends on the electronic coherences $a_{mn}^* = c_m^* c_n$; generally, it can be written as $b_{mn} = 2 \operatorname{Im}(a_{mn}^* V_{mn}) - 2 \operatorname{Re}(a_{mn}^* T_{mn})$. In the adiabatic representation, this expression simplifies to $b_{mn} = 2 \operatorname{Re}(a_{mn}^* T_{mn})$. Such definition of the hopping probability ensures that no transitions will occur in regions of vanishing coupling since $b_{mn} = 0$. Also, the smaller the time step of the time integration, the smaller the probability of hopping, but there will be more steps, so the net probability does not depend on the size of the time step.

If a switch occurs, the component of the velocity in the direction of the nonadiabatic coupling vector is adjusted to reflect the change in the potential on the kinetic energy part. This ensures the conservation of the energy. The term “fewest switches” refers to the algorithm’s goal of minimizing the number of state hops while ensuring that the correct statistical distribution of state populations is always maintained. (37) Thus, the composition of the time-dependent electronic wavefunction is monitored through the population in each electronic state $|c_n(t)|^2$. When the population of the active state decreases, the probability to switch to any other state (surface hopping) is computed following the fewest switches algorithm.

2.3.2. Sampling of initial conditions from the Wigner distribution

In SH the quantum wavepacket is modeled as a swarm of trajectories, each with different initial conditions and independent one of the other. To recover the statistical character of the wavepacket propagation, the ensemble of trajectories must be averaged at each time step. For describing a photoexcitation process, the initial conditions should be sampled representatively from a statistical distribution that reflects the true quantum nature of the molecule in its ground vibrational and electronic state. In SHARC, the initial conditions $(\mathbf{R}_0(t), \mathbf{v}_0(t))$ are drawn from the quantum Wigner quasiprobability distribution. The Wigner function maps the stationary vibrational states of the nuclei to a probability distribution in the phase space of the molecule. The complex vibration of the nuclei about the equilibrium geometry can be approximated by a set of 3N-6 (or – 5) quantum harmonic oscillators of mass μ , corresponding to the reduced mass of the group of atoms involved in the normal mode and angular frequency ω , where the Hamiltonian takes the form

$$\hat{\mathcal{H}} = \frac{\hat{p}^2}{2\mu} + \frac{1}{2}\mu\omega^2\hat{R}^2 \quad (2.76)$$

Where \hat{R}, \hat{p} are the nuclear position and momentum operators that define the phase space and satisfy $[\hat{R}, \hat{p}] = i\hbar$ and $\hat{p} = -i\hbar\hat{\nabla}_R$. The potential in the vicinity equilibrium can be approximated by the quadratic term $V(R) = \frac{1}{2}\mu\omega^2(R - R_{eq})^2 = \frac{1}{2}k(R - R_{eq})^2$, where $k = \mu\omega^2$ is the force constant matrix determined from the Hessian of the potential at equilibrium

$$\mathbf{H}_{ij} = \left(\frac{\partial^2 V}{\partial R_i \partial R_j} \right)_{\text{Eq}} \quad (2.77)$$

The eigenvalues of the Hessian, after projecting out rotational and translational degrees of freedom, correspond to the squares of the vibrational frequencies (ω) and the eigenvectors serve as a basis for the normal modes (coordinates) of vibration which describes the collective motion

of the nuclei in the molecule. The stationary vibrational states of the harmonic oscillator are determined by the eigenvalue equation

$$\hat{\mathcal{H}}|\psi\rangle = \mathcal{E}_n|\psi\rangle \quad (2.78)$$

with $\mathcal{E}_n = \left(n + \frac{1}{2}\right) \hbar\omega$ being the evenly spaced quantized vibrational energy levels: $n = 0, 1, \dots$ is the vibrational quantum number, \hbar is the reduced Planck's constant, and ω is the angular frequency of the oscillator related to the force constant k by $\omega = \sqrt{k/\mu}$. The eigenfunctions $|\psi\rangle$ are given in terms of Hermite polynomials $H_n(\xi)$ as follows

$$\psi_n(R) = \frac{1}{\sqrt{n! 2^n}} \sqrt{\frac{\alpha}{\pi}} \left(e^{-\frac{\alpha R^2}{2}} \right) H_n(\sqrt{\alpha}R) \quad (2.79)$$

Where $\alpha = \sqrt{\frac{k\mu}{\hbar^2}}$. And the Hermite polynomials $H_n(\xi)$ are a family of orthogonal polynomials that satisfy the recurrence relation $H_{n+1}(\xi) = 2\xi H_n(\xi) - H_n'(\xi)$. The first Hermite polynomial is $H_0(\xi) = 1$.

The ground vibrational state ($n = 0$) has a non-zero energy $\mathcal{E}_0 = \frac{1}{2} \hbar\omega_0$ which shows that even at equilibrium, the nuclei are not static but rather constantly vibrating. Since the Hermite polynomial for $n = 0$ is $H_0(\sqrt{\alpha}R) = 1$, the ground state wavefunction $\psi_0(R)$ becomes:

$$\psi_0(R) = \left(\frac{\alpha}{\pi}\right)^{1/4} e^{-\frac{\alpha R^2}{2}} \quad (2.80)$$

This is a Gaussian wavefunction centered at the equilibrium position \mathbf{R}_{eq} with no nodes. It decays to zero as the distance from the equilibrium increases. This means that the nuclei's vibrational motion is most likely localized around the equilibrium geometry. However, the molecule's ground state is more accurately represented by a probability distribution of both positions and momenta rather than by a single geometry and velocity, as we do classically. To capture this behavior in the surface hopping dynamics, we need to sample the Wigner quasiprobability distribution, which gives the probability of any state of the nuclei given by geometry and momentum. For a pure quantum state $|\psi\rangle$ with the vibrational wavefunction ψ expressed in the position representation, the Wigner probability function $W(R, p)$ is defined as follows

$$W(R, p) = \frac{1}{\pi\hbar} \int_{-\infty}^{\infty} \psi^* \left(R + \frac{R'}{2} \right) \psi \left(R - \frac{R'}{2} \right) e^{-ipR'/\hbar} dR' \quad (2.81)$$

The same Wigner function can be obtained if the wavefunction were to be expressed in the momentum representation $\tilde{\psi}$

$$W(R, p) = \frac{1}{\pi\hbar} \int_{-\infty}^{\infty} \tilde{\psi}^* \left(p + \frac{p'}{2} \right) \tilde{\psi} \left(p - \frac{p'}{2} \right) e^{-iRp'/\hbar} dp' \quad (2.82)$$

Substituting the expression of the ground state wavefunction (Equation 2.80) into the Wigner function (Equation 2.81), we obtain the ground vibrational Wigner distribution which is from where SHARC samples the initial conditions for the SH dynamics.

$$W(R, p) = \frac{1}{\pi\hbar} e^{-\alpha R^2} e^{-\frac{p^2}{\alpha\hbar^2}} \quad (2.83)$$

Introducing the dimensionless operators for coordinate $\hat{Q} = (\mu\omega_0/\hbar)^{1/2}\hat{R}$ and momentum $\hat{P} = (\mu\omega_0/\hbar)^{-1/2}\hat{p}$ such as $[\hat{Q}, \hat{P}] = i$, the ground state Wigner distribution becomes:

$$W(Q, P) = \frac{1}{\pi} e^{-(Q^2+P^2)} \quad (2.84)$$

To sample the initial conditions (R, v) needed for the classical propagation of the nuclei in the SH dynamics, SHARC uses the optimized equilibrium geometry R_{eq} , the set of vibrational frequencies $\{v_i\}$ and the normal modes vectors $\{\mathbf{n}_i\}$ in mass-weighted Cartesian coordinates for every vibrational degree of freedom i . The last two can be obtained from any quantum chemistry code by computing and diagonalizing the Hessian. To obtain a set of N initial conditions $\{(\mathbf{R}_j, \mathbf{v}_j)\}$ for $j = 1 \dots N$, SHARC follows the procedure indicated below for each $(\mathbf{R}_j, \mathbf{v}_j)$

1. Start from the equilibrium geometry and zero velocities: $\mathbf{R}_j = \mathbf{R}_{eq}$ and $\mathbf{v}_j = 0$
2. For each vibrational degree of freedom i a decision of whether use it to update the coordinates and velocities or not is made. To accomplish this, a pair Q_i , and P_i are randomly generated from the interval $[-5, 5]$ and the ground state Wigner distribution is calculated and compared with a uniform random number $\eta_i \in [0, 1]$. Only if $W(Q_i, P_i) > \eta_i$ the coordinates and velocities are updated using Equation 2.85 and Equation 2.86.

$$\mathbf{R}_j \rightarrow \mathbf{R}_j + \frac{Q_i}{\sqrt{2v_i}} \mathbf{n}_i \quad (2.85)$$

$$\mathbf{v}_j \rightarrow \mathbf{v}_j + \frac{P_i\sqrt{v_i}}{\sqrt{2}} \mathbf{n}_i \quad (2.86)$$

2.4 References

1. I. N. Levine, *Quantum chemistry*. (Pearson, Boston, ed. Seventh edition, 2014), pp. 700.
2. A. Szabo, N. S. Ostlund, *Modern quantum chemistry: introduction to advanced electronic structure theory*. (Dover Publications, Mineola, N.Y, 1996), pp. 466.
3. J. Gräfenstein, E. Kraka, M. Filatov, D. Cremer, Can Unrestricted Density-Functional Theory Describe Open Shell Singlet Biradicals? *IJMS* **3**, 360-394 (2002).
4. Y. Shao *et al.*, Advances in molecular quantum chemistry contained in the Q-Chem 4 program package. *Molecular Physics* **113**, 184-215 (2015).
5. D. Hegarty, M. A. Robb, Application of unitary group methods to configuration interaction calculations. *Molecular Physics* **38**, 1795-1812 (1979).

6. B. O. Roos, P. R. Taylor, P. E. M. Sigbahn, A complete active space SCF method (CASSCF) using a density matrix formulated super-CI approach. *Chemical Physics* **48**, 157-173 (1980).
7. H.-J. Werner, W. Meyer, A quadratically convergent multiconfiguration–self-consistent field method with simultaneous optimization of orbitals and CI coefficients. *The Journal of Chemical Physics* **73**, 2342-2356 (1980).
8. T. Helgaker, P. Jørgensen, J. Olsen, *Molecular electronic-structure theory*. (Wiley, Chichester Weinheim, ed. Repr. as paperback, 2012), pp. 908.
9. P. J. Knowles, H.-J. Werner, An efficient second-order MC SCF method for long configuration expansions. *Chemical Physics Letters* **115**, 259-267 (1985).
10. D. A. Kreplin, P. J. Knowles, H.-J. Werner, Second-order MCSCF optimization revisited. I. Improved algorithms for fast and robust second-order CASSCF convergence. *The Journal of Chemical Physics* **150**, 194106 (2019).
11. H.-J. Werner, P. J. Knowles, A second order multiconfiguration SCF procedure with optimum convergence. *The Journal of Chemical Physics* **82**, 5053-5063 (1985).
12. D. A. Kreplin, P. J. Knowles, H.-J. Werner, MCSCF optimization revisited. II. Combined first- and second-order orbital optimization for large molecules. *The Journal of Chemical Physics* **152**, 074102 (2020).
13. H.-J. Werner *et al.*, The Molpro quantum chemistry package. *The Journal of Chemical Physics* **152**, 144107 (2020).
14. H. J. Werner, P. J. Knowles, G. Knizia, F. R. Manby, M. Schütz, Molpro: a general-purpose quantum chemistry program package. *WIREs Comput Mol Sci* **2**, 242-253 (2012).
15. P.-O. Löwdin, Quantum Theory of Many-Particle Systems. I. Physical Interpretations by Means of Density Matrices, Natural Spin-Orbitals, and Convergence Problems in the Method of Configurational Interaction. *Phys. Rev.* **97**, 1474-1489 (1955).
16. G. Grynberg, A. Aspect, C. Fabre, C. Cohen-Tannoudji, *Introduction to Quantum Optics: From the Semi-classical Approach to Quantized Light*. (Cambridge University Press, ed. 1, 2010).
17. M. Cardosa-Gutierrez, R. D. Levine, F. Remacle, Electronic coherences built by an attopulse control the forces on the nuclei. *J. Phys. B: At. Mol. Opt. Phys.*, (2024).
18. F. Krausz, M. Ivanov, Attosecond physics. *Rev. Mod. Phys.* **81**, 163-234 (2009).
19. M. Galli *et al.*, Generation of deep ultraviolet sub-2-fs pulses. *Opt. Lett.* **44**, 1308 (2019).
20. V. Wanie *et al.*, Ultraviolet supercontinuum generation using a differentially-pumped integrated glass chip. *J. Phys. Photonics* **6**, 025005 (2024).
21. C. Cohen-Tannoudji, B. Diu, F. Laloë, *Quantum mechanics*. (Wiley, New York, 1977), pp. 2.
22. M. Baer, *Beyond Born-Oppenheimer: conical intersections and electronic non-adiabatic coupling terms*. (Wiley, Hoboken, N.J., 2006).
23. S. Matsika, P. Krause, Nonadiabatic Events and Conical Intersections. *Annu. Rev. Phys. Chem.* **62**, 621-643 (2011).
24. M. Lucchini *et al.*, Few-Femtosecond C₂H₄⁺ Internal Relaxation Dynamics Accessed by Selective Excitation. *J. Phys. Chem. Lett.* **13**, 11169-11175 (2022).
25. B. K. Kendrick, C. Alden Mead, D. G. Truhlar, Properties of nonadiabatic couplings and the generalized Born–Oppenheimer approximation. *Chemical Physics* **277**, 31-41 (2002).
26. T. Pacher, C. A. Mead, L. S. Cederbaum, H. Köppel, Gauge theory and quasidiabatic states in molecular physics. *The Journal of Chemical Physics* **91**, 7057-7062 (1989).

27. S. van den Wildenberg, B. Mignolet, R. D. Levine, F. Remacle, Temporal and spatially resolved imaging of the correlated nuclear-electronic dynamics and of the ionized photoelectron in a coherently electronically highly excited vibrating LiH molecule. *The Journal of Chemical Physics* **151**, 134310 (2019).
28. A. Nikodem, R. D. Levine, F. Remacle, in *Progress in Ultrafast Intense Laser Science XIII*, K. Yamanouchi, W. T. Hill III, G. G. Paulus, Eds. (Springer International Publishing, Cham, 2017), pp. 41-65.
29. S. Reiter, D. Keefer, R. De Vivie-Riedle, in *Quantum Chemistry and Dynamics of Excited States*, L. González, R. Lindh, Eds. (Wiley, 2020), pp. 355-381.
30. D. J. Tannor, *Introduction to quantum mechanics: a time-dependent perspective*. (University Science Books, Sausalito, Calif, 2007), pp. 662.
31. J. S. Ajay, K. G. Komarova, S. Van Den Wildenberg, F. Remacle, R. D. Levine, in *Attosecond Molecular Dynamics*, M. J. J. Vrakking, F. Lepine, Eds. (The Royal Society of Chemistry, 2018), pp. 308-347.
32. C. Leforestier *et al.*, A comparison of different propagation schemes for the time dependent Schrödinger equation. *Journal of Computational Physics* **94**, 59-80 (1991).
33. J. Crank, P. Nicolson, A practical method for numerical evaluation of solutions of partial differential equations of the heat-conduction type. *Math. Proc. Camb. Phil. Soc.* **43**, 50-67 (1947).
34. H. Tal-Ezer, R. Kosloff, An accurate and efficient scheme for propagating the time dependent Schrödinger equation. *The Journal of Chemical Physics* **81**, 3967-3971 (1984).
35. M. D. Feit, J. A. Fleck, A. Steiger, Solution of the Schrödinger equation by a spectral method. *Journal of Computational Physics* **47**, 412-433 (1982).
36. C. Lanczos, An iteration method for the solution of the eigenvalue problem of linear differential and integral operators. *J. RES. NATL. BUR. STAN.* **45**, 255 (1950).
37. J. C. Tully, Molecular dynamics with electronic transitions. *The Journal of Chemical Physics* **93**, 1061-1071 (1990).
38. S. Mai, P. Marquetand, L. González, Nonadiabatic dynamics: The SHARC approach. *WIREs Comput Mol Sci* **8**, e1370 (2018).
39. M. Barbatti, Nonadiabatic dynamics with trajectory surface hopping method. *WIREs Comput Mol Sci* **1**, 620-633 (2011).
40. M. Barbatti *et al.*, Newton-X: a surface-hopping program for nonadiabatic molecular dynamics. *WIREs Comput Mol Sci* **4**, 26-33 (2014).

Chapter 3 Ab initio modeling of the molecular response to an external mechanical force

Table of Contents

Chapter 3	Ab initio modeling of the molecular response to an external mechanical force	78
3.1	<i>Theoretical methods to simulate the response to an external force</i>	78
3.1.1	Free energies and rate constants from ab initio computations	80
3.2	<i>Summary of key findings</i>	81
3.3	<i>Summary of contributions</i>	83
3.4	<i>References</i>	83
3.5	<i>Publication: “Bond breaking of furan–maleimide adducts via a diradical sequential mechanism under an external mechanical force”</i>	84

3.1 Theoretical methods to simulate the response to an external force

There are several ways to model the pulling of a mechanophore in the context of SMFS experiments. Isometric approaches indirectly measure the effect of the external force by a series of relaxed constrained geometry optimizations. The isometric approach CoGEF (Constrained Geometry optimization simulates the External Force) was proposed by Beyer (2000)(1, 2). It allows us to model how the potential energy changes as the molecular system is stretched by the pulling force of the cantilever or by the hydrodynamic drag in sonication experiments. For every step of the elongation, the end-to-end distance of the molecular system, defined by the attachment to the surface and the attachment to the tip of the cantilever, is constrained, see Figure 3.1. Then, the geometry of the molecule is relaxed from the deformed state to a state of equilibrium with the constraint, at which the energy is minimal. In practice, it is often the case that one cannot include the entire polymer chain in the quantum chemistry computation of the equilibrium geometry of the constrained geometry, and one defines ‘effective’ pulling atoms that substitute the long polymer chain. In our case, the PMA chains on each end of the mechanophore are replaced by methyl groups in the quantum mechanical calculations, and the constraints are defined between the two carbon atoms of the methyl groups.

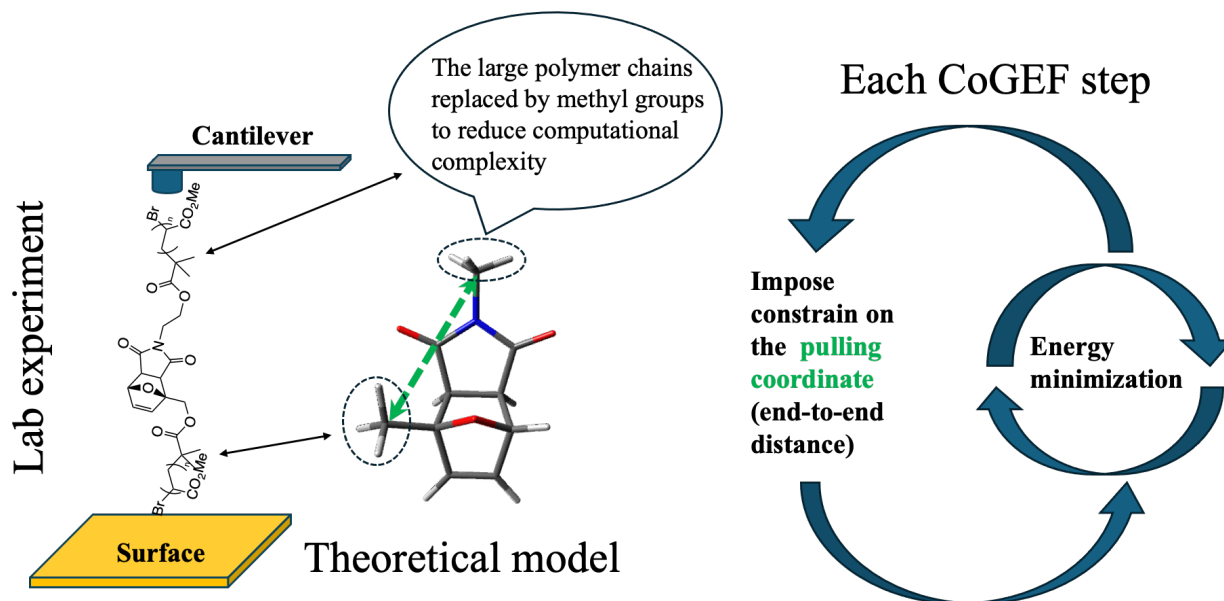


Figure 3.1: Illustration of the CoGEF approach followed to indirectly model the response of furan/maleimide adducts to an external force mimicked by a pulling distortion acting on the two ends of the molecule, which represents the attachments to the tip and the surface in an SMFS experiment.

Because we deal with constraints on geometrical coordinates associated with the pulling of the mechanophore rather than with a force itself, this approach can only assess the effect of the force in an indirect way. However, since the potential energy is a function of coordinates rather than forces, this method has proved helpful in studying chemical reactions and their pathways under force. Moreover, as shown by Ribas-Arino (2009) (3), at equilibrium, the potential energy obtained in the CoGEF approach is related to the potential energy from simulations with explicit external force via a Legendre transform, and the internal pulling coordinate and the force are conjugate variables. Isotensional approaches include an external force directly in the quantum chemistry calculations. The external force is added to the nuclear gradient, contributing an extra term to the SCF electronic energy. Three approaches have been implemented: the ab initio steered molecular dynamics (AISMD),(4) the external force is explicitly included (EFEI)(3), and the enforce geometry optimization (EGO)(5). AISMD pulls a set of "anchoring" atoms in the molecule towards fixed lab-frame "pulling" points. The resulting potential energy surface depends on the molecule's orientation because the pulling points do not rotate with the molecular frame. This approach is implemented in TeraChem (6) software and can be used to simulate the dynamics of a molecule under a constant external force. The EFEI and EGO methods apply a compressing, or elongating, constant external force to a pair of atoms along a line connecting their nuclei. Selecting this orientation prevents any effects associated with molecular translations and rotations of the center of mass induced by the external force (5). Note that this is also the case for the COGEF approach discussed above. EFEI and EGO methods work on the molecular frame representation of the molecule. They are well suited for static calculations with external forces like searching transition states, local minima geometry optimizations, and minimum energy paths. This thesis used the EFEI approach implemented in the software Q-Chem (7).

The differences between the EFEI and AISMD models that simulate the external force are schematized in Figure 3.2.



Figure 3.2: Key differences between EFEI and AISMD approaches. In EFEI, the external force is applied along the line that connects the terminal anchoring atoms (A_1 and A_2). In contrast, in AISMD, the force pulls each anchoring atom towards an associated pulling point (P_1 and P_2) in the lab frame.

In the AISMD approach, the external force modifies the electronic ab initio potential energy, as indicated by Equation 3.1.

$$V_{AISMD}(\mathbf{r}) = V_{ab\text{ initio}}(\mathbf{r}) + \sum_i^N F_0 (\|\mathbf{r}_i^{fix}(P_i) - \mathbf{r}_i(A_i)\| - \|\mathbf{r}_i^{fix}(P_i) - \mathbf{r}_i^0(A_i)\|) \quad (3.1)$$

In Equation 3.1 $V_{ab\text{-initio}}$ represents the electronic potential energy of the molecule computed with the electronic structure calculation of choice (DFT, CASSCF, etc.) to which the work done by the external force (second term) is added, resulting in a modified potential V_{FMPES} . F_0 is the magnitude of the steering force, $\mathbf{r}_i^{fix}(P_i)$ is the fixed position of each pulling point, while $\mathbf{r}_i(A_i)$ and $\mathbf{r}_i^0(A_i)$ represents the initial and current position of the anchoring points, respectively, during the dynamics.

3.1.1 Free energies and rate constants from ab initio computations

The thermochemistry analysis procedure available in most quantum chemistry packages is based on statistical mechanics. It allows us to estimate thermodynamic properties, such as entropy, enthalpy, and free energy, by evaluating the molecular partition function for an individual molecule at equilibrium, which is then used to construct the canonical partition function for the system in the context of the canonical ensemble (with fixed volume, temperature, and composition).

Using the thermochemistry analysis, we computed the activation free energy ($\Delta^\ddagger G^0$) for the furan/maleimide rDA reaction at room temperature and different force values within the EFEI approach. The activation free energy is the difference between the free energy of the transition state (TS) and the equilibrium geometries (Equation 3.2).

$$\Delta^\ddagger G^0 = G^0(TS) - G^0(Eq) \quad (3.2)$$

The rate constants at a given temperature ($k(T)$) are estimated using the Eyring transition state theory:

$$k(T) = \frac{k_B T}{h c^0} e^{-\frac{\Delta^\ddagger G^0}{RT}} \quad (3.3)$$

Where:

- $c^0 = 1$ is the standard concentration.
- $\Delta^\ddagger G^0$ is the free energy of activation, and T is temperature.
- $k_B, h, R,$ are Boltzmann, Planck, and ideal gas constants, respectively.

3.2 Summary of key findings

In the work published in ref. (8), we modeled the response of furan/maleimide Diels-Alder adducts, serving as mechanophores in SMFS experiments performed on PMA polymer chains. The weak dynamic character of the covalent bonds found in these Diels Alder adducts makes them easily breakable under external forces applied by the AFM cantilever and in sonication experiments. This justifies its application as mechanophore and the interest in using them in mechanochemistry to design self-healing materials and logic devices driven by external forces. We applied both CoGEF and EFEI methodologies to model the response of the furan/maleimide mechanophore to the external mechanical force, mimicking the situation observed in SMFS experiments. In those experiments, the AFM cantilever grabs a single-PMA polymer, with the furan/maleimide mechanophore in the center, from a bulk sample and stretches it until the weakest bonds break. Two stereoisomers, proximal endo (Pendo) and proximal exo (Pexo) were studied, motivated by the findings of Wang *et al.*(9), who show that the endo stereoisomer is more labile than the exo counterpart, meaning it breaks at lower forces. We corroborate this fact with our theoretical computations and provide insights explaining the observed trend.

The CoGEF and EFEI geometry optimizations and single-point characterizations were carried out at both unrestricted DFT and multireference CASSCF with the basis set 6-31G(d,p)(10-12). After benchmarking several DFT functionals, we chose the long-range dispersion corrected functional wB97X-D(13), implemented in Q-Chem. (7)The multireference calculations are singlet and triplet state-specific CASSCF, where the selected active space comprises 4 electrons in 4 orbitals (CAS(4,4)). All the calculations are done on the ground state of the molecule as both the CoGEF and EFEI approaches assume that the force acts adiabatically on the system; that is to say, at every value of the force or constraint, the electrons are in a state of equilibrium with the nuclei. The choice of unrestricted and multireference methodologies is compulsory as the diradical singlet intermediate, present in the sequential pathway of the furan-maleimide retro-DA reaction, has an open-shell electronic structure. So, strong correlation effects affect the electronic structure of the diradical species at equilibrium geometry at zero force and under force, and a single-reference unrestricted formalism or a multireference computational method must be used.

CoGEF was used to determine the reaction path under force along a coordinate corresponding to the pulling of the polymer, which, in our case, we mimicked by the distance between two methyl groups on the edges of the mechanophore. Due to the importance of defining the pulling coordinate in CoGEF, we show in Figure 3.3 a scheme highlighting it and the scissile bonds of the adduct SB₁ and SB₂.

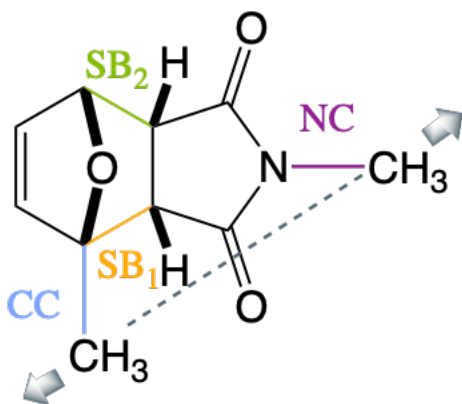


Figure 3.3: Drawing of the endo furan/maleimide mechanophore, showing the bonds that break during the retro-Diels-Alder reaction, called scissile bonds SB1 and SB2, and the direction of the external force, indicated by the arrows, modeled as a geometric constrain imposed in the pulling coordinate at every step of CoGEF.

The EFEI method was used to determine the transition states and minima under force, from which we could also obtain the profile of free energies of activation for the retro-DA reaction. From the analysis of the free energies, we conclude that the reaction is inhibited at lower values of the external force. In contrast, the reaction is enhanced at forces larger than 3 nN, and already at ~ 4 nN, the activation energy is lower than at zero force. Importantly, we report a switch from the concerted to the sequential mechanism at external forces of approximately 1 nN. This contrasts with the thermally activated [4 + 2] retro-Diels–Alder reaction, which predominantly proceeds via a concerted mechanism in the ground electronic state. The shift in mechanism is produced due to the asymmetry in the direction of the external force, which, upon stretching, initially has a larger projection in one of the scissile bonds (SB₁) than on the other (SB₂). Thus, the external force destabilizes the concerted mechanism, favoring the sequential pathway.

We studied in detail the sequential mechanism proposed in this work and characterized the intermediate structures, which have diradical character. We proved the diradical open-shell electronic structure of the intermediate by analyzing the CASSCF configurations and the natural orbitals. We show that after the first bond rupture, the intermediate species have degenerate HOMO and LUMO natural orbitals; that is, both of them are occupied by one electron. In addition, we observed that the HOMO orbital is localized in the maleimide part. In contrast, the LUMO localizes in the furan part of the adduct, indicating an open-shell structure. However, since this could correspond to either a diradical or a zwitterion, we computed the dipole moment along the CoGEF pathway. We also analyzed the separation of charges between the furan and maleimide parts of the adduct. Both charges and dipole moment remain small throughout the reaction pathway, which excludes the possibility that the intermediate would be a zwitterion. This confirmed the presence of diradicals in the intermediate stage of the sequential furan/maleimide [4 + 2] retro-Diels–Alder.

We also reported that the lowest triplet state becomes nearly degenerate with the singlet ground state where the reaction under force occurs. This is a consequence of the diradical electronic structure, whose open-shell structure can lead to either a singlet superposition of spin-up and spin-down functions of the electrons occupying the HOMO and the LUMO orbitals or to a triplet

configuration where both electrons have spin-up or down. See Figure 2.3 in Chapter 2, which illustrates all the possible diradical configurations.

Our work not only contributed to advancing the understanding of the furan/maleimide reaction under force, showing that the sequential pathway can be favored when asymmetric forces come into play but also provided insights on how to model the molecular response to the external force whose applicability goes beyond the molecules we studied and can be extended to other systems. This work also contributed greatly to understanding the challenges that our experimental partners can face while performing the SMFS experiments since they do not have a fine control of the behavior of the polymers when interacting with the AFM cantilever or beyond that. Many phenomena are very difficult or impossible to resolve at the current level of the experiments. That is why our theoretical insights help them better plan the experiments and can guide their decision-making. Certainly, our findings pave the way for the rational design of DA mechanophores for polymer science and photochemistry.

3.3 Summary of contributions

All authors contributed to the organization of the manuscript, the analysis of the results, and the development and refinement of ideas, providing valuable advice and feedback on both the text and figures. Manuel Cardosa Gutierrez performed all computational work, including CoGEF, EFEI, and electronic structure calculations (DFT and CASSCF). He was responsible for writing inputs for the software, monitoring the calculations, analyzing the results, and reporting the findings. He benchmarked DFT functionals and CASSCF active spaces to select the most appropriate computational methods, balancing accuracy with efficiency. He modeled all species considered in the study, including equilibrium geometries of the furan/maleimide system (with and without force), transition states, and intermediate species.

Manuel Cardosa conducted an in-depth review of the literature on state-of-the-art methods for modeling the force response in molecules. He determined the reaction pathways under force for the two stereoisomers analyzed, exo and endo furan/maleimide, and provided the necessary evidence supporting the transition to a sequential mechanism under force—an observation reported for the first time. Additionally, he analyzed the CASSCF wavefunctions and molecular orbitals, demonstrating that the intermediate species exhibit diradical character, with nearly degenerate singlet and triplet states. He applied Eyring theory to determine the activation energies and reaction rates under force, based on the free energies of both reactants and transition states.


Françoise Remacle provided guidance and supervision throughout the study, contributing her expertise in quantum chemistry and dynamical modeling, in the use of adequate software, and in the analysis and interpretation of results.

3.4 References

1. M. K. Beyer, The mechanical strength of a covalent bond calculated by density functional theory. *The Journal of Chemical Physics* **112**, 7307-7312 (2000).
2. M. K. Beyer, H. Clausen-Schaumann, Mechanochemistry: The Mechanical Activation of Covalent Bonds. *Chem. Rev.* **105**, 2921-2948 (2005).

3. J. Ribas-Arino, M. Shiga, D. Marx, Understanding Covalent Mechanochemistry. *Angew Chem Int Ed* **48**, 4190-4193 (2009).
4. M. T. Ong, J. Leiding, H. Tao, A. M. Virshup, T. J. Martínez, First Principles Dynamics and Minimum Energy Pathways for Mechanochemical Ring Opening of Cyclobutene. *J. Am. Chem. Soc.* **131**, 6377-6379 (2009).
5. K. Wolinski, J. Baker, Geometry optimization in the presence of external forces: a theoretical model for enforced structural changes in molecules. *Molecular Physics* **108**, 1845-1856 (2010).
6. I. S. Ufimtsev, T. J. Martinez, Quantum Chemistry on Graphical Processing Units. 3. Analytical Energy Gradients, Geometry Optimization, and First Principles Molecular Dynamics. *J. Chem. Theory Comput.* **5**, 2619-2628 (2009).
7. Y. Shao *et al.*, Advances in molecular quantum chemistry contained in the Q-Chem 4 program package. *Molecular Physics* **113**, 184-215 (2015).
8. M. Cardoso-Gutierrez, G. De Bo, A.-S. Duwez, F. Remacle, Bond breaking of furan–maleimide adducts *via* a diradical sequential mechanism under an external mechanical force. *Chemical Science* **14**, 1263-1271 (2023).
9. Z. Wang, S. L. Craig, Stereochemical effects on the mechanochemical scission of furan–maleimide Diels–Alder adducts. *Chemical Communications* **55**, 12263-12266 (2019).
10. W. J. Hehre, R. Ditchfield, J. A. Pople, Self–Consistent Molecular Orbital Methods. XII. Further Extensions of Gaussian–Type Basis Sets for Use in Molecular Orbital Studies of Organic Molecules. *The Journal of Chemical Physics* **56**, 2257-2261 (1972).
11. P. C. Hariharan, J. A. Pople, The influence of polarization functions on molecular orbital hydrogenation energies. *Theoret. Chim. Acta* **28**, 213-222 (1973).
12. M. M. Francl *et al.*, Self-consistent molecular orbital methods. XXIII. A polarization-type basis set for second-row elements. *The Journal of Chemical Physics* **77**, 3654-3665 (1982).
13. J.-D. Chai, M. Head-Gordon, Long-range corrected hybrid density functionals with damped atom–atom dispersion corrections. *Phys. Chem. Chem. Phys.* **10**, 6615 (2008).

3.5 Publication: “Bond breaking of furan–maleimide adducts via a diradical sequential mechanism under an external mechanical force”

Cite this: *Chem. Sci.*, 2023, 14, 1263 All publication charges for this article have been paid for by the Royal Society of Chemistry

Bond breaking of furan–maleimide adducts *via* a diradical sequential mechanism under an external mechanical force†

Manuel Cardosa-Gutierrez,^a Guillaume De Bo,^b Anne-Sophie Duwez^b and Francoise Remacle^b

Substituted furan–maleimide Diels–Alder adducts are bound by dynamic covalent bonds that make them particularly attractive mechanophores. Thermally activated [4 + 2] retro-Diels–Alder (DA) reactions predominantly proceed *via* a concerted mechanism in the ground electronic state. We show that an asymmetric mechanical force along the anchoring bonds in both the *endo* and *exo* isomers of proximal dimethyl furan–maleimide adducts favors a sequential pathway. The switching from a concerted to a sequential mechanism occurs at external forces of ≈ 1 nN. The first bond rupture occurs for a projection of the pulling force on the scissile bond at ≈ 4.3 nN for the *exo* adduct and ≈ 3.8 nN for the *endo* one. The reaction is inhibited for external forces up to ≈ 3.4 nN for the *endo* adduct and 3.6 nN for the *exo* one after which it is activated. In the activated region, at 4 nN, the rupture rate of the first bond for the *endo* adduct is computed to be ≈ 3 orders of magnitude larger than for the *exo* one in qualitative agreement with recent sonication experiments [Z. Wang and S. L. Craig, *Chem. Commun.*, 2019, 55, 12263–12266]. In the intermediate region of the path between the rupture of the first and the second bond, the lowest singlet state exhibits a diradical character for both adducts and is close in energy to a diradical triplet state. The computed values of spin–orbit coupling along the path are too small for inducing intersystem crossings. These findings open the way for the rational design of DA mechanophores for polymer science and photochemistry.

Received 9th September 2022
Accepted 27th December 2022

DOI: 10.1039/d2sc05051j

rsc.li/chemical-science

Introduction

Dynamic covalent bonds, like the archetypal furan–maleimide Diels–Alder (DA) adduct, are vastly used in synthetic chemistry and polymer science, and are now expanding into biology.^{1–3} Furan–maleimide adducts are characterized by dynamic covalent bonds that are more labile and slightly longer than typical carbon–carbon covalent ones. The dynamic covalent bonds of Diels–Alder (DA) adducts make them attractive mechanophores when embedded in polymers and networks.^{4–11} DA reactions on these adducts proceed *via* a low reaction barrier that leads to reversible reactions. In solution, the adducts need to be heated at high temperatures to break open.^{1,12} The retro-DA reaction can also take place at room temperature when the adduct is

sonicated, thus subjected to mechanical forces.^{5,10,11} There is however not yet a detailed understanding on the rupture mechanism of these adducts under tension, in particular on the concerted or sequential nature of the reaction path.¹³

Beyond stabilizing intermediates and shifting chemical equilibria, due to the vector character of the force, mechanochemical reactions can follow specific pathways yielding products that may differ from those of non-directional thermal activation in solution.^{4,13–19} It was shown that the *cis* or *trans* anchoring of benzocyclobutene to a polymer chain controls the stereochemistry of the ring opening.^{20,21} Under tension, the *cis* attachment leads to a disrotatory ring opening in violation of the Woodward–Hoffmann rules²² and yields the same product as the *trans* attachment. *Ab initio* steered molecular dynamics simulations on cyclobutene and the determination of the minimum energy pathway provided a mechanistic interpretation on the force modified potential energy surface.¹⁴ In *cis* and *trans gem*-difluoro-cyclopropane (gDFC), it was shown that under tension, the *trans* gDFC undergoes a Woodward–Hoffmann thermally forbidden conrotatory ring opening, and that both *cis* and *trans* gDFC open *via* a diradical intermediate that is stabilized under tension.²³ Upon releasing the tension, the diradical returns to the *cis* gDFC for which the barrier is smaller on the field free potential. The diradical character of the

^aUR Molecular Systems, Department of Chemistry, University of Liège, 4000 Liège, Belgium. E-mail: fremacle@uliege.be

^bDepartment of Chemistry, University of Manchester, Manchester, M13 9PL, UK

† Electronic supplementary information (ESI) available: A detailed description of computational methods and results of the thermodynamics and kinetics analysis and of the electronic structure methodology. Zip files provide the geometries of both adducts along the CoGEF path computed at the DFT and CAS(4,4) levels, the geometries of the reactant and transition states computed at the DFT level and the geometries at minimum energy intersystem crossing computed at the CAS(4,4) level. See DOI: <https://doi.org/10.1039/d2sc05051j>



intermediate under tension was demonstrated by trapping it with a radical chromophore. Cyclobutane cores embedded in mechanophores were reported to open sequentially^{24–27} and shown to proceed *via* a diradical intermediate, the product stereochemistry being determined by whether or not the intermediate undergoes isomerization after the first bond rupture.^{28,29} Diradical intermediates were also recently reported to play a role in the mechanochemical reactivity of vinyl-addition polynorbornene that contains norbornane units³⁰ and in the release of CO by sonication activation of the norborn-2-en-7-one scaffold.³¹

Various [4 + 2] mechanophores have been investigated,¹⁹ and among them furan–maleimide is a popular structural motif.^{5,6,9–11,32–38} Furan–maleimide adducts embedded in a polymethyl acrylate (PMA) polymer were shown to selectively break under sonication.⁵ Stevenson and De Bo¹⁰ pointed to the regioselectivity of the rupture of a furan–maleimide mechanophore embedded in PMA activated by sonication; the two proximal stereoisomers, where the anchoring of the polymer chain on the furan is on a carbon atom near neighbor to the furan/maleimide junction, being more labile than the distal ones where the anchoring is on the next near neighbor atom on the furan moiety. Wang *et al.*¹¹ benchmarked the mechanical resistance to activation by sonication of two proximal stereoisomers with respect to the ring opening of *gem*-dichlorocyclopropane. They concluded that the proximal-*exo* adduct is mechanically less labile than the proximal-*endo* one. This stereoselectivity in the rupture under force follows the trend of thermal activation. It is corroborated by the differences in the computed force-free activation barriers and in the efficiency of the mechanochemical coupling to the polymer chain.

Motivated by these results,^{10,11} we theoretically investigated the mechanism of the [4 + 2] retro-Diels–Alder (rDA) ring opening of proximal-*endo*, P_{endo} , and proximal-*exo*, P_{exo} , dimethyl furan–maleimide adducts under tension. We report on a shift from a concerted mechanism at zero force to

a sequential one at external pulling forces on the weakest scissile bond smaller than 1 nN due to the directionality of the force applied to the methyl groups used to model the tethering of the adduct into a polymer. We further show that the tension inhibits the bond rupture up to pulling forces of ≈ 3 nN before inducing a preferential activation of the P_{endo} stereoisomer in qualitative agreement with the experimental results of Wang *et al.*¹¹

In the ground electronic state at room temperature, thermally activated [4 + 2] retro-Diels–Alder (rDA) reactions proceed most of the time *via* a concerted and stereospecific pathway involving a single concerted transition state at room temperature.^{39,40} Activation energies of 25–30 kcal mol^{−1} for the concerted rupture of the two scissile bonds at room temperature endow them with a dynamic character. *Endo* adducts are more reactive than *exo* ones because of their lower activation barriers.^{41–43} A sequential mechanism involving diradicals or zwitterion species is also thermally possible, depending on the substitution of DA adducts.⁴⁴ Studies involving molecular dynamics showed that for some adducts at high temperature (>1000 K) and for substituted ones a small fraction of the trajectories involves two transition states (TSS) and diradical open shell singlet intermediates along the reaction path.⁴⁰ The photoactivation of DA adducts with a UV pulse was shown to proceed *via* non-concerted pathways through successive bond cleavages, depending on the nature of the conical intersections (CoIn) leading back to the ground electronic state.^{45–48} Studies investigating activation by using an external static electric field also reported going through a sequential pathway involving zwitterionic intermediates.^{41,49}

We show here that diradical intermediates can be stabilized under tension in the rDA of the substituted P_{endo} and P_{exo} furan–maleimide adducts, where the methyl groups model the anchoring on the polymer chain and control the directionality of the external force. The two adducts and the four bonds of interest, the two scissile bonds, SB1 and SB2, and the CN and

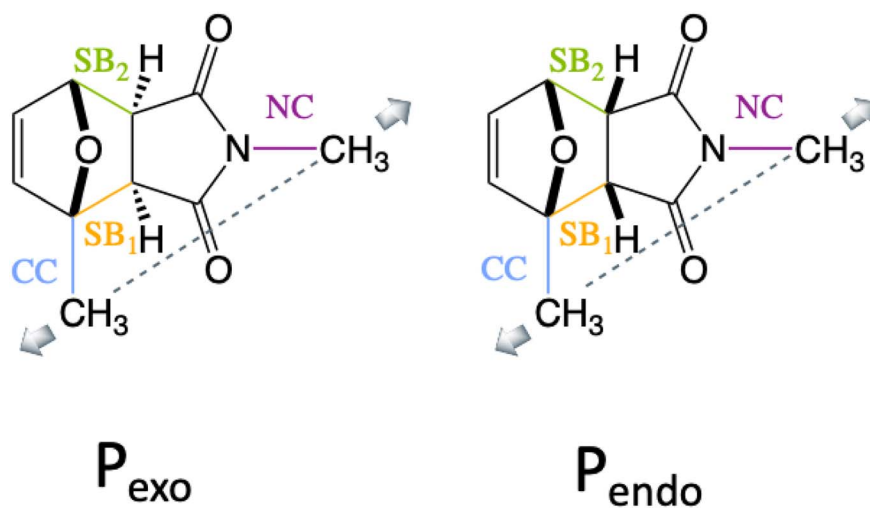


Fig. 1 Stereochemistry of the P_{endo} and P_{exo} adducts, the labeling of the two scissile bonds, SB1 (orange) and SB2 (green) and of the two anchoring bonds, CC (blue) and NC (violet) and the direction of the stretching coordinate in dashes. The pulling coordinate has a larger projection on SB1 than on SB2.



the CC anchoring bonds of the methyl groups are drawn in Fig. 1. Because of the difference in the stereo-character of P_{endo} and P_{exo} , in the force free equilibrium geometry, SB1 and SB2 are essentially of equal length in P_{endo} (1.57 Å), while in P_{exo} , SB1 is longer (1.58 Å) than SB2 (1.56 Å).

Computational methods

The effect of the external force on the potential energy surface (PES) can be computed by an isometric or an isotensional approach.⁵⁰ The isometric method CoGEF (constrained geometries simulate external force)⁵¹ consists in constrained geometry optimization where typically the constraint is the distance between the two atoms to which the pulling force is applied. This approach yields the most stable geometry of the system that satisfies a given value of the constraint and provides the energy and other molecular properties through electronic structure computations. In the isotensional method, the external force is explicitly added as a term in the expression of the nuclear gradient of the energy during the geometry optimization. Three approaches have been implemented, the force-modified-potential-energy surface (FMPEs),¹⁴ the external force is explicit included (EFEI)¹⁵ and the enforce geometry optimization (EGO).⁵² The isotensional approaches can be used to determine the reactant, transition state and activation energies on the FMPEs and to carry out *ab initio* molecular dynamics under force.¹⁴ It was shown in ref. 53 that at stationarity, the EFEI potential, $V_{EFEI}(F_0)$, is the Legendre transform of the CoGEF potential $V_{CoGEF}(q_0)$, so that the external force and the geometrical constraint can be considered conjugate variables: $V_{EFEI}(F_0) \equiv V_{CoGEF}(q_0) - F_0 q_0$.

The reaction mechanism was studied by using the CoGEF isometric protocol, for the two adducts at the UDFT level with the

wB97XD⁵⁴ functional and at the CAS-SCF(4,4) level with the 6-31G(d,p) basis set for the lowest singlet, S_0 , and triplet, T_0 , states. The mechanical coordinate is taken to be the distance between the two C atoms of the methyl anchoring groups (dashed line in Fig. 1). For each relaxed geometry under force, the spin-orbit coupling between S_0 and T_0 was computed along the CoGEF path as well as the 4 lowest singlet and three lowest triplet states at the state average (SA) complete active space⁵⁵ CAS-SCF level. The CoGEF path computed at the CAS(4,4) level/6-31G(d,p) is consistent with that obtained at the UDFT level, see the ESI† for more details. The UDFT computations were carried out with the quantum chemistry software QChem⁵⁶ and the CAS-SCF computation with the MOLPRO quantum chemistry package.^{57,58}

The TSs were determined at the UDFT/wB97XD level scanning external pulling force values corresponding to the stretching coordinate.⁵⁹ Consistent force modified CoGEF paths and activation barriers were obtained with the PBE0DH⁶⁰ and the BH&HLYP⁶¹ functionals, Fig. S2.† These three functionals describe correctly the diradical species that appear when the pulling force induces a switch from a concerted to a sequential rupture mechanism and give results consistent with the CAS-SCF level.

The computed values of the barrier for the rupture of the weakest bond SB1 using UDFT/wB97XD/6-31G(d,p) in the gas phase at zero force are in good agreement with previously reported values in the gas phase^{41,42} or the M06-2X⁴⁹ functional in DMSO for unsubstituted adducts. They are systematically higher by ≈ 5 –6 kcal mol⁻¹ than those reported values for similar furan–maleimide adducts using the B3LYP¹¹ functional in THF. A detailed comparison with previous results at zero force and the computed values of the barriers using different functionals is provided in the ESI.†

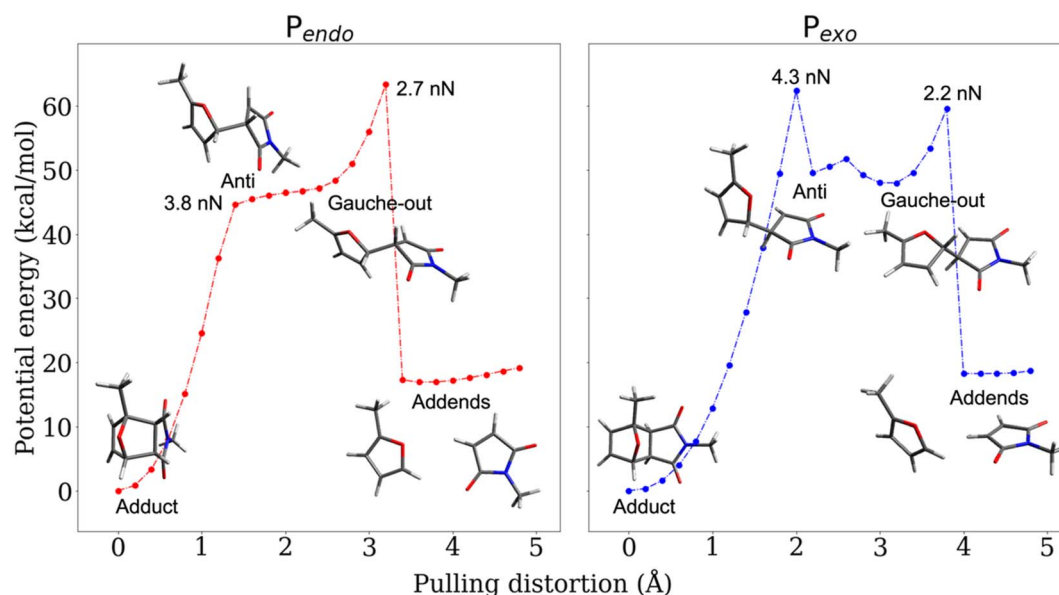


Fig. 2 CoGEF UDFT wB97XD potential energy profiles for the P_{endo} (a) and P_{exo} (b) adducts as a function of the pulling distortion ($R_{pulling} - R_{pulling-0}$) as well as relaxed geometries under force for maxima and minima. The CoGEF path computed at the CAS(4,4) level is given in Fig. S1† and the one computed with the PBE0DH and BH&HLYP functionals in Fig. S2.† The relaxed geometries along the CoGEF paths computed at the DFT wB97XD and CAS(4,4) levels are given in the ESI.†



Since the value of the stretching coordinate at equilibrium at zero force, $R_{\text{pulling-0}}$, is different in the two stereoisomers, we report below the variation of the structural and energetic observables as a function of the pulling distortion, defined as $(R_{\text{pulling}} - R_{\text{pulling-0}})$, where R_{pulling} is the stretching distortion imposed in the CoGEF protocol.

Results and discussion

Switching from a concerted to a sequential mechanism under tension

The CoGEF UDFT/wB97XD potential energy profiles are reported as a function of the pulling distortion, $(R_{\text{pulling}} - R_{\text{pulling-0}})$, in Fig. 2a and b for P_{endo} and P_{exo} respectively. Similar profiles are obtained at the CAS(4,4) level, see Fig. S1.† Both adducts undergo a sequential bond rupture. The energy curves exhibit two sharp rises separated by an intermediate region. The breaking of SB1 occurs at the end of the first sharp energy rise, while that of SB2 occurs at the end of the second one. This can be seen from the relaxed geometries under force reported as insets in Fig. 2a and b, and from the elongation of the bond lengths as a function of the pulling distortion plotted in Fig. 3a. During the first energy rise, SB1 is elongated while SB2 remains essentially at its equilibrium value (Fig. 3a). In this range, the projection of the pulling force on SB2 (Fig. 3b) is smaller than on SB1 and not large enough for inducing bond breaking. The SB1 bond of P_{endo} ruptures for a projection of the pulling force of 3.8 nN, that is slightly smaller than the breaking projection of pulling force for P_{exo} (4.3 nN). These values are in good agreement with those reported in ref. 10. After the SB1 breaking, the projection of the pulling force (Fig. 3b) on the two scissile bonds drops sharply to values close to zero. In the intermediate region between the two bond breakings, the energy profile of P_{endo} (Fig. 2a) continues to rise with a much smaller slope, starting from an anti-like unstable *endo* rotamer that evolves to an unstable *endo* gauche out one just before the breaking of SB2. On the other hand, in P_{exo} the anti- and gauche out rotamers correspond to minima (see Fig. 2b), separated by a small rotation barrier of 3 kcal mol⁻¹, which is overcome by a small value of the force of 0.2 nN as can be seen from Fig. 3b. These intermediates have been reported previously for similar DA adducts for zero force reaction paths.^{40,44,48} Such a rotation around the unbroken bond has also been reported for the sequential ring opening of cyclobutane cores under tension.^{24–27,29} The breaking of SB2 occurs after a second sharp rise in the projection of the pulling force for a smaller value for P_{exo} (2.2 nN) than for P_{endo} (2.7 nN), Fig. 3b. Then the potential energy drops sharply to the dissociation asymptote.

The results discussed above imply that there is a switching of the rupture mechanism from a concerted one to a sequential one at low values of the pulling force, before the rupture of the first scissile bond. In order to get further insights, we computed the transition state (TS) and the free energy of the activation barrier, $\Delta G_{\text{F}}^{\ddagger}$, at 298 K, using the EFEI¹⁵ isotensional protocol at the same UDFT level from zero force up to values of the pulling force on SB1 approaching that of the rupture in the UDFT CoGEF path shown in Fig. 3b. It is plotted in Fig. 4.

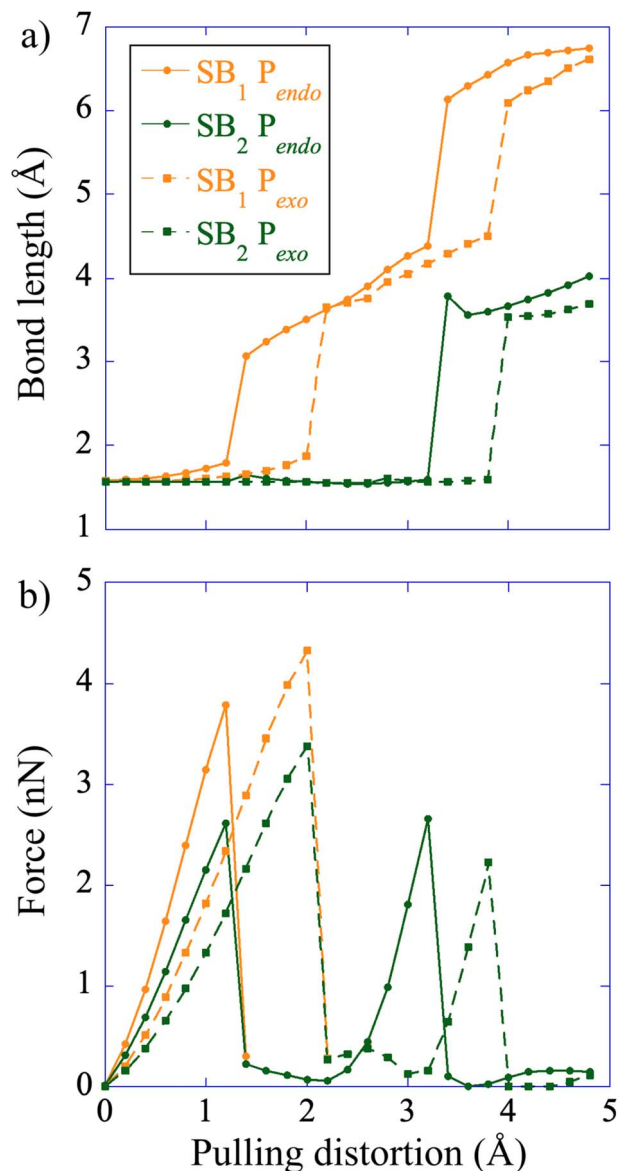


Fig. 3 (a) SB1 (orange) and SB2 (green) elongation plotted as a function of the pulling distortion for P_{endo} (full lines) and P_{exo} (dashes). (b) Projection of the pulling force on SB1 and SB2 for the two adducts. The bond rupture and the maximum in the projection of the pulling force on the scissile bonds do not occur at the same value for P_{endo} and P_{exo} because of the difference in the geometries of the two stereoisomers.

At zero force, at 298 K, the free energy barrier is smaller for the P_{endo} adduct (28.2 kcal mol⁻¹) than for the P_{exo} adduct (30.8 kcal mol⁻¹), which leads to a computed $\Delta(\Delta G^{\ddagger})$ between P_{exo} and P_{endo} of 2.6 kcal mol⁻¹. For both adducts, as the pulling force increases, the activation barrier first increases, which means that rupture is inhibited, and then goes through a plateau, before sharply decreasing up to the rupture of the SB1 bond, see Fig. 4. The maximum of the activation barrier occurs for both P_{endo} and P_{exo} at 1.8 nN. The barrier is higher for P_{exo} (44.5 kcal mol⁻¹) than for P_{endo} (35.4 kcal mol⁻¹). At pulling forces larger than 3.4 nN, the rupture of SB1 is activated in P_{endo} compared to the zero-force barrier. For P_{exo} , activation occurs



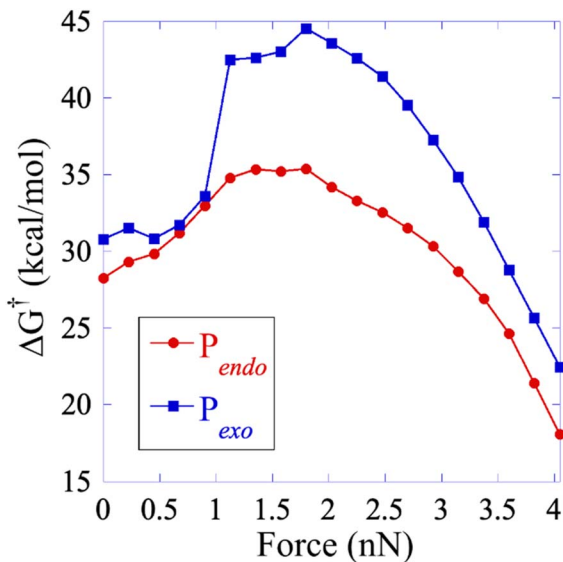


Fig. 4 Free energy activation barrier computed using the EFEI protocol for values of the pulling force up to the rupture of the SB1 bond. P_{endo} is plotted in red with full circles and P_{exo} in blue with diamonds. The geometries of the reactant and the transition states are given in the ESI†

for a pulling force larger than 3.8 nN (Fig. 4). Above 3.5 nN, the computed $\Delta(\Delta G^\ddagger)$ decays sharply, but remains higher for P_{exo} , which makes the P_{endo} adduct more labile, in agreement with the experimental results of Wang *et al.*¹¹ At 4 nN, just before the rupture of SB1, the computed barrier is 18 kcal mol⁻¹ for P_{endo} (rate constant of 0.36 s⁻¹ (lifetime of 2.8 s)), while it is 22.5 kcal mol⁻¹ (rate constant of 2.1×10^{-4} s⁻¹ (lifetime of 77 min)) for P_{exo} , see Fig. S3 and the ESI† for more details. The crossover from a concerted mechanism to a sequential one occurs before the first bond rupture at pulling forces ≈ 1 nN (1.1 nN for P_{exo} and 0.9 nN for P_{endo}). It coincides with the inflexion point of the pulling force on SB1. Above 1 nN, the sequential mechanism is favored over the concerted one and it dominates for forces above 3 nN.

Diradical species in the sequential mechanism

The electronic structure of S_0 is very similar for both adducts along the CAS(4,4) CoGEF path. The main configurations correspond to a diradical open shell singlet in the intermediate region between the two bond ruptures, see the ESI for details and Fig. S4† that shows the coefficients of the S_0 state in the electronic configurations as a function of the pulling distortion.

At zero force, the value of the permanent dipole moment of P_{endo} is very small (0.5 D). It increases to 2.5 D in the intermediate region, after the first bond rupture, because the pulling distortion increases the extension of the P_{endo} adduct and makes it comparable to that of P_{exo} , Fig. 5. The geometry of P_{exo} is more extended at zero force because of its stereo-character and the dipole moment is larger, 3 D, than that of the P_{endo} adduct. It slightly decreases in the intermediate region to 2 D. The partial positive and negative charges on the two addends are small at zero force (furan (donor), +0.1 |e| and maleimide

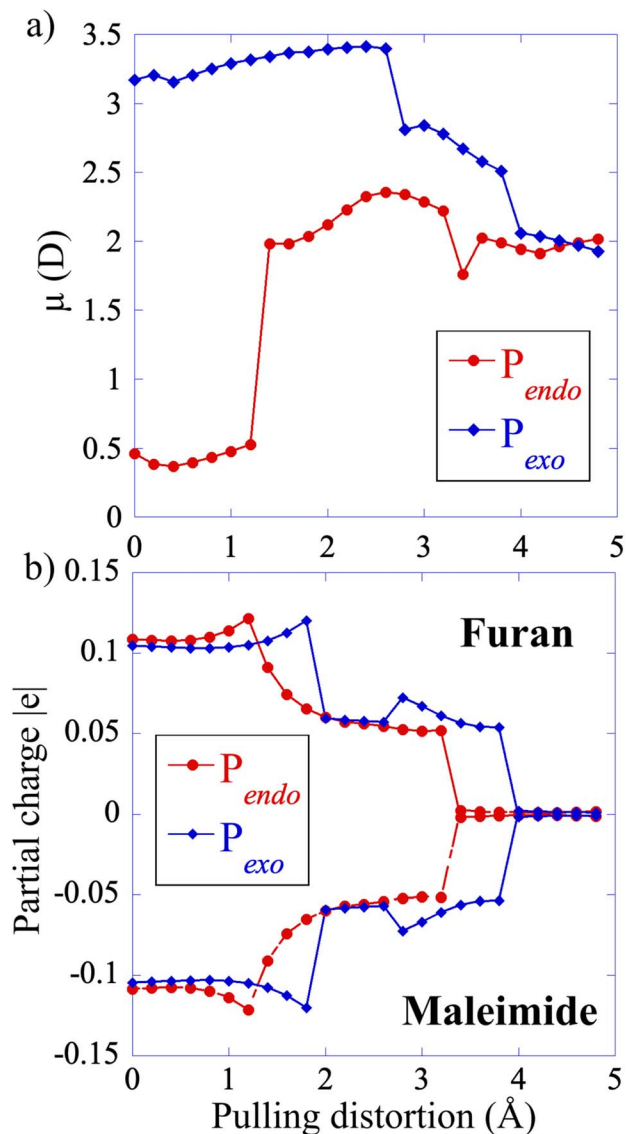


Fig. 5 (a) Permanent dipole of the two adducts along the CAS(4,4) CoGEF path for P_{endo} (red-filled circles) and P_{exo} (blue-diamonds). (b) Computed partial charge on the furan and maleimide addends along the CAS CoGEF path.

(acceptor), -0.1 |e|) and decrease in the intermediate region along the CoGEF path confirming the diradical character of S_0 in the intermediate region.

For both adducts, the lowest triplet state, T_0 , becomes close in energy to S_0 in the intermediate region with energy differences of the order of 0.05 eV (Fig. 6). The weight of the $|2a_0\rangle$ configuration in the intermediate region is 93% (Fig. S6†). In the case of P_{endo} , the triplet state energy becomes lower than that of S_0 at the beginning of the intermediate region, for distortion in the range of 1.8 to 2.4 Å (see Fig. S7† for a plot of the S_0/T_0 energy difference). The spin-orbit coupling remains extremely small, of the order of 10^{-5} eV for both adducts throughout the intermediate region (see Table S1†), which makes intersystem crossing unlikely along the minimum energy path under force. However, the S_0/T_0 minimum energy



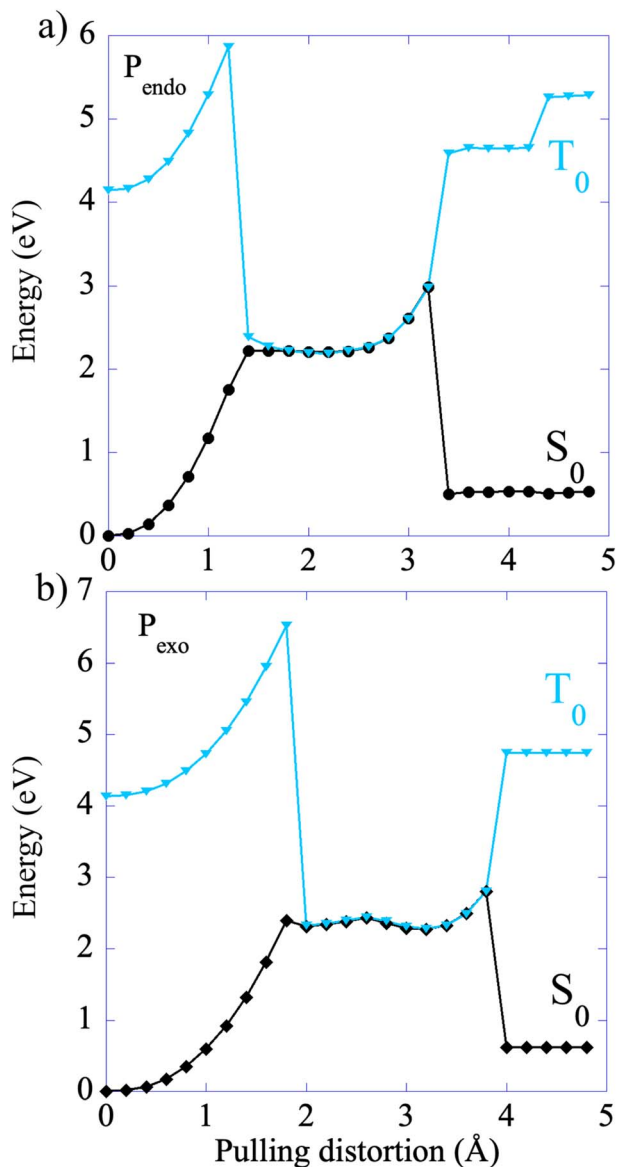


Fig. 6 Energy profiles of the singlet S_0 and the lowest triplet T_0 along the CAS(4,4)-CoGEF path. The energy of the T_0 state is computed in the relaxed geometry of S_0 . The values of the spin-orbit coupling are reported in Table S1 of the ESI.† The S_0/T_0 energy differences are plotted in Fig. S6† and the minimum energy intersystem crossing (MEIC) geometries in Fig. S7.† Files of geometries of the S_0 state along the CoGEF path as well as at the MEIC are given in the ESI.†

crossing occurs in the vicinity of second bond rupture for both adducts, see Fig. S8.† Therefore, one could observe spin-orbit transitions using steered molecular dynamics,^{14,29} which will be the subject of future work. The first excited singlet state S_1 which has also a diradical character in the intermediate region, is much higher in energy along the minimum path, with a S_0/S_1 energy difference larger than 3 eV.

Conclusions

Our computations uncover a rich and complex electronic and structural reorganization of the P_{endo} and P_{exo} adducts along the

stretching mechanical path. The directionality of the force as dictated by the carbon atoms of the two methyl substituents that model the anchoring into the polymer leads to an uneven activation of the two scissile bonds. This in turn induces a switch from a concerted mechanism at zero pulling force to a sequential one for force larger than 1 nN along the minimum energy path. As the external force increases, the reaction is first inhibited and then activated. Pulling forces on the most activated scissile bond larger than 3.4 nN (P_{endo}) and 3.6 nN (P_{exo}) lead to a faster rupture rate constant than at zero force. The values of the pulling force leading to the switch of the mechanism and to bond rupture for the reactant state of P_{endo} and P_{exo} are very close. However, the response P_{endo} occurs systematically at slightly lower forces than those computed for P_{exo} . The free energy activation barrier of P_{endo} for the first bond breaking is systematically lower by 7 to 3 kcal mol⁻¹ as the external force increases, which explains the more labile character of P_{endo} under tension observed experimentally.¹¹

In the intermediate region between the two sequential bond ruptures, the singlet ground state has a diradical character and adopts an extended geometry for both adducts. In this region, the triplet state becomes very close in energy to S_0 but the spin-orbit coupling remains too small to induce an intersystem transition along the minimum energy path. However, the minimum energy crossing between T_0 and S_0 occurs in the vicinity of the second bond rupture along the P_{exo} adduct minimum energy path.

Diradical intermediates resulting from an activation by an external mechanical force have been identified experimentally in the case of ring opening of cyclopropanes²³ and in the sequential opening of [2 + 2] cyclobutane mechanophores.^{24,25,29,62-64} Our results suggest that diradical intermediates are also formed in the mechanically activated sequential cycloreversion of [4 + 2] furan-maleimide DA adducts due to the directionality of the pulling force. The effect of the mechanical force is to modify the level structure of the various singlet and triplet states in the intermediate region, inducing several conical intersections within the singlet and triplet manifolds, as well as intersystem singlet-triplet crossings for geometries close to those of the minimum energy path. In particular, the mechanical force stabilizes the diradical intermediates in the lowest singlet and triplet states and does not induce the formation of a zwitterion, as has been reported in the case of an activation by a static electric field^{41,49} or for substituted addends,⁴⁴ which leads to a larger charge separation. After the first bond rupture, in the case of the P_{exo} adduct, small forces of less than 1 nN along the minimum path induce an isomerization of the diradical intermediate from an anti- to a gauche out stereoisomer, which are separated by a small rotational barrier of 3 kcal mol⁻¹. Such internal rotations have been reported for DA adducts undergoing a sequential cycloreversion at zero force,^{40,44,48} and also the opening of cyclobutane under mechanical force was observed.^{24,25,29,62-64}

The presence of several crossings between electronic states in the vicinity of the minimum energy path as well as the fact that the rotational barriers between stereoisomers of the diradical intermediate can be overcome by small external forces



could lead to different adducts upon ring closure when the force is relaxed.⁴⁴ The switching to a sequential mechanism under force and the predicted production of intermediate diradicals could be potentially observed experimentally with the help of a radical trap,²³ and the eventual formation of alternative adducts confirmed by spectroscopy.

Single-molecule force spectroscopy (SMFS) has contributed to further developments in mechanochemistry^{4,65} by enabling the mechanical activation of covalent bonds,^{66–68} with applications in irreversible bond scission,^{17,69–77} and opening of mechanophores.^{17,26,78–83} Our results offer new perspectives for investigating DA mechanophores by SMFS, in particular the force-clamp characterization of a reversible partial opening by breaking the weakest bond of the adduct only and the investigation of the effect of a photoexcitation of the mechanophore by UV light under force. A recent study indeed reported the involvement of fluorescent radical species in SMFS spectroscopy of a tetraaryl succinonitrile mechanophore.⁸⁴ In a broader perspective, our results are also relevant for the photochemistry of DA adducts.^{46,47} They provide insights into the regions of the potential energy surfaces involved in a sequential bond rupture as well as on the relevant conical intersections and spin-orbit intersystem crossings between excited states along the sequential reaction path that could be probed using ultrashort few femtosecond optical pulses that became recently available.⁸⁵

Data availability

Data for this paper, including optimized geometries for the COGEF path and EFEI and minimum energy intersystem crossings, are available on ZENODO at <https://doi.org/10.5281/zenodo.7473211>.

Author contributions

M. C.-G. carried out the computations. All authors designed the research, analyzed the results and wrote the manuscript.

Conflicts of interest

The authors declare no conflict of interest.

Acknowledgements

The work of M.C.-G., A.S.D. and F.R. is supported by the action of concerted research MECHANOCHEM (ARC 19/23-20, ULiege). Computational resources have been provided by the Consortium des Equipements de Calcul Intensif (CECI), funded by the F.R.S.-FNRS under grant # 2.5020.11. G.D.B. is a Royal Society University Research Fellow.

References

- S. Kotha and S. Banerjee, *RSC Adv.*, 2013, **3**, 7642–7666.
- Z. P. Zhang, M. Z. Rong and M. Q. Zhang, *Prog. Polym. Sci.*, 2018, **80**, 39–93.
- P. Chakma and D. Konkolewicz, *Angew. Chem., Int. Ed.*, 2019, **58**, 9682–9695.
- Polymer Mechanochemistry*, ed. R. Boulatov, Springer, Cham, 2015.
- H.-Y. Duan, Y.-X. Wang, L.-J. Wang, Y.-Q. Min, X.-H. Zhang and B.-Y. Du, *Macromolecules*, 2017, **50**, 1353–1361.
- B. Lyu, W. Cha, T. Mao, Y. Wu, H. Qian, Y. Zhou, X. Chen, S. Zhang, L. Liu, G. Yang, Z. Lu, Q. Zhu and H. Ma, *ACS Appl. Mater. Interfaces*, 2015, **7**, 6254–6259.
- X. Hu, M. E. McFadden, R. W. Barber and M. J. Robb, *J. Am. Chem. Soc.*, 2018, **140**, 14073–14077.
- J. Kida, K. Imato, R. Goseki, D. Aoki, M. Morimoto and H. Otsuka, *Nat. Commun.*, 2018, **9**, 3504.
- Y. Min, S. Huang, Y. Wang, Z. Zhang, B. Du, X. Zhang and Z. Fan, *Macromolecules*, 2015, **48**, 316–322.
- R. Stevenson and G. De Bo, *J. Am. Chem. Soc.*, 2017, **139**, 16768–16771.
- Z. Wang and S. L. Craig, *Chem. Comm.*, 2019, **55**, 12263–12266.
- A. Gandini, *Prog. Polym. Sci.*, 2013, **38**, 1–29.
- S. Akbulatov and R. Boulatov, *ChemPhysChem*, 2017, **18**, 1422–1450.
- M. T. Ong, J. Leiding, H. Tao, A. M. Virshup and T. J. Martinez, *J. Am. Chem. Soc.*, 2009, **131**, 6377–6379.
- J. Ribas-Arino, M. Shiga and D. Marx, *Angew. Chem.*, 2009, **48**, 4190–4193.
- D. A. Davis, A. Hamilton, J. Yang, L. D. Cremer, D. Van Gough, S. L. Potisek, M. T. Ong, P. V. Braun, T. J. Martinez, S. R. White, J. S. Moore and N. R. Sottos, *Nature*, 2009, **459**, 68–72.
- J. Wang, T. B. Kouznetsova, Z. Niu, M. T. Ong, H. M. Klukovich, A. L. Rheingold, T. J. Martinez and S. L. Craig, *Nat. Chem.*, 2015, **7**, 323–327.
- R. Nixon and G. De Bo, *Nat. Chem.*, 2020, **12**, 826–831.
- E. Izak-Nau, D. Campagna, C. Baumann and R. Göstl, *Polym. Chem.*, 2020, **11**, 2274–2299.
- C. R. Hickenboth, J. S. Moore, S. R. White, N. R. Sottos, J. Baudry and S. R. Wilson, *Nature*, 2007, **446**, 423–427.
- C. L. Brown, B. H. Bowser, J. Meisner, T. B. Kouznetsova, S. Seritan, T. J. Martinez and S. L. Craig, *J. Am. Chem. Soc.*, 2021, **143**, 3846–3855.
- R. B. Woodward and R. Hoffmann, *Angew. Chem.*, 1969, **8**, 781–853.
- J. M. Lenhardt, M. T. Ong, R. Choe, C. R. Evenhuis, T. J. Martinez and S. L. Craig, *Science*, 2010, **329**, 1057.
- M. J. Kryger, M. T. Ong, S. A. Odom, N. R. Sottos, S. R. White, T. J. Martinez and J. S. Moore, *J. Am. Chem. Soc.*, 2010, **132**, 4558–4559.
- Z. S. Kean, Z. Niu, G. B. Hewage, A. L. Rheingold and S. L. Craig, *J. Am. Chem. Soc.*, 2013, **135**, 13598–13604.
- Z. Chen, J. A. M. Mercer, X. Zhu, J. A. H. Romaniuk, R. Pfattner, L. Cegelski, T. J. Martinez, N. Z. Burns and Y. Xia, *Science*, 2017, **357**, 475–479.
- M. Horst, J. Yang, J. Meisner, T. B. Kouznetsova, T. J. Martinez, S. L. Craig and Y. Xia, *J. Am. Chem. Soc.*, 2021, **143**, 12328–12334.



- 28 Z. Chen, X. Zhu, J. Yang, J. A. M. Mercer, N. Z. Burns, T. J. Martinez and Y. Xia, *Nat. Chem.*, 2020, **12**, 302–309.
- 29 Y. Liu, S. Holm, J. Meisner, Y. Jia, Q. Wu, J. Woods Toby, J. Martinez Todd and S. Moore Jeffrey, *Science*, 2021, **373**, 208–212.
- 30 D. C. Lee, V. K. Kensy, C. R. Maroon, B. K. Long and A. J. Boydston, *Angew. Chem.*, 2019, **131**, 5695–5698.
- 31 Y. Sun, W. J. Neary, Z. P. Burke, H. Qian, L. Zhu and J. S. Moore, *J. Am. Chem. Soc.*, 2022, **144**, 1125–1129.
- 32 T. Zeng, X. Hu and M. J. Robb, *Chem. Commun.*, 2021, **57**, 11173–11176.
- 33 M. Zhang and G. De Bo, *J. Am. Chem. Soc.*, 2020, **142**, 5029–5033.
- 34 M. Zhang and G. De Bo, *J. Am. Chem. Soc.*, 2018, **140**, 12724–12727.
- 35 R. Stevenson, M. Zhang and G. De Bo, *Polym. Chem.*, 2020, **11**, 2864–2868.
- 36 X. Hu, T. Zeng, C. C. Husic and M. J. Robb, *ACS Cent. Sci.*, 2021, **7**, 1216–1224.
- 37 X. Hu, T. Zeng, C. C. Husic and M. J. Robb, *J. Am. Chem. Soc.*, 2019, **141**, 15018–15023.
- 38 L. C. Wu and G. De Bo, *Synlett*, 2022, **33**, st-2022-r0064-c.
- 39 R. C. Cioc, M. Crockatt, J. C. van der Waal and P. C. A. Bruijninx, *Angew. Chem.*, 2022, **61**, e202114720.
- 40 K. Black, P. Liu, L. Xu, C. Doubleday and K. N. Houk, *Proc. Natl. Acad. Sci. U. S. A.*, 2012, **109**, 12860.
- 41 R. Meir, H. Chen, W. Lai and S. Shaik, *ChemPhysChem*, 2010, **11**, 301–310.
- 42 L. Rulišek, P. Šebek, Z. Havlas, R. Hrabal, P. Čapek and A. Svatoš, *J. Org. Chem.*, 2005, **70**, 6295–6302.
- 43 A. Ogawa and H. Fujimoto, *Tetrahedron Lett.*, 2002, **43**, 2055–2057.
- 44 J. Sauer and R. Sustmann, *Angew. Chem.*, 1980, **19**, 779–807.
- 45 S. De Feyter, E. W. G. Diau, A. A. Scala and A. H. Zewail, *Chem. Phys. Lett.*, 1999, **303**, 249–260.
- 46 E. W. G. Diau, S. De Feyter and A. H. Zewail, *Chem. Phys. Lett.*, 1999, **304**, 134–144.
- 47 B. A. Horn, J. L. Herek and A. H. Zewail, *J. Am. Chem. Soc.*, 1996, **118**, 8755–8756.
- 48 S. Wilsey, K. N. Houk and A. H. Zewail, *J. Am. Chem. Soc.*, 1999, **121**, 5772–5786.
- 49 C. Yang, Z. Liu, Y. Li, S. Zhou, C. Lu, Y. Guo, M. Ramirez, Q. Zhang, Y. Li, Z. Liu, K. N. Houk, D. Zhang and X. Guo, *Sci. Adv.*, 2021, **7**, eabf0689.
- 50 T. Stauch and A. Dreuw, *Chem. Rev.*, 2016, **116**, 14137–14180.
- 51 M. K. Beyer, *J. Chem. Phys.*, 2000, **112**, 7307–7312.
- 52 K. Wolinski and J. Baker, *Mol. Phys.*, 2009, **107**, 2403–2417.
- 53 J. Ribas-Arino, M. Shiga and D. Marx, *J. Am. Chem. Soc.*, 2010, **132**, 10609–10614.
- 54 J.-D. Chai and M. Head-Gordon, *Phys. Chem. Chem. Phys.*, 2008, **10**, 6615–6620.
- 55 P. J. Knowles and H.-J. Werner, *Chem. Phys. Lett.*, 1985, **115**, 259–267.
- 56 Y. Shao, Z. Gan, E. Epifanovsky, A. T. B. Gilbert, M. Wormit, J. Kussmann, A. W. Lange, A. Behn, J. Deng, X. Feng, D. Ghosh, M. Goldey, P. R. Horn, L. D. Jacobson, I. Kaliman, R. Z. Khaliullin, T. Kuš, A. Landau, J. Liu, E. I. Proynov, Y. M. Rhee, R. M. Richard, M. A. Rohrdanz, R. P. Steele, E. J. Sundstrom, H. L. Woodcock, P. M. Zimmerman, D. Zuev, B. Albrecht, E. Alguire, B. Austin, G. J. O. Beran, Y. A. Bernard, E. Berquist, K. Brandhorst, K. B. Bravaya, S. T. Brown, D. Casanova, C.-M. Chang, Y. Chen, S. H. Chien, K. D. Closser, D. L. Crittenden, M. Diedenhofen, R. A. DiStasio, H. Do, A. D. Dutoi, R. G. Edgar, S. Fatehi, L. Fusti-Molnar, A. Ghysels, A. Golubeva-Zadorozhnaya, J. Gomes, M. W. D. Hanson-Heine, P. H. P. Harbach, A. W. Hauser, E. G. Hohenstein, Z. C. Holden, T.-C. Jagau, H. Ji, B. Kaduk, K. Khistyayev, J. Kim, J. Kim, R. A. King, P. Klunzinger, D. Kosenkov, T. Kowalczyk, C. M. Krauter, K. U. Lao, A. D. Laurent, K. V. Lawler, S. V. Levchenko, C. Y. Lin, F. Liu, E. Livshits, R. C. Lochan, A. Luenser, P. Manohar, S. F. Manzer, S.-P. Mao, N. Mardirossian, A. V. Marenich, S. A. Maurer, N. J. Mayhall, E. Neuscammann, C. M. Oana, R. Olivares-Amaya, D. P. O'Neill, J. A. Parkhill, T. M. Perrine, R. Peverati, A. Prociuk, D. R. Rehn, E. Rosta, N. J. Russ, S. M. Sharada, S. Sharma, D. W. Small, A. Sodt, T. Stein, D. Stück, Y.-C. Su, A. J. W. Thom, T. Tsuchimochi, V. Vanovschi, L. Vogt, O. Vydrov, T. Wang, M. A. Watson, J. Wenzel, A. White, C. F. Williams, J. Yang, S. Yeganeh, S. R. Yost, Z.-Q. You, I. Y. Zhang, X. Zhang, Y. Zhao, B. R. Brooks, G. K. L. Chan, D. M. Chipman, C. J. Cramer, W. A. Goddard, M. S. Gordon, W. J. Hehre, A. Klamt, H. F. Schaefer, M. W. Schmidt, C. D. Sherrill, D. G. Truhlar, A. Warshel, X. Xu, A. Aspuru-Guzik, R. Baer, A. T. Bell, N. A. Besley, J.-D. Chai, A. Dreuw, B. D. Dunietz, T. R. Furlani, S. R. Gwaltney, C.-P. Hsu, Y. Jung, J. Kong, D. S. Lambrecht, W. Liang, C. Ochsenfeld, V. A. Rassolov, L. V. Slipchenko, J. E. Subotnik, T. Van Voorhis, J. M. Herbert, A. I. Krylov, P. M. W. Gill and M. Head-Gordon, *Mol. Phys.*, 2015, **113**, 184–215.
- 57 H.-J. Werner, P. J. Knowles, F. R. Manby, J. A. Black, K. Doll, A. Heßelmann, D. Kats, A. Köhn, T. Korona, D. A. Kreplin, Q. Ma, T. F. Miller, A. Mitrushchenkov, K. A. Peterson, I. Polyak, G. Rauhut and M. Sibae, *J. Chem. Phys.*, 2020, **152**, 144107.
- 58 H.-J. Werner, P. J. Knowles, G. Knizia, F. R. Manby and M. Schütz, *Wiley Interdiscip. Rev. Comput. Mol. Sci.*, 2012, **2**, 242–253.
- 59 J. M. Seminario, *Int. J. Quantum Chem.*, 1996, **60**, 1271–1277.
- 60 E. Brémond and C. Adamo, *J. Chem. Phys.*, 2011, **135**, 024106.
- 61 A. D. Becke, *J. Chem. Phys.*, 1993, **98**, 1372–1377.
- 62 M. J. Kryger, A. M. Munaretto and J. S. Moore, *J. Am. Chem. Soc.*, 2011, **133**, 18992–18998.
- 63 H. M. Klukovich, Z. S. Kean, S. T. Iacono and S. L. Craig, *J. Am. Chem. Soc.*, 2011, **133**, 17882–17888.
- 64 J. Wang, T. B. Kouznetsova, R. Boulatov and S. L. Craig, *Nat. Commun.*, 2016, **7**, 13433.
- 65 S. Garcia-Manes and A. E. M. Beedle, *Nat. Chem.*, 2017, **1**, 0083.
- 66 A.-S. Duwez, S. Cuenot, C. Jérôme, S. Gabriel, R. Jérôme, S. Rapino and F. Zerbetto, *Nat. Nanotechnol.*, 2006, **1**, 122–125.



- 67 M. K. Beyer and H. Clausen-Schaumann, *Chem. Rev.*, 2005, **105**, 2921–2948.
- 68 F. R. Kersey, W. C. Yount and S. L. Craig, *J. Am. Chem. Soc.*, 2006, **128**, 3886–3887.
- 69 A. P. Wiita, S. R. K. Ainaravapu, H. H. Huang and J. M. Fernandez, *Proc. Natl. Acad. Sci. U. S. A.*, 2006, **103**, 7222–7227.
- 70 P. Zheng, G. M. Arantes, M. J. Field and H. Li, *Nat. Commun.*, 2015, **6**, 7569.
- 71 S. Akbulatov, Y. Tian, Z. Huang, T. J. Kucharski, Q.-Z. Yang and R. Boulatov, *Science*, 2017, **357**, 299–303.
- 72 M. Grandbois, *Science*, 1999, **283**, 1727–1730.
- 73 P. Zheng and H. Li, *J. Am. Chem. Soc.*, 2011, **133**, 6791–6798.
- 74 S. W. Schmidt, P. Filippov, A. Kersch, M. K. Beyer and H. Clausen-Schaumann, *ACS Nano*, 2012, **6**, 1314–1321.
- 75 A. E. M. Beedle, A. Lezamiz, G. Stirnemann and S. Garcia-Manyes, *Nat. Commun.*, 2015, **6**, 7894.
- 76 M. F. Pill, A. L. L. East, D. Marx, M. K. Beyer and H. Clausen-Schaumann, *Angew. Chem.*, 2019, **58**, 9787–9790.
- 77 D. Schütze, K. Holz, J. Müller, M. K. Beyer, U. Lüning and B. Hartke, *Angew. Chem.*, 2015, **54**, 2556–2559.
- 78 M. M. Hansmann, R. L. Melen, M. Rudolph, F. Rominger, H. Wadepohl, D. W. Stephan and A. S. K. Hashmi, *J. Am. Chem. Soc.*, 2015, **137**, 15469–15477.
- 79 P. A. May and J. S. Moore, *Chem. Rev. Soc.*, 2013, **42**, 7497.
- 80 J. Li, C. Nagamani and J. S. Moore, *Acc. Chem. Res.*, 2015, **48**, 2181–2190.
- 81 H. M. Klukovich, Z. S. Kean, A. L. B. Ramirez, J. M. Lenhardt, J. Lin, X. Hu and S. L. Craig, *J. Am. Chem. Soc.*, 2012, **134**, 9577–9580.
- 82 M. F. Pill, K. Holz, N. Preußke, F. Berger, H. Clausen-Schaumann, U. Lüning and M. K. Beyer, *Chem.–Eur. J.*, 2016, **22**, 12034–12039.
- 83 H. Li and G. C. Walker, *ACS Nano*, 2017, **11**, 28–30.
- 84 M. van Galen, J. P. Kaniraj, B. Albada and J. Sprakel, *J. Phys. Chem. C*, 2022, **126**, 1215–1221.
- 85 M. Nisoli, P. Decleva, F. Calegari, A. Palacios and F. Martín, *Chem. Rev.*, 2017, **117**, 10760–10825.



Bond breaking of furan-maleimide adducts via a diradical sequential mechanism under an external mechanical force

Manuel Cardosa-Gutierrez,¹ Guillaume De Bo,² Anne-Sophie Duwez,¹ *Francoise Remacle¹

¹ UR Molecular Systems, Department of Chemistry, University of Liège, 4000 Liège, Belgium

² Department of Chemistry, University of Manchester, Manchester M13 9PL, UK

Electronic Supplementary Information

Computational details

S1 Comparison between the UDFT and the CAS(4,4) CoGEF paths.

S2 Choice of the functional for the UDFT computation.

S3 Activation barriers and rate constants for the breaking of the first scissile bonds.

S4 Diradical character of S_0 and T_0 and spin-orbit interaction.

ZIP files

S5 Geometries along the CoGEF path for the P_{endo} and P_{exo} adducts computed at the DFT/wB97XD/6-31G(d,p) level.

S6 Geometries along the CoGEF path for the P_{endo} and P_{exo} adducts computed at the CAS(4,4)/6-31G(d,p) level for S_0 .

S7 Geometries of the reactant and transition states computed as a function of the external force at the wB97XD/6-31G(d,p) level.

S8 Geometries at the S_0/T_0 MEIC for the P_{endo} and P_{exo} adducts computed at the CAS(4,4)/6-31G(d,p) level.

S1. Comparison between the UDFT and the CAS(4,4) CoGEF paths

The reaction mechanism was studied by the CoGEF isometric protocol¹ for the two adducts at the UDFT level with the wB97XD² and at the complete active space³ CAS-SCF (4,4) level with the 6-31G(d,p) basis set for the lowest singlet, S₀. Files of the geometries along the CoGEF path computed at the DFT and the CAS(4,4) level are given in the SI (S5 and S6).

The computed force modified minimum energy paths are fully consistent, as can be seen from Figure S1, as well as the relaxed geometries obtained for each value of the applied distortion.

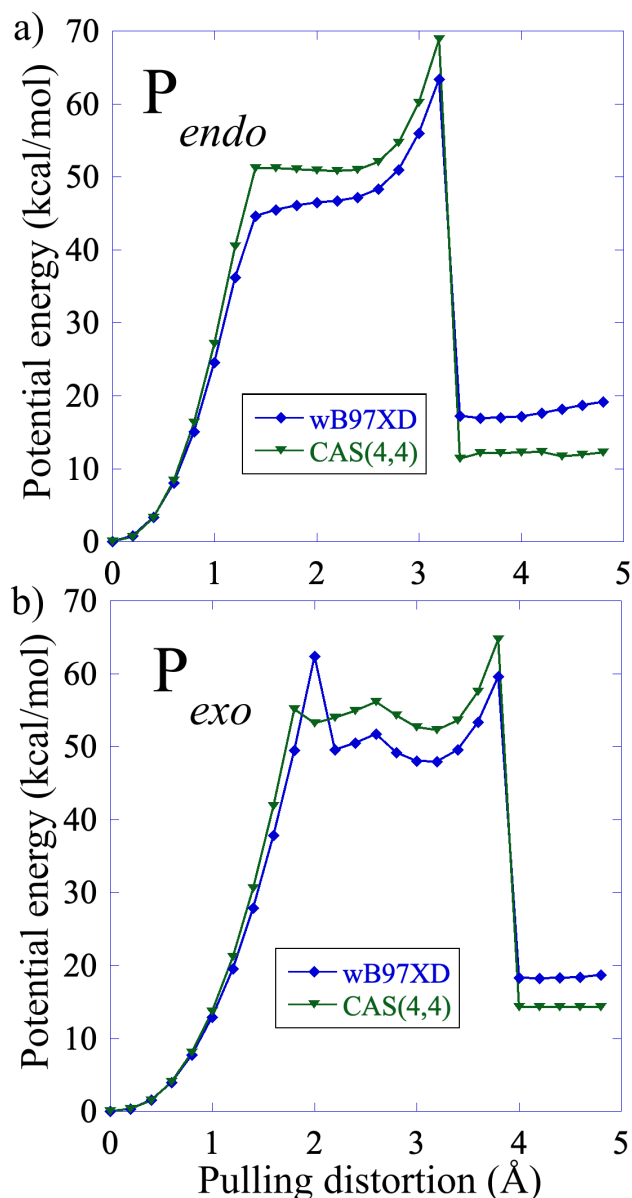


Figure S1 Comparison between the CAS (4,4) CoGEF path and the UDFT/wB97XD with 6-31G(d,p) for the P_{endo} and P_{exo} adducts.

S2 Choice of the functional for the UDFT computation

In order to properly describe the diradical character of the open shell S_0 state in the intermediate region, we use the range-separated hybrid functional wB97XD.² PBE0DH⁴ and BH&HLYP⁵ which includes 50% not Coulomb-attenuated HF exchange gives similar results. A D3 Grimme correction^{2,6} was used for the BH&HLYP and PBE0DH computations.

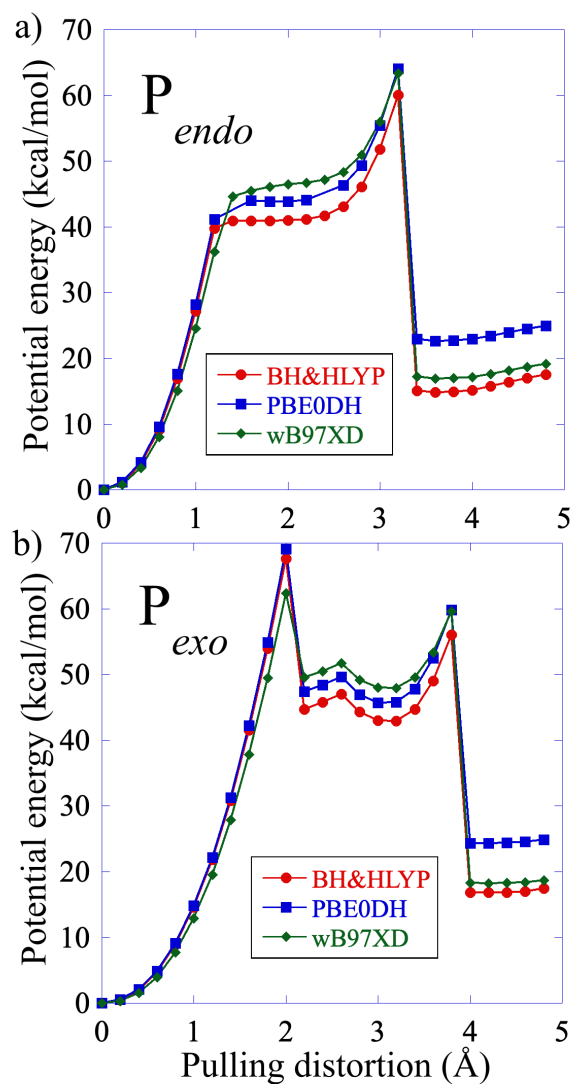


Figure S2 Energy profiles and activation barriers for the P_{endo} (a) and the P_{exo} (b) adducts computed with the WB97XD, BH&HLYP and PBE0DH functionals.

The UDFT computations were carried out with the quantum chemistry software QChem v5.4⁷ and the CAS-SCF computation with the quantum chemistry code MOLPRO 2021.^{8,9}

S3 Activation barriers and rate constants for the breaking of the first scissile bond

The activation free energy ($\Delta^\ddagger G^0$) for the four adducts was computed at room temperature, for different values of the force by taking the difference between the free energy of the transition states (TS) and the equilibrium geometries (Eq. 1). A vibrational analysis of the optimized TS and equilibrium geometries was carried out for each adduct under force using the EFEI approach in order to compute the free energy.

$$\Delta G^{\ddagger 0} = G^0(TS) - G^0(Eq) \quad (S1)$$

The rates constants at a given temperature ($k(T)$) are estimated using Eyring transition states theory:

$$k(T) = \frac{k_B T}{h c^0} e^{-\Delta G^{\ddagger 0}/RT} \quad (S2)$$

- $c^0 = 1$ is the standard concentration.
- $\Delta G^{\ddagger 0}$ is the free energy of activation, and T is the temperature.
- $k_B, h, R,$ are Boltzmann, Planck, and ideal gas constants, respectively.

At zero force, at 298 K, at the DFT wb97XD/6-31G(p,d) level that we use, we compute values of 28.2 kcal/mol and 30.8 kcal/mol for the barrier of the concerted rupture of the P_{endo} and P_{exo} adducts in the gas phase, which leads to a $\Delta(\Delta G^\ddagger)$ value of 2.6 kcal/mol. These values are higher than the values reported by Craig et al in ref¹⁰. Craig et al report 22.8 and 24.8 kcal/mol respectively for computations at the B3LYP/6-31G(d) level in THF for a slightly longer acetoxy anchoring chains (CH₂-O-CO-CH₃ on furane and CH₂-CH₂-O-CO-CH₃ on maleimide instead of CH₃ in our computations). Their $\Delta(\Delta G^\ddagger)$ of 2.2 kcal/mol between the P_{endo} and P_{exo} adducts is in good agreement with our computed values. Our computed values are closer to those reported by Meir et al in the gas phase (ref¹¹) (30.9 and 32.3 kcal/mol) at the B3LYP/6-311++G(d,p) for geometry optimization carried out at the BP86/6-31G(d) level. They are \approx 2-3 kcal higher than those of Yang et al (ref¹²): 25.1 and 28.9 kcal/mol computed at the M06-2X/6-311+G(d,p) level in DMSO using a SMD solvation model and those of Rulisek et al¹³ (24.6 kcal/mol and 26.4 kcal/mol) obtained in the gas phase from equilibrium geometries at the MP2/6-31G(d) level and a single point CCSD(T) computation with a Aug-cc-pVDZ basis set.

A full geometry optimization at the BH&HLYP/6-31G(d,p) level gives barriers of 30.51 kcal/mol and 32.24 kcal/mol for P_{endo} and P_{exo} respectively at 0nN and 22.02 and 25.54 kcal/mol respectively at 4nN. A full geometry optimization at the CAM-B3LYP/6-311++G(2df,2p) at 0 nN gives 26.22 kcal/mol for P_{endo} and 28.08 kcal/mol for P_{exo} . The barrier values computed at the B3LYP/6-31G(d,p) level are lowered to 20.96 and 21.86 kcal/mol for the P_{endo} and P_{exo} adducts respectively at zero nN and to 20.02 and 26.26 at 2.7 nN. Computations of full COGEF path under tension with the CAM-B3LYP and the B3LYP functionals led to severe convergence issues because these functionals are not well-suited to describe the diradical species that appear for values of the forces close to the first bond rupture and beyond.

At zero force and at 4 nN, single point barriers values computed at the wb97xD/6-311++G(d,p) level are essentially the same as those computed at wb97XD/6-31G(d,p) for the P_{endo} and the P_{exo} adducts. These results are summarized in Table S1 below.

Table S1. Computed values of the activation barrier at 298K for several functionals and basis sets.

‘SP’ means a single point computation on the geometry optimized at the UwB97XD/6-31G(d,p) level.

0 nN	Barrier ($\Delta G^{\ddagger 0}$) kcal/mol		Rates (Eyring) s⁻¹	
Level	P_{endo}	P_{exo}	P_{endo}	P_{exo}
UwB97XD/6-31G(d,p).	28.26	30.76	1.19 10 ⁻⁸	1.75 10 ⁻¹⁰
UBH&HLYP/6-31G(d,p)	30.51	32.24	2.67 10 ⁻¹⁰	1.44 10 ⁻¹¹
CAMB3LYP/6-311++G(2df,2p)	26.22	28.08	3.73 10 ⁻⁷	1.62 10 ⁻⁸
UwB97XD/6-311++G(d,p) SP	27.86	30.25	2.34 10 ⁻⁸	4.15 10 ⁻¹⁰
UB3LYP/6-31G(d,p) SP	20.65	not converged	4.52 10 ⁻³	
UB3LYP/6-31G(d,p)	20.96	21.86	0.0027	0.0006

2.7 nN	Barrier ($\Delta G^{\ddagger 0}$) kcal/mol		Rates (Eyring) s⁻¹	
Level	P_{endo}	P_{exo}	P_{endo}	P_{exo}
UwB97XD/6-31G(d,p)	31.46	39.62	5.38 10 ⁻¹¹	5.61 10 ⁻¹⁷
UBHLYP/6-31G(d,p)	34.06	40.51	6.68 10 ⁻¹³	1.25 10 ⁻¹⁷
UB3LYP/6-31G(d,p) SP	25.39	32.57	1.51 10 ⁻⁶	8.26 10 ⁻¹²
UB3LYP/6-31G(d,p)	20.02	26.26	1.31 10 ⁻²	3.49 10 ⁻⁷

4.05 nN	Barrier ($\Delta G^{\ddagger 0}$) kcal/mol		Rates (Eyring) s⁻¹	
Level	P_{endo}	P_{exo}	P_{endo}	P_{exo}
UwB97XD/6-31G(d,p)	18.09	22.40	0.34	2.36 10 ⁻⁴
UwB97XD/6-311++G(d,p) SP	18.58	22.02	0.15	4.48 10 ⁻⁴
UBHLYP/6-31G(d,p)	22.03	25.55	4.40 10 ⁻⁴	1.16 10 ⁻⁶
UB3LYP/6-31G(d,p) SP	not converged	not converged		
UB3LYP/6-31G(d,p)	not converged	not converged		

The rates of the first bond rupture for P_{exo} and P_{endo} computed with the wB97XD functional at 298K are shown in figure S3.

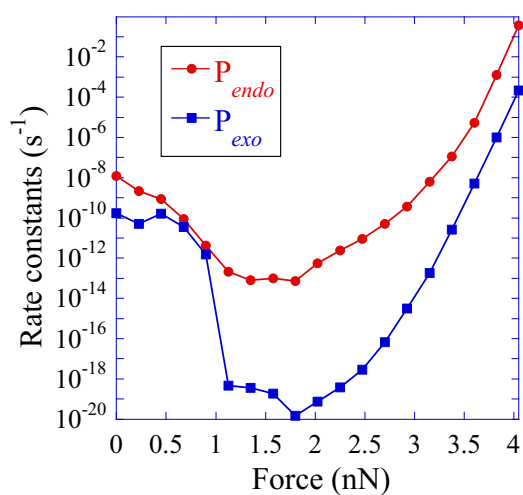


Figure S3: Computed rate constants at the UDFT/wB97XD level as a function of the pulling force up to the SB1 rupture for the two adducts. Files of the geometries of the reactant and transition states are given in the SI (S7).

S1.4 Diradicalar character of S_0 and T_0 and spin-orbit interaction

The CAS -SCF computations were carried out with an active space of 4 molecular orbitals and 4 active electrons (CAS(4,4)). S_0 has a diradical character in the intermediate region between the two bond ruptures. In that region, the two main configurations are that of the GS, $|2200\rangle$ and the HOMO-LUMO doubly excited configuration $|2020\rangle$. The CI coefficients are reported in Figure S4. In Figure S5, we report isocontours of the natural CAS orbitals. One can see that for distortions between 1.4 and 3.2 Å, the HOMO and the LUMO natural CAS MO's are delocalized on the two moieties. Since the coefficients on the $|2200\rangle$ and $|2020\rangle$ configurations are of opposite sign and roughly of the same magnitude, in the intermediate region, the S_0 wave function has a diradicalar character, see for example ref. ¹⁴.

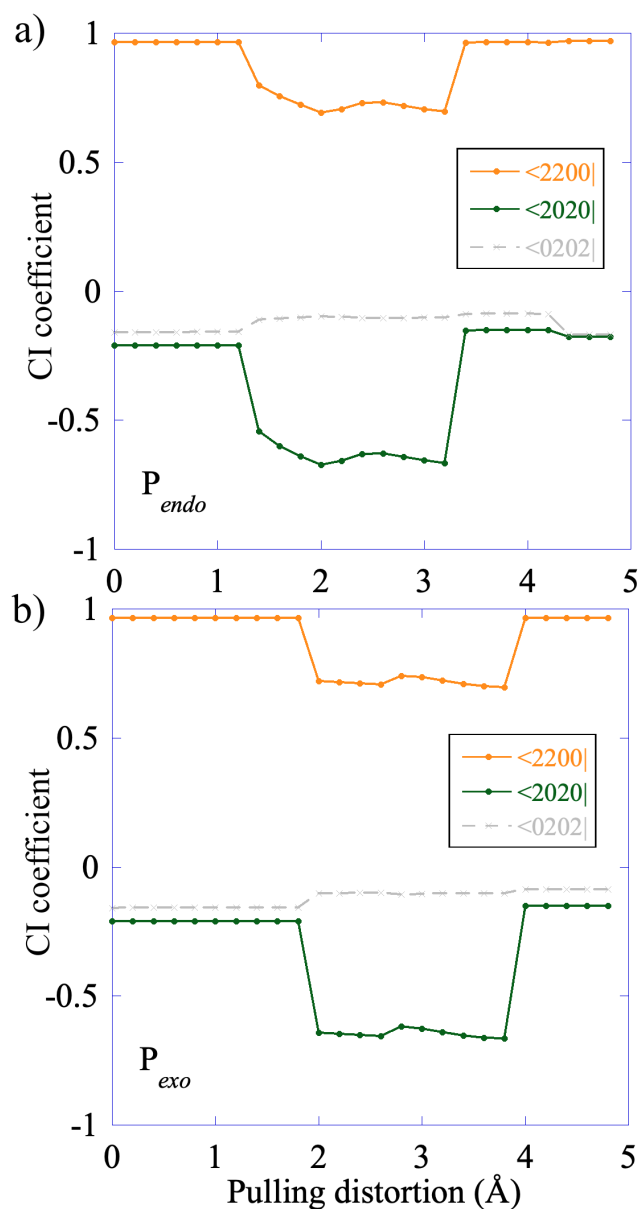
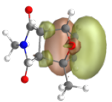
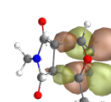
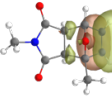
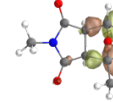


Figure S4. CI coefficients of the S_0 for the P_{endo} and the P_{exo} adducts. In the intermediate region, the coefficients of $|2200\rangle$ and $|2020\rangle$ are $\approx \sqrt{2}$ which leads to a diradical character since the natural HOMO and LUMO are delocalized over the two moieties, see Figure S5.

P_{endo}				P_{exo}			
CoGEF Point	Distortion [Å]	HOMO	LUMO	HOMO	LUMO	Distortion [Å]	CoGEF Point
0	0.0					0.0	0

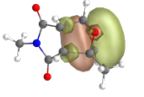
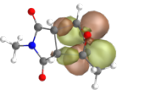
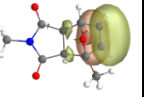
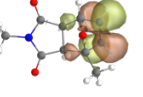
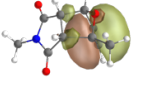
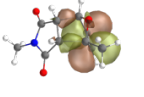
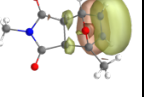
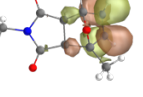
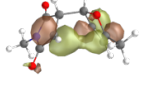
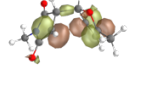
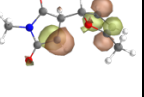
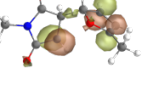
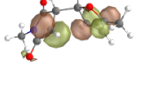
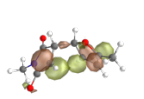
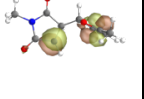
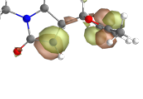
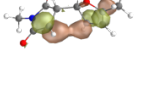
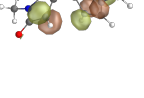
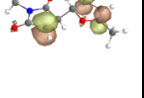
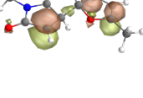
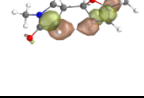
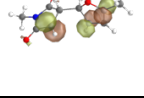
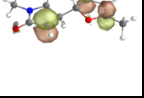
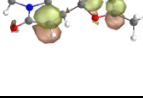
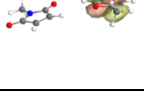
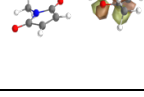
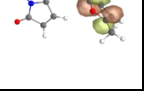
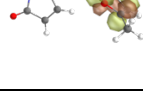
4	0.8					1.2	6
6	1.2					1.8	9
7	1.4					2.0	10
10	2.0					2.6	13
14	2.8					3.2	16
16	3.2					3.8	19
17	3.4					4.0	20

Figure S5. Isocontours of the natural CAS orbitals as a function of the pulling distortion along the CoGEF path for the P_{endo} and the P_{exo} adducts.

The energy of the lowest triplet state T_0 was computed along the CoGEF path at the geometries of the singlet S_0 . The main configuration is the $|2aa0\rangle$ configuration throughout the CoGEF path, with a weight larger than 93 % (Figure S6).

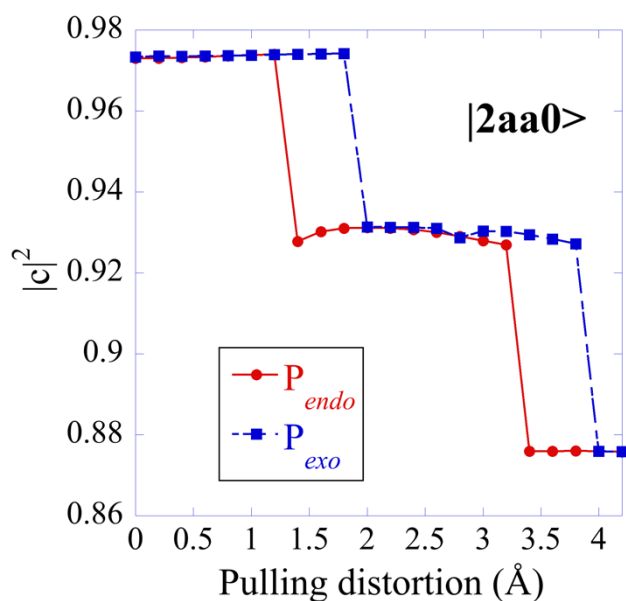


Figure S6: The weight of the $|2aa0\rangle$ configuration in the T_0 state determinantal composition along the CoGEF path.

We show in Figure S7 the S_0/T_0 energy difference along the CAS CoGEF path for the two adducts. The value of the spin-orbit coupling is reported in Table S1. The geometries of the minimum energy intersystem crossing (MEIC) for the P_{endo} and P_{exo} adducts are reported in Figure S8. One MEIC was identified for P_{endo} with a geometry close to the anti geometry along the minimum path. Two MEIC were localized for the P_{exo} adduct, one close to *anti* conformer and one close to *gauche* one.

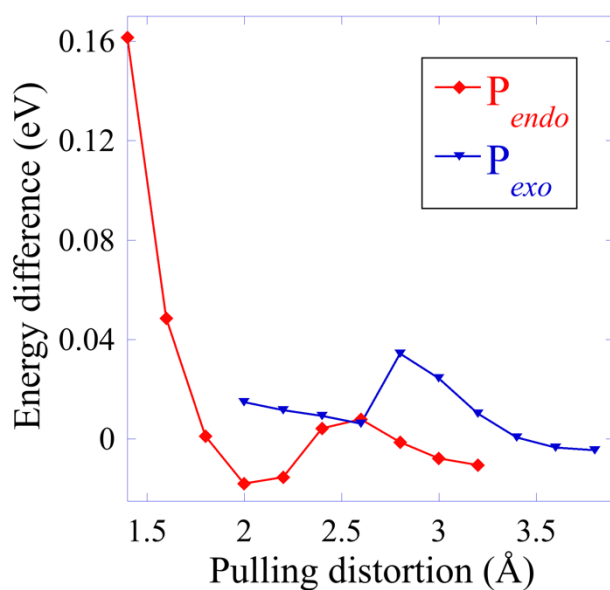


Figure S7: Energy differences T_0/S_0 computed at the CAS(4,4) level in the intermediate region.

Table S1: Spin-orbit coupling constants (cm^{-1}) computed at the geometries of the CoGEF pathway.

Distortion	P_{endo}	P_{exo}
0.0	0.733112	0.724825
0.20	0.717576	0.730484
0.40	0.699826	0.734509
0.60	0.683551	0.734170
0.80	0.669061	0.729655
1.0	0.655881	0.721678
1.2	0.644751	0.709301
1.4	0.121106	0.693892
1.6	0.067589	0.674935
1.8	0.031070	0.652809
2.0	0.002896	0.026728
2.2	0.026061	0.024470
2.4	0.046159	0.022635
2.6	0.047017	0.020343
2.8	0.034450	0.044373
3.0	0.023332	0.043400
3.2	0.014914	0.032134
3.4	0.033447	0.019743
3.6	0.079095	0.012212
3.8	0.080286	0.009061
4.0	0.087997	0.067316
4.2	0.099456	0.066679
4.4	0.116234	0.066630
4.6	0.118341	0.064166
4.8	0.116921	0.067069

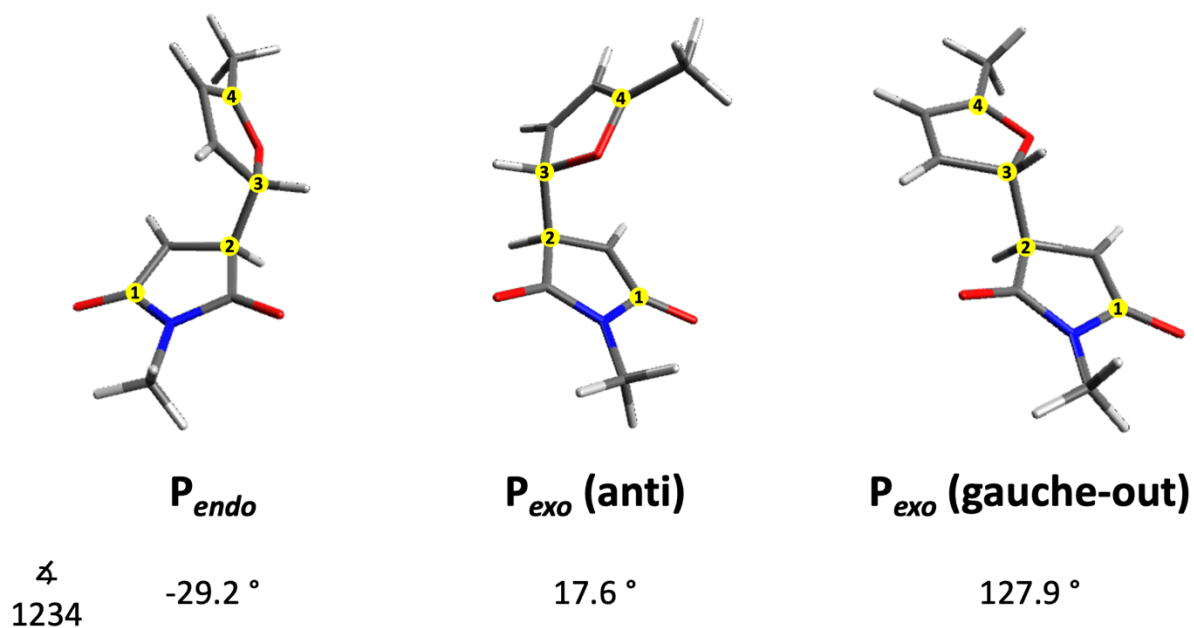


Figure S8: Geometries at the minimum energy intersystem crossings for P_{endo} and P_{exo}. The geometries are given in the SI (S8).

References

1. Beyer, M. K., The mechanical strength of a covalent bond calculated by density functional theory. *J. Chem. Phys.* 2000, 112, 7307-7312.
2. Chai, J.-D.; Head-Gordon, M., Long-range corrected hybrid density functionals with damped atom–atom dispersion corrections. *Phys. Chem. Chem. Phys.* 2008, 10, 6615-6620.
3. Knowles, P. J.; Werner, H.-J., An efficient second-order MC SCF method for long configuration expansions. *Chem. Phys. Lett.* 1985, 115, 259-267.
4. Brémond, E.; Adamo, C., Seeking for parameter-free double-hybrid functionals: The PBE0-DH model. *J. Chem. Phys.* 2011, 135, 024106.
5. Becke, A. D., A new mixing of Hartree–Fock and local density-functional theories. *J. Chem. Phys.* 1993, 98, 1372-1377.
6. Grimme, S.; Antony, J.; Ehrlich, S.; Krieg, H., A consistent and accurate ab initio parametrization of density functional dispersion correction (DFT-D) for the 94 elements H–Pu. *J. Chem. Phys.* 2010, 132, 154104.
7. Shao, Y., et al., Advances in molecular quantum chemistry contained in the Q-Chem 4 program package. *Mol. Phys.* 2015, 113, 184-215.
8. Werner, H.-J., et al., The Molpro quantum chemistry package. *J. Chem. Phys.* 2020, 152, 144107.
9. Werner, H.-J.; Knowles, P. J.; Knizia, G.; Manby, F. R.; Schütz, M., Molpro: a general-purpose quantum chemistry program package. *Wiley Interdiscip. Rev. Comput. Mol. Sci* 2012, 2, 242-253.
10. Wang, Z.; Craig, S. L., Stereochemical effects on the mechanochemical scission of furan–maleimide Diels–Alder adducts. *Chem. Comm.* 2019, 55, 12263-12266.

11. Meir, R.; Chen, H.; Lai, W.; Shaik, S., Oriented Electric Fields Accelerate Diels–Alder Reactions and Control the endo/exo Selectivity. *ChemPhysChem* 2010, 11, 301-310.
12. Yang, C., et al., Electric field–catalyzed single-molecule Diels-Alder reaction dynamics. *Sci. Adv.* 2021, 7, eabf0689.
13. Rulíšek, L.; Šebek, P.; Havlas, Z.; Hrabal, R.; Čapek, P.; Svatoš, A., An Experimental and Theoretical Study of Stereoselectivity of Furan–Maleic Anhydride and Furan–Maleimide Diels–Alder Reactions. *J. Org. Chem.* 2005, 70, 6295-6302.
14. Salem, L.; Rowland, C., The Electronic Properties of Diradicals. *Angew. Chem.* 1972, 11, 92-111.

Chapter 4. Isotope effects in the ultrafast excited state photodissociation of the ethylene cation.

Table of Contents

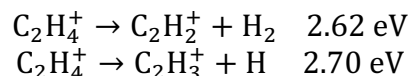
Chapter 4. Isotope effects in the ultrafast excited state photodissociation of the ethylene cation.	85
4.1. <i>Overview of photorelaxation of ethylene cation in pump-probe experiments.....</i>	85
4.2. <i>Modeling the non-adiabatic dynamics in the four lowest electronic states of the ethylene cation</i>	87
4.3. <i>Explanation of the isotope effect on the oscillations of the experimental yields</i>	91
4.4. <i>Summary of contributions</i>	95
4.5. <i>References</i>	96
4.6. <i>Publication: “Isotope effect on the few-femtosecond relaxation dynamics of the ethylene cation”</i>	97

4.1. Overview of photorelaxation of ethylene cation in pump-probe experiments

Pump-probe experiments provide valuable insights into the photoinduced chemical processes of molecules. In our study of isotopic substitution effects on the photorelaxation dynamics of the ethylene cation, the pump pulses are few-fs EUV pulses generated by High Harmonic Generation (HHG) in a gas cell, driven by 15 fs IR pulses with a central wavelength of 811 nm. When the 9th harmonic (H9) of the IR pulse is directed at a neutral ethylene sample, it produces a superposition of the cationic ground state (D_0) and the first excited state (D_1), with the D_0 dominating. For the 11th harmonic (H11), the population is again primarily in the D_0 and D_1 states, but with a reduced contribution from higher states (D_2 and D_3), and the D_0/D_1 population ratio is inverted compared to the H9 case. With the 13th harmonic (H13), the wave packet exhibits significant contributions from D_2 and D_3 , which are close in energy in the FC region due to the higher energy of this harmonic. The aim of this work is to investigate the causes of the strong isotope effect observed experimentally in the fragmentation yields. A joint publication with the group of Mauro Nisoli (Politecnico – Milano) has been submitted to the journal *J. Phys. Chem. Lett.* It is attached at the end of this chapter.

Since both ionization and excitation occur on timescales much faster than nuclear motion, see discussion of the FC principle in Chapter 2, Section 2.2, the cation is formed in the FC region of the neutral equilibrium geometry, which has D_{2h} symmetry. This configuration is stable for the neutral singlet ground state, but the cationic D_0 is degenerate, making it unstable. Consequently, the cation undergoes a Jahn-Teller rearrangement, which breaks the D_{2h} symmetry and lifts the degeneracy, driving the nuclei away from this symmetry.

The dynamics are monitored experimentally with few-fs IR probe pulses like those used in ref. (1), which was devoted to the $C_2H_4^+$ isotopomer only and focused on the short-time behavior of the fragmentation yields. In this study, the photodissociative ionization of both isotopomers, which exhibits a strong isotope effect, is analyzed. For each delay time between the pump and probe pulses, the dissociation yields are measured via mass spectrometry of the parent ions ($C_2H_4^+$ or $C_2D_4^+$) as well as the heavy fragment ions ($C_2H_3^+$, $C_2H_2^+$, and $C_2D_3^+$, $C_2D_2^+$). Under these experimental conditions, the ethylene cation exhibits two competing low-energy dissociation channels (2, 3): one leading to H/D-loss and the other to H_2/D_2 -loss (see scheme below)



As reported in ref. (1), the IR probe pulse alters the dissociation yields. This occurs because, once the cation relaxes to the ground state D_0 , it can absorb three IR photons, leading to re-excitation to the excited state D_3 . This adds more energy to the cation, favoring the dissociation mechanisms. The probability of re-excitation from D_0 to D_3 is highest when the geometry of the cation on D_0 corresponds to a large transition dipole moment $\mu_{D_0D_3}$, and the energy difference between D_0 and D_3 corresponds to three times the energy of an IR photon. This mechanism is referred to as three-photon resonant excitation.

The change in dissociation yields of the two isotopomers for every delay time measured in the experiments is shown in Figure 4.1. The y-axis represents the relative yield for each fragment, defined as the ratio $\frac{Y_{IR}-Y_0}{Y_0}$, where Y_0 represents the yield in the absence of the IR pulse and Y_{IR} is the yield after probing with the IR pulse at delay time τ .

Photoionization by H9 leaves the molecule mostly in the ground state of the cation, D_0 , with a smaller fraction in the first excited state, D_1 . In this case, interaction with the IR pulse causes bleaching of the parent ion, observed around delay zero for both isotopomers (compare the blue curves in Figures 4.1(a) and 4.1(d)). The term “bleaching” refers to a decrease in the yield of the parent ion due to dissociation induced by the IR pulse. After excitation by H11 (green curves in Figure 4.1) and H13 (orange curves in Figure 4.1), the cation is left in a higher excited electronic state. The bleaching occurs at a delay time of ~ 25 -fs, where a shoulder appears in the $C_2H_4^+$ relative yield from H9 (Figure 4.1(a), blue curve). The shoulder is nearly absent in the $C_2D_4^+$ H9 yield (Figure 4.1(d), blue curve) due to the mass effect on the rate of motion of the wave packet on D_1 for the heavier isotopomer.

The bleaching peak in the parent ion yield is attributed to re-excitation to D_3 of the population that relaxed to D_0 from higher electronic states or that was ionized to D_0 by the IR probing pulse via the three-photon resonant process, as discussed in (1). The same mechanism is responsible for the delayed shoulder observed in Figure 4.1(a), which is attributed to re-excitation to D_3 of the population initially excited to D_1 by H9 and later relaxing to D_0 . For the H11 and H13 ionizations of $C_2D_4^+$ (green and orange curves in Figure 4.1(d)), the bleaching peak occurs at a slightly longer delay time (~ 25 -30 fs) than in $C_2H_4^+$.

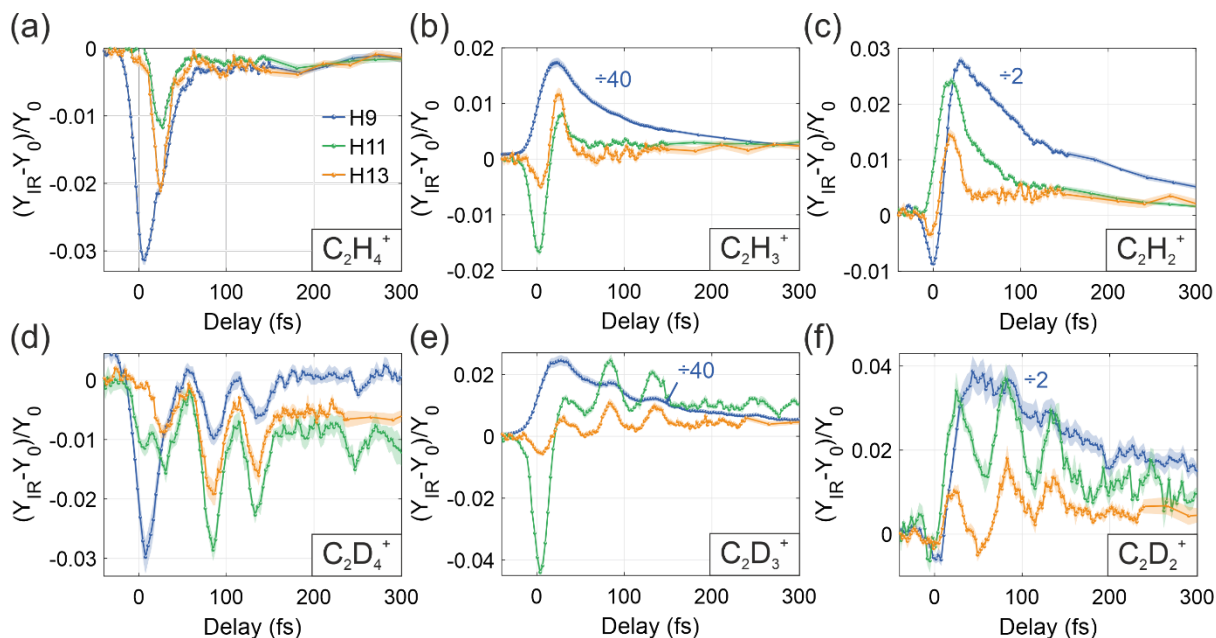


Figure 4.1. Relative yield as a function of the EUV-IR delay for the fragments top row hydrogenated species C_2H_4 . (a) $C_2H_4^+$, (b) $C_2H_3^+$, and (c) $C_2H_2^+$, obtained by ionizing ethylene with H9 (blue), H11 (green) and H13 (orange). The second row shows the results in case of ionization of the deuterated species C_2D_4 : (d) $C_2D_4^+$, (e) $C_2D_3^+$, and (f) $C_2D_2^+$. In all panels, the markers represent the average over 10 independent pump–probe measurements, while the shaded areas cover twice their standard deviation (error of the mean).

A pronounced isotope effect is observed in the dynamics of the fragmentation yields, as shown in Figures 4.1(b), (c) and (e), (f), which display the ion yields as a function of the pump–probe time delay at later times. The temporal evolution of the relative ion yield for the deuterated species (Figures 4.1(d)–(f)) exhibits large oscillations with a period of approximately 50 fs, with peaks at ~ 85 fs and ~ 135 fs. In contrast, the ion yields for the hydrogenated species (Figures 4.1(a)–(c)) show much weaker oscillations, which are clearly visible only in the parent ion, with a comparable ~ 50 -fs period.

4.2. Modeling the non-adiabatic dynamics in the four lowest electronic states of the ethylene cation

Using surface hopping (see Chapter 3), we studied the ultrafast relaxation and structural dynamics following the sudden ionization of neutral ethylene from the ground state to the four lowest excited states of the cation. For the SH simulations, we used a similar description of the electronic structure for $C_2D_4^+$ as in ref. (1) for $C_2H_4^+$. Briefly, we carried out surface hopping (SH) ab initio dynamics for ensembles of trajectories using the SA(7)-CAS-SCF(11,9)/6-311G(d,p) level of electronic structure on the D_1 , D_2 , D_3 states as implemented in SHARC (4) coupled to MOLPRO (5, 6) with four active electronic states (D_0 , D_1 , D_2 , D_3), followed after the trajectory relaxed on D_0 by Born-Oppenheimer ab initio molecular dynamics (BOMD) (7, 8) at the B3LYP/6-311G++(3df,3pd) level up to 2 ps. In the BOMD simulation, the positions and velocities of the nuclei are propagated in time like in surface hopping, except that hops between two electronic states are not allowed. Thus, the dynamic of the molecule is followed in a single electronic state (the ground state in our case). The initial states of the SH trajectories were sampled from a Wigner distribution of the ground

vibrational state of the neutral ground electronic state. In addition, SH hopping dynamics at the same CAS level were run on D₀ for 200 fs and for 2 ps in BOMD. The D₀ loss and D₂ loss were monitored using a threshold bond length of 3.5 Å. As in the case of the C₂H₄⁺ ion, in C₂D₄⁺, the H-loss and the H₂ loss occur on D₀ during the BOMD dynamics.

Figure 4.2 illustrates the protocol followed in the software SHARC to set up and run the trajectories in the surface hopping (see Figure 4.1).

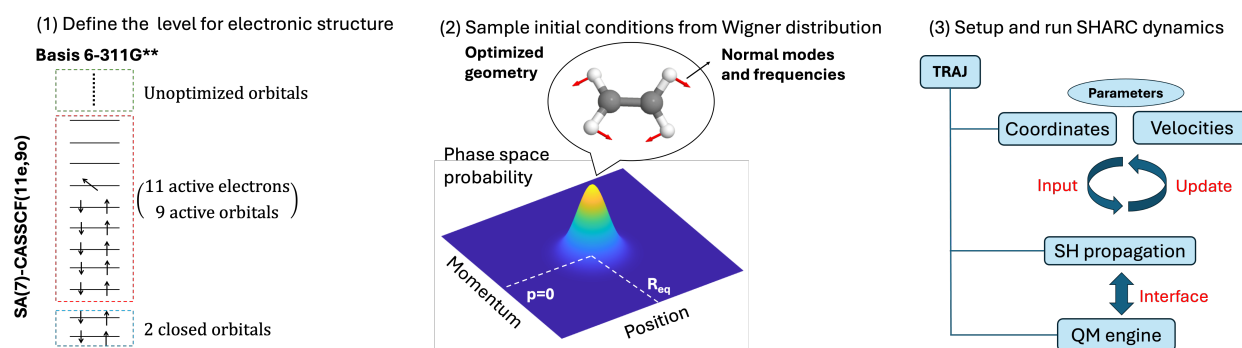


Figure 4.2. Scheme illustrating the process of setting up and running SH simulations with SHARC. The first step involves selecting the electronic structure level, including the choice of basis set and active space. This can be assisted by prior knowledge of the molecule or similar systems found in the literature, and by exploratory studies at lower levels of theory. In the second step, the ground state minimum is optimized, and the vibrational frequencies and normal modes are computed, which SHARC uses to sample an ensemble of initial conditions. Finally, in the third step, for each initial condition (comprising velocities and positions), a trajectory is set up starting from the chosen initial electronic state. This step also requires selecting the software for on-the-fly quantum chemistry calculations (Molpro in this case) and generating input files with parameters for time propagation such as time step, number of timesteps, surface hopping algorithm, and other relevant settings

Table 4.1 shows the number of trajectories per ensemble that were simulated using semiclassical surface hopping. Each trajectory is stopped when it has spent at least 10 fs in the ground state D₀; then, we switch to classical propagation with BOMD for 2 ps or until the cation dissociates.

Table 4.1 Number of trajectories analyzed per ensemble. The ensemble refers to the group of trajectories started at the same electronic state.

Isotopomer	D0 ensemble	D1 ensemble	D2 ensemble	D3 ensemble
C ₂ H ₄ ⁺	297	221	137	102
C ₂ D ₄ ⁺	200	141	210	163

The temporal evolution of the populations for three ensembles started on D₁, D₂, and D₃ electronic states is presented in Figure 4.3. The mass isotope effect slows the motion of C₂D₄⁺ and delays the relaxation from D₁ to D₀, as seen in the computed decay curve of the D₁ ensemble plotted in Figure 4.3(d). In contrast, there is only a small delay in the relaxation of the D₂ and D₃ ensembles (see

Figures 4.3(b), (c), and (e), (f), respectively), which leads to comparable computed lifetimes of these two higher excited states (see Table 4.2).

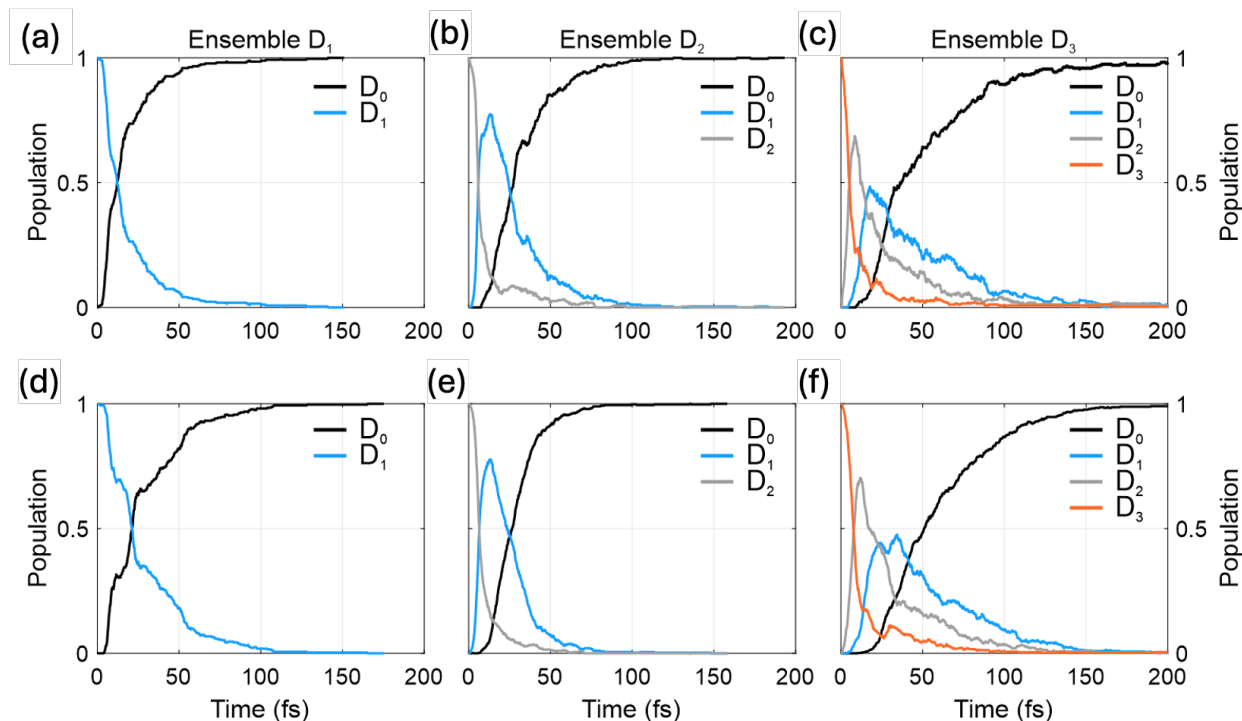


Figure 4.3. (a)-(c) Population dynamics for the hydrogenated molecule corresponding to initial excitation to D_1 , D_2 , and D_3 . (d)-(f) same as (a)-(c) but for the deuterated molecule.

Table 4.2: Computed lifetimes of the D_1 , D_2 , and D_3 excited states from the ensembles of trajectories. They are estimated by fitting an exponential decay to the populations' curve (second column) and as the time that it takes the population to decay to D_0 by 50 % (third column)

Ensemble	Lifetime (fs) Exp Fit	Lifetime (fs) 50 % decay
D1 Hydrogen	14.6	12.3
D1 Deuterium	26.5	21.4
D2 Hydrogen	6.6	5.8
D2 Deuterium	7.2	6.8
D3 Hydrogen	6.7	5.2
D3 Deuterium	8.3	8.3

Because the ultrafast few-fs EUV pulses (H9, H11, and H13) have a broad energy bandwidth, they create a superposition wavepacket that involves simultaneously several electronic states. This initial coherent superposition state cannot be modeled in SH simulations because SH assumes that the nuclei follow a single potential energy surface at every time. However, knowing the

probabilities to ionize the neutral molecule to a given excited state of the cation, which is given by the experimental photoionization cross sections (Table 4.3), we can calculate a weighted average of the initial ensembles that were run in SH for each cationic electronic state. This approximate procedure contrasts with the more exact one followed to simulate the photoionization of the CD₄ molecule, where we carried out full quantum dynamics in a grid (see Chapter 5 section 5.3) and can describe the electronic coherences between the excited electronic states populated during the sudden ionization process.

Table 4.3. Relative photoionization yields to the D₀, D₁, and D₂/D₃ states of the ethylene cation derived from the experimental photoionization cross section reported in ref. (9). The ionization yields of higher excited states are $\leq 1\%$ and have been neglected.

C ₂ H ₄ /C ₂ D ₄	H9	H11	H13
D ₀	0.64	0.23	0.11
D ₁	0.35	0.52	0.28
D ₂ /D ₃	0.01	0.25	0.61

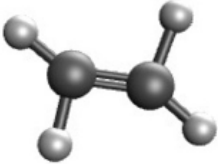
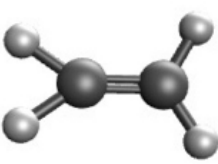
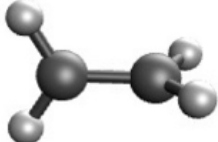
The photoionization cross-sections are taken to be identical for the two isotopomers. While the H9 pulse accesses primarily D₀ (64%) and D₁ (35%), photoionization with the higher harmonic, H11, inverts this ratio with 52% of ionization to the D1 state, 23% in D₀ and the remaining 25% to the higher D₂ and D₃ states. For H13, the D₂ and D₃ states are primarily ionized (61%), with about lower populations in D₁ and D₀ (28% and 11%, respectively); see Table 4.3.

The conical intersections (CIs) sampled by the SH trajectories have been previously reported (3, 10). The D₂/D₃ minimum energy conical intersection (MECI) through which the relaxation occurs for the D₃ ensemble is peaked, with a planar geometry and a slightly elongated C-C bond (1.4 Å) compared to that of the D_{2h} neutral ground state (1.33 Å) and very close to the FC region in configuration space. Its non-adiabatic derivative coupling vector (NAC) significantly activates the ‘in plane’ C-C and C-H modes. For these reasons, as can be seen from Figures 4.3 c (C₂H₄⁺) and f (C₂D₄⁺), the D₃/D₂ relaxation is very fast and occurs within 5 fs, without any major isotope effect. In the SH dynamics, the D₂/D₁ relaxation also occurs through a peaked CI with a planar geometry. The MECI geometry has a slightly elongated C-C bond at 1.4 Å that activates the same ‘in plane’ modes, C-C and C-H stretching. For the D₂ and the D₃ ensembles (Figures 4.3 b, c, and e, f), some population is transferred from D₂ to D₁ within 5 to 10 fs, with a shoulder at 15 fs for the D₃ ensemble (Figures 4.3 c and f). Overall, for the two isotopomers, most of the population that reaches D₁ within the first 10 fs is essentially planar with activated C-C bonds and H-C-H angles for the D₂ and D₃ ensembles, which makes it different from the Wigner distribution of the D₁ ensemble of initial conditions.

Three CIs are involved in the D₁/D₀ relaxation: two planar and a twisted one. We refer to them as planar I, planar II, and twisted (see pictures in Table 4.4). The planar I MECI is located 2.45 eV above the energy of the planar, D_{2h}, D₀ cation. It has a distorted geometry with modified HCH angles and a slightly compressed C-C bond (1.28 Å). It plays a major role in the relaxation dynamics to D₀ for both isotopomers (see Table 4.4). The second MECI, planar II, is slightly higher

in energy (2.56 eV) and does not play a significant role in the relaxation dynamics sampled by the trajectories. Both planar D_1/D_0 CIs are sloped and activate C-C elongation and CH modes as the D_3/D_2 and D_2/D_1 ones, and in addition to low frequency, out-of-plane motions: the CH_2 torsion, wagging, and HCH in plane scissoring modes. Their geometries differ more from the planar geometry of the neutral ground state than the D_3/D_2 and the D_2/D_1 MECIs. As a result, the initial decay of the D_1 population to D_0 in Figures 4.3(a) and (d) is slower than that of the D_2 and D_3 populations to D_1 , see Figures 4.3(b), (c), (e), and (f). The third major MECI playing a role in the D_1/D_0 relaxation dynamics has a twisted geometry with a torsion angle of 90° . This CI is lower in energy than the two planar MECI and 1.57 eV above the planar D_{2h} geometry of D_0 . It activates the out-of-plane low-frequency mode CH_2 torsion, wagging, and in-plane HCH anti-symmetric bending scissoring, as well as the C-H stretching. Unlike the other two planar CIs, the C-C stretching is not activated in the twisted CI.

Table 4.4. Fraction of trajectories that reach D_0 through a hop from D_1 via the three D_1/D_0 CIs

Hydrogen Deuterium			
	Planar Type I	Planar Type II	Twisted
Ensemble D3	68.37	6.05	25.58
	70.00	4.29	25.51
Ensemble D2	81.48	9.43	9.09
	96.12	3.07	0.65
Ensemble D1	77.46	21.13	1.41
	86.35	13.37	0.28

4.3. Explanation of the isotope effect on the oscillations of the experimental yields

The SH non-adiabatic dynamics reveal that the two isotopomers, $C_2H_4^+$ and $C_2D_4^+$, follow distinct relaxation pathways through the network of CIs from the excited states to the ground state D_0 (Figure 4.4).

The nuclear relaxation is influenced by the passage of the wave packet through both the planar I and the twisted D_1/D_0 conical intersections, which constrain the geometric distribution in D_0 . The planar I CI favors the three-photon resonant re-excitation mechanism, altering the relative dissociation yields and giving rise to the observed oscillations (Figure 4.1). This occurs by activating the CC stretching and HCCH torsion modes, which, in turn, control the probability of re-excitation to D_3 and modulate the dissociation yields.

Since the twisted CI is located farther from the initial Wigner distribution in the configurational space than the planar CI, the wave packet in deuterated ethylene preferentially follows the pathway

funneled by the planar I CI. This results in a pronounced isotopic effect in the dissociation yields, with clear oscillations observed in the deuterated case but low amplitude oscillations that are barely discernable in the hydrogenated case (see Figure 4.1).

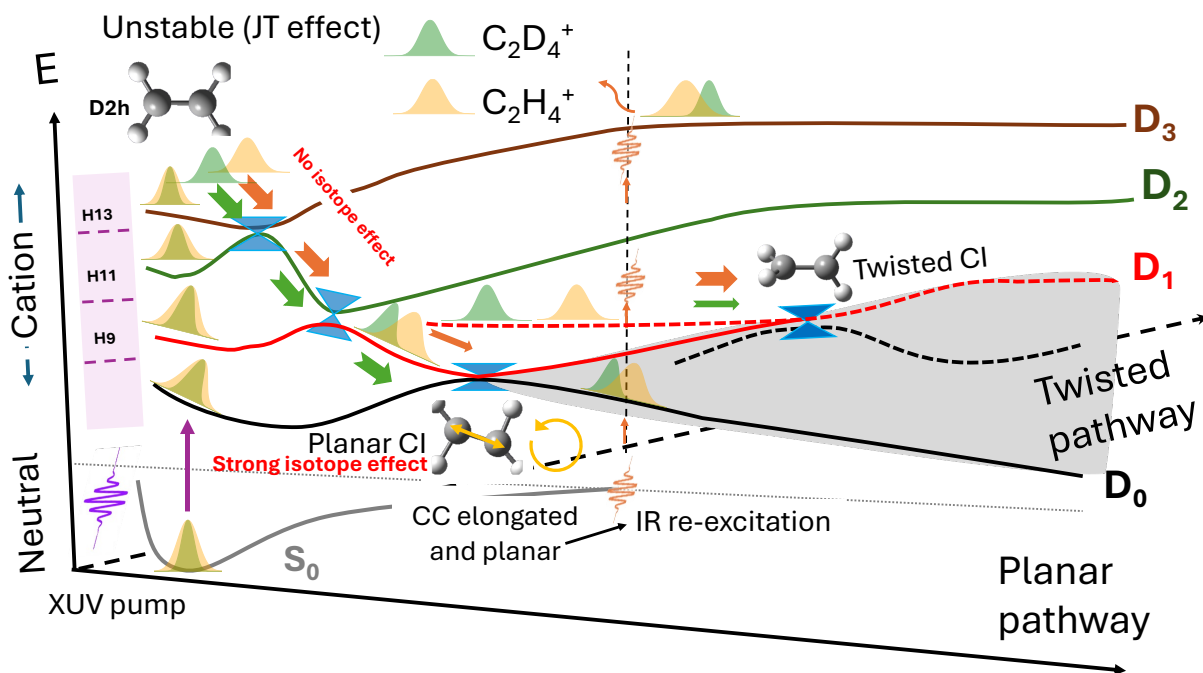


Figure 4.4. Cartoon illustrating the two relaxation paths through the network of CIs between the four lowest electronic states (D_0 , D_1 , D_2 , and D_3) of the ethylene cation for $C_2H_4^+$ (orange wavepacket) and $C_2D_4^+$ (green wavepacket). Also shown is the neutral's ground electron state, S_0 , which is suddenly ionized by the EUV pulse (violet on the left). The thickness of the green and orange arrows indicates the difference in the fraction of trajectories that follow a given pathway. The relaxation pathway of the two isotopomers differs on D_1 , where a larger fraction of the heavier $C_2D_4^+$ relaxes to D_0 through the planar I CI than for $C_2H_4^+$, see Table 4.4. The difference in the relaxation pathways, together with the isotope effect on the frequencies of the torsion and scissoring modes on D_0 , explains the oscillations observed experimentally in the ions yields.

There are two isotope effects on the dynamics, which affect the fraction of the photoionized population that is present or has relaxed to D_0 from the higher excited states and is available for re-excitation by the IR probe pulse. The first isotope effect is the slowdown of the motion of the wave packets of the deuterated species due to the mass effect, which alters the relaxation paths through the network of the CIs. For the D_1 ensemble, this favors the relaxation through the planar I CI. The geometries of the $C_2D_4^+$ cation on D_0 resulting from short times D_1/D_0 hops are planar and have a C-C bond length elongated to ~ 1.4 to ~ 1.6 Å on the average (see Figure 4.5(a)), which favors a large transition dipole from D_0 to D_3 compared to $C_2H_4^+$. A large value of the transition dipole also requires a bending angle of $\sim 120^\circ$, a condition that is satisfied for both isotopomers, see Figure 4.6.

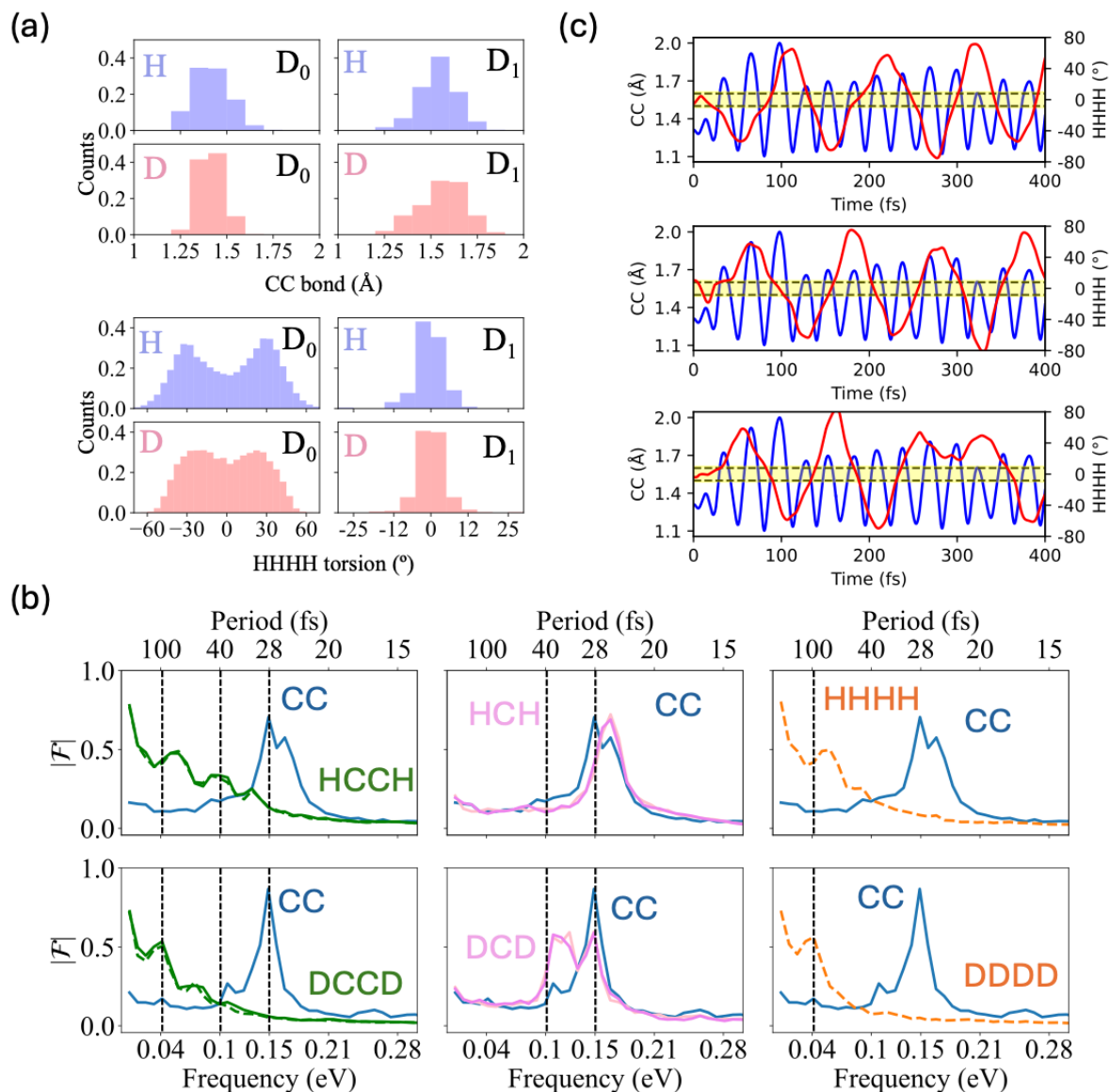


Figure 4.5: a) Histograms of the C-C bond length and HHHH dihedral angle for the Wigner distributions of initial conditions of the D_0 ensemble and after relaxation through the planar I CI in the first 10 fs of the SH dynamics for the D_1 ensemble. b) Average Fourier transform of the C-C bond length (blue), HCH angles (pink and violet), HCCH torsion angles (green full lines and dashes), and of HHHH torsion (dashed orange) for $C_2H_4^+$ (top) and $C_2D_4^+$ (bottom) computed for the trajectories of D_1 ensemble that relaxes on D_0 through the type I CI. c) correlation between the torsion and the C-C elongation in the range that favors a large D_0 to D_3 transition dipole (C-C in the range 1.55 to 1.6 Å, marked by dashed lines, and HCCH between -10 to 10 degrees highlighted in yellow) for three selected trajectories.

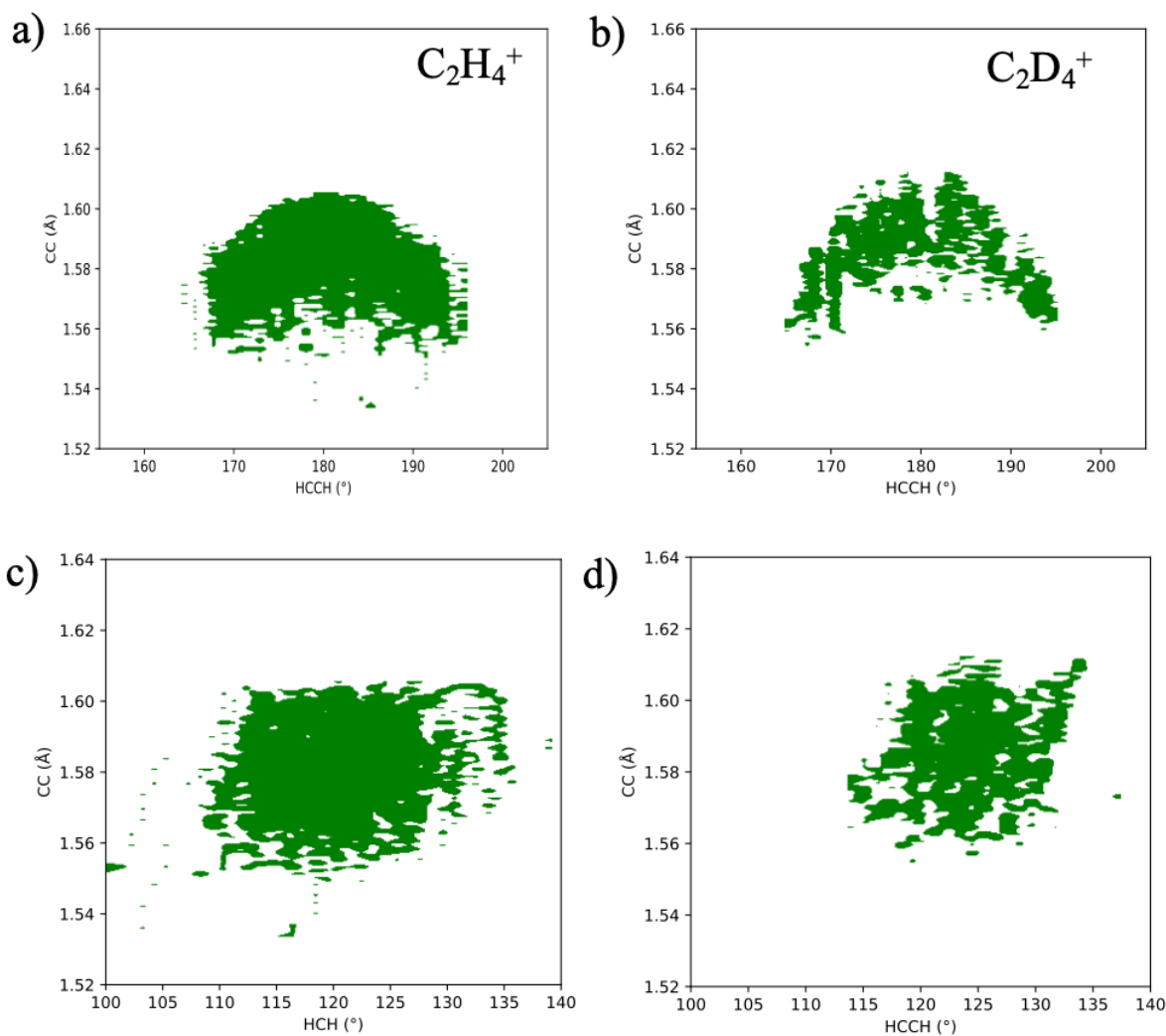


Figure 4.6: Heatmaps of the C-C elongation and HCCH angles values (a and b) and CC vs. HCH (c and d) on D_0 that corresponds to an energy difference that is 3 photons resonant with D_3 and a value of the transition dipole ≥ 1 a.u.

The second isotope effect involves the mass-dependent changes in the vibrational frequencies of the D_0 state (Figure 4.5b). In the case of $C_2D_4^+$, the isotope effect on the vibrational periods that involve a motion of the H/D atoms leads to almost identical periods for the C-C elongation and the antisymmetric scissoring DCD modes, which in addition, are commensurate with the excited states of the torsion mode. The coupling between these vibrational modes allows their simultaneous excitation resulting in combination bands, which do not occur for $C_2H_4^+$. The periods of these modes for the trajectories of the D_1 ensemble that relaxed to D_0 through the planar type I CI are computed by Fourier Transform (FT) of the C-C, HCH, HCCH, and HHHH coordinates plotted in Figure 4.5(b) for both isotopomers. The FTs of the C-C coordinate is shown in blue, that of the two HCH angles in pink and violet, of the two HCCH angles in green full and dashed lines and that of the HHHH angle in orange. For $C_2D_4^+$, bottom row in Figure 4.5(b), the computed periods of the C-C bond and of the antisymmetric scissoring DCD mode appear at ~ 28 fs, the symmetric scissoring DCD mode at ~ 38 fs and the DCCD torsion mode at ~ 100 fs. From the

bottom middle panel, one sees that C-C is strongly coupled to the two DCD modes. In addition, the C-C mode exhibits a small peak at 100 fs (marked by a vertical black dashed line in the bottom left and right panels of Figure 4.5(b)), indicating that the two modes are coupled. In C_2H_4^+ (top row of Figure 4.5(b)), the isotope effect on the period of the torsion mode (~ 70 fs) prevents an effective coupling between the torsion and the C-C mode, whose period is unaffected. As a result, as seen from the top left and right panels of Figure 4.5(b), there is no peak at 70 fs in the C-C mode. On the other hand, the periods of the two DCD scissoring modes are shifted to shorter values by the ~ 1.3 factor. The antisymmetric scissoring HCH mode has a period of ~ 21 fs, and the symmetric one is ~ 29 fs which leads to a strong coupling with the C-C mode. For both isotopomers, the broad peaks in the HCCH coordinate at ~ 45 -50 fs for C_2H_4^+ and at ~ 55 -60 fs for C_2D_4^+ correspond to the wagging modes.

In C_2D_4^+ , the computed period of 100 fs for the torsion mode implies that the ion is planar every half period, that is, every ~ 50 fs, which roughly corresponds to two vibrations of the C-C mode, as can be seen from Figure 4.53c) where the C-C distance is plotted in blue and the HHHH dihedral angle in red for three selected trajectories. Moreover, for the fraction of trajectories of the D_1 ensemble that relaxes to D_0 through the planar I CI, the C-C bond is elongated. Therefore, for C_2D_4^+ , a larger transition probability to D_3 occurs each time the C-C is elongated between 1.55 and 1.60 Å (marked in dashed lines in Figure 4.5c)) and the cation is planar (shaded in yellow), that is, every ~ 50 fs. On average, this correlation is present in 77 trajectories out of the 141 runs for the D_1 ensemble (55 %). The re-excitation to D_3 leads to a bleaching of the parent yield and a simultaneous increase in the fragment yields since fragmentation is favored by the higher excitation energy that is gained through the excitation to D_3 by the 3 IR photons.

In conclusion, by elucidating the enhanced oscillations observed in the relative fragmentation yields of C_2D_4^+ , [this work](#) sheds light on the physical origins of the isotope effect in the ultrafast relaxation process of the ethylene cation. The experimentally measured yields for the deuterated isotopomer exhibit pronounced oscillations (Figure 4.1) with a ~ 50 -fs period, which are not clearly discernable for the hydrogenated one. We show that the slower motion of the wave packet out the FC region of the heavier C_2D_4^+ for the population ionized to the D_1 electronic state favors the relaxation through the planar type I D_1/D_0 CI. This CI functions as both a geometrical and temporal funnel, transferring a substantial population to D_0 within the initial 10 fs of relaxation with elongated C-C bonds and planar geometries. In addition, in C_2D_4^+ , because of the isotope effect on the vibrational periods, the torsion mode is efficiently coupled to the C-C mode, and the cation is planar, with an elongated C-C bond every 50 fs, which corresponds to half the period of the torsion and two periods of the C-C elongation. As a result, the re-excitation to D_3 occurs every 50 fs, which explains the larger oscillations in the measured ion yields (Figure 4.1) as a function of the EUV-IR pump-probe delay. The periods of these two modes are not commensurate in C_2H_4^+ , which precludes the observation of large oscillations in the ion yields as a function of the EUV-IR pump-probe delay.

4.4. Summary of contributions

All authors contributed to writing the manuscript, analyzing the results, and developing and refining the ideas.

Manuel Cardosa Gutierrez performed the surface hopping and Born-Oppenheimer molecular dynamics (BOMD) simulations used to study the photorelaxation of the deuterated ethylene cation, using the same computational approach as in previous joint study between the two groups(1) on the hydrogenated one. He analyzed the trajectories of C₂D₄⁺ and those of the previous study on C₂H₄⁺ using various methods, including linear regression of population decay and Fourier transforms of time-dependent coordinates and molecular properties.

Matteo Lucchini, Mario Murari, Fabio Frassetto, Luca Poletto, and Mauro Nisoli conducted the experiments and processed the data collected from the measurements.

Manuel Cardosa and Françoise Remacle developed an explanation for the isotope effect observed time dependence of the ions measured from the dissociation of C₂D₄⁺ and C₂H₄⁺ using an IR probe pulse. Manuel Cardosa gathered evidence supporting the dominant role of the excited state D1 in the photorelaxation process in the case of C₂D₄⁺. He also characterized all the conical intersections (CIs) encountered by the surface hopping trajectory, with a particular focus on the planar I CI, which played a crucial role in the relaxation to the ground state for the deuterated species.

Manuel Cardosa analysis showed that, due to the slower motion of the C₂D₄⁺ wavepacket, most of the relaxation occurs through the planar I CI, while in C₂H₄⁺, a significant part relaxes through a different CI. He also demonstrated that the planar I CI constrains the geometries of the ground state to have an elongated C–C bond and activated torsion, conditions that favor a large transition dipole to excited state D3. This, in turn, enables a three-photon resonant re-excitation mechanism, induced by the IR probe pulse, which modulates the experimental yields for C₂D₄⁺. A faster dephasing precludes a clear observation of these oscillations in the case of the C₂H₄⁺ cation.

4.5. References

1. M. Lucchini *et al.*, Few-Femtosecond C₂H₄⁺ Internal Relaxation Dynamics Accessed by Selective Excitation. *J. Phys. Chem. Lett.* **13**, 11169-11175 (2022).
2. R. Stockbauer, M. G. Inghram, Threshold photoelectron–photoion coincidence mass spectrometric study of ethylene and ethylene-d₄. *The Journal of Chemical Physics* **62**, 4862-4870 (1975).
3. B. Joalland, T. Mori, T. J. Martínez, A. G. Suits, Photochemical Dynamics of Ethylene Cation C₂H₄⁺. *J. Phys. Chem. Lett.* **5**, 1467-1471 (2014).
4. S. Mai, P. Marquetand, L. González, Nonadiabatic dynamics: The SHARC approach. *WIREs Comput Mol Sci* **8**, e1370 (2018).
5. H.-J. Werner *et al.*, The Molpro quantum chemistry package. *The Journal of Chemical Physics* **152**, 144107 (2020).
6. H. J. Werner, P. J. Knowles, G. Knizia, F. R. Manby, M. Schütz, Molpro: a general-purpose quantum chemistry program package. *WIREs Comput Mol Sci* **2**, 242-253 (2012).
7. J. M. Millam, V. r. Bakken, W. Chen, W. L. Hase, H. B. Schlegel, *Ab initio* classical trajectories on the Born–Oppenheimer surface: Hessian-based integrators using fifth-order polynomial and rational function fits. *The Journal of Chemical Physics* **111**, 3800-3805 (1999).
8. M. J. Frisch *et al.* (Wallingford, CT, 2016).

9. J. Berkowitz, *Atomic and molecular photoabsorption: absolute partial cross sections*. (Elsevier, Amsterdam, 2015).
10. L. Fransén, T. Tran, S. Nandi, M. Vacher, Dissociation and Isomerization Following Ionization of Ethylene: Insights from Nonadiabatic Dynamics Simulations. *J. Phys. Chem. A* **128**, 1457-1465 (2024).

4.6. Publication: “Isotope effect on the few-femtosecond relaxation dynamics of the ethylene cation”

Isotope effect on the few-femtosecond relaxation dynamics of the ethylene cation

Matteo Lucchini^{1,2*}, Manuel Cardosa-Gutierrez^{3*}, Mario Murari¹, Fabio Frassetto⁴, Luca Poletto⁴, Mauro Nisoli^{1,2}, Françoise Remacle³

¹Department of Physics, Politecnico di Milano, 20133 Milano, Italy

²Institute for Photonics and Nanotechnologies, IFN-CNR, 20133 Milano, Italy

³Theoretical Physical Chemistry, UR MOLSYS, University of Liège, B4000 Liège, Belgium

⁴Institute for Photonics and Nanotechnologies, IFN-CNR, via Trasea 7, 35131 Padova, Italy

*Equal contribution

Abstract

Few-femtosecond extreme-ultraviolet (EUV) pulses with tunable energy are employed to initiate the Jahn-Teller structural rearrangement in the ethylene cation. We report on a combined experimental and theoretical investigation of an unusual isotope effect on the low energy competing H/D-loss and H₂/D₂-loss channels observed in the ultrafast dynamics induced by an EUV pump pulse and probed by an infrared (IR) pulse. The relative production yield of C₂D₄⁺, C₂D₃⁺, and C₂D₂⁺ exhibit pronounced oscillations with a period of ~50 fs as a function of the pump-probe delay, while the oscillatory patterns are less pronounced for C₂H₄⁺. By using surface hopping to model the non-adiabatic dynamics in the four lowest electronic states of the cation, we show that the enhanced oscillations in deuterated fragment yields arise from a synergy between the isotope effect on the wave packet relaxation through the network of conical intersections and on the vibrational frequencies of the cation.

Recent studies have renewed interest in the ultrafast relaxation and the dynamics of the structural Jahn-Teller rearrangement that follow the sudden ionization of ethylene (C_2H_4) neutral ground state to the lowest electronic states of its cation ($C_2H_4^+$)¹⁻⁶. This renewed focus is driven by significant advances in generating ultrashort extreme-ultraviolet (EUV) and infrared (IR) pulses, which allow researchers to capture time-resolved electronic and vibronic dynamics with unprecedented detail⁷⁻¹⁰. These ultrashort pulses have enabled direct observation of the intricate molecular motions that occur as the ethylene cation undergoes rapid structural rearrangement, illuminating the crucial roles of conical intersections (CIs) and vibronic couplings in guiding these ultrafast processes. Such insights provide a more detailed understanding of the mechanisms underlying electronic relaxation and molecular reconfiguration on femtosecond time scales. A comprehensive overview of foundational studies in this field can be found in Ref. ⁵. The ethylene cation serves as a model system for investigating electronic relaxation pathways, structural dynamics, and energy redistribution after ionization. Dynamics simulations indicate that excited $C_2H_4^+$ relaxes to the lowest electronic doublet state through CIs, which occur at both twisted and planar molecular geometries. These CIs facilitate distinct dissociation pathways, leading to H- and H₂-loss. Specifically, simulations suggest that twisted CIs inhibit the isomerization from ethylene to ethylidene, thereby favouring H-loss, while planar CIs along the H-migration coordinate promote ethylene-ethylidene isomerization, increasing the likelihood of H₂-loss.¹ EUV-pump and IR-probe schemes, which ionize neutral ethylene and then track the ensuing nuclear and electronic dynamics, have confirmed many of these mechanisms experimentally. The high time resolution of these methods has provided critical insights into the relationship between excitation energy, relaxation pathways, and fragment ion yields.

Extreme-ultraviolet time-resolved photoelectron spectroscopy has further expanded our understanding by examining isotope effects in these ultrafast relaxation dynamics. Experiments using ethylene-d₄ (C_2D_4) reveal notable isotope influences on the time scales and yields of fragmentation processes¹¹. Specifically, deuteration increases the time scale for internal conversion steps by a factor of approximately $\sqrt{2}$, consistent with theoretical predictions that account for the mass-dependent nature of nuclear motion. This delay in dynamics highlights the critical impact of isotopic substitution on the molecular relaxation pathways of ethylene cations.

In this work, we provide evidence for an unexpected isotope effect on charged fragmentation yields, utilizing an advanced few-femtosecond EUV-pump/IR-probe

experimental setup. Our results reveal new details on the time-dependent fragmentation and isomerization pathways in ethylene cation photochemistry, demonstrating that isotope substitution can significantly modulate both dissociation and isomerization processes on femtosecond time scales. This study contributes to a deeper understanding of the molecular-level mechanisms driving photochemical reactions in ethylene cations, with broader implications for interpreting isotope effects in other systems undergoing ultrafast nonadiabatic dynamics.

Briefly, the ethylene neutral ground state is ionized to the four lowest electronic states of the cation, D₀, D₁, D₂ and D₃, using ~10-fs EUV pulses produced by high-order harmonic generation (HHG) in a gas cell, driven by ~15-fs IR pulses with a central wavelength of about 800 nm. The low order harmonics (9th, 11th and 13th, hereafter indicated as H9, H11 and H13, respectively) are spectrally selected by employing a time-delay compensated monochromator¹²⁻¹⁴ (see Fig. S1 in the Supporting Information (SI)).

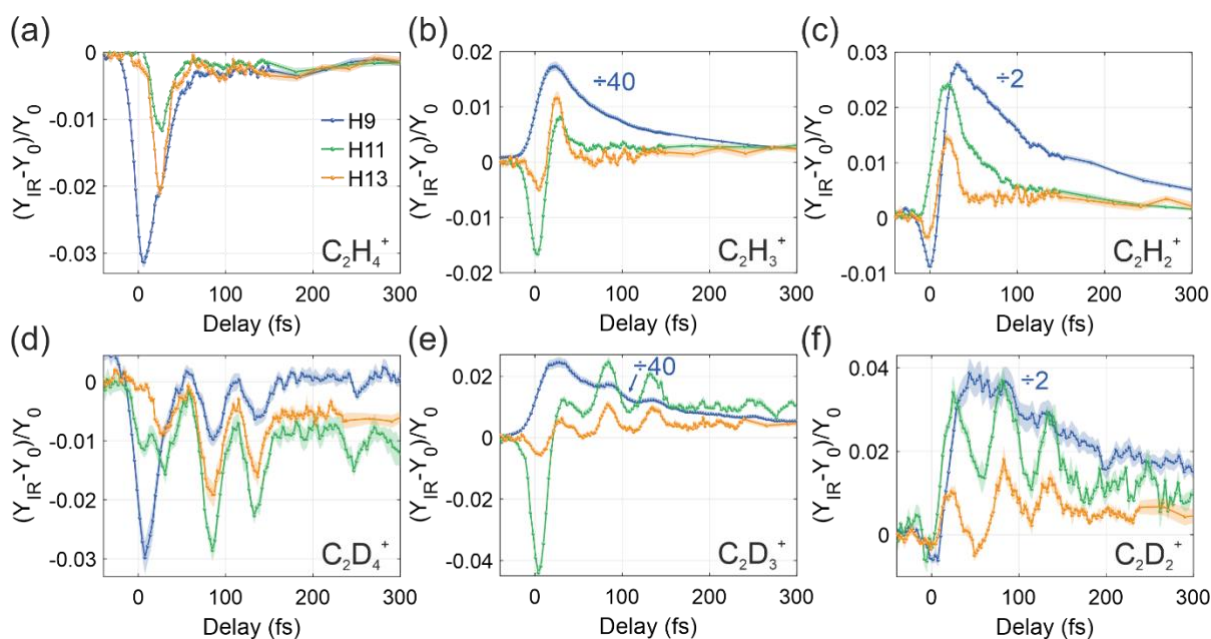


Figure 1: Relative yield as a function of the EUV-IR delay for the fragments (a) C₂H₄⁺, (b) C₂H₃⁺, and (c) C₂H₂⁺, obtained by ionizing ethylene with H9 (blue), H11 (green) and H13 (orange). The second row shows the results in case of ethylene-d₄ ionization: (d) C₂D₄⁺, (e) C₂D₃⁺, and (f) C₂D₂⁺. In all panels, the markers represent the average over 10 independent pump-probe measurements, while the shaded areas cover twice their standard deviation (error of the mean).

Figure 1 shows the differential ion yield, defined as the difference between the ion yield measured with and without the IR pulse, divided by the latter, for the first three heaviest fragments of ethylene (figs. 1(a)-(c)) and ethylene-d₄ (Figs. 1(d)-(f)). The deuterated fragments qualitatively agree with their related hydrogenated counterpart, besides clear amplitude

oscillations with a period of ~ 50 fs. Photoionization by H9 leaves the molecule mostly on the ground state of the cation, D_0 , with a smaller fraction on the first excited state, D_1 (see Table 1). The photoionization cross-sections are taken to be identical for the two isotopomers and were derived from the experimental data of Ref.¹⁵. The interaction with the IR pulse induces a bleaching of the parent ion, occurring near delay zero (i.e., when pump and probe pulses temporally overlap) for both isotopomers (compare the blue curves in Figs. 1(a) and 1(d)).

Table 1. Relative photoionization yields to the D_0 , D_1 and D_2/D_3 states of the ethylene cation derived from the experimental photoionization cross section reported in Ref. ¹⁵ and the harmonic spectra used in this work. The ionization yields of higher excited states are $\leq 1\%$ and have been neglected.

C₂H₄/C₂D₄	H9	H11	H13
D ₀	0.64	0.23	0.11
D ₁	0.35	0.52	0.28
D ₂ /D ₃	0.01	0.25	0.61

After excitation by H11 (green curves in Fig. 1) and H13 (orange curves in Fig. 1) the cation is left in a higher excited state (see Table 1) and the bleaching occurs at ~ 25 -fs delay time, where a shoulder is observed in $C_2H_4^+$ relative yield from H9 (Fig. 1(a), blue curve). In our previous study³ we have used dynamical surface hopping (SH) for ensembles of trajectories initially started on the ground cationic state and the first three excited states, followed by Born Oppenheimer Molecular Dynamics (BOMD) simulations once the population of the excited cationic states relaxed back to D_0 . We showed that the bleaching peak in the $C_2H_4^+$ yield is due to a re-excitation to D_3 of the population that relaxed to D_0 from higher states or that was ionized to D_0 by the IR probing pulse through a multiphoton process³ (see Fig. 2(a) for a cartoon of the relaxation paths). Re-excitation is favored when a notable fraction of the trajectories on D_0 adopt a geometry that corresponds to a large transition dipole and is three-photon resonant with D_3 . The bleaching peak for H11 and H13 ionization is delayed relative to

that for H9 ionization due to the ~ 20 fs needed for the population in the D_1 , D_2 , and D_3 states to relax to D_0 , establishing favorable conditions for re-excitation.

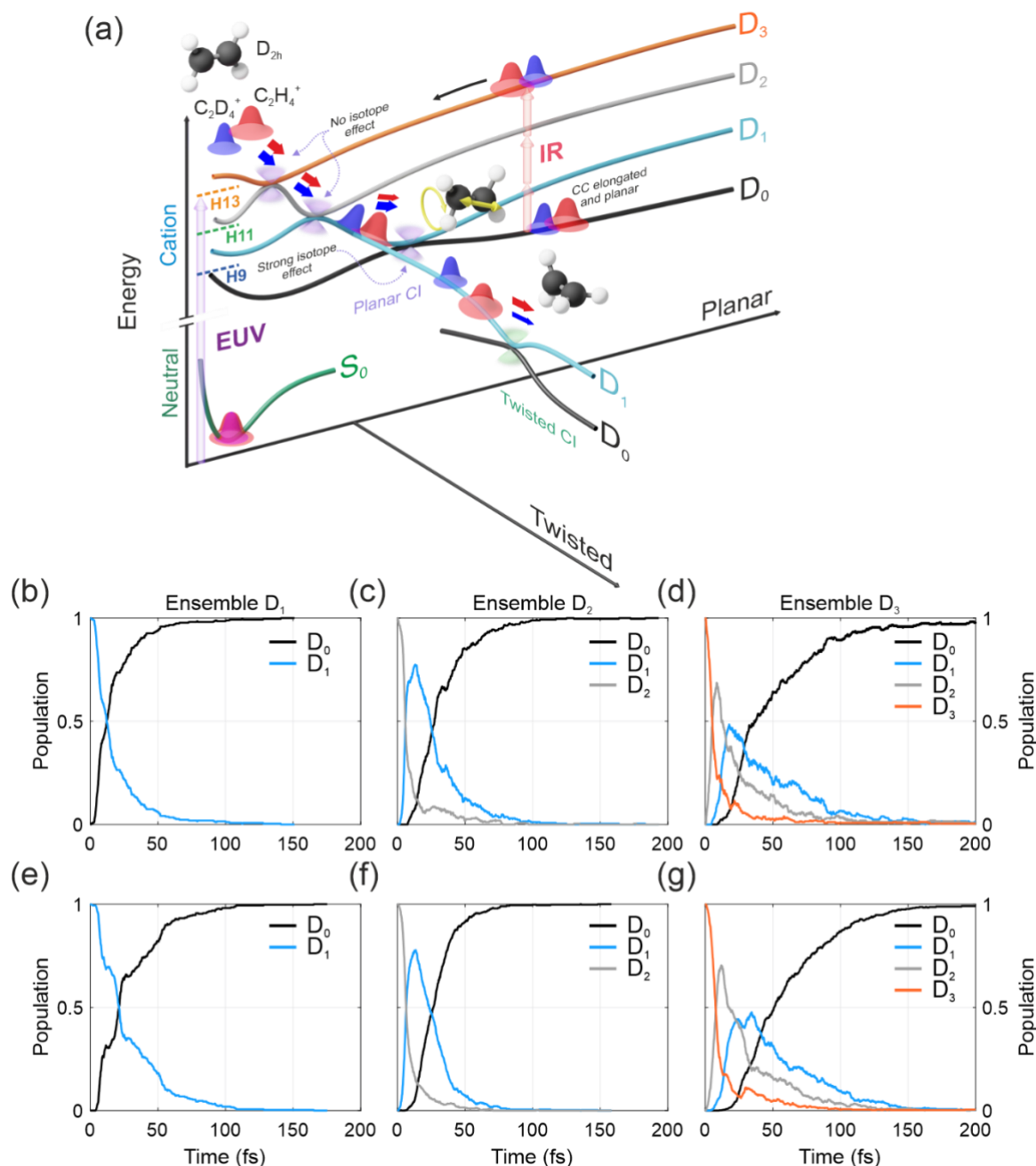


Figure 2: (a) Cartoon of the relaxation paths through the network of CIs between the 4 lowest electronic states, D_0 (black), D_1 (light blue), D_2 (grey) and D_3 (orange), of the ethylene cation for $C_2H_4^+$ (red wavepacket) and $C_2D_4^+$ (blue wavepacket). Also shown is the ground electron state, S_0 green curve, of the neutral which is suddenly ionized by the EUV pulse (violet arrow on the left). The thickness of the red and blue arrows indicates the difference in the fraction of trajectories that follows a given pathway. The relaxation pathway of the two isotopomers differ on D_1 , where a larger fraction of the heavier $C_2D_4^+$ relaxes to D_0 through the planar I CI (violet cone) than for $C_2H_4^+$, see Table 2. The green cone indicates the twisted CI between D_1 and D_0 . Molecular geometries are given after excitation (D_{2h}) or at the highlighted D_0/D_1 CIs. For the case of the planar I CI, the yellow arrows indicate the torsional motion and CC stretching that are activated at the CI geometry. Finally, the red vertical arrows on the left picture the 3-photon re-excitation process discussed in Ref. ³. (b)-(d), Population dynamics for the hydrogenated molecule corresponding to initial excitation to D_1 , D_2 and D_3 . (e)-(g) same as (b)-(d) but for the deuterated molecule.

The same mechanism is responsible for the delayed shoulder observed in Fig. 1(a), which is attributed to the re-excitation to D_3 of the population initially excited to D_1 by H9 and that later

relaxes to D_0 .³ The short computed lifetime for D_1 (~ 12 fs, see Table S2) in $C_2H_4^+$ supports this argument and is in agreement with similar semiclassical studies.^{1-2, 4-5}

The shoulder is almost absent for the $C_2D_4^+$ H9 yield (Fig. 1(d), blue curve) because of the mass effect on the rate of motion of the wave packet on D_1 for the heavier isotopomer which leads to a longer computed relaxation lifetime of 26 fs (Table S2) for the D_1 state of $C_2D_4^+$. For the H11 and H13 ionizations of C_2D_4 (green and orange curves in Fig. 1(d)), the delay of the bleaching is comparable to what observed in C_2H_4 . SH non-adiabatic modeling of the population dynamics (see SI, section S2), shows that the two isotopomers follow different relaxation paths through the network of CIs from the excited states to the ground state D_0 , qualitatively shown in the cartoon of Fig. 2(a). Figures 2(b)-(g) show the calculated temporal evolution of the electronic state populations following initial excitation to D_1 (Figs. 2(b) and (e)), D_2 (Figs. 2(c) and (f)) and D_3 (Figs. 2(d) and (g)). The mass isotope effect slows the motion of $C_2D_4^+$ and delays the relaxation from D_1 to D_0 , as shown in the computed decay curve for the D_1 ensemble (compare Figs. 2(b) and (e)). In contrast, there is only a small delay in the relaxation of the D_2 and D_3 ensembles (see Figs. 2(c)-(d) and compare with Figs. 2(f)-(g), respectively) resulting in similar computed lifetimes of these two higher excited states (see Table S2).

Beyond the isotope effect on the timing of the bleaching peak of the parent and the correlated first maximum in the other fragments in Fig. 1, there is a pronounced isotope effect on the dynamics of the fragmentation yields. The temporal evolution of the relative ion yield of the deuterated species (displayed in Figs. 1(d)-(f)) shows large oscillations with a period of ~ 50 fs (with peaks at ~ 85 fs and ~ 135 fs). In contrast, in the ion yields of the hydrogenated species (Figs. 1(a)-(c)) the oscillations are much weaker, and visible only in the parent ion³, with a comparable ~ 50 -fs period. In $C_2D_4^+$ the oscillations dephase after ~ 150 fs and exhibit a revival after ~ 250 fs for the H11 and H13 ionization (see Fig. S3). A previously experimental-theoretical study of the isotope effect on the fragmentation of the ethylene cation using a higher energy EUV attosecond pulse train and a longer IR pulse probe⁶, focused on monitoring the yields in higher energy fragments (H^+/D^+ , CH_2^+/CD_2^+). Faster dynamics was reported for $C_2H_4^+$, but no oscillations were resolved in the fragmentation yields.

In this Letter, we demonstrate that the large oscillations in the fragment yield in the case of ethylene-d₄ originate from the synergy between two isotope effects on the dynamics, which affect the fraction of the photoionized population that is present or has relaxed to D_0 from the higher excited states and is available for re-excitation by the IR pulse. The first isotope effect is the slowdown of the motion of the wave packets of the deuterated species due to the

mass effect, which alters the relaxation paths through the network of the CIs between the electronic states of the cation (see Fig. 2(a)). The second effect involves the mass-dependent changes in the vibrational frequencies of the D_0 state which leads to stronger coupling between the CC stretching and the torsion and scissoring modes in the vibrationally excited $C_2D_4^+$ cation, which control the magnitude of the transition dipole from D_0 to D_3 .

Upon sudden ionization of the neutral ground electronic state in its equilibrium geometry, due to the Jahn-Teller effect, the ethylene cation is produced in an unstable planar D_{2h} geometry which initiates nuclear motion on the four lowest excited electronic states of the cation, D_0 , D_1 , D_2 and D_3 , that can be populated by EUV photoionization in this study (see Fig. 2(a)). The nuclear motion in the excited states triggers ultrafast electronic relaxation in ~ 50 fs through a network of planar and twisted CIs, which leads to fragmentations and isomerizations on the ground electronic state D_0 . Several theoretical studies^{1-6, 16-20} have already identified the essential of the excited state dynamics for the four lowest states of the cation. The CIs seams between the excited states act like geometrical funnels that constrain the geometry of the cation when it relaxes from a higher excited state to a lower one, thereby activating specific nuclear motions. The CIs sampled by the SH trajectories at the level of electronic structure that we use agree with recent previous works^{1, 5}. We provide a detailed discussion about the characteristics of the minimum energy CIs (MECIs) in Section S4.1 of the SI.

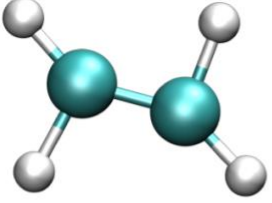
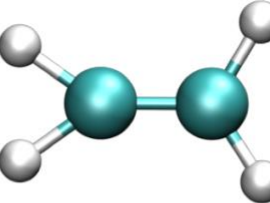
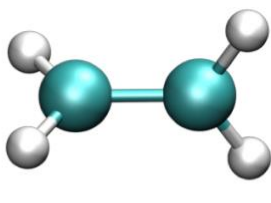
In brief, the D_2/D_3 and D_2/D_1 relaxations occur through the seams of two peaked MECIs with planar geometries and elongated C-C bonds ($\sim 1.4\text{\AA}$) (marked with violet cones in Fig. 2(a), see also Section S4.1 of the SI). These geometries are close to the planar geometry of the neutral ground state of the Franck-Condon (FC) region which explains why the relaxation is ultrafast and not subject to isotope effect. The D_3/D_2 transfer occurs within 5 fs for both isotopomers (Figs. 2(d) and 2(g)). The population transfer from D_2 to D_1 , instead, happens within 5 to 10 fs for both initial population on D_2 (Figs. 2(c) and 2(f)), and on D_3 (Figs. 2(d) and 2(g)). In this latter case we observe an additional shoulder at about 15 fs. Overall, for the two isotopomers, the majority of the population that reaches D_1 within the first 10 fs has essentially planar geometries with activated C-C bonds and H-C-H angles. The distributions of CC distances, HCH and HCCH angles of the trajectories that reach D_1 from D_2 and D_3 are therefore different from the Wigner distributions of initial conditions on D_1 and on D_0 (see Fig. S5).

As established in previous works,^{1, 5} three CIs are involved in the D_1/D_0 relaxation: two planar and a twisted one. The planar ones correspond to the two CIs identified in Ref.¹. We call

them planar I and II, respectively. The planar I MECI (violet cones in Fig. 2(a) between D_1 and D_0) is located 2.45 eV above the energy of the planar, D_{2h} , D_0 cation (see Table S3). It has a distorted geometry with modified HCH angles and a slightly compressed C-C bond (1.28 Å). It plays a major role in the relaxation dynamics to D_0 for both isotopomers (see Table 2). The second MECI, planar II (not shown in Fig. 2(a)), is slightly higher in energy (2.56 eV, Table S3) and does not play a significant role in the relaxation dynamics sampled by the trajectories. Both planar D_1/D_0 CIs are sloped and activate C-C elongation and CH modes as the D_3/D_2 and D_2/D_1 ones, and in addition to low frequency, out-of-plane motions: the CH_2 torsion, wagging, and HCH in plane scissoring modes (see SI Section S4.1). Their geometries (see the molecular cartoon in Fig. 2(a) for planar I) differ more from the planar geometry of the neutral ground state than the D_3/D_2 and the D_2/D_1 MECIs. As a result, the initial decay of the D_1 population to D_0 in Figs. 2(b) and (e) is slower than that of the D_2 and D_3 populations to D_1 , see Figs. 2(c)-(f).

The third major MECI playing a role in the D_1/D_0 relaxation dynamics for the energy range of the three ionization energies discussed here has a twisted MECI geometry with a torsion angle of 90° as previously reported (marked with green cones in Fig. 2(a)).^{1, 5, 16-17} This CI is lower in energy than the two planar MECI (1.57 eV above the planar D_{2h} geometry of D_0 , Table S3) and activates the out-of-plane low frequency mode CH_2 torsion, wagging, and in plane HCH anti-symmetric bending scissoring, as well as the C-H stretching. Unlike the other two planar CIs, the C-C stretching is not activated in the twisted CI.

Table 2. Fraction of trajectories that reach D_0 through a hop from D_1 via the three D_1/D_0 CIs (see Fig. S2 for the distribution in time of the last D_1/D_0 hop for the three ensembles of initial conditions).

			
	Planar Type I	Planar Type II	Twisted
Hydrogen	68.37	6.05	25.58
	70.00	4.29	25.51
Deuterium	81.48	9.43	9.09
	96.12	3.07	0.65
Ensemble D1	77.46	21.13	1.41
	86.35	13.37	0.28

The two planar CIs dominate the relaxation from D_1 to D_0 for the D_1 and D_2 ensembles of initial conditions for both isotopomers (see Table 2). The major channel for the D_1/D_0 relaxation is the planar I CI. Compared to $C_2H_4^+$, this channel contributes more to the relaxation to D_0 in the heavier $C_2D_4^+$ because the seams of the planar I MECI, which is sloped, are closer in configuration space to the FC region. For the D_1 ensemble, this isotope mass effect leads to a longer relaxation time, 21.4 fs for $C_2D_4^+$ vs 12.3 fs for $C_2H_4^+$ (see Table S2). The amount of relaxation of the D_1 ensemble through the twisted CI is negligible, $\sim 1\%$ for $C_2H_4^+$ and less than 1% for $C_2D_4^+$. For the D_2 ensemble, for $C_2H_4^+$ the fraction that relaxes through the twisted D_1/D_0 CI reaches 9% and is comparable to the fraction going through the planar II D_1/D_0 CI, while for $C_2D_4^+$ because of the isotope mass effect, these fractions reduce to 3.1 and 0.6% respectively. In the deuterated molecules, this makes the planar I CI the overwhelming channel ($>95\%$) for relaxation for the D_2 ensemble. For the D_3 ensemble, because of the higher excitation energy, we observe a significant rise in the fraction of trajectories that relax through the twisted D_1/D_0 CI for both isotopomers ($\sim 25\%$). Nevertheless, relaxation through the planar I CI remains dominant ($\sim 70\%$ for $C_2H_4^+$ and $C_2D_4^+$).

The geometrical constraints imposed by the relaxation through CIs lead to specific distributions of C-C distances, and HCH and HHHH angles on D_0 for the D_1 , D_2 and D_3 ensembles of initial conditions (see Fig. S5), which are in turn different from their Wigner distributions on D_0 . The Wigner distributions on D_0 reflect the mass isotope effect on the vibrational motion leading to narrower distributions for the deuterated species. The Wigner distributions of CC distance (see Fig. 3(a)) and HCH angles on D_0 are narrower than the distributions resulting from the higher electronic states which are centered on larger mean values. The major difference however is seen in the torsion mode, whose Wigner distribution for the D_0 ensemble is peaked at $\sim \pm 23^\circ$, the values of the twisting angle in the equilibrium geometry (see left panel of Fig. 3(b)). Instead, the distributions of the torsion angle on D_0 are centered around 0° for the ensembles of trajectories initiated on excited electronic states (see right panel of Fig. 3(b)), as a result of the planarity constraint imposed by the D_1/D_0 type I CI and the D_2/D_3 and D_1/D_2 ones. Note that for the D_1 ensemble the distribution of the CC distance peaks at higher value for the $C_2D_4^+$ than for $C_2H_4^+$.

We now examine the origins of the isotope effect leading to the large amplitude oscillations observed in the experimental relative yields of $C_2D_4^+$ (Fig. 1(d)), $C_2D_3^+$ (Fig. 1(e)) and $C_2D_2^+$ (Fig. 1(f)). As discussed above, the reason for the first bleaching peak in the parent yields, accompanied by a maximum in the yield of the other fragments, is common to both C_2D_4 and C_2H_4 , and due to a 3-photon re-excitation process from D_0 to D_3 initiated by the IR

pulse (red arrows in Fig. 2(a)).³ After the first bleaching peak, the presence of the oscillations in the yields with a period of ~ 50 fs in Figs. 1(d), (e) and (f) for the deuterated cations results from two isotope effects that primarily affect the fraction that was ionized to D_1 . This fraction contributes 35% for the H9 ionization, 52% for the H11 and 28% for the H13 one (Table 1). For the D_1 ensemble, the slower motion of the $C_2D_4^+$ cation due to the mass isotope effect favors the relaxation through the planar I CI. The geometries of the $C_2D_4^+$ cation on D_0 resulting from short times D_1/D_0 hops are planar and have a C-C bond length elongated to ~ 1.4 to ~ 1.6 Å on the average (see Fig. 3(a)), which favors a large transition dipole from D_0 to D_3 (see Fig. S6) compared to $C_2H_4^+$.

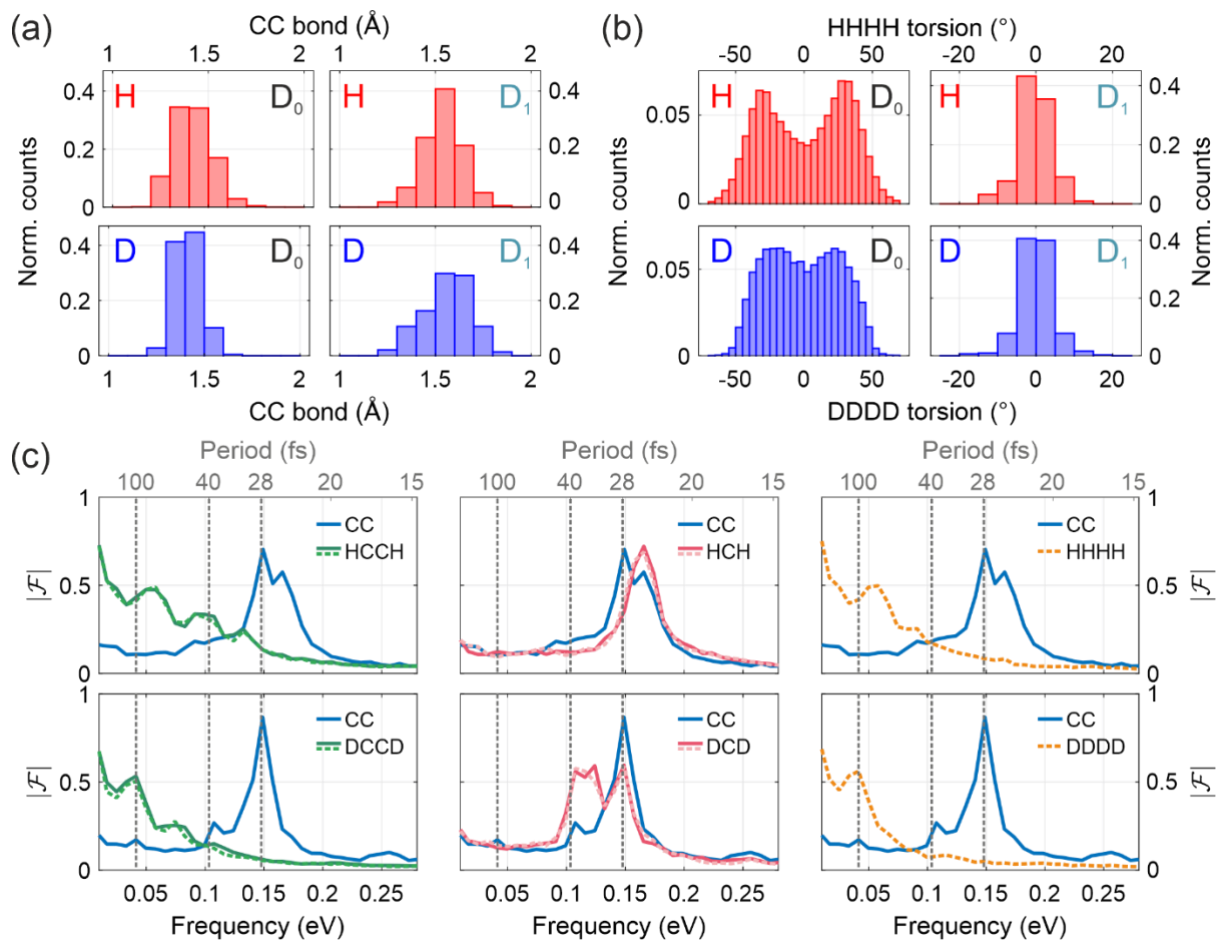


Figure 3: a) Histograms of the C-C bond length for ethylene (red, upper row) and ethylene-d₄ (blue, lower row). The left column shows the results for the Wigner distributions of initial conditions of the D_0 ensemble. The right column shows the distribution after relaxation through the planar I CI in the first 10 fs of the SH dynamics for the D_1 ensemble. b) Same as in a), but for the HHHH (red) and DDDD (blue) angles. Both in a) and b) the number of counts is normalized by the total number of considered trajectories. c) Average Fourier transform of the C-C bond length (blue), HCCH torsion angles (dashed-light and solid-dark green), HCH angles (dashed-light and solid-dark pink), and of HHHH torsion (dashed orange) for $C_2H_4^+$ (top) and $C_2D_4^+$ (bottom) computed for the trajectories of D_1 ensemble that relax on D_0 through the type I CI.

A large value of the transition dipole also requires a bending angle of $\sim 120^\circ$, a condition that is satisfied for both isotopomers (see Fig. S6). The second isotope effect is on the vibrational

periods. In the case of $C_2D_4^+$, the isotope effect on the vibrational periods that involve a motion of the D atoms, leads to almost identical periods for the C-C elongation and the antisymmetric scissoring DCD modes, which in addition are commensurate with the excited states of torsion mode. The coupling between these modes results in combination bands,¹⁸⁻¹⁹ which do not occur for $C_2H_4^+$. The periods of these modes for the trajectories of the D_1 ensemble that relaxed to D_0 through the planar type I CI are computed by Fourier Transform (FT) of the C-C, HCH (DCD), HCCH (DCCD) and HHHH (DDDD) coordinates²¹. The average amplitudes of the FTs are shown in Fig. 3(c) for the two isotopomers. The computed periods are in good agreement with the ones computed at the BOMD level of electronic structure for the equilibrium geometry of D_0 , see Table S4 of the SI. For $C_2D_4^+$, bottom row in Fig. 3(c), the computed periods of the C-C bond and of the antisymmetric scissoring DCD mode appear at ~ 28 fs, the symmetric scissoring DCD mode at ~ 38 fs and the DCCD torsion mode at ~ 100 fs. From the bottom middle panel, one sees that C-C is strongly coupled to the two DCD modes. In addition, the C-C mode exhibits a small peak at 100 fs (marked by a vertical black dashed line in the bottom left and right panels of Fig. 3(c)) which indicates that the two modes are coupled. In $C_2H_4^+$ (top row of Fig. 3(c)) the isotope effect on the period of the torsion mode (~ 70 fs) prevents an effective coupling between the torsion and the C-C mode, whose period is unaffected. As a result, as seen from the top left and right panels of Fig. 3(c), there is no peak at 70 fs in the C-C mode. On the other hand, the periods of the two DCD scissoring modes are shifted to shorter values by a factor of ~ 1.3 . The antisymmetric scissoring HCH mode has a period of ~ 21 fs and the symmetric one ~ 29 fs which leads to a strong coupling with the C-C mode. For both isotopomers, the broad peaks in the HCCH coordinate at $\sim 45-50$ fs for $C_2H_4^+$ and at $\sim 55-60$ fs for $C_2D_4^+$ correspond to the wagging modes.

In $C_2D_4^+$, the computed period of ~ 100 fs for the torsion mode implies that the ion is planar every half period, that is, every ~ 50 fs, which roughly corresponds to two vibrations of the C-C mode. Moreover, for the fraction of trajectories of the D_1 ensemble that relaxes to D_0 through the planar I CI, the C-C bond is elongated. Therefore, for $C_2D_4^+$, a larger transition probability to D_3 occurs each time the C-C is elongated between 1.55 and 1.60 Å and the cation is planar that is every ~ 50 fs. On average, this correlation is present in 77 trajectories out of the 141 runs for the D_1 ensemble (55 %). The re-excitation to D_3 leads to a bleaching of the parent yield and a simultaneous increase in the fragment yields since fragmentation is favored by the higher excitation energy that is gained through the excitation to D_3 by the 3 IR photon.

Figure 4 shows, as a function of time, the active fraction of trajectories on D_0 that relax from D_1 through the planar CI I with planar geometry (within $\pm 10^\circ$) and with a C-C bond between 1.4 and 1.6 Å, normalized to the total number of trajectories run on each electronic state. For $C_2H_4^+$ (shown in Fig. 4(a)), the calculated active fraction shows no clear periodic maxima beyond the bleaching peak at ~ 20 fs. In contrast, $C_2D_4^+$ (shown in Fig. 4(b)) exhibits peaks at around 35.8 fs, 85 fs and 135 fs, closely matching the timing of the maxima observed in the experimental yields in Figs. 1(d)-(f). The reason is the isotope effect on the vibrational frequencies, which precludes an efficient coupling between the CC and the torsion modes. In addition, the shorter periods of the $C_2H_4^+$ ion induce a faster dephasing between the CC and the torsion modes and the other vibrational modes.

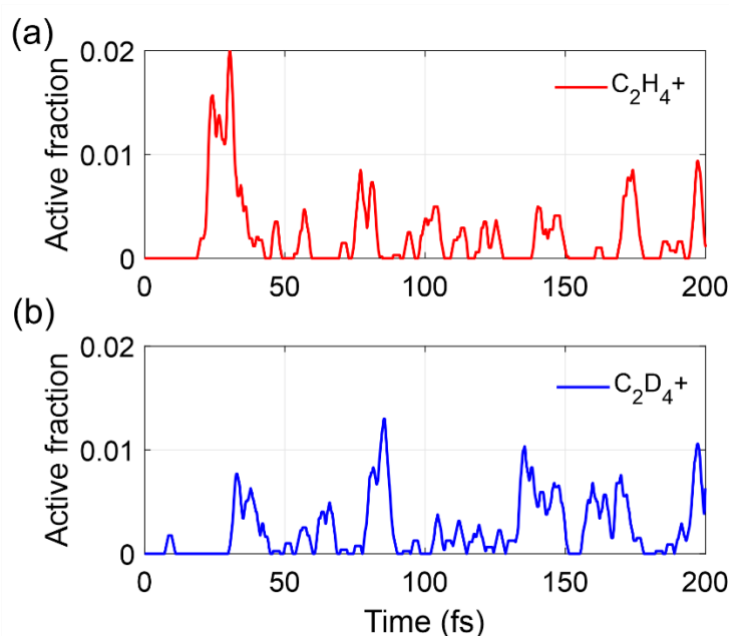


Figure 4: Active fraction of trajectories on D_0 that relax from D_1 through the planar I CI with geometries planar, within $\pm 10^\circ$, and with a CC bond in the range [1.55-1.60] Å that can be re-excited to D_3 for $C_2H_4^+$ (red, panel a)) and for $C_2D_4^+$ (blue, panel b)). The continuous thick curves are the result of a mobile average over 25 time points.

In conclusion, by elucidating the enhanced oscillations observed in the relative fragmentation yields of $C_2D_4^+$ our work sheds light on the physical origins of the isotope effect in the ultrafast relaxation process of a prototypical molecular cation. The experimentally measured yields for the deuterated isotopomer exhibit pronounced oscillations with a ~ 50 -fs period which are not clearly discernable for the hydrogenated one. We show that the slower motion of the wave packet out of the FC region of the heavier $C_2D_4^+$ for the population ionized to the D_1 electronic state favors the relaxation through the planar type I D_1/D_0 CI. This CI functions as both a geometrical and temporal funnel, transferring a substantial population to D_0 within the initial 10 fs of relaxation with elongated C-C bonds and planar geometries. In addition, in $C_2D_4^+$, because of the isotope effect on the vibrational periods, the torsion mode is

efficiently coupled to the C-C mode and the cation is planar, with an elongated C-C bond every 50 fs, which corresponds to half the period of the torsion and two periods of the C-C elongation. As a result, the re-excitation to D₃ occurs every 50 fs which explains the larger oscillations in the measured ion yields as a function of the EUV-IR pump-probe delay. The periods of these two modes are not commensurate in C₂H₄⁺ which precludes the observation of large oscillations in the ion yields as a function of the EUV-IR pump probe delay.

Our results show that pump-probe scheme based on few-fs tunable EUV radiation in combination with few-fs IR pulses and isotope substitution, provide a fine probe of the geometrical and temporal constraints that the ultrafast relaxation through a network of CIs between excited electronic states imposes on the vibrational motion on the ground electronic state. Our results pave the way for exploiting these constraints for better controlling the reaction outcomes.

Acknowledgments

This project has received funding from the European Research Council (ERC): ERC Synergy grant agreement no. 951224, TOMATTO. FR and MCG acknowledge the support of the Fonds National de la Recherche (F.R.S.-FNRS, Belgium), #T0205.20, and of the action of concerted research MECHANOCHEM (ARC 19/23-20, ULiege). Computational resources have been provided by the Consortium des Equipements de Calcul Intensif (CECI), funded by the F.R.S.-FNRS under Grant # 2.5020.11 The authors thank the COST action ATTOCHEM (CA18222).

References

1. Joalland, B.; Mori, T.; Martínez, T. J.; Suits, A. G., Photochemical Dynamics of Ethylene Cation C₂H₄⁺. *J. Phys. Chem. Lett.* **2014**, *5*, 1467-1471.
2. Ludwig, A.; Liberatore, E.; Herrmann, J.; Kasmi, L.; López-Tarifa, P.; Gallmann, L.; Rothlisberger, U.; Keller, U.; Lucchini, M., Ultrafast Relaxation Dynamics of the Ethylene Cation C₂H₄⁺. *J. Phys. Chem. Lett.* **2016**, *7*, 1901-1906.
3. Lucchini, M.; Mignolet, B.; Murari, M.; Gonçalves, C. E. M.; Lucarelli, G. D.; Frassetto, F.; Poletto, L.; Remacle, F.; Nisoli, M., Few-Femtosecond C₂H₄⁺ Internal Relaxation Dynamics Accessed by Selective Excitation. *J. Phys. Chem. Lett.* **2022**, *13*, 11169-11175.
4. Zinchenko, K. S.; Ardana-Lamas, F.; Seidu, I.; Neville, S. P.; van der Veen, J.; Lanfaloni, V. U.; Schuurman, M. S.; Wörner, H. J., Sub-7-Femtosecond Conical-Intersection Dynamics Probed at the Carbon K-Edge. *Science* **2021**, *371*, 489.
5. Fransén, L.; Tran, T.; Nandi, S.; Vacher, M., Dissociation and Isomerization Following Ionization of Ethylene: Insights from Nonadiabatic Dynamics Simulations. *J. Phys. Chem. A* **2024**, *128*, 1457-1465.

6. Vacher, M.; Boyer, A.; Loriot, V.; Lépine, F.; Nandi, S., Few-Femtosecond Isotope Effect in Polyatomic Molecules Ionized by Extreme Ultraviolet Attosecond Pulse Trains. *J. Phys. Chem. A* **2022**, *126*, 5692-5701.
7. Krausz, F.; Ivanov, M., Attosecond Physics. *Rev. Mod. Phys.* **2009**, *81*, 163-234.
8. Nisoli, M.; Decleva, P.; Calegari, F.; Palacios, A.; Martín, F., Attosecond Electron Dynamics in Molecules. *Chem. Rev.* **2017**, *117*, 10760-10825.
9. Borrego-Varillas, R.; Lucchini, M.; Nisoli, M., Attosecond Spectroscopy for the Investigation of Ultrafast Dynamics in Atomic, Molecular and Solid-State Physics. *Rep. Prog. Phys.* **2022**, *85*, 066401.
10. Merritt, I. C. D.; Jacquemin, D.; Vacher, M., Attochemistry: Is Controlling Electrons the Future of Photochemistry? *J. Phys. Chem. Lett.* **2021**, *12*, 8404-8415.
11. Boyer, A.; Humeniuk, A.; Karashima, S.; Suzuki, T., Deuterium Isotope Effect on Internal Conversion of Ethylene Studied by Time-Resolved Photoelectron Spectroscopy. *J. Phys. Chem. A* **2024**, *128*, 7068-7072.
12. Lucchini, M.; Lucarelli, G. D.; Murari, M.; Trabattoni, A.; Fabris, N.; Frassetto, F.; De Silvestri, S.; Poletto, L.; Nisoli, M., Few-Femtosecond Extreme-Ultraviolet Pulses Fully Reconstructed by a Ptychographic Technique. *Opt. Express* **2018**, *26*, 6771-6784.
13. Poletto, L.; Villorresi, P.; Frassetto, F.; Calegari, F.; Ferrari, F.; Lucchini, M.; Sansone, G.; Nisoli, M., Time-Delay Compensated Monochromator for the Spectral Selection of Extreme-Ultraviolet High-Order Laser Harmonics. *Rev. Sci. Instrum.* **2009**, *80*, 123109.
14. Csizmadia, T., et al., Spectrally Tunable Ultrashort Monochromatized Extreme Ultraviolet Pulses at 100 Khz. *APL Photonics* **2023**, *8*, 056105.
15. Berkowitz, J., "Absolute Partial Cross-Sections of Ethylene (C₂H₄). In *Atomic and Molecular Photoabsorption*, Elsevier: Amsterdam, 2015; pp 442–458.
16. Lorquet, J. C.; Sannen, C.; Raseev, G., Dissociation of the Ethylene Cation: Mechanism of Energy Randomization. *J. Am. Chem. Soc.* **1980**, *102*, 7976-7977.
17. Sannen, C.; Raşeev, G.; Galloy, C.; Fauville, G.; Lorquet, J. C., Unimolecular Decay Paths of Electronically Excited Species. Ii. The C₂H₄⁺ Ion. *J. Chem. Phys.* **1981**, *74*, 2402-2411.
18. Pollard, J. E.; Trevor, D. J.; Reutt, J. E.; Lee, Y. T.; Shirley, D. A., Torsional Potential and Intramolecular Dynamics in the C₂H₄⁺ Photoelectron Spectra. *J. Chem. Phys.* **1984**, *81*, 5302-5309.
19. Willitsch, S.; Hollenstein, U.; Merkt, F., Ionization from a Double Bond: Rovibronic Photoionization Dynamics of Ethylene, Large Amplitude Torsional Motion and Vibronic Coupling in the Ground State of C₂H₄⁺. *J. Chem. Phys.* **2004**, *120*, 1761-1774.
20. Wörner, H. J.; Merkt, F., Jahn–Teller Effects in Molecular Cations Studied by Photoelectron Spectroscopy and Group Theory. *Angew. Chem. Int. Ed.* **2009**, *48*, 6404-6424.
21. Sewell, T. D.; Thompson, D. L.; Levine, R. D., Mode Selectivity in the Classical Power Spectra of Highly Vibrationally Excited Molecules. *J. Phys. Chem.* **1992**, *96*, 8006-8022.

Isotope effect on the few-femtosecond relaxation dynamics of the ethylene cation

Matteo Lucchini*, Manuel Cardoso-Gutierrez*, Mario Murari, Fabio Frassetto, Luca Poletto,
Mauro Nisoli, Françoise Remacle

*Equal contribution

Supplementary information

Section S1: Additional experimental information.

Section S2 : Details on the electronic structure and the surface hopping dynamics

Section S3 : Measurements of longer time delays

Section S4 : Details on the features of the MECI's between the 4 lowest states of the cation and relaxation paths

Section S5: Analysis of the spectra of the coordinates CC, HCH , HCCH and HHHH

S1. Experimental methods

Infrared (IR) pulses with a time duration of 35 fs, central wavelength of 800 nm, pulse energy of about 1.2 mJ and a repetition rate of 1 kHz are spectrally broadened in a hollow core fiber setup filled with Ne¹⁻². The resulting pulses are temporally compressed with a set of chirped mirrors, resulting in a time duration of 15 fs and a pulse energy of about 800 μ J. The beam is later divided by an 80/20 beam splitter and steered into an evacuated beam line. The most intense part is used to obtain extreme-ultraviolet (EUV) radiation through high-order harmonic generation (HHG) in a static gas cell filled with Xe. The resulting harmonic comb is sent to a time-delay compensated monochromator (TDCM)³ which is composed of two identical stages in a subtractive configuration in order to achieve tunability, while preserving the temporal characteristics of the pulses⁴. Each stage contains two toroidal mirrors and a dispersive grating working in conical diffraction.⁵ The experimental spectra selected by the TDCM are reported in Fig. S0: the blue curve represents the ninth harmonic (H9), green and orange the eleventh (H11) and thirteenth (H13), respectively.

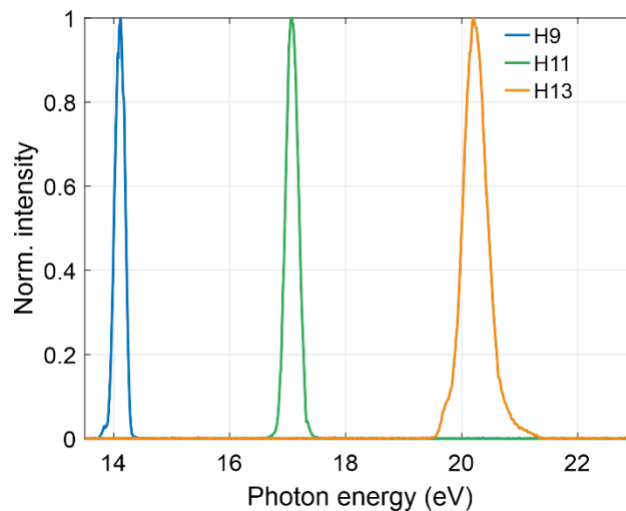


Figure S1: Normalized spectral intensity of the EUV pulses used in the experiment.

The weaker part of the IR beam is collinearly recombined with the selected harmonic radiation through a drilled mirror at the end of the TDCM. Both beams are later focused onto a molecular gas target placed in the interaction region of a time-of-flight (TOF) spectrometer which allows the detection of electrons and photoions, according to the chosen driving voltages. For the experiments reported in this work, we followed the same procedure adopted in Ref. ⁶, and used

an IR intensity on target of $\approx 3.5 \times 10^{12}$ W/cm². The harmonics are used to ionize the molecules and populate the first excited states of the cation while a delayed IR pulse modifies

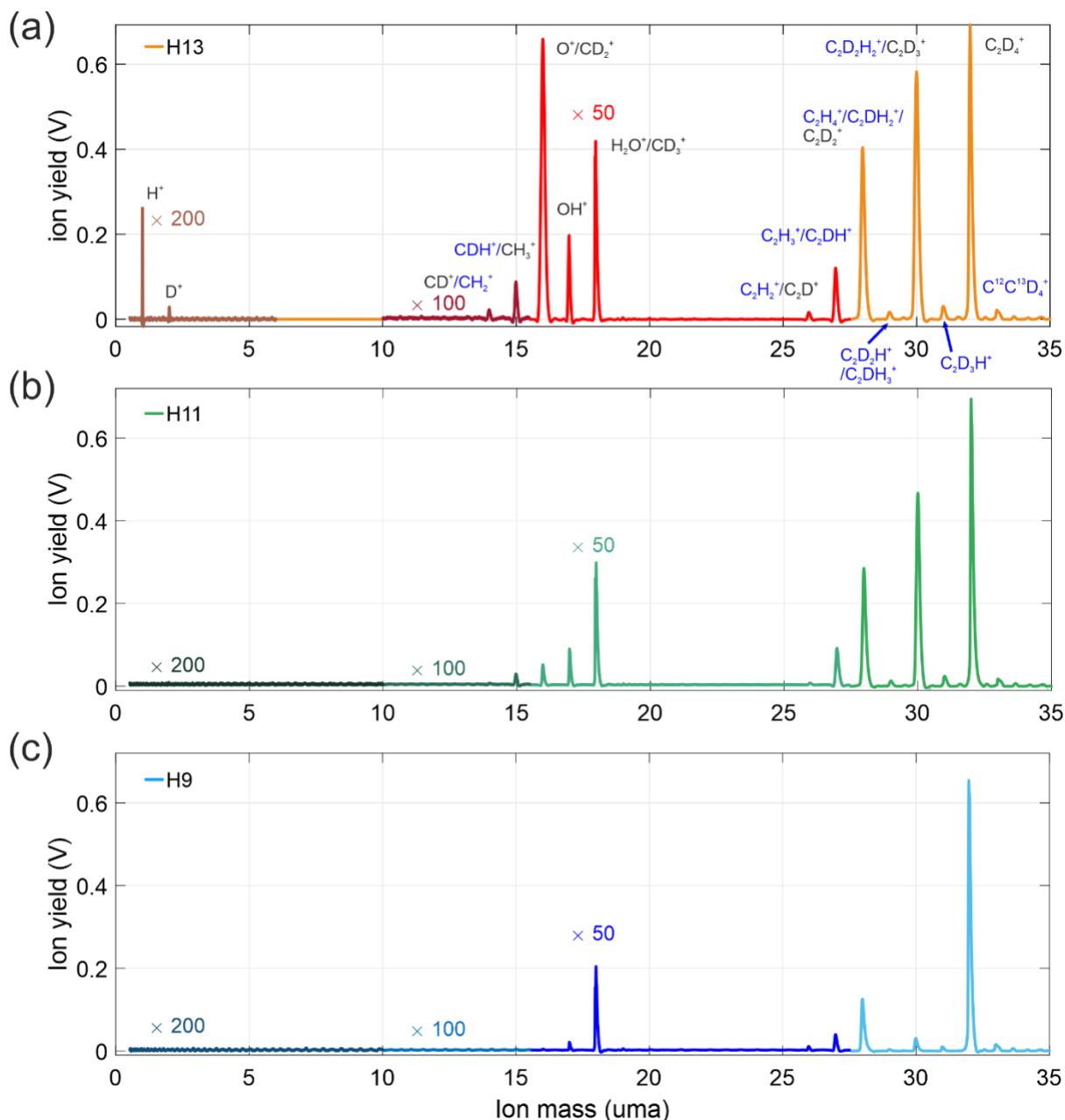


Figure S2: Fragment mass spectrum measured with the TOF spectrometer after ionization of ethylene-d₄ by H13 (a), H11 (b) and H9 (c). Different color marks the different amplification factor applied for better visualization. In panel (a) the labels mark a possible assignment of the observed peaks. Blue labels indicate possible fragments which are expected to give negligible contribution. For the mass spectra of ethylene, we refer the reader to the SI of ref.⁶.

the subsequent relaxation dynamics. The resulting molecular fragments are collected with the TOF spectrometer (see Fig. S02 for the mass spectra of ethylene-d₄) where a signal proportional to the total yield, Y , for a specific ion is obtained by integration along the mass axis, in a window of 0.2 uma centred at the particular fragment peak. In our setup, a mechanical

chopper is used to modulate the IR arm at 500 Hz in order to acquire the IR-on, IR-off fragment spectra in fast sequence. This allows the evaluation of the differential ion yield, defined as:

$$\frac{\Delta Y}{Y}(\tau) = \frac{Y_{IR}(\tau) - Y_0}{Y_0}$$

where Y_0 is the ion yield obtained only with the EUV radiation, while $Y_{IR}(\tau)$ is the ion yield recorded when the IR pulse is shone onto the sample at a delay τ . The results displayed in Fig. 1 of the main manuscript report the $\frac{\Delta Y}{Y}$ discussed above and obtained by averaging the 10 separate delay scans. The error bars represent the associated standard error of the mean. A photoelectron pump-probe measurements (see SI of Ref. ⁶) is performed soon before and after the photoion measurements for a double purpose: (1) to obtain a photoelectron cross-correlation signal from which the EUV duration is estimated (see Table S1) and (2) to define the delay zero and correct for any eventual thermal instability of the interferometer during the measurement time (typically 1h/1h 30').

Table S1: Full-width half-maximum (FWHM) cross-correlation and harmonic duration extracted from the photo-electron pump-probe experiment considering a duration of the IR equal to 15 fs.

HH	Cross-correlation (fs)		Harmonic duration (fs)	
	C ₂ H ₄ ⁺	C ₂ D ₄ ⁺	C ₂ H ₄ ⁺	C ₂ D ₄ ⁺
9	21.1±1.6	22.8±0.9	15±2.4	17.2±1.2
11	18.5±1.44	20.4±0.9	10.8±2.7	13.8±1.4
13	16.9±1.23	19.7±0.7	7.8±3.2	12.8±1.4

S2. Summary of the surface hopping computations

We adopted the same approach to describe the dynamics of the C₂D₄⁺ upon photoionization as in ref. ⁷ for C₂H₄⁺. Briefly, we carried out surface hopping (SH) ab initio dynamics for ensembles of trajectories using the SA(7)-CAS-SCF(11,9)/6-311G(d,p) level of electronic structure on the D₁, D₂, D₃ states as implemented in SHARC⁸ coupled to MOLPRO⁹ with 4 active electronic states (D₀, D₁, D₂, D₃), followed after the trajectory relaxed on D₀ by Born-Oppenheimer ab initio molecular dynamics (BOMD)¹⁰ at the B3LYP/6-311G++(3df,3pd) on D₀ up to 2 ps. The initial states of the SH trajectories were sampled from a Wigner distribution of the ground vibrational state of neutral ground electronic state. In addition, SH hopping dynamics at the same CAS level were run on D₀ for 200 fs and for 2ps in BOMD. The D loss

and D₂ loss were monitored using a threshold bond length of 3.5 Å. As in the case of the C₂H₄⁺ ion, in C₂D₄⁺, the H-loss and the H₂ loss all occur on D₀ during the BOMD dynamics.

Number of trajectories analyzed per ensemble.

Isotopomer	D0 ensemble	D1 ensemble	D2 ensemble	D3 ensemble
C ₂ H ₄ ⁺	297	221	137	102
C ₂ D ₄ ⁺	200	141	210	163

Table S2: Computed lifetimes of the D₁, D₂ and D₃ excited states from the ensembles of trajectories

Ensemble	Lifetime (fs) Exp Fit	Lifetime (fs) 50 % decay
D1 Hydrogen	14.6	12.3
D1 Deuterium	26.5	21.4
D2 Hydrogen	6.6	5.8
D2 Deuterium	7.2	6.8
D3 Hydrogen	6.7	5.2
D3 Deuterium	8.3	8.3

S3. Measurements for longer delay times

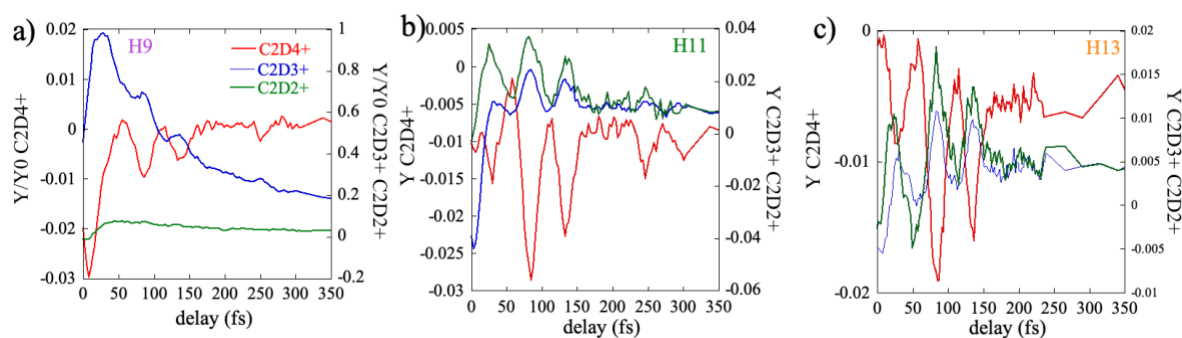


Figure S3: Measured parent and fragmentation yields for C₂D₄⁺ as a function of the EUV-IR delay time for the three ionization energies.

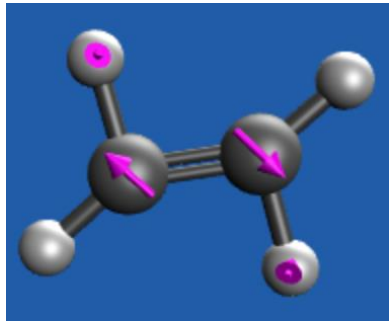
S4. Detailed analysis of the minimum energy conical intersections (CI) sampled by the dynamics in the 4 lowest excited states of the cation.

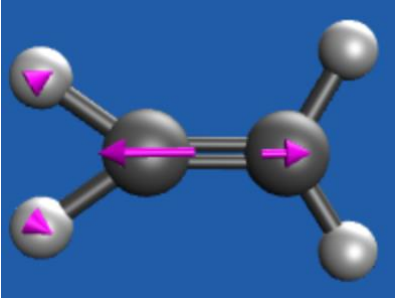
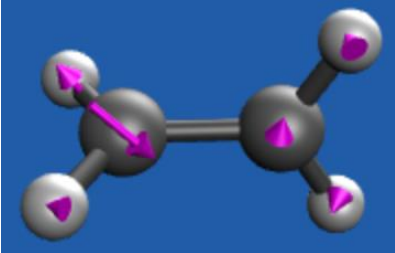
S4.1 Geometries of the MECI between the states D₀, D₁, D₂ and D₃.

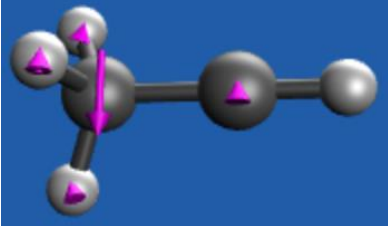
Level of electronic structure: SA(7)CASSCF(11e,9o)/6-311G** using the MULTI CAS-SCF implementation of MOLPRO.⁹

We show the equilibrium geometry of MECI as well as the components of the NAC vector on the nuclei in pink arrows. We report the energies of the four electronic states at the MECI geometry as well as the value of the D₀/D₃ transition dipole. Activated modes obtained by projection of the NAC vector on the normal modes of D₀ at its equilibrium geometry, see Table S8 below for the normal modes.

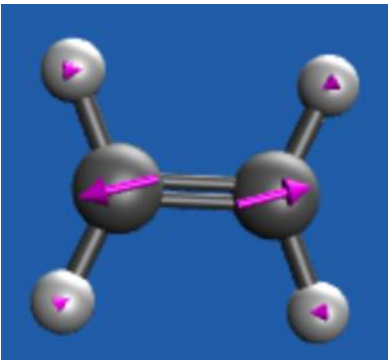
MECIs D₀/D₁

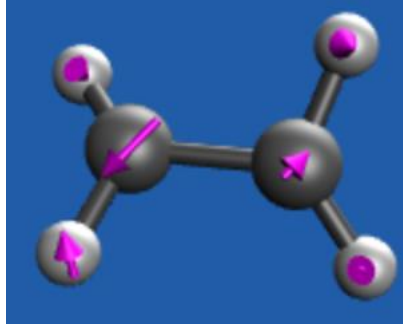
MECI	Projection on Normal Modes of Ethylene	
Energy (Hartree)	Vibrational mode, Frequency, Component	
Transition Dipole (Debye)		
Planar	Type	I
		v1 0.33 H-C-H out-of-plane twisting
		v2 -0.01
		v3 0.21 H-C-H out-of-plane wagging
		v4 -0.04
		v5 0.32 C-C-H in-plane rocking
		v6 0.12 in plane HCH symmetric scissoring
		v7 -0.04 in plane HCH antisymmetric scissoring
		v8 -0.29 C-C stretching
		v9 -0.12
		v10 0.15
		v11 0.16
		v12 -0.13
Energy D ₀ = -77.69163501		sloped
Energy D ₁ = -77.69163471		C-C = 1.28 Å
Energy D ₂ = -77.50216883		C-C equilibrium neutral : 1.33 Å
Energy D ₃ = -77.49468027		
Trans Dip D ₀ /D ₃ = 0.381433 D		

<p>Planar Type II</p>  <p>NAC Energy $D_0 = -77.68857060$ Energy $D_1 = -77.68856710$ Energy $D_2 = -77.52298200$ Energy $D_3 = -77.48793358$ Trans Dip $D_0/D_3 = 0.302223$ D</p>	<p>v1 0.07 v2 0.00 v3 0.01 v4 -0.03 v5 -0.01 v6 -0.07 v7 0.30 H-C-H in-plane symmetric scissoring v8 -0.56 C-C stretching v9 -0.11 v10 -0.00 v11 0.19 v12 0.03</p> <p>sloped C-C $i=1.29$ Å</p>
<p>Twisted</p>  <p>NAC Energy $D_0 = -77.72633209$ Energy $D_1 = -77.72394078$ Energy $D_2 = -77.51624757$ Energy $D_3 = -77.48328766$ Trans Dip $D_0/D_3 = 0.519516$ D</p>	<p>v1 -0.28 H-C-H out-of-plane twisting v2 0.00 v3 0.08 v4 -0.29 H-C-H out-of-plane wagging v5 0.12 v6 -0.14 v7 -0.31 H-C-H in-plane antisymmetric scissoring v8 -0.03 v9 0.10 v10 0.05 v11 -0.38 C-H stretching v12 -0.28 C-H stretching C-C 1.43 Å</p>
<p>C3v Ethylidene (not sampled in the SH trajectories)</p>	<p>v1 0.12 v2 0.02 v3 0.33 H-C-H out-of-plane wagging v4 -0.35 H-C-H out-of-plane wagging</p>

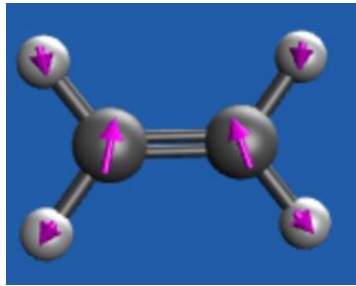
 <p>NAC</p>	<p>v5 -0.11 v6 -0.03 v7 -0.21 H-C-H in-plane anti symm scissoring v8 0.31 C-C stretching v9 -0.03</p>
<p>Energy D₀ = -77.71154099 Energy D₁ = -77.71154094 Energy D₂ = -77.45510115 Energy D₃ = -77.45402147 Trans Dip D₀/D₃ = 1.32376 D</p>	<p>v10 0.06 v11 -0.09 v12 0.01</p>

MECIs D₁/D₂

Planar Energy (Hartree)	Projection on Normal Modes of Ethylene Vibrational mode, Frequency, Component
<p>Planar (abundant)</p>  <p>NAC</p> <p>Energy D₀ = -77.76993829 Energy D₁ = -77.64201739 Energy D₂ = -77.64201699 Energy D₃ = -77.53230823</p>	<p>v1 -0.00 v2 -0.00 v3 -0.00 v4 -0.02 v5 0.12 v6 -0.13 v7 0.05 v8 -0.42 C-C stretching v9 -0.22 C-H stretching v10 0.09 v11 0.32 C-H stretching v12 -0.07</p> <p>peaked c-c = 1.4Å</p>
<p>Twisted (2 % of trajectories)</p>	<p>v1 0.47 H-C-H out-of-plane twisting v2 0.09 v3 0.02</p>

	<p>v4 -0.01</p> <p>v5 0.29 C-C-H in-plane rocking</p> <p>v6 0.29 H-C-H in-plane symmetric scissoring</p> <p>v7 -0.02</p> <p>v8 -0.01</p> <p>v9 -0.05</p> <p>v10 0.06</p> <p>v11 0.35 C-H stretching</p> <p>v12 -0.24 C-H stretching</p>
<p>Energy D₀ = -77.75831017</p> <p>Energy D₁ = -77.61972622</p> <p>Energy D₂ = -77.61972591</p> <p>Energy D₃ = -77.55190641</p>	

MECIS D₃/D₂

PlanarI Energy (Hartree)	Projection on Normal Modes of Ethylene Vibrational mode, Frequency, Component
<p>Planar (abundant)</p>  <p>NAC</p> <p>Energy D₀ = -77.76765234</p> <p>Energy D₁ = -77.67843060</p> <p>Energy D₂ = -77.58472487</p> <p>Energy D₃ = -77.58472472</p>	<p>v1 0.00</p> <p>v2 -0.09</p> <p>v3 0.00</p> <p>v4 -0.00</p> <p>v5 -0.02</p> <p>v6 0.13</p> <p>v7 -0.02</p> <p>v8 0.16 C-C stretching</p> <p>v9 0.05</p> <p>v10 0.49 C-H stretching</p> <p>v11 -0.02</p> <p>v12 0.54 C-H stretching</p> <p>peaked</p> <p>c-c=1.4Å</p>
<p>Twisted (<1% of trajectories)</p>	<p>v1 -0.04</p> <p>v2 -0.05</p> <p>v3 0.47 H-C-H out-of-plane wagging</p>

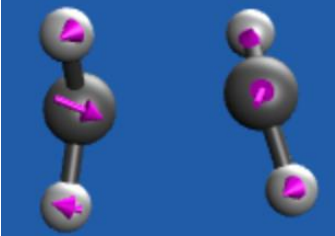
 NAC	v4 0.11
	v5 0.28 C-C-H in-plane rocking
Energy D ₀ = -77.59380595	v6 -0.04
Energy D ₁ = -77.58921517	v7 -0.44 H-C-H in-plane anti symmetric scissoring
Energy D ₂ = -77.54082829	v8 0.14
Energy D ₃ = -77.54082813	v9 0.03
	v10 -0.03
	v11 -0.14
	v12 0.01

Table S3: Energies of MECIs with respect to the energy of the planar geometry of the GS cation

Level SA(4) CASSCF(11e,9o)/6-311G**

Geometry	GS Energy (au) SA(4)CASSCF	GS Energy (eV)
Ethylene cation (planar)	-77.78265676	0.00
Planar Type I D ₀ /D ₁	-77.69163501	2.45
Planar Type II D ₀ /D ₁	-77.68857060	2.56
Twisted D ₀ /D ₁	-77.72481388	1.57
C _{3v} Ethylidene D ₀ /D ₁	-77.71154099	1.94

S4.2 Detailed discussion of the role of the CI's in the relaxation dynamics

Upon sudden ionization of the neutral ground state in its equilibrium geometry, the ethylene cation is produced in an unstable planar D_{2h} geometry. The four lowest excited electronic states of the cation, D₀, D₁, D₂ and D₃, that can be populated by photoionization in this study, are coupled through a network of planar and twisted CIs, which triggers fragmentations and isomerizations.^{7, 11-18} Several theoretical studies^{11-12, 16, 18} already identified the essential of the excited state dynamics for the four lowest states of the cation. The equilibrium geometry of the ground state D₀ is slightly twisted, with a torsion angle of $\approx 23^\circ$ and a D₂ symmetry. The excited states D₁, D₂ and D₃ are connected to D₀ by a network of CI's. The CI's sampled by the SH trajectories at the level of electronic structure that we use are in agreement with recent previous works,^{16, 18}. The D₂/D₃ MECI through which the relaxation occurs for the D₃ ensemble is peaked, with a planar geometry and a slightly elongated C-C

bond (1.4 Å) compared to that of the D_{2h} neutral ground state (1.33 Å) and very close to the FC region in configuration space. Its non adiabatic derivative coupling vector activates significantly the ‘in plane’ C-C and C-H modes. For these reasons, as can be seen from Figs. 2 b and c ($C_2H_4^+$) and e and f ($C_2D_4^+$) of the main text, the D_3/D_2 relaxation is very fast and occurs within 5 fs, without any major isotope effect. In the SH dynamics, the D_2/D_1 relaxation also occurs through a planar geometry, peaked, CI. The MECI geometry has a slightly elongated C-C bond at 1.4 Å, that activates the same ‘in plane’ modes, C-C and C-H stretching. For the D_2 and the D_3 ensembles (Figs. 2 b, c, and e, f), population is transferred from D_2 to D_1 within 5 to 10 fs, with a shoulder at 15 fs for the D_3 ensemble (Figs. 2c and f). Overall, for the two isotopomers, the majority of the population that reaches D_1 within the first 10 fs is essentially planar with activated C-C bonds and H-C-H angles for the D_2 and D_3 ensembles which makes it different from the Wigner distribution of the D_1 ensemble of initial conditions.

As established in previous works,^{16, 18} three CIs are involved in the D_1/D_0 relaxation: two planar and a twisted one. The planar ones correspond to the two CIs identified in ref.¹⁶. We call them planar I and II respectively. The planar I MECI has a sloped character and a planar distorted geometry with modified HCH angles and a slightly compressed C-C bond (1.28 Å). Its geometry differs more from the geometries sampled in the Wigner distribution of the D_1 ensemble of initial conditions than those of D_3/D_2 and D_2/D_1 MECI discussed above, which explains why the initial decay of the D_1 population in Fig. 2a and d is slower than that of the D_2 and D_3 populations plotted in Figs. 2 b,c, e, and f of the main text. The planar I MECI is located 2.45 eV above the energy of the planar, D_{2h} , D_0 cation (Table S3). It plays a major role in the relaxation dynamics to D_0 for both isotopomers, see Table 2. The second MECI, planar II, is slightly higher in energy (2.56 eV, see Table S3) and does not play a significant role in the relaxation dynamics sampled by the trajectories. Its C-C bond is also slightly compressed (1.29 Å). In addition of the C-C and C-H stretching found in the D_3/D_2 and D_2/D_1 planar MECI CIs, both planar D_1/D_0 CIs activate low frequency, out of plane motions: the CH_2 torsion and wagging for planar I and the CH_2 in plane scissoring for planar II. The third major MECI playing a role in the D_1/D_0 relaxation dynamics for the energy range of the three ionization energies discussed here has a twisted MECI geometry with a torsion angle of 90° as reported previously.^{11-12, 16, 18} Its C-C bond is elongated (1.43 Å). It is lower in energy with respect to the two planar MECI (1.57 eV above the planar D_{2h} geometry of D_0 , Table S3) and activates the out of plane low frequency mode CH_2 torsion, wagging and in plane HCH anti symmetric bending scissoring as well as the C-H stretching. Unlike for the other two planar CIs, the C-C stretching is not activated in the twisted CI. We have also identified a D_1/D_0 MECI with an

ethylidene geometry, at 1.94 eV above the planar D₀ cation. This CI is not sampled in the 100 fs of the SH trajectories launched from D₃, D₂ and D₁. It is related to ethylene/ethylidene isomerization discussed in ref. ¹⁸

In the SH dynamics, the two planar CIs dominate the relaxation from D₁ to D₀ for the D₁ and D₂ ensembles for both isotopomers, see Table 2 of the main text. The major channel for the D₁/D₀ relaxation is the planar I CI. For the D₁ ensemble, 77.5 % of the trajectories of C₂H₄⁺ relax through the planar I CI and 21.1% through planar II while for C₂D₄⁺, the fraction relaxing through planar I increases to 86.3 %. The slower motion of the heavier C₂D₄⁺ favors the relaxation through the seams of the planar I MECI which is sloped and closer in configuration space to the FC region. The relaxation through the planar II CI is delayed and clearer for C₂D₄⁺ (see Fig. 2 a and d). For the D₁ ensemble, this isotope mass effect leads to a longer relaxation time, 21.4 fs for C₂D₄⁺ vs 12.3 fs for C₂H₄⁺ (see Table S2). 1.4 % of the trajectories of the D₁ ensemble relax through the twisted CI for C₂H₄⁺ and only 0.3 % for C₂D₄⁺ which makes this relaxation pathway negligible for the heavier isotopomer. For the D₂ ensemble, for C₂H₄⁺, the fraction that relaxes through the twisted D₁/D₀ CI reaches 9% and is comparable to the fraction going through the planar II D₁/D₀ CI, while the fractions for C₂D₄⁺ go down to 3.1 and 0.6 % respectively. This leads to 96.1 % of the trajectories going through the planar I CI for C₂D₄⁺ and 81.5 for C₂H₄⁺. For the D₃ ensemble, because of the higher excitation energy, we observe a significant rise of the fraction of trajectories that relax through the twisted D₁/D₀ CI for both isotopomers (25.6 % for C₂H₄⁺ and 25.5 % for C₂D₄⁺). Nevertheless, the relaxation through the planar I CI remains dominant (68.4 and 70 % for C₂H₄⁺ and C₂D₄⁺ respectively).

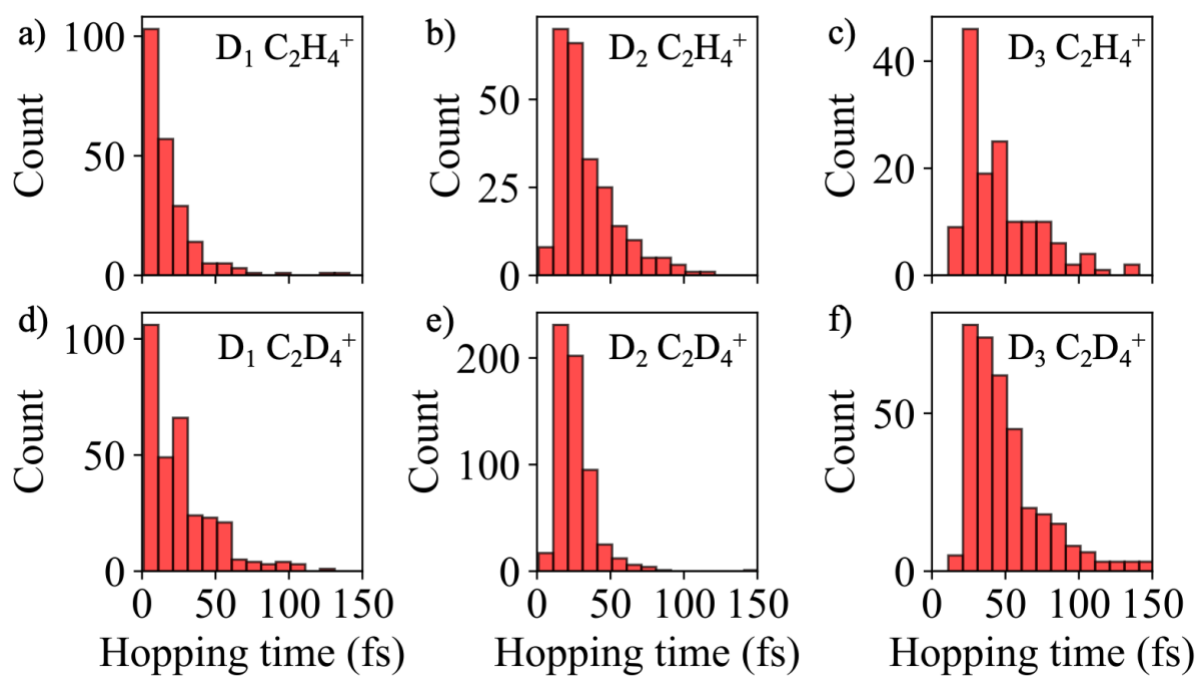


Figure S4. Histograms of the last D_1/D_0 hopping times through the planar type I CI for the three ensembles.

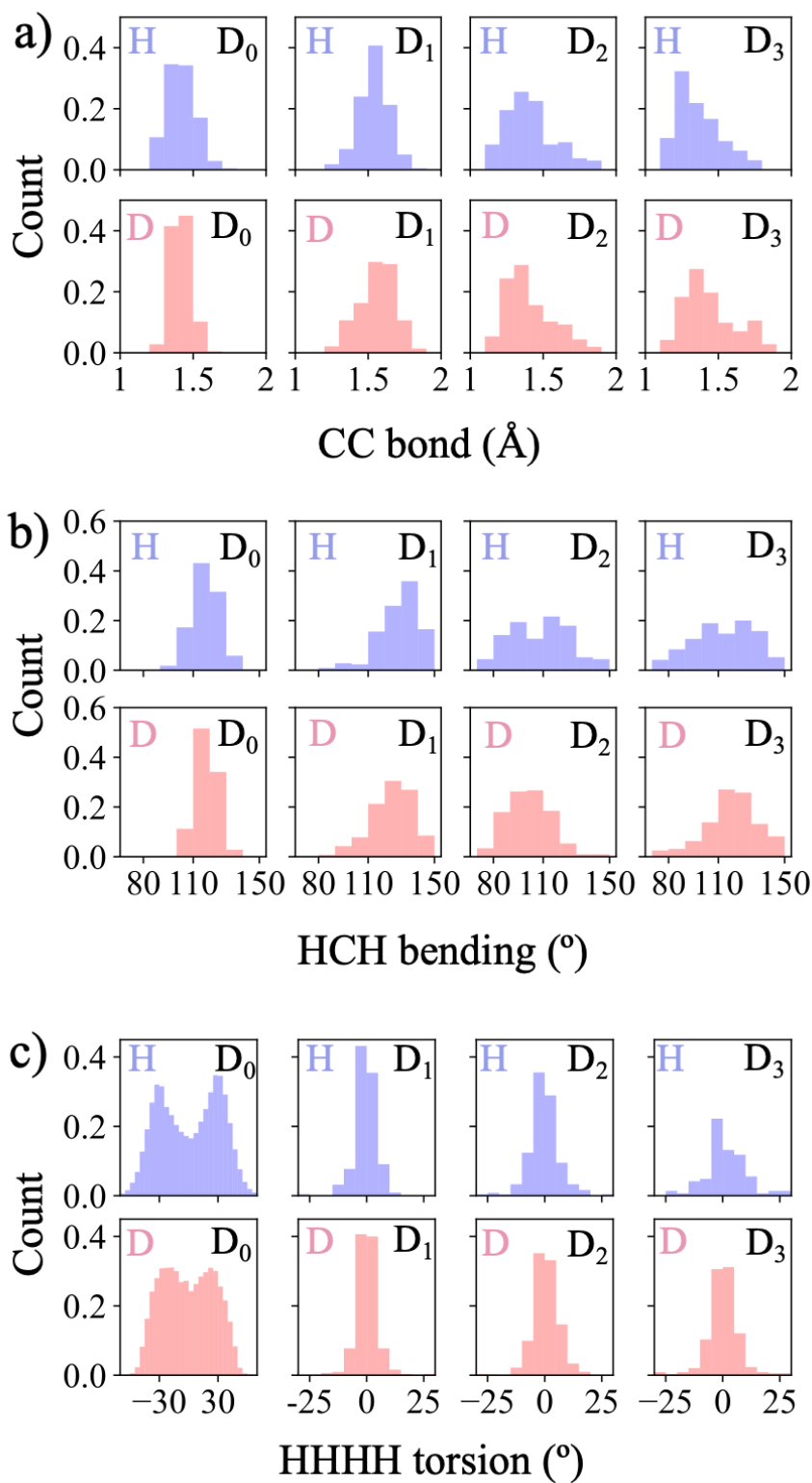


Figure S5. Histograms of the distributions of C-C distances (a), HCH angles (b) and HHHH angles (c) on D_0 computed for $C_2H_4^+$ (blue) and $C_2D_4^+$ (red) for the four ensembles of initial conditions : The SH dynamics initiated on D_3, D_2, D_1 or D_0 as indicated.

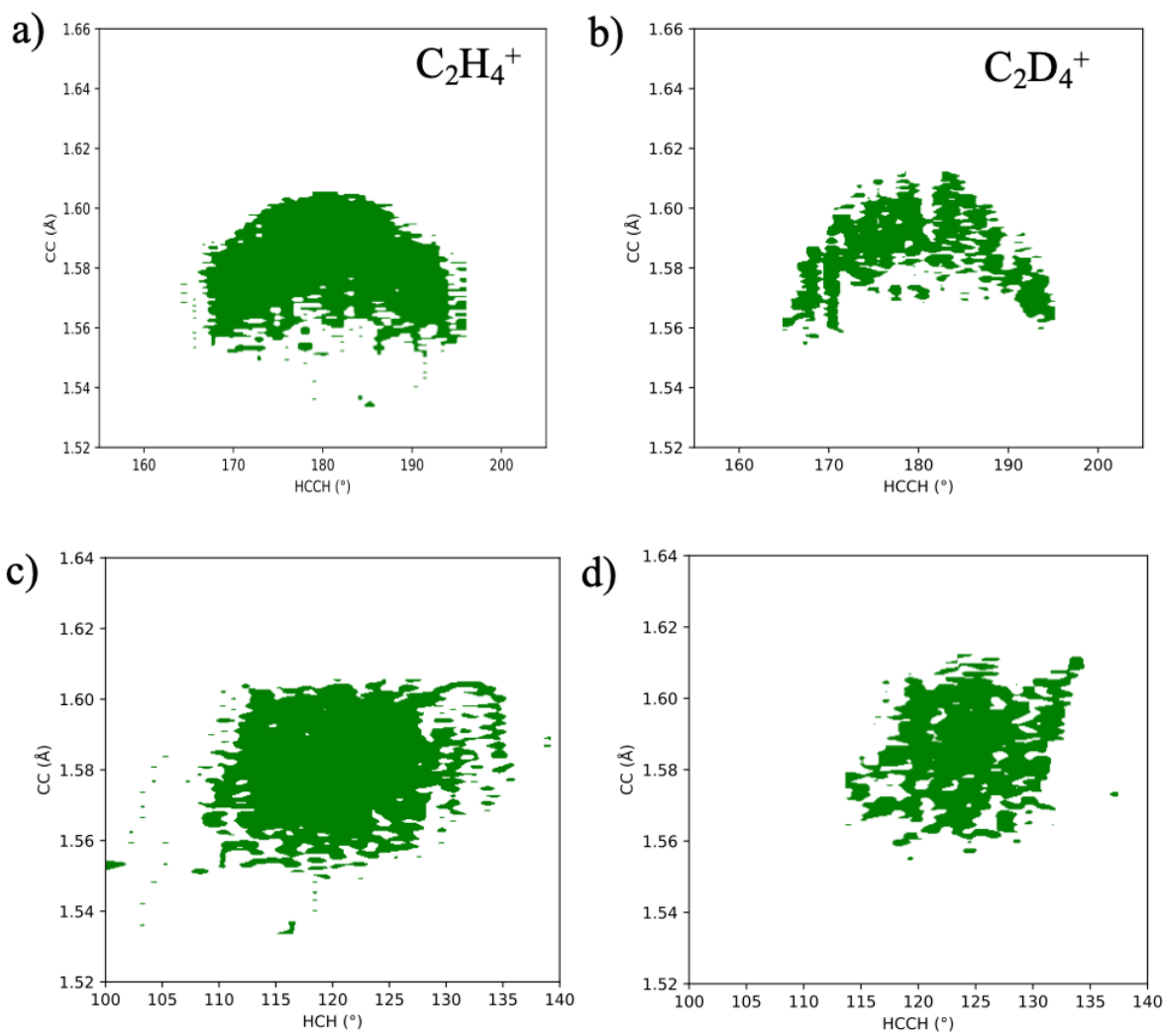


Figure S6. Heatmaps of the C-C elongation and HCCH angles values (a and b) and CC vs HCH (c and d) on D_0 that corresponds to an energy difference that is 3 photon resonant with D_3 and a value of the transition dipole ≥ 1 a.u..

S4. Detailed analysis of the spectra of the C-C, HCH, HCCH and HHHH coordinates in ensembles of trajectories and the features of the active fraction

To assess to which motion the periods seen in the active fractions of trajectories plotted as a function of time in Fig. 4 of the main text, correspond, we show in Fig. S7a the spectra of the HCCH angles (green and orange), of the HCH angles (light and dark pink), of HHHH angle (orange dashes) and of the C-C coordinate (blue) computed for the first 200 fs of the dynamics for $C_2H_4^+$ (top row) and for $C_2D_4^+$ (bottom row) for the D_0 ensemble of initial conditions (Fig. S7a) and for the set of trajectories that relaxed to D_0 through the planar type I CI for the D_1 ensemble of initial conditions, Fig. S7b, which corresponds to Fig. 3 b) of the main text and is reproduced here for completeness). These spectra, obtained by the Fourier transform of the ensemble of trajectories, provide the frequencies of the normal modes involved in these coordinates. The spectra of the two dihedral angles superimpose almost exactly and appear in green. The spectra of the two HCH angles are more different and can be distinguished. The left column of Fig. S7 compares the spectra of the HCCH angles (green) and the CC distance (blue), the middle one HCH angle (two pink color) and CC (blue) and the right column the HHHH angle (orange) and CC (blue). When the frequency of a given mode appears in the spectra of two coordinates, it means that the two coordinates are coupled.¹⁹

We begin by discussing the spectra of the coordinates of the D_0 ensemble, Fig. S7a. For $C_2H_4^+$ (Fig. S7a, top row) in the spectrum of the HCH angle (pink, middle column), the symmetric HCH scissoring appears at 26 fs in good agreement with the computed frequency of 1304 cm^{-1} of the D_0 cation (see Table S4 and Figure S8 for the computed frequency values). The antisymmetric scissoring appears at a period of 23 fs (1400 cm^{-1}) which coincides with that of the CC bond (blue). In Table S4, both frequencies are a little higher (1504 cm^{-1} and 1636 cm^{-1}) which can be understood considering the anharmonicity and coupling of the motions. One can see that the scissoring modes are coupled to the CC elongation the HCH scissoring and C-C frequencies appear in the spectra of both coordinates in the middle panel of Fig. S8a, top row. The spectra of the dihedral angles (left panels of Fig. S7a, top row) exhibit the periods of the wagging/rocking modes at $\approx 35\text{-}40$ fs and of the torsion at ≈ 70 fs. The wagging modes are not coupled to C-C for $C_2H_4^+$ and only very weakly coupled to the symmetric HCH scissoring. From this analysis we can hence conclude that the fast oscillations of the active fraction on D_0 in Fig. 3a are dominated to the C-C elongation and the symmetric and antisymmetric scissoring motions. They are modulated by a longer period of ≈ 70 fs of the torsion motion which is very anharmonic. The spectrum of the HHHH dihedral angle (orange

dashes, right column) exhibits only the period of ≈ 90 fs of the torsion mode as expected for this coordinate.

The main peak at 36 fs observed in the D_0 active fraction initially started on D_1 plotted in Fig. 3b of the main text (red) for $C_2H_4^+$, corresponds to those trajectories that have relaxed through the planar type I CI for which the C-C mode is activated. Then the C-C elongation and torsion motion of this fraction dephase which does not lead to clear patterns as a function of time, see Fig. 3b. The spectra of the C-C, HCH and HCCH coordinates for the fraction of the D_1 ensemble that relaxes to D_0 through the planar type I CI are shown in Fig. S7b, top row for $C_2H_4^+$ and bottom row for $C_2D_4^+$. They are less rich in structure when compared to the spectra of D_0 shown in Fig. S7a because of the filtering action of the planar type I CI on these coordinates. The main difference is the peak of the torsion mode (green curve, left panel of the top row) that shifts to a shorter period of 74 fs, closer to the computed equilibrium frequency (see Table S4). This can be understood from the filtering action of the planar type I CI, which leads to planar initial geometries on D_0 , with a narrower distribution of HCCH angles (see Figure S5) than the Wigner distribution on D_0 . One also note that the relative intensity of the CC peaks and of the two wagging modes are different for the D_1 ensemble (compare the top row of the middle panel of Fig S7a with the top row of the middle panel of Fig. S7b)

Compared to $C_2H_4^+$, the $C_2D_4^+$ active fraction of the D_0 ensemble (Fig. 3a, blue of the main text) exhibits a slightly delayed maximum corresponding to bleaching peak of the parent at ≈ 36 fs, followed by lower intensity peaks which reflect several periods: maxima at 88 fs and 190 fs secondary ones at 38 fs, 60 fs, 116fs and 165 fs. In $C_2D_4^+$, because of the isotope effect, the two scissoring DCD modes are shifted to longer periods, 36 fs and 31 fs respectively as can be seen from Fig. S7a bottom row, middle panel (1009 cm^{-1} and 1138 cm^{-1} , in good agreement with the frequencies of the normal modes reported in Table S4), while the period of the CC bond does not change (Fig. S7a, bottom row middle panel, blue curve). The wagging-rocking modes are also shifted to lower frequencies (≈ 45 fs) and coupled to the symmetric scissoring mode. The main difference with the spectra of $C_2H_4^+$ is a complex pattern of peaks at low frequency (142 fs, 100 fs, 77 fs, 60 fs and 47 fs), see bottom row, left panel of Fig. S7a. In $C_2D_4^+$, the isotope effect on the torsion, wagging and scissoring modes results in strong coupling with the CC mode which explains the complex spectra at low frequency. This strong coupling leads combination bands observed in high resolution spectroscopy of $C_2D_4^+$.¹³⁻¹⁴ This complex pattern does not appear in the spectra of the dihedral angles computed for the fraction of D_1 ensemble (bottom row of Fig. S7b, left panel) that relaxes through the planar type I CI (Fig. 3d), because of its filtering action which leads to different distributions of these

coordinates (see Figure S5) which also leads to a slightly longer CC period (28 fs) (bottom row of Fig. S7b, middle panel).

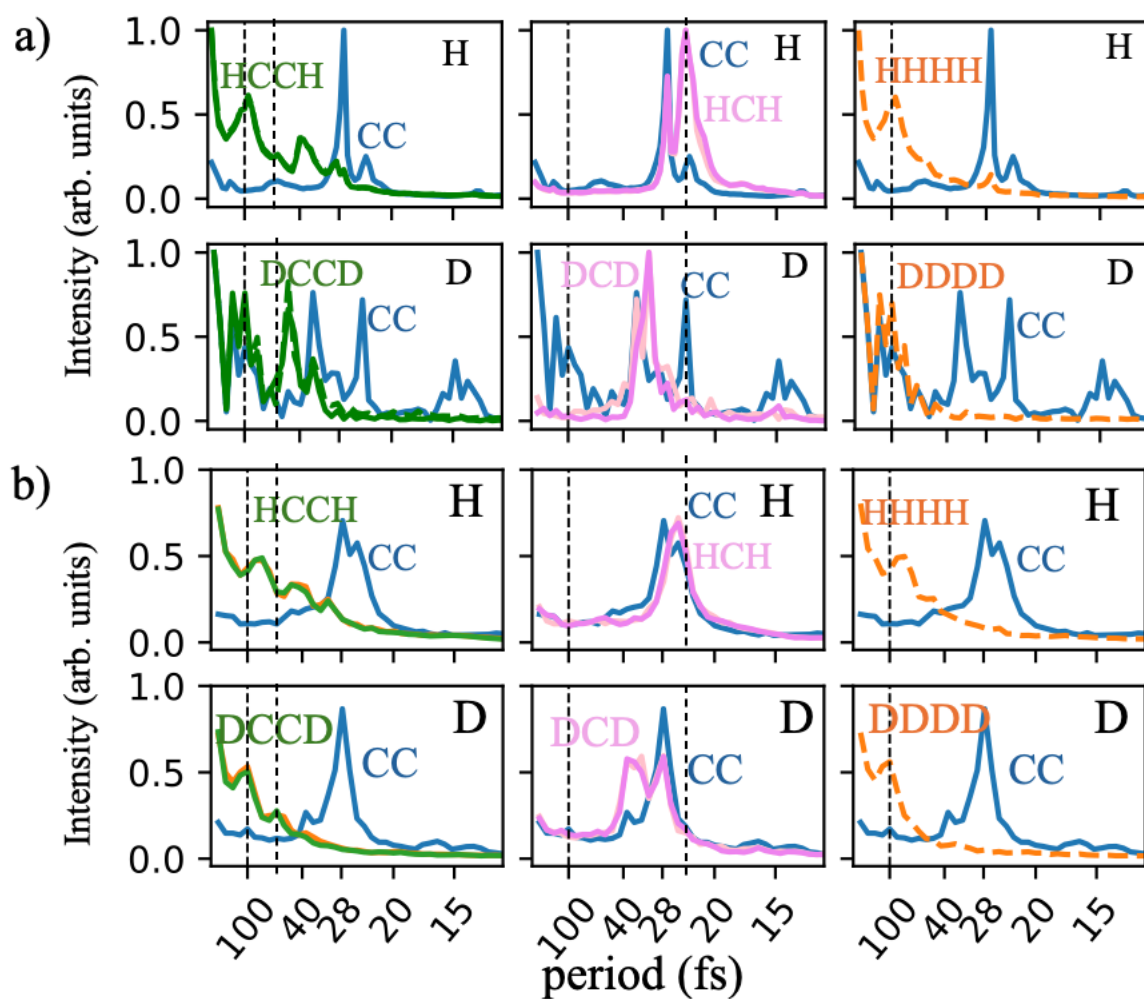
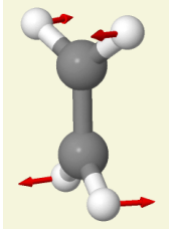
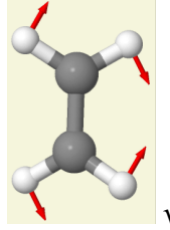
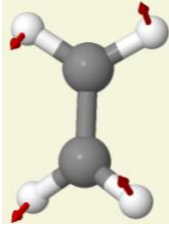
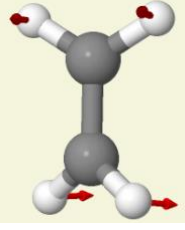
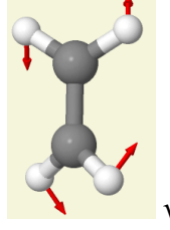
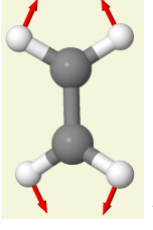
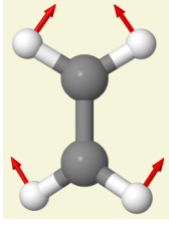
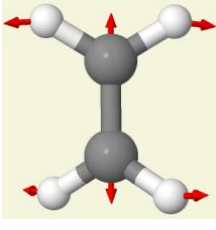
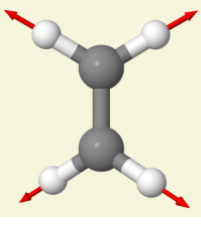
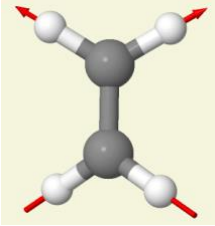
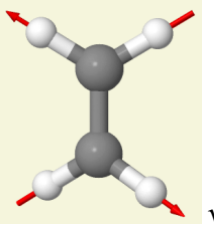
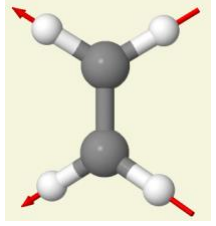


Figure S7: Spectra of the three coordinates that control the value of the transition dipole. a) for the ensemble of trajectories initiated on D_0 . b) for the ensemble of trajectories initiated on D_1 (Fig 3. b) of the main text.

Table S4: Frequencies of the D_0 cation at its equilibrium geometry computed at the single state CAS SCF level for D_0

 <p>v1</p> <p>H-C-H twisting Freq($C_2H_4^+$) = 449 cm⁻¹ Freq($C_2D_4^+$) = 318 cm⁻¹ Isotope effect = 1.41</p>	 <p>v2</p> <p>H-C-H rocking Freq($C_2H_4^+$) = 864 cm⁻¹ Freq($C_2D_4^+$) = 621 cm⁻¹ Isotope effect = 1.39</p>	 <p>v3</p> <p>Sym H-C-H wagging Freq($C_2H_4^+$) = 979 cm⁻¹ Freq($C_2D_4^+$) = 744 cm⁻¹ Isotope effect = 1.32</p>
 <p>v4</p> <p>Asym H-C-H wagging Freq($C_2H_4^+$) = 1069 cm⁻¹ Freq($C_2D_4^+$) = 955 cm⁻¹ Isotope effect = 1.12</p>	 <p>v5</p> <p>C-C-H rocking Freq($C_2H_4^+$) = 1265 cm⁻¹ Freq($C_2D_4^+$) = 1016 cm⁻¹ Isotope effect = 1.25</p>	 <p>v6</p> <p>Sym H-C-H in plane scissoring Freq($C_2H_4^+$) = 1304 cm⁻¹ Freq($C_2D_4^+$) = 1009 cm⁻¹ Isotope effect = 1.29</p>
 <p>v7</p> <p>Antisym H-C-H in plane scissoring Freq($C_2H_4^+$) = 1515 cm⁻¹ Freq($C_2D_4^+$) = 1138 cm⁻¹ Isotope effect = 1.33</p>	 <p>v8</p> <p>C-C stretching Freq($C_2H_4^+$) = 1639 cm⁻¹ Freq($C_2D_4^+$) = 1425 cm⁻¹ Isotope effect = 1.15</p>	 <p>v9</p> <p>C-H symmetric stretching Freq($C_2H_4^+$) = 3067 cm⁻¹ Freq($C_2D_4^+$) = 2234 cm⁻¹ Isotope effect = 1.37</p>

 <p style="text-align: right;">V10</p>	 <p style="text-align: right;">V11</p>	 <p style="text-align: right;">V12</p>
<p>C-H symmetric stretching Freq($C_2H_4^+$) = 3119 cm^{-1} Freq($C_2D_4^+$) = 2377 cm^{-1} Isotope effect = 1.31</p>	<p>C-H asymmetric stretching Freq($C_2H_4^+$) = 3292 cm^{-1} Freq($C_2D_4^+$) = 2398 cm^{-1} Isotope effect = 1.37</p>	<p>C-H asymmetric stretching Freq($C_2H_4^+$) = 3416 cm^{-1} Freq($C_2D_4^+$) = 2554 cm^{-1} Isotope effect = 1.34</p>

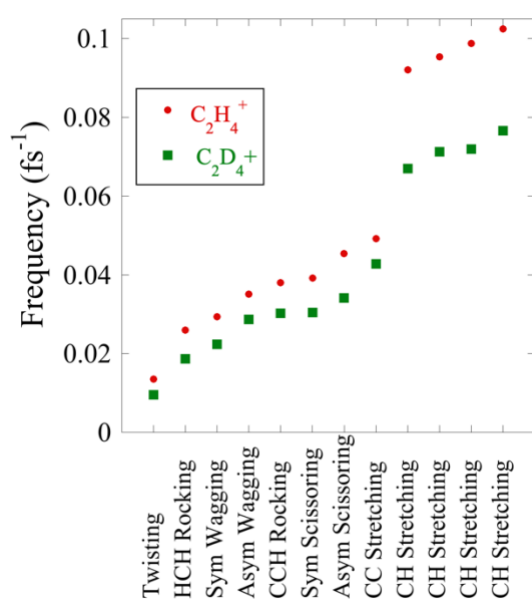


Figure S8 Spectrum of the vibrational frequencies of the two isotopes computed at the SS CAS-SCF level.

References

1. Nisoli, M.; De Silvestri, S.; Svelto, O., Generation of High Energy 10 Fs Pulses by a New Pulse Compression Technique. *Appl. Phys. Lett.* **1996**, *68*, 2793-2795.
2. Nisoli, M., Hollow Fiber Compression Technique: A Historical Perspective. *IEEE Journal of Selected Topics in Quantum Electronics* **2024**, *30*, 1-14.
3. Poletto, L.; Villaresi, P.; Frassetto, F.; Calegari, F.; Ferrari, F.; Lucchini, M.; Sansone, G.; Nisoli, M., Time-Delay Compensated Monochromator for the Spectral Selection of Extreme-Ultraviolet High-Order Laser Harmonics. *Rev. Sci. Instrum.* **2009**, *80*, 123109.
4. Lucchini, M.; Lucarelli, G. D.; Murari, M.; Trabattoni, A.; Fabris, N.; Frassetto, F.; De Silvestri, S.; Poletto, L.; Nisoli, M., Few-Femtosecond Extreme-Ultraviolet Pulses Fully Reconstructed by a Ptychographic Technique. *Opt. Express* **2018**, *26*, 6771-6784.
5. Poletto, L.; Frassetto, F.; Villaresi, P., Ultrafast Grating Instruments in the Extreme Ultraviolet. *IEEE Journal of Selected Topics in Quantum Electronics* **2012**, *18*, 467-478.
6. Lucchini, M.; Mignolet, B.; Murari, M.; Gonçalves, C. E. M.; Lucarelli, G. D.; Frassetto, F.; Poletto, L.; Remacle, F.; Nisoli, M., Few-Femtosecond C₂H₄⁺ Internal Relaxation Dynamics Accessed by Selective Excitation. *J. Phys. Chem. Lett.* **2022**, *13*, 11169-11175.
7. Lucchini, M.; Mignolet, B.; Murari, M.; Gonçalves, C. E. M.; Lucarelli, G. D.; Frassetto, F.; Poletto, L.; Remacle, F.; Nisoli, M., Few-Femtosecond C₂H₄⁺ Internal Relaxation Dynamics Accessed by Selective Excitation. *The Journal of Physical Chemistry Letters* **2022**, 11169-11175.
8. Mai, S.; Marquetand, P.; González, L., Nonadiabatic Dynamics: The Sharc Approach. *WIREs Computational Molecular Science* **2018**, *8*, e1370.
9. Werner, H.-J.; Knowles, P. J.; Knizia, G.; Manby, F. R.; Schütz, M., Molpro: A General-Purpose Quantum Chemistry Program Package. *Wiley Interdisciplinary Reviews: Computational Molecular Science* **2012**, *2*, 242-253.
10. Frisch, M. J., et al. *Gaussian 16 Rev. C.01*, Wallingford, CT, 2016.
11. Lorquet, J. C.; Sannen, C.; Raseev, G., Dissociation of the Ethylene Cation: Mechanism of Energy Randomization. *J. Am. Chem. Soc.* **1980**, *102*, 7976-7977.
12. Sannen, C.; Raşeev, G.; Galloy, C.; Fauville, G.; Lorquet, J. C., Unimolecular Decay Paths of Electronically Excited Species. Ii. The C₂H₄⁺ Ion. *J. Chem. Phys.* **1981**, *74*, 2402-2411.
13. Pollard, J. E.; Trevor, D. J.; Reutt, J. E.; Lee, Y. T.; Shirley, D. A., Torsional Potential and Intramolecular Dynamics in the C₂H₄⁺ Photoelectron Spectra. *J. Chem. Phys.* **1984**, *81*, 5302-5309.
14. Willitsch, S.; Hollenstein, U.; Merkt, F., Ionization from a Double Bond: Rovibronic Photoionization Dynamics of Ethylene, Large Amplitude Torsional Motion and Vibronic Coupling in the Ground State of C₂H₄⁺. *J. Chem. Phys.* **2004**, *120*, 1761-1774.
15. Wörner, H. J.; Merkt, F., Jahn–Teller Effects in Molecular Cations Studied by Photoelectron Spectroscopy and Group Theory. *Angew. Chem. Int. Ed.* **2009**, *48*, 6404-6424.
16. Joalland, B.; Mori, T.; Martínez, T. J.; Suits, A. G., Photochemical Dynamics of Ethylene Cation C₂H₄⁺. *J. Phys. Chem. Lett.* **2014**, *5*, 1467-1471.
17. Zinchenko, K. S.; Ardana-Lamas, F.; Seidu, I.; Neville, S. P.; van der Veen, J.; Lanfaloni, V. U.; Schuurman, M. S.; Wörner, H. J., Sub-7-Femtosecond Conical-Intersection Dynamics Probed at the Carbon K-Edge. *Science* **2021**, *371*, 489.
18. Fransén, L.; Tran, T.; Nandi, S.; Vacher, M., Dissociation and Isomerization Following Ionization of Ethylene: Insights from Nonadiabatic Dynamics Simulations. *J. Phys. Chem. A* **2024**, *128*, 1457-1465.
19. Sewell, T. D.; Thompson, D. L.; Levine, R. D., Mode Selectivity in the Classical Power Spectra of Highly Vibrationally Excited Molecules. *J. Phys. Chem.* **1992**, *96*, 8006-8022.

Chapter 5. Control of the chemical reactivity by leveraging the electronic coherences built with an attopulse

Table of Contents

Chapter 5. Control of the chemical reactivity by leveraging the electronic coherences built with an attopulse	98
5.1 Quantum description of the intramolecular forces in a coherent vibronic wavepacket	98
5.2 Steering reactivity in LiH with an attopulse: role of the electronic coherences in the control of the force on the nuclei	102
5.3 Summary of contributions	103
5.4 References	103
5.5 Publication: “Electronic coherences built by an attopulse control the forces on the nuclei”	104

5.1 Quantum description of the intramolecular forces in a coherent vibronic wavepacket

Although the force is not an observable in quantum mechanics, we can use the Ehrenfest theorem to define the molecular force as the rate of change of the mean momentum of the nuclei over the coherent vibronic wavepacket represented by the wavefunction $\Psi(\mathbf{r}, \mathbf{R}, t)$. The derivation of the expression of the force and the application to the analysis of the quantum dynamics of LiH molecule have been published; see ref (1).

The Ehrenfest theorem (Equation 5.1) allows us to compute the time derivative of the mean value of any operator \hat{A} in terms of the mean value of its time derivative and of the commutator with the Hamiltonian. This theorem is valid for both pure states, described by a wavefunction such as $\Psi(\mathbf{r}, \mathbf{R}, t)$, and for mixed states, described by a Hermitian density operator $\rho(\mathbf{r}, \mathbf{R}, t)$

$$\frac{d}{dt}\langle\hat{A}\rangle = \left\langle\frac{\partial\hat{A}(x,t)}{\partial t}\right\rangle + \frac{i}{\hbar}\langle[\hat{H},\hat{A}]\rangle \quad (5.1)$$

If the operator \hat{A} is the nuclear momentum $\hat{p}_N = -i\hbar\hat{\nabla}_R$, which is an observable, and considering from now atomic units ($\hbar = 1$), the Ehrenfest theorem simplifies as:

$$\frac{d}{dt}\langle\hat{p}_N\rangle = i\langle[\hat{H},\hat{p}_N]\rangle = \langle[\hat{H},\hat{\nabla}_R]\rangle = -\langle[\hat{\nabla}_R,\hat{H}]\rangle \quad (5.2)$$

Equation 5.2 allows us to define the force much like in classical mechanics where $\vec{F} = d\vec{p}/dt$, but considering purely quantum effects, such as the nonadiabatic couplings and the entanglement

with the electric field of the pulse. For a molecular system in a coherent quantum superposition of several electronic states described by the vibronic wavefunction $\Psi(\mathbf{r}, \mathbf{R})$, the total molecular force in such a state is given formally by Equation 5.3.

$$F_{tot} = -\langle \Psi(\mathbf{r}, \mathbf{R}) | [\hat{\nabla}_{\mathbf{R}}, \hat{H}] | \Psi(\mathbf{r}, \mathbf{R}) \rangle \quad (5.3)$$

where the integration runs over both nuclear (\mathbf{R}) and electronic (\mathbf{r}) coordinates.

Substituting the expression of the molecular Hamiltonian $\hat{H} = \hat{H}^{el} + \hat{T}_N - \mathbf{E} \cdot \hat{\mu}$ and that of the expansion of the wavefunction $\Psi(\mathbf{r}, \mathbf{R}) = \sum_n \phi_n(\mathbf{r}; \mathbf{R}) \chi_n(\mathbf{R})$ in the adiabatic electronic basis into Equation 5.3, we obtained the following

$$F_{tot} = -\left\langle \sum_n \phi_n(\mathbf{r}; \mathbf{R}) \chi_n(\mathbf{R}) \left| [\hat{\nabla}_{\mathbf{R}}, (\hat{H}^{el} + \hat{T}_N - \mathbf{E} \cdot \hat{\mu})] \right| \sum_m \phi_m(\mathbf{r}; \mathbf{R}) \chi_m(\mathbf{R}) \right\rangle \quad (5.4a)$$

$$F_{tot} = -\left(\sum_{nm} \langle \phi_n(\mathbf{r}; \mathbf{R}) \chi_n(\mathbf{R}) | [\hat{\nabla}_{\mathbf{R}}, (\hat{H}^{el} + \hat{T}_N - \mathbf{E} \cdot \hat{\mu})] | \phi_m(\mathbf{r}; \mathbf{R}) \chi_m(\mathbf{R}) \rangle \right) \quad (5.4b)$$

Since the nuclear kinetic energy operator of the nuclei is given by the Laplacian $\hat{T}_N = -\hat{\nabla}_{\mathbf{R}}^2/2$ and it commutes with the momentum, the kinetic energy term vanishes from the commutator relation in Equation 5.4b, leaving only two sources for the force, the one coming from the electronic potentials and the one due to the interaction with the light pulse.

$$F_{tot} = -\sum_{nm} \langle \phi_n(\mathbf{r}; \mathbf{R}) \chi_n(\mathbf{R}) | [\hat{\nabla}_{\mathbf{R}}, \hat{H}^{el}] | \phi_m(\mathbf{r}; \mathbf{R}) \chi_m(\mathbf{R}) \rangle - \mathbf{E} \cdot \left(\sum_{nm} \langle \phi_n(\mathbf{r}; \mathbf{R}) \chi_n(\mathbf{R}) | [\hat{\nabla}_{\mathbf{R}}, \hat{\mu}] | \phi_m(\mathbf{r}; \mathbf{R}) \chi_m(\mathbf{R}) \rangle \right) \quad (5.5)$$

We can expand the term due to $[\hat{\nabla}_{\mathbf{R}}, \hat{H}^{el}] = \hat{\nabla}_{\mathbf{R}} \hat{H}^{el} - \hat{H}^{el} \hat{\nabla}_{\mathbf{R}}$ in Equation 5.5 as follows

$$F_{pot} = -\sum_{nm} \langle \phi_n(\mathbf{r}; \mathbf{R}) \chi_n(\mathbf{R}) | \hat{\nabla}_{\mathbf{R}} \hat{H}^{el} | \phi_m(\mathbf{r}; \mathbf{R}) \chi_m(\mathbf{R}) \rangle + \sum_{nm} \langle \phi_n(\mathbf{r}; \mathbf{R}) \chi_n(\mathbf{R}) | \hat{H}^{el} \hat{\nabla}_{\mathbf{R}} | \phi_m(\mathbf{r}; \mathbf{R}) \chi_m(\mathbf{R}) \rangle \quad (5.6)$$

Remembering that the electronic Hamiltonian in the adiabatic basis satisfies $\hat{H}^{el} \phi_n(\mathbf{r}; \mathbf{R}) = V_n(\mathbf{R}) \phi_n(\mathbf{r}; \mathbf{R})$, where $V_n(\mathbf{R})$ represents the potential energy, we get:

$$F_{pot} = - \sum_{nm} \langle \phi_n(\mathbf{r}; \mathbf{R}) \chi_n(\mathbf{R}) | \widehat{\nabla}_R V_m(\mathbf{R}) | \phi_m(\mathbf{r}; \mathbf{R}) \chi_m(\mathbf{R}) \rangle + \sum_{nm} \langle \phi_n(\mathbf{r}; \mathbf{R}) \chi_n(\mathbf{R}) | V_n(\mathbf{R}) \widehat{\nabla}_R | \phi_m(\mathbf{r}; \mathbf{R}) \chi_m(\mathbf{R}) \rangle \quad (5.7)$$

Using the chain rule for the gradient operator since it acts on both the energy $V_m(\mathbf{R})$ and the wavefunction:

$$F_{pot} = - \sum_{nm} \langle \phi_n(\mathbf{r}; \mathbf{R}) \chi_n(\mathbf{R}) | \widehat{\nabla}_R V_m(\mathbf{R}) | \phi_m(\mathbf{r}; \mathbf{R}) \chi_m(\mathbf{R}) \rangle - \sum_{nm} \langle \phi_n(\mathbf{r}; \mathbf{R}) \chi_n(\mathbf{R}) | V_m(\mathbf{R}) \widehat{\nabla}_R | \phi_m(\mathbf{r}; \mathbf{R}) \chi_m(\mathbf{R}) \rangle + \sum_{nm} \langle \phi_n(\mathbf{r}; \mathbf{R}) \chi_n(\mathbf{R}) | V_n(\mathbf{R}) \widehat{\nabla}_R | \phi_m(\mathbf{r}; \mathbf{R}) \chi_m(\mathbf{R}) \rangle \quad (5.8)$$

Which leads to

$$F_{pot} = - \sum_{nm} \langle \phi_n(\mathbf{r}; \mathbf{R}) \chi_n(\mathbf{R}) | \widehat{\nabla}_R V_m(\mathbf{R}) | \phi_m(\mathbf{r}; \mathbf{R}) \chi_m(\mathbf{R}) \rangle + \sum_{nm} \langle \phi_n(\mathbf{r}; \mathbf{R}) \chi_n(\mathbf{R}) | (V_n(\mathbf{R}) - V_m(\mathbf{R})) \widehat{\nabla}_R | \phi_m(\mathbf{r}; \mathbf{R}) \chi_m(\mathbf{R}) \rangle \quad (5.9)$$

The first term corresponds to the classical analog of a conservative force written as minus the gradient of the potential energy. We called this term F_V , and can be written concisely as

$$F_V = - \langle (\widehat{\nabla}_R V(\mathbf{R})) \rangle \quad (5.10)$$

The second term involves the energy difference between pairs of electronic states times the gradient of the electronic and nuclear wavefunctions. It can be expanded further:

$$\sum_{nm} (V_n(\mathbf{R}) - V_m(\mathbf{R})) \langle \phi_n(\mathbf{r}; \mathbf{R}) \chi_n(\mathbf{R}) | \widehat{\nabla}_R | \phi_m(\mathbf{r}; \mathbf{R}) \chi_m(\mathbf{R}) \rangle = \sum_{nm} (V_n(\mathbf{R}) - V_m(\mathbf{R})) \langle \phi_n(\mathbf{r}; \mathbf{R}) \chi_n(\mathbf{R}) | \widehat{\nabla}_R \phi_m(\mathbf{r}; \mathbf{R}) | \chi_m(\mathbf{R}) \rangle + \sum_{nm} (V_n(\mathbf{R}) - V_m(\mathbf{R})) \langle \phi_n(\mathbf{r}; \mathbf{R}) \chi_n(\mathbf{R}) | \widehat{\nabla}_R \chi_m(\mathbf{R}) | \phi_m(\mathbf{r}; \mathbf{R}) \rangle \quad (5.11)$$

Integrating over electronic coordinates, the second term vanishes since $\langle \phi_n(\mathbf{r}; \mathbf{R}) | \phi_m(\mathbf{r}; \mathbf{R}) \rangle = \delta_{nm}$ due to the orthonormality condition of the adiabatic basis, and $V_n(\mathbf{R}) - V_m(\mathbf{R}) = 0$ for $n = m$. The first term, on the other hand, involves the gradient of the electronic wavefunction with respect to the nuclear coordinates, which is none other than the nonadiabatic coupling (NAC) term

discussed before; see Equation 2.52i in Chapter 2: $\tau_{nm}(\mathbf{R}) = \langle \phi_n(\mathbf{r}; \mathbf{R}) | \hat{\nabla}_R \phi_m(\mathbf{r}; \mathbf{R}) \rangle$. Notice that $\tau_{nm} = 0$ for the case $n = m$ and that $\tau_{nm}(\mathbf{R}) = -\tau_{mn}(\mathbf{R})$ due to the antihermiticity of the gradient operator. This component of the force coming from the electronic Hamiltonian is designed as $F_{[\tau,V]}$ as it can be written more concisely leveraging the antihermitian character of the NAC. See the following equation:

$$F_{[\tau,V]} = \sum_{n \neq m} \langle \chi_n(\mathbf{R}) | \tau_{nm}(\mathbf{R}) (V_n(\mathbf{R}) - V_m(\mathbf{R})) | \chi_m(\mathbf{R}) \rangle = \langle [\hat{\tau}, \hat{V}(\mathbf{R})] \rangle \quad (5.12)$$

This way the force that drives the motion of the nuclei in the coupled potential energy surfaces F_{pot} has two terms

$$F_{pot} = F_V + F_{[\tau,V]} = -\langle (\hat{\nabla}_R V(\mathbf{R})) \rangle + \langle [\hat{\tau}, \hat{V}(\mathbf{R})] \rangle \quad (5.13)$$

These two terms were first derived by F. T. Smith in ref. (2). Similarly, as we have done with the commutator $[\hat{\nabla}_R, \hat{H}^{el}]$ in Equation 5.5, we can expand the term of the total force coming from $[\hat{\nabla}_R, \hat{\mu}]$, which quantifies the force due to the interaction with the electric field of the pulse, and we also get two terms,

$$F_{dip} = F_\mu + F_{[\tau,\mu]} = -\mathbf{E} \cdot \langle (\hat{\nabla}_R \mu(\mathbf{R})) \rangle + \mathbf{E} \cdot \langle [\hat{\tau}, \hat{\mu}(\mathbf{R})] \rangle \quad (5.14)$$

These two terms were not derived before and show that one can shape the initial force on the nuclei with the parameters of the exciting optical pulse (I)

In summary, the total force is a sum of four terms:

$$F_{tot} = -\langle (\hat{\nabla}_R V(\mathbf{R})) \rangle + \langle [\hat{\tau}, \hat{V}(\mathbf{R})] \rangle - \mathbf{E} \cdot \langle (\hat{\nabla}_R \mu(\mathbf{R})) \rangle + \mathbf{E} \cdot \langle [\hat{\tau}, \hat{\mu}(\mathbf{R})] \rangle \quad (5.15)$$

Provided the molecular wavefunction and the operators are expressed in an algebraic representation that allows the numerical propagation, our approach can be used to compute the vibronic force acting on the nuclei comprising both electronic (PES) and nuclear-electronic (NAC) effects for any number of dimensions. For a single dimension, as in the case of the linear LiH molecule, this is rather straightforward, and we utilized it to describe a proof-of-principle of our method, summarized in Section 5.2 and which was summarized in a publication (I).

For multidimensional systems, the complexity increases, and it is often unfeasible to solve the TDSE to compute the wave function and obtain the mean values of the operators describing the force. Nevertheless, a reduced set of nuclear coordinates can be identified for the time scale and dynamical processes under consideration to reduce the dimensionality, thereby simplifying the representations of the wavefunction and operators and the numerical computations. As an example, for the study of the ultrafast Jahn-Teller reorganization of CH_4^+ cation following sudden ionization of the stable T_d neutral molecule, the dynamics taking place in the first ≈ 50 fs in all dimensions for the nuclear motion has been well approximated by a reduced two-dimensional grid composed of two relevant nuclear coordinates which are linear combinations of cartesian displacements in Goncalves *et al.*, (3). We used the non-adiabatic couplings, potential energies, and wavefunctions

obtained in the work of Goncalves *et al.* and computed the forces developed during the motion of the wavepacket using our approach. Results and analysis are summarized in Chapter 7. They will be the object of a publication.

5.2 Steering reactivity in LiH with an attopulse: role of the electronic coherences in the control of the force on the nuclei

Using the Hamiltonian derived in Chapter 2 Section 2.2.4, we obtained the corresponding vibronic forces for LiH and LiT molecules, which characterize the time evolution of the wavepacket in the coupled electronic potential energy surfaces and its interaction with the electric field of the exciting essentially one cycle IR strong 2 fs pulse. The molecule of LiH is assumed to be oriented along the Z axis, with the Li atom pointing to Z+ and the H atom pointing to Z-. Experimentally, it is possible to orient molecules using various techniques (4-8), and LiH can be oriented since it has a large permanent dipole moment in its ground electronic state.

We integrated the TDSE to obtain the time-dependent wavefunctions including the interaction with the electric field of the pulse. Then, we computed the forces exerted on the nuclei by the vibronic wavepacket built by the pulse. The analysis of the different components of the force (Equation 5.13) showed the interplay between intrinsic molecular effects, such as the electronic potentials and non-adiabatic couplings, and external effects coming from the interaction with the electric field, which ultimately determines the course of dynamics of the molecule, and its reactivity. This allowed us to identify optimal parameters of the optical pulses to photoexcite the ground state to a specific combination of electronic states, which renders different forces on the nuclei and can favor one pathway or another. For LiH, the electronic states have alternating polarity in the FC region, which means that when the molecules are oriented in the laboratory frame, and the pulse is polarized along the intermolecular axis, the states can be populated or not based on the sign of the electric field at the maximum of the one cycle IR pulse, which can be controlled by controlling the CEP. For example, for IR pulses with CEP= π , the electric field is negative at its maximum, targeting mainly the S1 excited state, which has positive polarity in the FC region. On the other hand, when tuning the CEP=0, the electric field is positive at its maximum and induces a totally different excitation because it allows mainly the excitation to the S4 state of negative polarity. Since the molecule on each electronic state follows a different asymptote in the dissociation limit, which is determined by the electronic state of the Li atom, the control of the composition of the wavepacket that can be induced with the pulse will influence the reactivity of the molecule, here the fragmentation products. The forces that arise from the vibronic wavepacket will drive the nuclei in a direction that the parameters of the exciting pulse could predetermine. By analyzing the forces, we can test on the computer if the pulses to be designed will have the intended effect, and we can “edit” the pulses by identifying which parameters could be tuned to improve the outcomes.

From a theoretical perspective, in ref. (1), we showed that the nonclassical force $F_{[\tau,V]}$ alters the motion of the wavepacket like a friction force on the different potential surfaces and competes with the gradient term F_V , slowing down or accelerating the wave packet motion depending on whether it is positive or negative. The sign of the $F_{[\tau,V]}$ is also found to determine the direction of the population transfer between the two states that are non-adiabatically coupled. Finally, we presented a method based on isotopic substitution and a gated Fourier transform and illustrated how to use it to differentiate between the vibrational and electronic effects of the forces. This

allows the identification of relevant coordinates that are activated during the dynamics, which can be used to inquire about possible relaxation pathways driven by the excitation and opens the way to the rational design of experiments that aim to control chemical reactivity using attosecond pulses. Overall, the analysis of the force can help us understand the patterns observed in the dynamics and discern between purely vibrational effects and electronic ones. We have published this work in ref (1), which is presented at the end of this chapter.

5.3 Summary of contributions

All the authors contributed to the organization of the manuscript, the analysis of the results, and the development and refinement of ideas, providing valuable advice and feedback on both the text and figures.

Manuel Cardosa Gutierrez processed the LiH grid data (potential energy curves of electronic states, dipole and non adiabatic couplings) computed by Stephan van den Wildenberg (9), and constructed the Hamiltonian, including an exact representation of the nonadiabatic couplings and the interaction with the electric field of the pulse, within the dipole approximation. He expressed the Hamiltonian in sparse matrix form for efficient storage, facilitating the numerical solution of the TDSE. He diagonalized the Hamiltonian to obtain the initial state and implemented the 4th-order Runge Kutta algorithm to solve the TDSE, obtaining the wavefunctions as a function of time.

All the authors derived the expression for the force exerted by the wavepacket on the nuclei from the Ehrenfest theorem of quantum mechanics, deriving two new terms, F_μ and $F_{[\hat{t},\mu]}$, arising from the interaction with the electric field, which had not been previously reported in the literature. Manuel Cardosa implemented the force equations in a Fortran program and applied this formalism to analyze the molecular response to the excitation with the attopulse.

Manuel Cardosa Gutierrez and Françoise Remacle studied the literature and selected appropriate pulse parameters and observables for analyzing the dynamics, ensuring the research would be of interest to the experimental attochemistry community. Their work demonstrated the significance of the force formalism for studying photoexcited molecules with few-femtosecond and attosecond pulses.

Raphael D. Levine contributed his vast expertise in quantum mechanics to the derivation of the analytical expression for the force. He proposed the term “friction” to describe the role of the NAC force, based on the behavior it exhibits. He also suggested investigating isotopic effects in the dynamics by comparing LiH and LiT isotopomers, which led to the development of a powerful analytical method that can be used to discern between vibrational and purely electronic contributions to the total force.

5.4 References

1. M. Cardosa-Gutierrez, R. D. Levine, F. Remacle, Electronic coherences built by an attopulse control the forces on the nuclei. *J. Phys. B: At. Mol. Opt. Phys.*, (2024).
2. F. T. Smith, Diabatic and Adiabatic Representations for Atomic Collision Problems. *Phys. Rev.* **179**, 111-123 (1969).

3. C. E. M. Gonçalves, R. D. Levine, F. Remacle, Ultrafast geometrical reorganization of a methane cation upon sudden ionization: an isotope effect on electronic non-equilibrium quantum dynamics. *Phys. Chem. Chem. Phys.* **23**, 12051-12059 (2021).
4. R. B. Bernstein, D. R. Herschbach, R. D. Levine, Dynamical aspects of stereochemistry. *J. Phys. Chem.* **91**, 5365-5377 (1987).
5. S. Fleischer, Y. Zhou, R. W. Field, K. A. Nelson, Molecular Orientation and Alignment by Intense Single-Cycle THz Pulses. *Phys. Rev. Lett.* **107**, 163603 (2011).
6. O. Ghafur *et al.*, Impulsive orientation and alignment of quantum-state-selected NO molecules. *Nature Phys* **5**, 289-293 (2009).
7. P. M. Kraus, D. Baykusheva, H. J. Wörner, Two-Pulse Field-Free Orientation Reveals Anisotropy of Molecular Shape Resonance. *Phys. Rev. Lett.* **113**, 023001 (2014).
8. H. Stapelfeldt, T. Seideman, *Colloquium*: Aligning molecules with strong laser pulses. *Rev. Mod. Phys.* **75**, 543-557 (2003).
9. S. van den Wildenberg, B. Mignolet, R. D. Levine, F. Remacle, Temporal and spatially resolved imaging of the correlated nuclear-electronic dynamics and of the ionized photoelectron in a coherently electronically highly excited vibrating LiH molecule. *The Journal of Chemical Physics* **151**, 134310 (2019).

5.5 Publication: “Electronic coherences built by an attopulse control the forces on the nuclei”

INVITED ARTICLE

Electronic coherences built by an attopulse control the forces on the nuclei

To cite this article: Manuel Cardosa-Gutierrez *et al* 2024 *J. Phys. B: At. Mol. Opt. Phys.* **57** 133501

View the [article online](#) for updates and enhancements.

You may also like

- [Long-lived oscillatory incoherent electron dynamics in molecules: *trans*-polyacetylene oligomers](#)
Ignacio Franco, Angel Rubio and Paul Brumer
- [Quantum mechanics of excitation transport in photosynthetic complexes: a key issues review](#)
Federico Levi, Stefano Mostarda, Francesco Rao *et al.*
- [Disentangling the complexity of coupled vibrations by two-dimensional electronic-vibrational spectroscopy](#)
Xuanchao Zhang, Zihui Liu, Ajay Jha *et al.*

Invited Article

Electronic coherences built by an attopulse control the forces on the nuclei

Manuel Cardosa-Gutierrez¹, R D Levine^{2,3,4} and F Remacle^{1,2,*} ¹ Theoretical Physical Chemistry, UR MOLSYS, University of Liege, Liège, Belgium² Fritz Haber Center, Institute of Chemistry, The Hebrew University of Jerusalem, Jerusalem 91904, Israel³ Department of Molecular and Medical Pharmacology, David Geffen School of Medicine, University of California, Los Angeles, CA 90095, United States of America⁴ Department of Chemistry and Biochemistry, University of California, Los Angeles, CA 90095, United States of AmericaE-mail: fremacle@ulg.ac.be

Received 31 January 2024, revised 1 May 2024

Accepted for publication 23 May 2024

Published 6 June 2024



CrossMark

Abstract

Att pulses have an energy bandwidth broad enough to coherently excite several electronic states of molecules. Towards the control of chemical reactivity by att pulses we derive the quantum mechanical expression for the force exerted on the nuclei in such a vibronic wave packet both during and after the exciting pulse. Tuning the pulse parameters allows accessing specific electronic coherences that determine the force strength and direction during and after the pulse. Following the pulse, the force due to the non adiabatic interactions accelerates or slows down the motion of the vibronic wave packet on the excited electronic states and its sign controls the direction of population transfer. Computational results for the LiH and LiT molecules and the probing by the emission dipole are discussed.

Supplementary material for this article is available [online](#)

Keywords: attochemistry, ultrafast vibronic quantum dynamics, quantum mechanical force

1. Introduction

Electronic coherences arise in molecules when wave packets on two different electronic states overlap. Broad-in-energy attosecond pulses [1–3] allow exciting coherently several electronic states in molecules, thereby creating electronic coherences in the Franck–Condon region. These electronic coherences drive the motion of the non-equilibrium electronic density on a purely electronic time scale, before a significant onset of the nuclear motion [4–7]. They induce ultrafast charge migration between different parts of the molecule during

which one could implement charge directed reactivity [8–12]. In molecules excited by att pulses, the vibronic dynamics is therefore in a post Born–Oppenheimer regime [13]. The electronic state is not in equilibrium with the instantaneous position of the nuclei and so can be exploited to control chemical reactivity. [4, 14–17] Tuning the parameters of the pulse, such as its carrier frequency, envelope duration, polarization and carrier envelope phase (CEP) provides control of the electronic motion in the initially pumped state and of the entanglement between the electronic and nuclear motions [18–20]. Towards this goal, we discuss here the relative importance of the different terms of the exact quantum mechanical force exerted by the vibronic wave packet on the nuclei during and after the pulse. By ‘exact’ force, we mean that the force is defined

* Author to whom any correspondence should be addressed.

by the equation of motion of the momentum operator given by the Ehrenfest theorem and its mean value computed over the total ‘exact’ vibronic wave function computed by solving the time-dependent Schrödinger equation numerically, see section 2.1 below. As a practical example (section 3), we use fully quantum dynamical simulations of the response of the LiH molecule to ultra short IR and VIS pulses that allow controlling the subsequent dynamics [14, 16, 17, 21, 22]. To further examine the force, we compare the dynamics in the LiH and its LiT isotopomer, $T = {}^3\text{H}$, and compute the emission dipole, whose time dependence tracks the force. Concluding remarks are given in section 4.

2. Quantum mechanical force exerted by a vibronic wavepacket

2.1. The four terms of the quantum mechanical force

The force exerted by the vibronic wave packet on the nuclei is defined as the time-derivative of the mean value of the nuclear momentum, for a diatomic molecule, $\hat{P}_N = -i\hbar\hat{\nabla}_R$, over the vibronic wave function. The vibronic wave function is expanded in a basis of separable terms, $\phi_n^{\text{el}}(\mathbf{r};R)\chi_n(t,R)$,

$$|\Psi(t, \mathbf{r}, R)\rangle = \sum_n \phi_n^{\text{el}}(\mathbf{r};R)\chi_n(t,R) \quad (1)$$

where \mathbf{r} stands for the electronic coordinates and R the internuclear distance. The electronic wave functions $\phi_n^{\text{el}}(\mathbf{r};R)$ ’s are the adiabatic electronic states, $\hat{H}^{\text{el}}\phi_n^{\text{el}}(\mathbf{r};R) = V_n(R)\phi_n^{\text{el}}(\mathbf{r};R)$, and $\chi_n(t,R)$ is the time-dependent nuclear wave function. Using the Ehrenfest theorem (atomic units (a.u.) are used throughout), one gets for the force:

$$F_{\text{tot}} = \frac{d\langle\hat{P}_N\rangle}{dt} = i\langle[\hat{P}_N, \hat{H}]\rangle = -\langle[\hat{\nabla}_R, \hat{H}]\rangle. \quad (2)$$

The full Hamiltonian, $\hat{H} = \hat{T}_N + \hat{H}^{\text{el}} - \mathbf{E}(t) \cdot \hat{\boldsymbol{\mu}}$, includes the interaction of the molecule with the electric field, $\mathbf{E}(t)$, of the pulse in the dipole approximation, $\hat{\boldsymbol{\mu}}$ is the molecular dipole. Note that in general, the polarization direction of the electric field can make an angle with respect to the molecular axis of the diatomic molecule [14]. In the examples below, we consider oriented LiH molecules for which the polarization direction is parallel to the internuclear axis. Computing the commutators and integrating over electronic coordinates, the total force is a sum of four terms:

$$F_{\text{tot}} = -\langle(\hat{\nabla}_R\hat{V}(R))\rangle + \langle[\hat{\tau}, \hat{V}(R)]\rangle + \mathbf{E}(t) \cdot \langle(\hat{\nabla}_R\hat{\boldsymbol{\mu}}(R))\rangle - \mathbf{E}(t) \cdot \langle[\hat{\tau}, \hat{\boldsymbol{\mu}}(R)]\rangle \quad (3)$$

where $\hat{V}(R)$ is the potential energy and $\hat{\tau}$ is the non adiabatic coupling (NAC) between the electronic states, $\tau_{nm} = \langle\phi_n^{\text{el}}|\hat{\nabla}_R|\phi_m^{\text{el}}\rangle$. The first two terms of equation (3) were derived by Smith [23] thereby defining a generalized momentum, $\hat{P} = \hat{P}_N + \hat{\tau}$, see also [24, 25]. The third and

fourth terms are due to the interaction with the light field. Their introduction and their role in control are the central subjects of this paper.

The force defined in equation (3) is an average over both electronic and nuclear degrees of freedom both of which are treated quantum mechanically. It is the instantaneous force on the nuclei and, as such, it is different from the mean field force for the motion of the classical nuclei derived in Ehrenfest dynamics, which is obtained by averaging over the electronic wave functions, ϕ_n^{el} ’s, only [26–28].

2.2. Explicit expressions for the quantum dynamics of a diatomic molecule

The vibronic dynamics in LiH is computed for several coupled electronic states using a grid description for the internuclear distance, R , as in previous works [16, 29]. The vibronic wave function is written as

$$|\Psi(t)\rangle = \sum_{g=1}^{N_g} \sum_{i=1}^{N_e} c_{gi}(t) |gi\rangle \quad (4)$$

where $|gi\rangle$ is a basis function localized at grid point R_g on the adiabatic electronic state i . In the results reported below, we include $N_g = 512$ grid points and $N_e = 7$ electronic states. The molecular Hamiltonian matrix, \mathbf{H} , used to integrate the time-dependent Schrödinger equation, $d\mathbf{c}/dt = -i\mathbf{H}\mathbf{c}$, includes all the NAC terms and the interaction with the pulse in the dipole approximation. For a diatomic molecule, we get

$$\begin{aligned} \mathbf{H} &= \mathcal{P}^2 + V(R) - \mathbf{E}(t) \cdot \boldsymbol{\mu} \\ &= -\frac{1}{2\mu} (\nabla_R^2 + 2\boldsymbol{\tau}(R) \cdot \nabla_R + (\nabla_R\boldsymbol{\tau}(R)) + \boldsymbol{\tau}(R) \cdot \boldsymbol{\tau}(R)) \\ &\quad + V(R) - \mathbf{E}(t) \cdot (\boldsymbol{\mu}^{\text{nuc}}(R) + \boldsymbol{\mu}^{\text{el}}(R)) \end{aligned} \quad (5)$$

where $V(R)$ is the diagonal matrix of the potential energies of the adiabatic electronic states, $V_i(R)$. The matrix of the dipole operator has a nuclear and electronic term:

$$\boldsymbol{\mu} = \boldsymbol{\mu}^{\text{nuc}}(R) + \boldsymbol{\mu}^{\text{el}}(R). \quad (6)$$

The electronic dipole matrix, $\boldsymbol{\mu}^{\text{el}}(R)$, is diagonal in grid points

$$\boldsymbol{\mu}^{\text{el}}(R) = \sum_{i,j=1}^{N_e} \boldsymbol{\mu}_{ij}^{\text{el}}(R). \quad (7)$$

The nuclear dipole matrix is given by

$$\boldsymbol{\mu}^{\text{nuc}}(R) = \sum_{\alpha=1}^{N_{\text{nuc}}} eZ_{\alpha}R_{\alpha} = fR, \quad (8)$$

with

$$f = (m_{\text{H}}Z_{\text{Li}} - m_{\text{Li}}Z_{\text{H}}) / (m_{\text{Li}} + m_{\text{H}}) = 0.5$$

in the molecular frame attached to the center mass, where the Li has a positive z coordinate, see figure S1. The explicit expression of the force (equation (3)) in terms of the vector of the time-dependent amplitudes, \mathbf{c} (equation (4)), takes the form:

$$F_{\text{tot}} = -\mathbf{c}^T (\nabla_R V) \mathbf{c} - \mathbf{c}^T [\boldsymbol{\tau}, \mathbf{V}] \mathbf{c} + \mathbf{E}(t) \cdot (\mathbf{c}^T (\nabla_R \boldsymbol{\mu}^{\text{nuc}}) \mathbf{c} + \mathbf{c}^T (\nabla_R \boldsymbol{\mu}^{\text{el}}) \mathbf{c}) + \mathbf{E}(t) \cdot (\mathbf{c}^T [\boldsymbol{\tau}, \boldsymbol{\mu}^{\text{el}}] \mathbf{c}). \quad (9)$$

In principle it is clear from equation (9) but in view of its importance we point out explicitly that in addition to terms diagonal in the electronic index of the states there is also significant contributions from the coherences between different electronic states. The control of these coherences is an essential part of our ability to control the force.

In equation (9) the third and fourth terms gather all the contributions to the force that result from the dipole interaction and can be controlled by the pulse parameters:

$$F_{\text{dip}} = +\mathbf{E}(t) (\mathbf{c}^T (\nabla_R \boldsymbol{\mu}^{\text{nuc}}) \mathbf{c} + \mathbf{c}^T (\nabla_R \boldsymbol{\mu}^{\text{el}}) \mathbf{c}) + \mathbf{E}(t) (\mathbf{c}^T [\boldsymbol{\tau}, \boldsymbol{\mu}^{\text{el}}] \mathbf{c}) = F_{\mu} + F_{[\boldsymbol{\tau}, \boldsymbol{\mu}^{\text{el}}]} \quad (10)$$

where

$$F_{\mu} = E(t) \sum_{gi} |c_{gi}(t)|^2 ((\nabla_R \mu_{gi}^{\text{nuc}}) + (\nabla_R \mu_{gi,gi}^{\text{ele}})) + \sum_{gi, gj, j \neq i} c_{gi}(t) c_{gj}^*(t) (\nabla_R \mu_{gi, gj}^{\text{ele}}) \quad (11)$$

and depends on the electronic coherences through its second term. $\mu^{\text{nuc}}(\mathbf{R})$ has a linear dependence with respect to \mathbf{R} (equation (8)), so that $\mathbf{E}(t) \sum_{gi} |c_{gi}(t)|^2 \nabla_R \mu_{gi}^{\text{nuc}} = 0.5 \mathbf{E}(t)$ and the nuclear dipole $\boldsymbol{\mu}^{\text{nuc}}$ does not contribute to the commutator $[\boldsymbol{\tau}, \boldsymbol{\mu}]$. The term $F_{[\boldsymbol{\tau}, \boldsymbol{\mu}^{\text{el}}]}$ also depends on the electronic coherences

$$F_{[\boldsymbol{\tau}, \boldsymbol{\mu}^{\text{el}}]} = \mathbf{E}(t) \sum_{i,j,k}^{Ne} \sum_g^{Ng} c_{gi}^*(t) c_{gk}(t) (\tau_{gi, gj} \mu_{gj, gk}^{\text{el}} - \mu_{gi, gj}^{\text{el}} \tau_{gi, gk}). \quad (12)$$

The first two terms of equation (9) depend on the potentials $V_i(\mathbf{R})$ of the electronic states

$$F_{\text{pot}} = -\mathbf{c}^T (\nabla_R V) \mathbf{c} - \mathbf{c}^T [\boldsymbol{\tau}, \mathbf{V}] \mathbf{c} = F_V + F_{[\boldsymbol{\tau}, V]} \quad (13)$$

$$F_V = \sum_{gi}^{NeNg} |c_{gi}|^2 (t) \nabla_R V_{gi} \quad (14)$$

$$F_{[\boldsymbol{\tau}, V]} = \sum_{i,k}^{Ne} \sum_g^{Ng} c_{gi}^*(t) c_{gk}(t) \tau_{gi, gk} (V_{gk} - V_{gi}). \quad (15)$$

In equations (10) and (13), the terms that depend on the gradients, $\nabla_R \boldsymbol{\mu}^{\text{nuc}}$ and $\nabla_R V$, are an average over the populations in each electronic state, while the other terms oscillate with the periods of the electronic coherences, $c_{gi}^*(t) c_{gk}(t)$. From equation (10) one can anticipate that the force due to the dipole interaction, F_{dip} , can be manipulated by tailoring the

magnitude, the time profile and the polarization of the electric field of the pulse, to either counteract or enhance the effect of the potential term, F_{pot} (equation (13)).

We illustrate the time-dependence of the force on the nuclei exerted by a fully quantal vibronic wave function both during and after the excitation of the LiH molecule by an attopulse. We show that tuning the force due to the interaction with the pulse electric field, F_{dip} (equation (10)), with the attopulse parameters can be effectively applied to control the force on the nuclei for realistic pulses. Two types of control are discussed: a control by one cycle strong NIR pulses that differ by their CEP values and by a several cycle 4 fs VIS pulse. Note that the time dependence of the total force can be computed straightforwardly by taking the numerical derivative of the mean value of the generalized momentum, $d\langle \mathcal{P} \rangle / dt$, with $\hat{\mathcal{P}} = -i\hat{\nabla}_R + \hat{\tau}$.

The quantum dynamics is computed using the potential energy, dipole and NAC curves of [16]. For completeness, they are plotted in figures S1–S3 of the SM. We take the pulse to be oriented along the molecular axis (see figure S1 for the orientation of LiH in the molecular frame) which is a reasonable approach because of the large value of the permanent dipole of the LiH molecule, (at equilibrium $\mu_{\text{eq}}^{\text{el}} = 2.1$ a.u.) [30, 31]. By optical selection rules, such a pulse excites the manifold of Σ states only. The time profile of the electric field of the pulse is defined by $\mathbf{E}(t) = -d\mathbf{A}(t)/dt$ and the vector potential $\mathbf{A}(t)$ has a Gaussian envelope. The expression for $\mathbf{E}(t)$ is

$$\mathbf{E}(t) = |E_0| \vec{\epsilon} \cdot \exp\left(-\frac{(t-t_p)^2}{2\sigma_p^2}\right) \left[\cos(\omega_p(t-t_p) + \phi) - \left(\frac{t-t_p}{\omega_p \sigma_p^2}\right) \sin(\omega_p(t-t_p) + \phi) \right] \quad (16)$$

where $|E_0|$ is the peak intensity of the pulse and $\vec{\epsilon}$ its polarization direction. ω_p is the carrier frequency and ϕ the CEP. The pulse is centered at the time t_p and its full width at half maximum (FWHM) equal to $2\sqrt{2 \ln 2} \sigma_p$.

3. Results and discussion

We begin by a NIR essentially one cycle pulse, with a carrier frequency of $\omega_p = 0.0633$ a.u. (720 nm), a FWHM = 0.8 fs, centered at $t_p = 12.1$ fs (500 a.u.) and a peak intensity, $|E_0|$ of 0.04 a.u. Here the relevant control parameter is the value of the CEP, ϕ , see equation (16). The LiH molecules are oriented (which is justified by the large permanent dipole (2.24 a.u., see figure S2) of the ground state) and the direction of polarization of the electric field $\hat{\epsilon}$ is parallel to the molecular axis. A CEP = 0 corresponds to the maximum of $\mathbf{E}(t)$ oriented towards the Li atom while a CEP = π corresponds to the maximum of $\mathbf{E}(t)$ oriented towards the H atom, see figure S1 of the SM. The populations in the electronic states of the LiH molecule during this pulse are plotted in figures 1(a) and (b) for the two CEP's. As discussed previously [14, 16, 17], for oriented LiH molecules, the CEP of the one cycle IR pulse allows selecting which electronic states are preferentially excited because they have alternating sign of their polarity in the FC region. For the pulse used here, a CEP = 0 favors the excitation

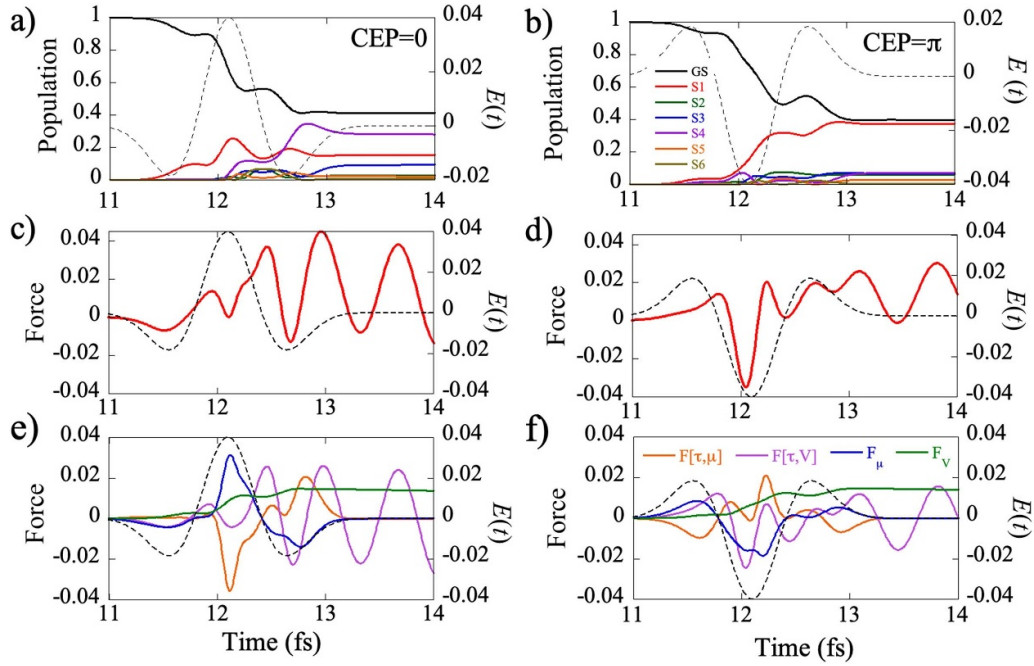


Figure 1. Transient population dynamics during the exciting NIR one cycle pulse (a) CEP = 0, (b) CEP = π . (c) And (d) time profile of the total force, F_{tot} (equation (9)) in atomic units (a.u.), in red, left ordinate, over the time interval during the pulse shown as a dashed curve in a.u., right ordinate. (e) And (f) time profile of the four terms of the total force during the pulse (equations (10) to (15)). See figure S5 for the different components of the force for the dynamics in LiT.

of the S4 state (figure 1(a)) with lower populations in S2 and S3 while for the CEP = π pulse, the largest population after the pulse is in S1 (figure 1(b)) and the population in S2 is larger than in S3 and S4. The CEP therefore allows controlling the population in the excited states, whose asymptotic populations determine the yields in fragments, each asymptote correlating to a different excited state of the Li atom see figure S4 of the SM. The total force (equation (9)) during the pulse is plotted in figures 1(c) and (d). At its maximum, the force is positive for a CEP = 0, while it is negative for the CEP = π pulse. However, at the maximum of the pulse, the total force (positive) for CEP = 0 (figure 1(c)) is significantly smaller than the force for the CEP = π pulse (figure 1(d)), which is large and negative (-0.04 a.u., one a.u. of force = 82 nN).

This can be understood by analyzing the time dependence and the phase of the different terms contributing to the force, shown in figures 1(e) and (f). During the pulse, the term F_V , equation (14), due to the potential gradients, remains small for both excitations and the force terms due to the interaction with the pulse, F_{dip} (equation (10)) dominate. The force due to the dipole gradient, F_μ , equation (11), (blue line in figures 1(e) and (f)), is dominated by the nuclear dipole contribution (equation (11)), the electronic contribution being smaller and of opposite sign, and follows the sign of the electric field. The terms that involve the NAC coupling and the electronic coherences, $F_{[\tau, \mu^{\text{el}}]}$ (equation (12), orange) and $F_{[\tau, V]}$ (equation (15), violet) play a key role, and either enhance or counteract the effect of the F_μ term. Note that the $F_{[\tau, \mu^{\text{el}}]}$ term is multiplied by the strength of the electric field. The $F_{[\tau, \mu^{\text{el}}]}$ term is large and of opposite sign to F_μ for the CEP = 0

excitation while the term $F_{[\tau, V]}$ (violet) remains small, which leads to a small value of the total force during the pulse. The situation is opposite for the CEP = π excitation, which populates the S1. In that case, the $F_{[\tau, \mu^{\text{el}}]}$ is small and the $F_{[\tau, V]}$ term is large and of the same sign as F_μ which leads to a large total force at the maximum of the pulse, aligned with the direction of the electric field. The resulting total force at the maximum of the electric field (-0.04 a.u., one a.u. of force = 82 nN).

During the short pulse, there is no significant mass effect and the patterns of the force terms for the LiT are very similar to those of LiH, see figure S5.

The effect of the force on the nuclei can be probed by two dynamical observables, the time-dependence of the emission dipole, and the variation of the mean value of the internuclear distance, $\langle R(t) \rangle$, as a function of time. We begin by discussing the effect of the force on the mean internuclear distance, $\langle R(t) \rangle = \sum_g^{N_g} \sum_i^{N_e} |c_{gi}(t)|^2 R_g$. Since it does not depend on the electronic index it can be written as an observable on the nuclear density matrix, $\bar{\rho}_{gg'} = \sum_{i=1}^{N_e} c_{gi}^*(t) c_{g'i}(t)$. The ultra short exciting pulse builds a superposition of several electronic states, and the nuclear and electronic motions are correlated throughout the dynamics. Insights on the role of the force on the nuclei exerted by the vibronic wave packet are therefore provided by the projection of $\langle R(t) \rangle$ on the different electronic states, i , $\langle R_i(t) \rangle$.

The time dependence of $\langle R_i(t) \rangle$ on a single bound excited electronic state was reconstructed using pump-probe spectroscopy in the diatomic molecules Na₂ [32] and D₂⁺ [33] monitoring the photoelectron kinetic energy and the kinetic

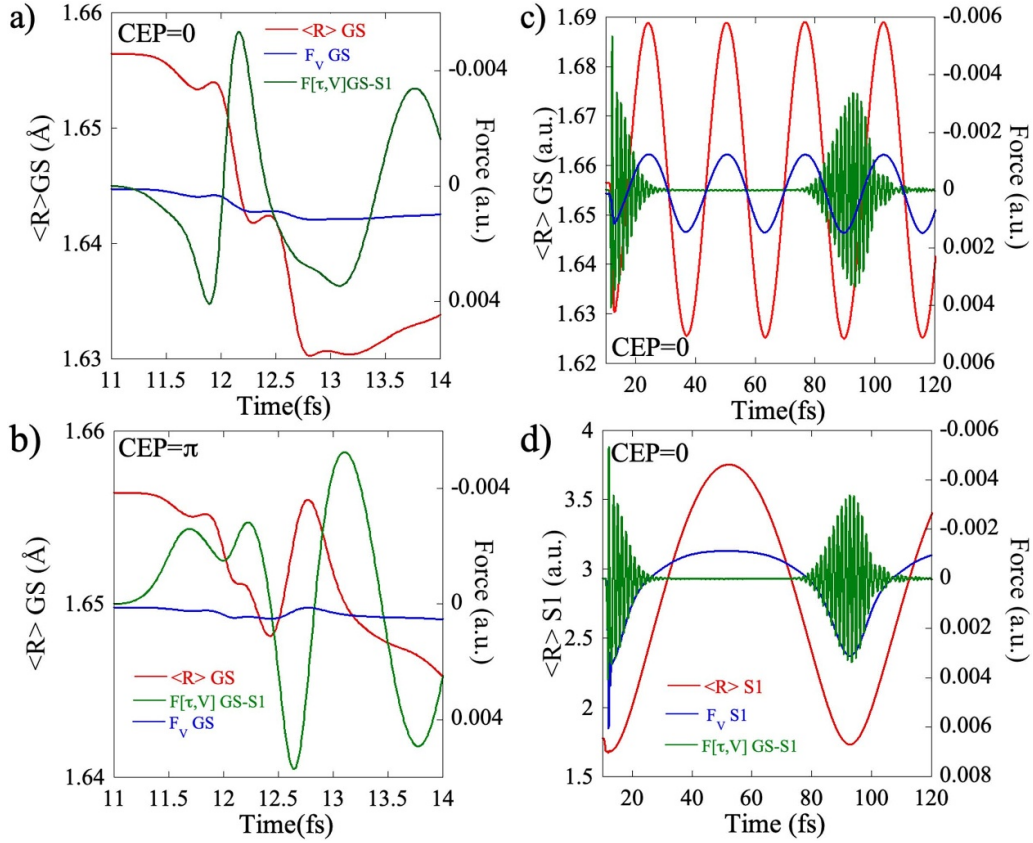


Figure 2. Time evolution of $\langle R_{GS}(t) \rangle$ and of the two components of the force that control it, F_V (blue) and $F_{[\tau,V]GS-S1}$ (green) during and right after the pulse for the CEP = 0 pulse (panel (a)) and the CEP = Π pulse (panel (b)). Panels (c) and (d): Long time evolution of the force terms and $\langle R_{GS}(t) \rangle$ (red) (c) and $\langle R_{S1}(t) \rangle$ (red) (d) as well as the two components of the force, $F_{[\tau,V]GS-S1}$ and F_V for CEP = 0. Note that the axis direction of the right ordinate (force) has been reversed to emphasize the correlation between the change of sign in $\langle R(t) \rangle$ and the sign of the force.

energy of the fragments respectively. $\langle R_i(t) \rangle$ is recovered from a priori knowledge of the potential curves of the neutral excited state and of the cation for Na_2 and the bound excited state and the dissociative one for D_2^+ . These measurements were later related to the nuclear flux [34–36] and extended to the electronic flux [37, 38]. In the case of the excitation by a broad-in energy-short-in-time pulse, several excited electronic are coherently populated and they exchange population because of the NAC, rendering the above flux procedures difficult to implement.

The effect of the sign of the force, in particular of its non classical term, $F_{[\tau,V]}$, on the spreading of the wave packet on the electronic states and on the associated $\langle R_i(t) \rangle$ values is shown in figures 2 and 3. Figure 2 shows the force and the mean value of R , $\langle R_i(t) \rangle$, for the bound motion on the GS. $\langle R_{GS}(t) \rangle$ is plotted in figures 2(a) and (b) for the two values of the CEP until the end of the exciting pulse. Also shown in figure 2 are the time evolution of the only two components of the force which affect $\langle R_{GS}(t) \rangle$ after the pulse, the term due the gradient, $F_{V,GS}$ (equation (14)), and the term due to the NAC coupling between the GS and S1, $F_{[\tau,V]GS-S1}$ (equation (15)). The internuclear distance, R , is defined as $R = z_{Li} - z_H$ with the origin of the molecular frame attached at

the center of mass and $z_{Li} > 0$, see figure S1. A negative force corresponds to an elongation of the bond, that is, an increase of R , while a positive force corresponds to a compression of the bond and a decrease of R .

Right after the pulse is over, after 13.5 fs, one can see that the major component of the force is the non classical $F_{[\tau,V]GS-S1}$ term, which is of opposite sign for the two CEP values of the exciting pulse. There is an increase of $\langle R_{GS}(t) \rangle$ after the pulse for the CEP = 0 pulse and a decrease of $\langle R_{GS}(t) \rangle$ for the CEP = Π . The value of the CEP therefore controls the phase of the vibrational motion on the GS.

At longer times, the electronic coherence GS-S1 vanishes until its revival due to the recurrence of the wave packet on S1 at ≈ 84 fs. So the force for the GS is only due to the potential term, F_V , which leads to oscillations of the bond distance with a period of ≈ 24 fs as shown in figure 2(c) for the CEP = 0 pulse. A similar behavior is obtained for the wave packet on S1, shown in figure 2(b), which oscillates with an 84 fs period.

Heatmaps of the localization of the wave packet vs time on the excited electronic states S2, S3 and S4 are plotted in figure 3. These excited states are dissociative and therefore the contribution of the potential gradient, F_V (black dotted line) to the force becomes negligible after the pulse. Then,

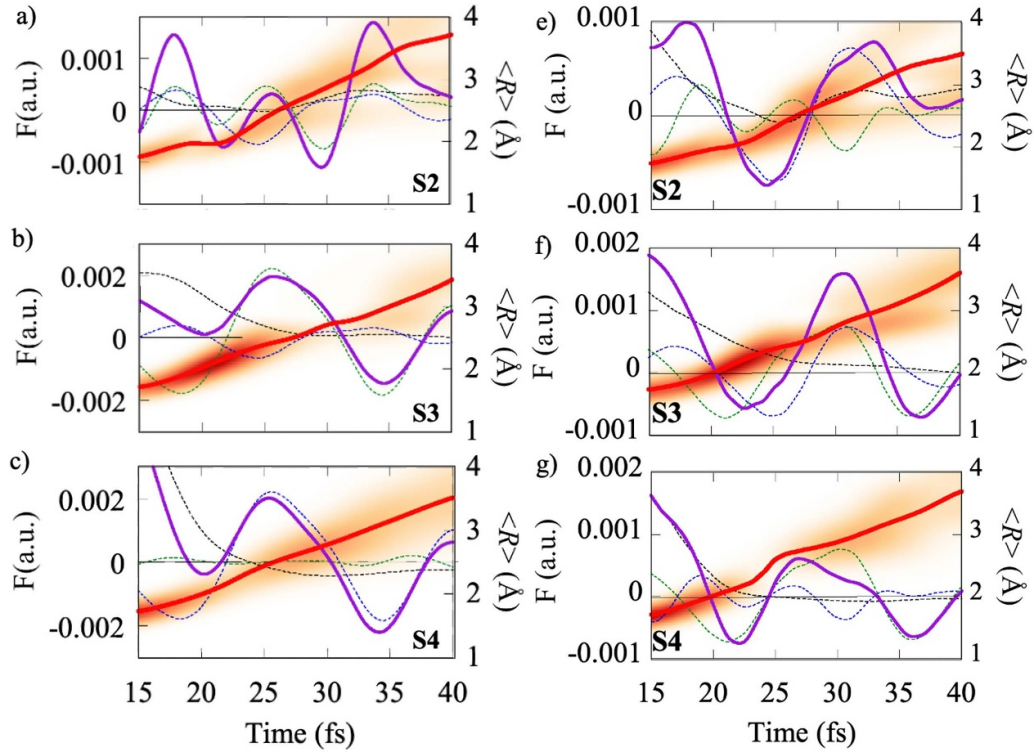


Figure 3. Heatmaps of the time-dependence of localization of the wave packet on the excited electronic states S2, S3 and S4 vs time for the exciting pulse with a CEP = 0 (panels (a)–(c)) and CEP = π (panels (e)–(g)). $\langle R_i(t) \rangle$ is plotted in red thick line (right ordinate). The total force affecting the nuclei on electronic state is plotted in thick violet line (left ordinate). Its components are plotted in dotted lines, F_V in black and $F_{[\tau,V]GS-S1}$ for the two states involved in blue and in green.

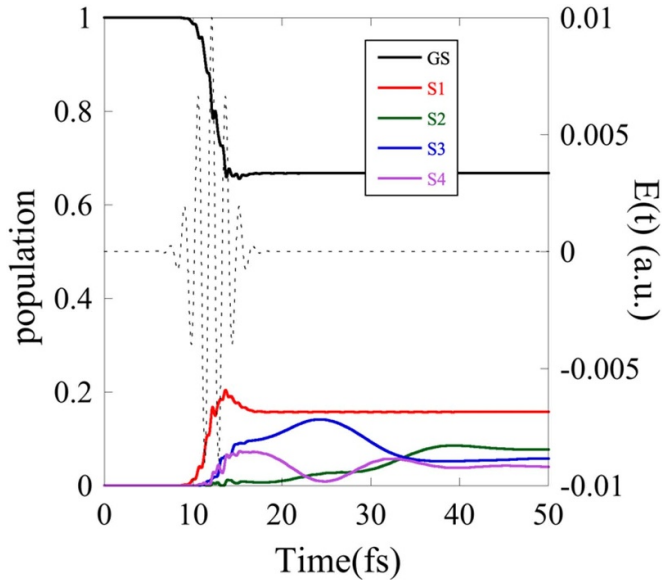


Figure 4. Populations in the excited electronic states resulting from the excitation by a 4 fs VIS $\omega_p = 2.6$ eV pulse ($|E_0| = 0.01$ a.u.). There is no effect of the CEP but tuning the wavelength and the duration of the pulse allows controlling the populations in the excited electronic states. Note how the population in S2 that was essentially zero at the end of the pulse is rising due to the NAC between S3 and S2.

the oscillating, non classical $F_{[\tau,V]}$ S2–S3 and S3–S4 terms (blue and green dotted lines) dominate the total force (violet). Their effect is either to slow down or to increase the rate of motion of the wave packet on each potential curve, depending on their sign: a positive sign of the total resulting force decelerates the motion of the wavepacket (and plays the role of a friction term on the considered electronic state) leading to a plateau in $\langle R_i(t) \rangle$, e.g. figure 3(a) around 20 fs. When negative, this term leads to an acceleration of the wavepacket motion, i.e. figure 3(g) around 25 fs. The sign of the $F_{[\tau,V]}$ terms also controls the direction of amplitude transfer, see figure 6 below and figure S6.

The effect of the $F_{[\tau,V]}$ terms on the motion of the wave packet on the different electronic states is not limited to one cycle strong NIR pulses of different CEP. It can also be observed in the case of two photon excitation to the S2, S3 and S4 states with a short but several cycle VIS ($\omega_p = 2.6$ eV (476.9 nm) pulse (FWHM 4 fs, $|E_0| = 0.01$ a.u.), see equation (16)) for which there is no CEP effects and no control through the polarity of the excited electronic states. Here the control is obtained through the carrier frequency and pulse duration. As can be seen from figure 4, a significant population transfer occurs through NAC between the S4 state (which is optically bright) and the S3 state (which is darker) during the second half of the pulse, which leads to

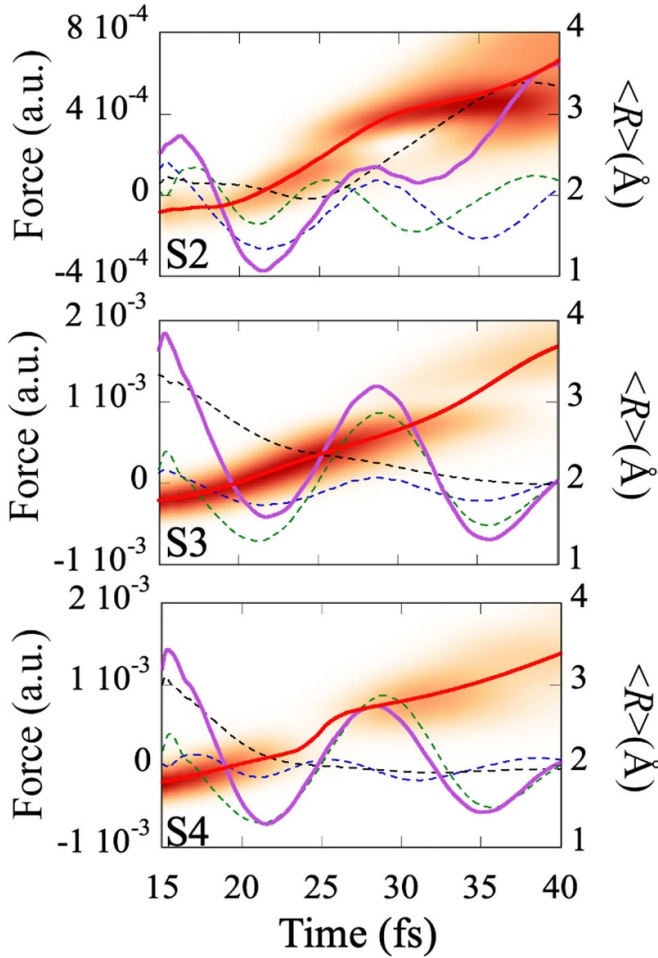


Figure 5. Heatmaps of the localization of the wave packet on the excited electronic states S2, S3 and S4 for the exciting pulse VIS pulse of figure 4. $\langle R_i(t) \rangle$ is plotted in red thick line. The total force affecting the nuclei in each electronic state is plotted in thick violet line. Its components are plotted in dotted lines, F_V in black and $F_{[\tau, \nu]}$ for the two states involved in blue and in green.

commensurate amounts of population in the S1, S3 and S4 states at the end of the pulse. The state S2 is then populated through NAC with the S3 state.

Heatmaps of the localization of the wave packet vs time are shown in figure 5 for the S2, S3 and S4 states. Here too, one clearly sees that a positive total force (violet) decelerates the motion of the wave packet (in the first 5 fs for all three states) while the wave packet is accelerated by a negative value of the total force. Note that for the excitation by the VIS pulse, the total force in each potential curve are in phase.

The key conclusion from the analytical results and the numerical examples discussed above is that the sign of the force strongly correlates with the direction of population transfer. This strengthens the point already made in [39]. Clear additional evidence is provided in figure 6 that shows the correlation between the population transfer in the excited states and the time-dependence of the force for both the LiH and LiT dynamics induced by the CEP = 0 the one cycle NIR pulse in the 15–40 fs time interval. For the CEP = 0 pulse, the

population transfers essentially involve the S3 and S4 states, with the population in S2 slowly increasing in the second half of the time interval. The terms of the force for the S3–S4 interaction, $F_{[\tau, \nu]}$ S3–S4 (red) and the two potential terms, F_V S3 (blue) and F_V S4 (violet), are plotted in figures 6(c) and (d). As discussed for LiH in figure 3 above, in the regions where the NAC terms are important, the $F_{[\tau, \nu]}$ S3–S4 term is larger than the F_V terms and oscillates with the period of the S3–S4 coherence, ≈ 25 –20 fs. As indicated by the vertical dotted lines in figure 6, when $F_{[\tau, \nu]}$ is negative, that is, when the force leads to an acceleration of the wave packet motion (figure 3), the population is transferred from S4 to S3. This transfer can be seen in figures 3(b) and (c) where one can observe a larger localization on S3 than on S4 in the heatmap, as well as in figure 1(a) that shows the population dynamics. When $F_{[\tau, \nu]}$ is positive, the transfer occurs in the opposite direction. The mass difference slows down the motion of the wave packet on the PEC for LiT, leading to a small dephasing in the oscillations of $F_{[\tau, \nu]}$ (the extrema are delayed with respect to LiH) and a less efficient population transfer in LiT than in LiH between 15 and 25 fs. As the wave packets leave the NAC region, the energy difference between S3 and S4 increases which leads to a shorter period of the electronic coherence. The population transfer patterns for the CEP = π LiH and LiT dynamics as well as the force profiles are more complex because three states, S2, S3 and S4 are involved. They are plotted in figure S6 of the SM.

As shown in the previous figures, the force terms have complex time profiles and oscillate with both electronic and vibrational periods. Their periods can be directly probed in time by time resolved electric field spectroscopy, a novel kind of time-resolved spectroscopy that provides probing in time of the molecular emission dipole that has been recently developed, [40, 41] or by pump-probe transient absorption spectroscopy [42], see also [15, 17]. The emission dipole is given by the mean value of the dipole, $\hat{\mu}$,

$$\mu(t) = \langle \Psi(t) | \hat{\mu} | \Psi(t) \rangle = f \sum_{gi}^{NgNe} |c_{gi}(t)|^2 R_g + \sum_{gi, gj}^{NgNe} c_{gi}^*(t) c_{gj}(t) \mu_{gigj}^{el} \quad (17)$$

It depends on both the electronic and the vibrational coherences as do the terms of the force. As is also the case for the force, the electronic part (second term on the rhs of equation (17)) reflects the electron-nuclei correlation. Note that the nuclear part of the dipole (first term on the rhs) is a direct probe of $\langle R(t) \rangle$ of a diatomic molecule, and that unlike the probing methods discussed above for $\langle R(t) \rangle$, the time resolved emitted electric field due to the nuclear dipole is directly proportional to $\langle R(t) \rangle$ without requiring an a priori knowledge of the potential curves.

We report in figure 7(a) the total force and in figure 7(b) the emission dipole for the CEP = 0 dynamics in LiH (green) and LiT (red). In both panels and for both isotopomers, one distinguishes short periods of ≈ 1 fs and smaller, that correspond

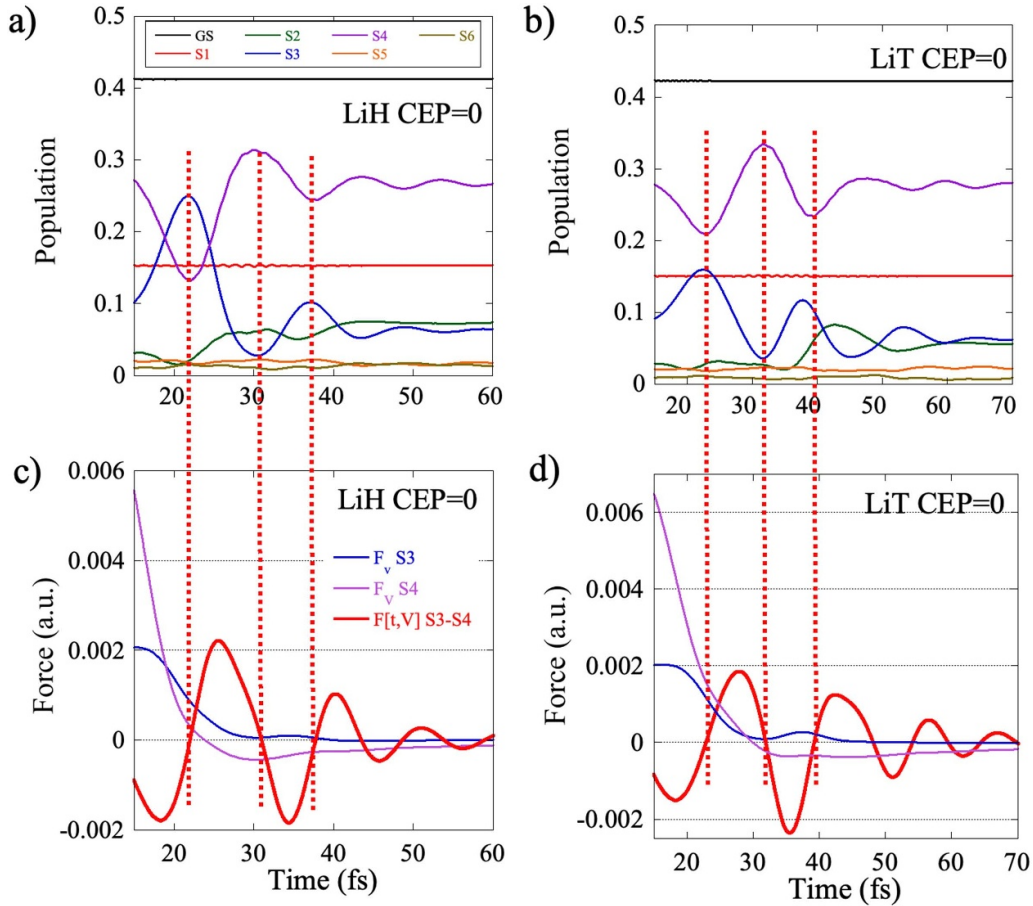


Figure 6. Correlation between the dynamics of population transfers between the S3 and the S4 states for the CEP = 0 LiH (panel (a)) and LiT (panel (b)) dynamics with the time profile of the force terms (LiH, panel (c) and LiT, panel (d)). The vertical dotted lines are drawn at the times when the S3–S4 $F_{[t,V]}$ term is zero. When the $F_{[t,V]}$ is negative, population is transferred from S4 to S3 and in the reverse direction when it is positive.

to the electronic transition frequencies between the GS and the excited states and between the S1 state and states S2, S3 and S4 and slower periods of ≈ 20 – 30 fs that correspond to the transition frequencies between the states of the S2–S3–S4 manifold. One can also distinguish in figures 7(a) and (b) a much longer period of ≈ 84 fs for LiH and ≈ 124 fs for LiT, which correspond to the vibrational period of the S1 state. When the vibronic wave packet on S1 revisits the FC region after a vibrational period (see figure 2(d)), there is revival of the GS–S1 electronic coherence that modulates this recurrence with a faster ≈ 1 fs period.

To disentangle the electronic and vibrational periods present in the total force, we show in figure 7(c) the Fourier Transform (FT) of the total force computed for the full range of transition frequencies below the IP, from 0 to 8 eV. There are three massifs of peaks in the force power spectrum, two at high frequencies, at ≈ 3 eV and at ≈ 5 – 6 eV and one below 1 eV. The peaks at ≈ 3 eV correspond to the electronic transitions GS–S1 and S1 to S2, S3, S4 and the massif at 5–6 eV to the transitions between the GS and the S2–S3–S4 states. Each massif is modulated by vibrational transitions in S1. Similar

patterns are obtained for the FT of the dipole moment, see SM, figure S7. The low frequency range of the force spectrum, below 1 eV, corresponds to the vibrational coherences and to the electronic coherences between the states of the S2–S3–S4 manifold which are commensurate. The inset of figure 7(c) zooms on the low frequency range < 0.5 eV of two of the non zero terms of the force after the pulse, F_V and $F_{[t,V]}$, plotted in full lines and in dashes respectively. The sharp lines in F_V shift upon isotopic substitution, which can therefore be used to distinguish between electronic and vibrational periods. They correspond to the vibrational frequencies of the GS (≈ 25.5 fs, 0.16 eV for LiH and ≈ 38 fs, 0.10 eV for LiT) and of S1 (≈ 84 fs, 0.050 eV for LiH and ≈ 124 fs, 0.033 eV for LiT) and their harmonics since a non-stationary vibrational wave packet is formed in these two bound states upon excitation. The fundamentals are the same as those computed by the FT of the total dipole moment of the individual electronic states shown in figure S8 of the SM and reported in table S1. The spectrum of the $F_{[t,V]}$ term is a broad peak in the range [0.1–0.3] eV common to both isotopomers. It corresponds to the electronic transition frequencies within the S2, S3 and S4 manifold with

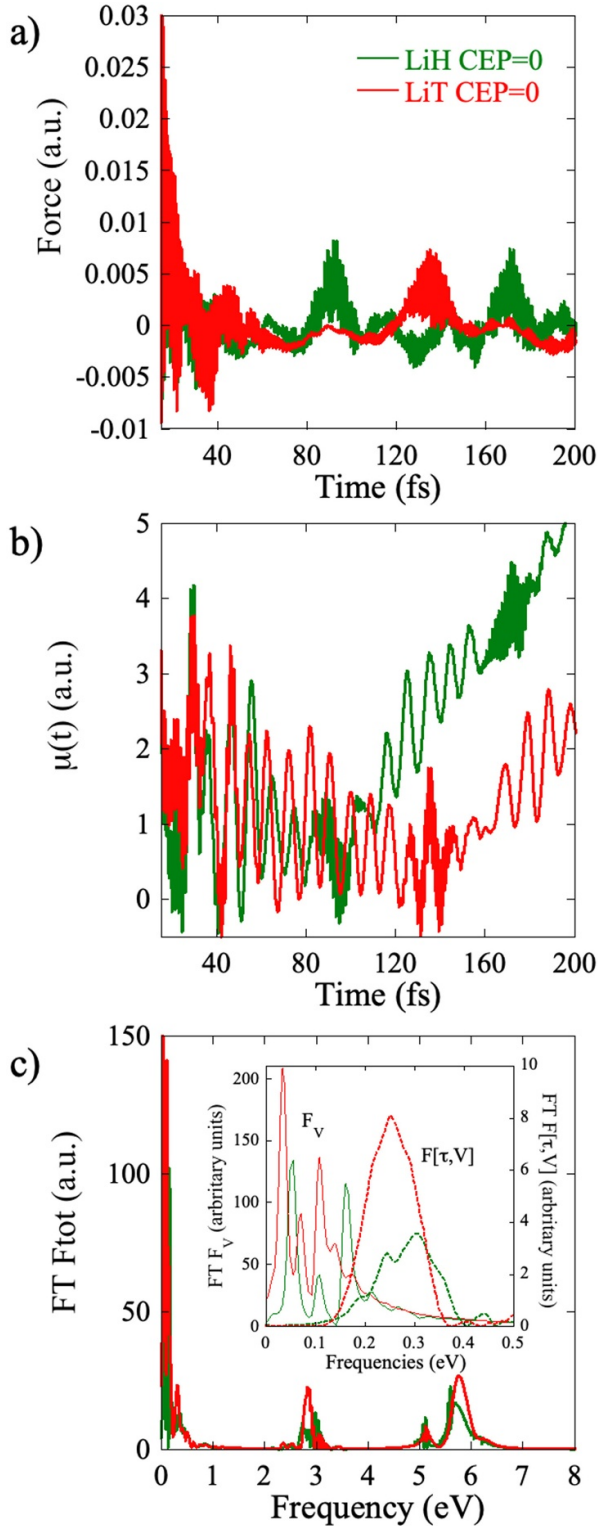


Figure 7. (a) The total force, F_{tot} (equation (9)), as function of time for the CEP = 0 LiH (green) and LiT (red) dynamics. (b) The total dipole moment (equation (17)) as a function of time. (c) the spectrum of the total force after the pulse as a function of frequency. Inset: the short frequency range of the spectra of the F_V and $F_{[\tau, V]}$ terms that contribute to the total force after the pulse.

a weak fine structure, more visible in the case of LiH. The origin of this fine structure can be resolved using gated FTs of $F_{[\tau, V]}$ term for specific pairs of states for a short range [15,50] fs and for the full range [15, 200] fs of the dynamics after the pulse, see figures S9 and S10. The fine structure only appears in the long range spectra of the $F_{[\tau, V]}$ terms that involve the S2 state, which is coupled to S1 in the FC region. Figure S11 provides a detailed analysis of the spectra of the $F_{[\tau, V]}$ and the F_V terms computed separately for the S1, S2, S3 and S4 states for the CEP = 0 LiH and CEP = π LiT dynamics.

4. Concluding remarks

We proposed an approach that includes exactly the role of electronically NACs and thereby allows for a detailed analysis of the force exerted by a vibronic wave packet. We presented numerically converged results for the wave packet built by multiphoton excitation of LiH and LiT with broad in energy-CEP controlled NIR pulses and a VIS pulse. The total force, equation (3), is the sum of four components, two resulting from the dipole interaction that are proportional to the electric field profile, $\mathbf{E}(t)$, of the exciting pulse, F_μ and $F_{[\tau, \mu^{el}]}$ and two components that depend on the potential, F_V and $F_{[\tau, V]}$. The second term in either contribution is due to the NAC τ . The terms that depend on the dipole interaction allow tuning the force with the pulse parameters and control the subsequent dynamics. After the pulse, the electronic coherences govern the oscillations of the force term due to the non adiabatic interaction, $F_{[\tau, V]}$. This force term plays the role of a friction for the motion of the wave packets on the different potential curves and competes with the F_V term, slowing down or accelerating the wave packet motion depending whether it is positive or negative. The sign of the $F_{[\tau, V]}$ is also found to determine the direction of the population transfer between the two states that are non adiabatically coupled. A Fourier analysis of the time dependence of the force allows an identification of the electronic and vibrational components in the force spectrum, as well as the electronic and vibrational periods typical of the passage of the vibronic wavepacket in the regions of NAC. Shifts upon isotopic substitution can be used to identify the vibrational periods in the force spectrum. The frequencies of the force spectra are also found in the spectrum of the time dependent dipole moment, which corresponds to the emitted electric field. The emission dipole can be probed directly as recently demonstrated by Krausz and coworkers using field resolved spectroscopy [40, 41] that allows probing electric field oscillations in real time in the THz to PHz range or by stimulated emission by a weak IR pulse as shown in [17] for LiH and in [15] for a larger polyatomic molecule. New light sources open the way to time resolved X-ray diffraction and electron diffraction which provide observables of the full density matrix that could also be used as a probe of the force exerted by the vibronic wave packet on the nuclei [43–47].

Data availability statement

All data that support the findings of this study are included within the article (and any supplementary files).

Acknowledgments

The authors acknowledge support from the COST action ATTOCHEM (CA18222). F R and M C G acknowledge the support of the Fonds National de la Recherche (F.R.S.-FNRS, Belgium), #T0205.20, and of the action of concerted research MECHANOCHEM (ARC 19/23-20, ULiege). Computational resources have been provided by the Consortium des Equipements de Calcul Intensif (CECI), funded by the F.R.S.-FNRS under Grant # 2.5020.11.

ORCID iD

F Remacle  <https://orcid.org/0000-0001-7434-5245>

References

- [1] Krausz F and Ivanov M 2009 *Rev. Mod. Phys.* **81** 163–234
- [2] Nisoli M, Decleva P, Calegari F, Palacios A and Martín F 2017 *Chem. Rev.* **117** 10760–825
- [3] Borrego-Varillas R, Lucchini M and Nisoli M 2022 *Rep. Prog. Phys.* **85** 066401
- [4] Remacle F and Levine R D 2006 *Proc. Natl Acad. Sci. USA* **103** 6793–8
- [5] Calegari F *et al* 2014 *Science* **346** 336–9
- [6] Li H *et al* 2015 *Phys. Rev. Lett.* **114** 123004
- [7] Kraus P M *et al* 2015 *Science* **350** 790–5
- [8] Remacle F, Levine R D and Ratner M A 1998 *Chem. Phys. Lett.* **285** 25–33
- [9] Remacle F, Levine R D, Schlag E W and Weinkauf R 1999 *J. Phys. Chem. A* **103** 10149–58
- [10] Cederbaum L S and Zobeley J 1999 *Chem. Phys. Lett.* **307** 205–10
- [11] Breidbach J and Cederbaum L S 2003 *J. Chem. Phys.* **118** 3983–96
- [12] Kuleff A I and Cederbaum L S 2007 *Chem. Phys.* **338** 320–8
- [13] Muskatel H B, Remacle F and Levine R D 2009 *Phys. Scr.* **80** 048101–7
- [14] Remacle F, Nest M and Levine R D 2007 *Phys. Rev. Lett.* **99** 183902
- [15] Valentini A, van den Wildenberg S and Remacle F 2020 *Phys. Chem. Chem. Phys.* **22** 22302–13
- [16] van den Wildenberg S, Mignolet B, Levine R D and Remacle F 2019 *J. Chem. Phys.* **151** 134310
- [17] Nikodem A, Levine R D and Remacle F 2017 *Phys. Rev. A* **95** 053404
- [18] Koll L-M, Maikowski L, Drescher L, Witting T and Vrakking M J J 2022 *Phys. Rev. Lett.* **128** 043201
- [19] Blavier M, Levine R D and Remacle F 2022 *Phys. Chem. Chem. Phys.* **24** 17516–25
- [20] Nabekawa Y and Midorikawa K 2023 *Phys. Rev. Res.* **5** 033083
- [21] Kling M F, von den Hoff P, Znakovskaya I and de Vivie-riedle R 2013 *Phys. Chem. Chem. Phys.* **15** 9448–67
- [22] Kling N G *et al* 2013 *Phys. Rev. Lett.* **111** 163004
- [23] Smith F T 1969 *Phys. Rev.* **179** 111–23
- [24] Baer M 2006 *Beyond Born-Oppenheimer: Electronic Nonadiabatic Coupling Terms and Conical Intersections* (Wiley)
- [25] Pacher T, Mead C A, Cederbaum L S and Köppel H 1989 *J. Chem. Phys.* **91** 7057–62
- [26] Nijjar P, Jankowska J and Prezhdo O V 2019 *J. Chem. Phys.* **150** 204124
- [27] Doltsinis N L 2006 Molecular dynamics beyond the Born-Oppenheimer approximation: mixed quantum-classical approaches *Computational Nanoscience: Do It Yourself!* ed J Grotendorst, S Blügel and D Marx (John von Neuman Institute for Computing)
- [28] Subotnik J E 2010 *J. Chem. Phys.* **132** 134112
- [29] Jayantha S A, Komarova K G, Wildenberg S V D, Remacle F and Levine R D 2018 AttoPhotoChemistry: coherent electronic dynamics and nuclear motion *Attosecond Molecular Dynamics* vol 13, ed M J J Vrakking and F Lepine (Royal Society of Chemistry) pp 308–47
- [30] Ghafur O, Rouzee A, Gijsbertsen A, Siu W K, Stolte S and Vrakking M J J 2009 *Nat. Phys.* **5** 289–93
- [31] Kraus P M, Baykusheva D and Wörner H J 2014 *Phys. Rev. Lett.* **113** 023001
- [32] Frohnmeyer T and Baumert T 2000 *Appl. Phys. B* **71** 259–66
- [33] Ergler T, Rudenko A, Feuerstein B, Zrost K, Schröter C D, Moshhammer R and Ullrich J 2006 *Phys. Rev. Lett.* **97** 193001
- [34] Thumm U, Niederhausen T and Feuerstein B 2008 *Phys. Rev. A* **77** 063401
- [35] Manz J, Pérez-Torres J F and Yang Y 2013 *Phys. Rev. Lett.* **111** 153004
- [36] Pérez-Torres J F 2015 *Phys. Rev. A* **91** 022510
- [37] Hermann G, Paulus B, Pérez-Torres J F and Pohl V 2014 *Phys. Rev. A* **89** 052504
- [38] Paulus B, Pérez-Torres J F and Stemmler C 2016 *Phys. Rev. A* **94** 053423
- [39] Komarova K G, van den Wildenberg S, Remacle F and Levine R D 2020 *J. Phys. B: At. Mol. Opt. Phys.* **53** 134001
- [40] Pupeza I *et al* 2020 *Nature* **577** 52–59
- [41] Sulzer P, Högnér M, Raab A-K, Fürst L, Fill E, Gerz D, Hofer C, Voronina L and Pupeza I 2022 *Nat. Photonics* **16** 692–7
- [42] Wu M, Chen S, Camp S, Schafer K J and Gaarde M B 2016 *J. Phys. B* **49** 062003
- [43] Keefer D, Aleotti F, Rouxel J R, Segatta F, Gu B, Nenov A, Garavelli M and Mukamel S 2021 *Proc. Natl Acad. Sci. USA* **118** e2022037118
- [44] Rouxel J R, Keefer D and Mukamel S 2021 *Struct. Dyn.* **8** 014101
- [45] Cao J and Wilson K R 1998 *J. Phys. Chem. A* **102** 9523–30
- [46] Bennett K, Kowalewski M, Rouxel J R and Mukamel S 2018 *Proc. Natl Acad. Sci. USA* **115** 6538–47
- [47] Yang J *et al* 2018 *Science* **361** 64

Electronic coherences built by an attopulse control the forces on the nuclei

Manuel Cardosa-Gutierrez¹, R. D. Levine², F. Remacle^{1,2*}

¹Theoretical Physical Chemistry, UR MOLSYS, University of Liege, Belgium

²Fritz Haber Center, Institute of Chemistry, The Hebrew University of Jerusalem, Jerusalem 91904, Israel

Supplemental Materials

Supplemental figures and tables

Figure S1: Potential energy curves of the 7 lowest Σ states of the LiH molecule

Figure S2: Selected electronic dipole curves

Figure S3: Selected non adiabatic coupling (NAC curves)

Figure S4: Long time population dynamics for the CEP=0 and CEP= Π NIR excitations in LiH and LiT.

Figure S5: Transient population dynamics and force profiles during the pulse for the LiT molecule, the CEP=0 and CEP= Π NIR excitations.

Figure S6: Correlation between the sign of the force and the direction of population transfers between the two pairs of states S3-S4 and S2-S3 LiH and LiT excited the CEP= Π NIR pulse.

Figure S7: Spectra of the total dipole moment for LiH and LiT

Figure S8: Spectra of the nuclear dipole moments of the electronic states

Table S1: Vibrational periods of the bound electronic states for LiH and LiT

Figure S9: Gated spectra $F_{[\tau, \nu]}$ term of the force for specific pairs of states for LiH and LiT excited by the CEP=0 NIR pulse.

Figure S10: Gated spectra $F_{[\tau, \nu]}$ term of the force for specific pairs of states for LiH and LiT excited by the CEP= Π NIR pulse.

Figure S11: Spectra of the force resolved per state for the dynamics LiH CEP=0 and LiT CEP= Π .

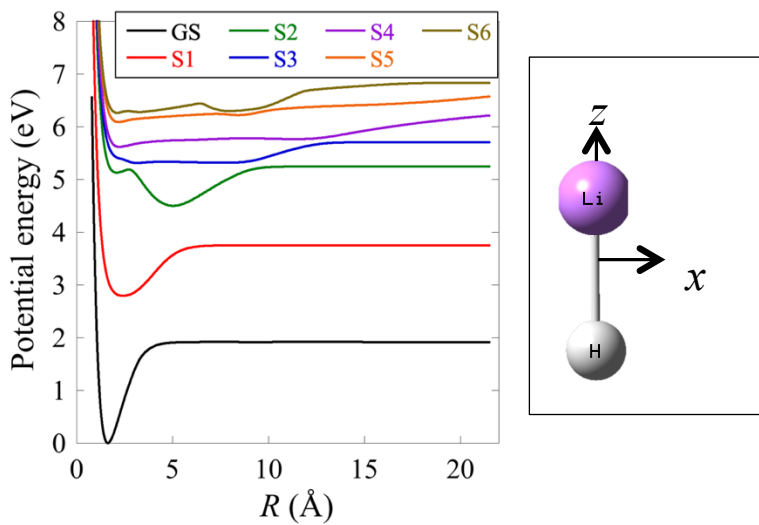


Figure S1: Potential energy curves of the 7 lowest electronic states, [1]. Left Orientation of LiH in the molecular frame.

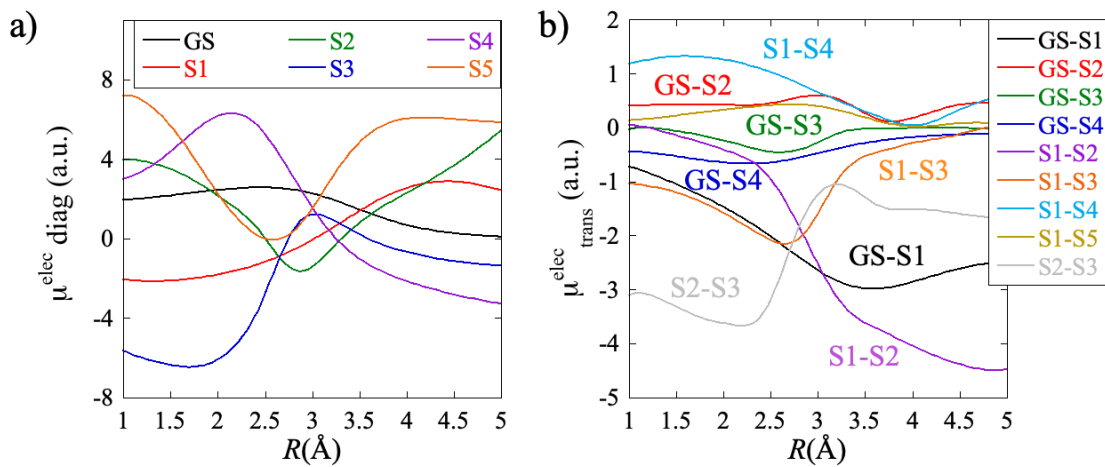


Figure S2: Selected electronic dipole curves a) diagonal dipoles of the electronic states b) transition dipoles, [1].

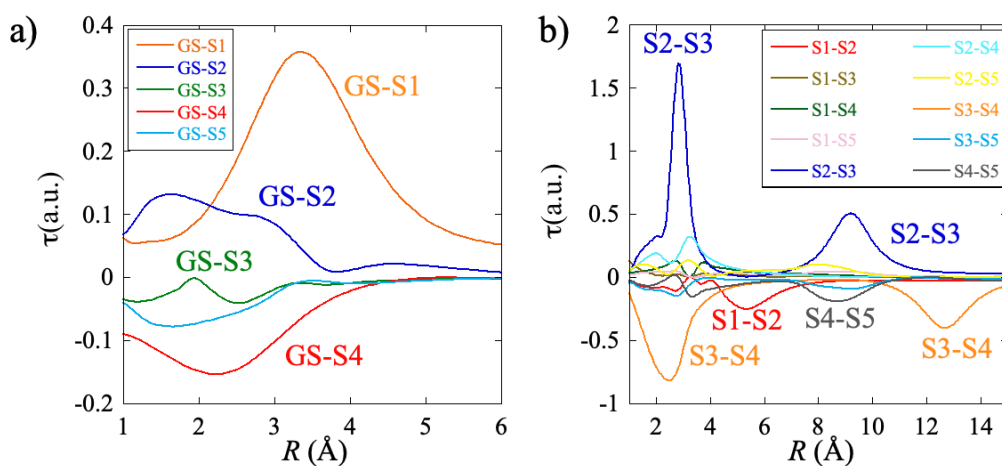


Figure S3 : Selected NAC curves a) Ground state to excited states at short distance. b) Between excited states, ref.[1]

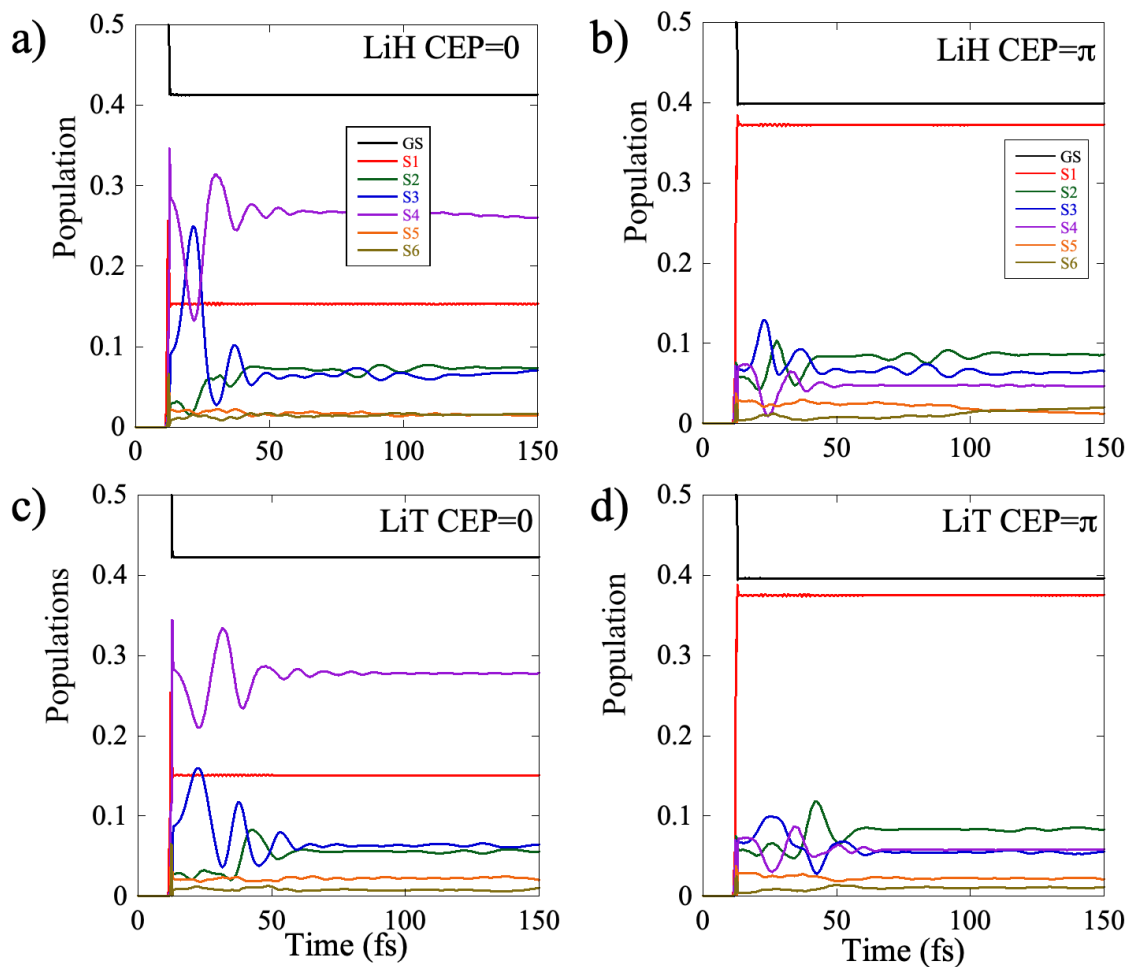


Figure S4. Long time dynamics in LiH (a) and b(b) and in LiT (c) and (d). The fragments corresponding to each electronic state differ by the excited state of the Li atom. The state S4 dissociate to the ion pair $\text{Li}^+(1S) + \text{H}^-(1S)$. [1]

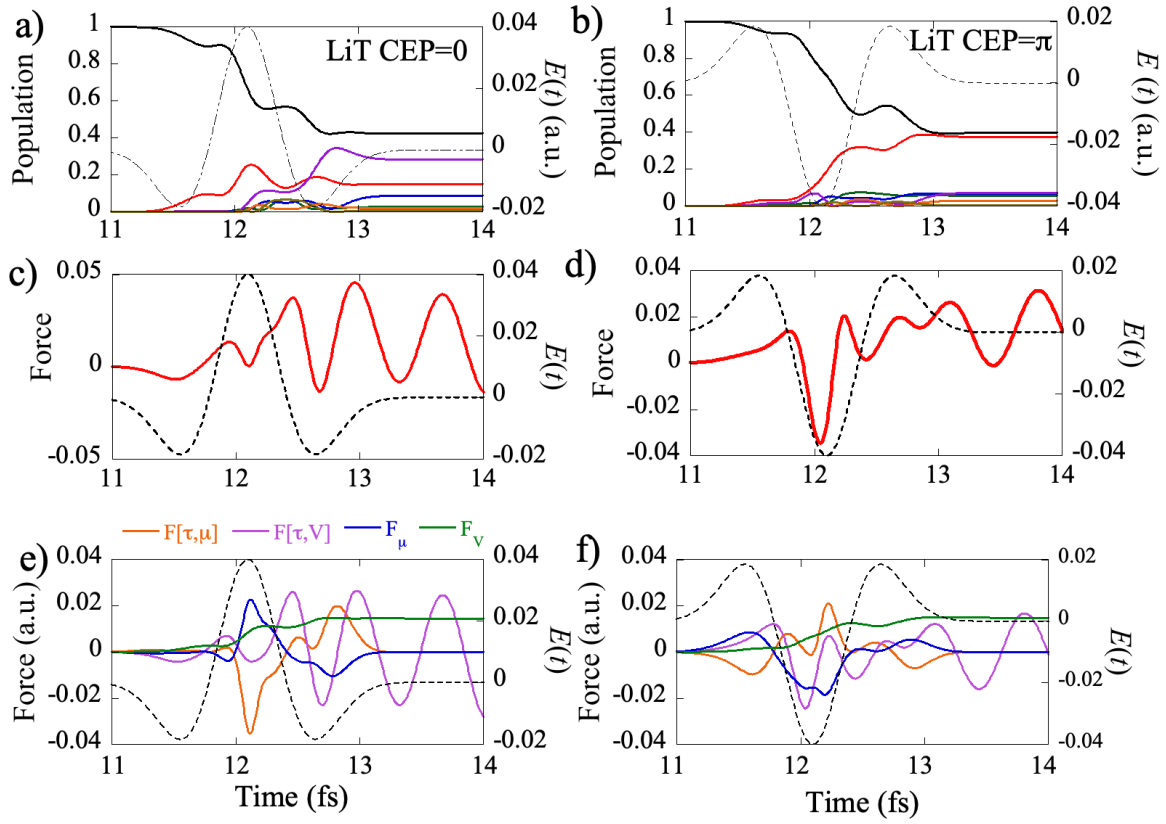


Figure S5 Time evolution of the populations of the electronic states and of components of the force (Eqs. (10) to (15)) for the LiT molecule. Left column: CEP=0, right column: CEP= π . a) and b) : transient dynamics during the pulse. c) and d) time profile of the total force, F_{tot} (Eq.(3)), during the pulse. e) and f) time profile of the four terms of the total force during the pulse (Eqs. (5) to (9)). The pulse is plotted in dashed line and its magnitude can be read on the left y axis.

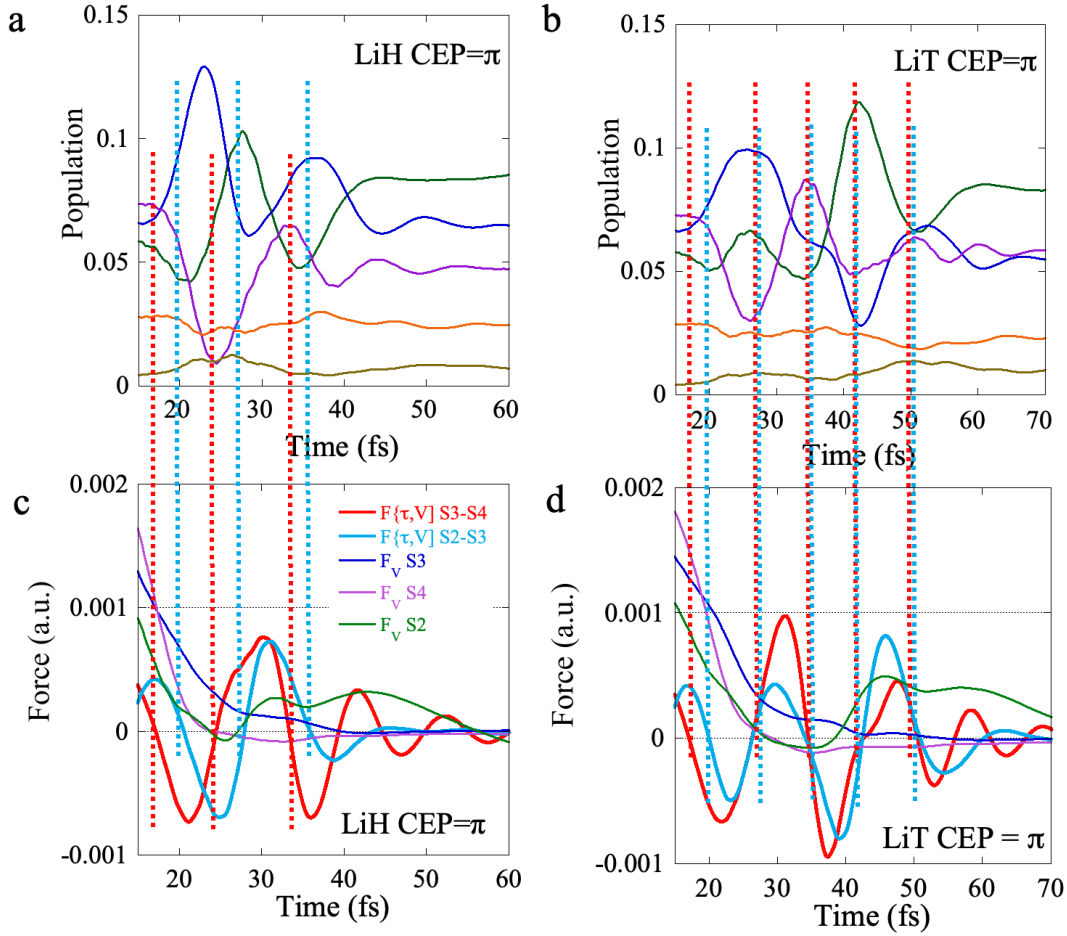


Figure S6: Correlation between the dynamics of population transfers between the two pairs of states S3-S4 and S2-S3 for the CEP=π LiH (panel a) and LiT (panel b) dynamics with the time evolution of the force terms (LiH, panel c, and LiT panel d). The vertical red dotted lines are drawn at the times when the S3-S3 $F_{[\tau, V]}$ is zero and the vertical azure ones at the times when the S2-S3 $F_{[\tau, V]}$ is zero. When the $F_{[\tau, V]}$ is positive, population is transferred from S3 to S4 (or S2 to S3) and in the reverse direction when it is negative. The time range is different for LiT than for LiH because of the slowing down of the wavepacket motion due to the mass difference. Note that in the CEP=π LiH dynamics, the two force terms are not in phase while there are in phase for the LiT one. The difference between the CEP=0 (figure 6 of the main text) and the CEP=π dynamics is in the opposite phases of the oscillation of the S3-S4 $F_{[\tau, V]}$ term which is controlled by the phase electronic coherence.

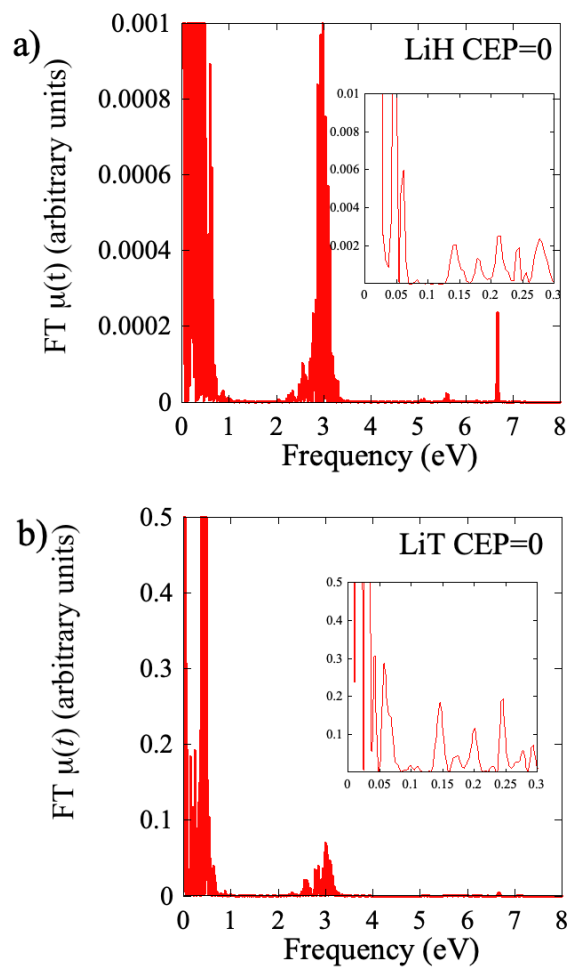


Figure S7. Fourier transform of the total dipole moment (Eq. (17) of the main text). The insets show the low frequency range. One can distinguish the vibrational periods of S0, S1 and S2 in the range below 0.15 eV for LiH and 0.1 eV for LiT.

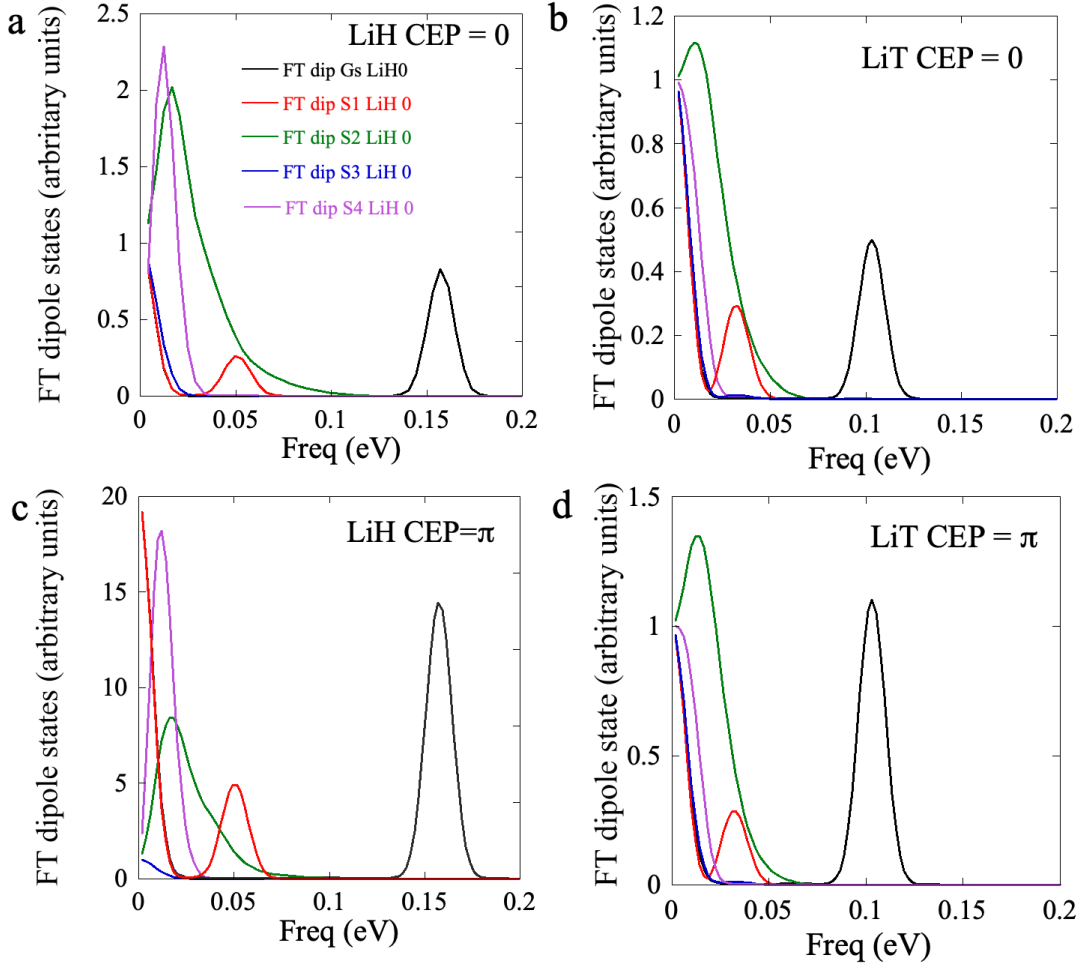


Figure S8. Fourier transform of the diagonal dipole terms for each electronic state separately,

$$\mu_{ii}^{ele}(t) = \sum_g^{Ng} |c_{gi}^*(t)|^2 (\mu_g^{nuc} + \mu_{gi,gi}^{ele}).$$

Table S1: Vibrational frequencies of the two isotopomers

Vibrational freq (eV)	LiH	LiT
GS	0.157 (26 fs)	0.103 (38 fs)
S1	0.050 (83 fs)	0.033 (125 fs)
S2	0.017 (243 fs)	0.012 (344 fs)
S4	0.012 (344 fs)	0.007 (from full dip LiT 0) 591 fs

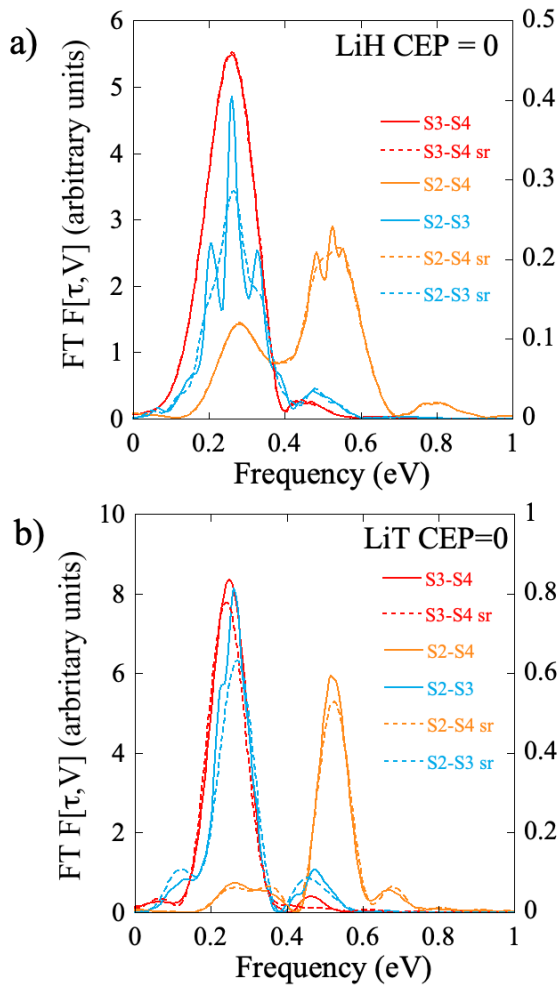


Figure S9: Gated FT of the $F_{[\tau,\nu]}$ term for the specific pairs of states S2-S3 (azure), S2-S4 (orange) and S3-S4 (red) for the CEP=0 LiH (a) and LiT (b) dynamics, computed for the full range of time [15,200] fs (full lines) and up to 50 fs [15,50] fs (dashes, indicated by 'sr' in the inset legend), before the recurrence of the S1 wp in the FC region. Note how the overlap between the different terms in the range [0.15-0.3] eV is much better for LiH than for LiT, which explains the more efficient population transfer, as seen in Figure 6 of the main text and Figure S6.

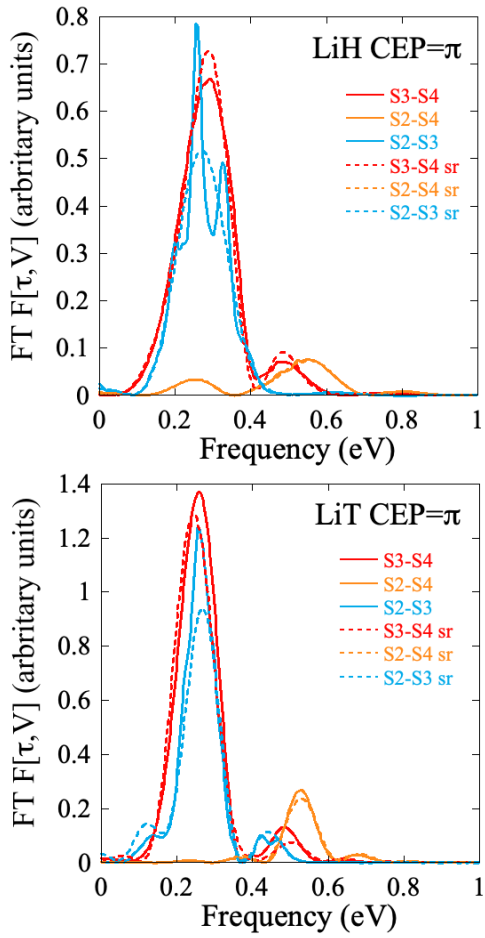


Figure S10: Gated Fourier Transform of the $F_{[\tau, V]}$ term for specific pairs of states as indicated for the full range of time [15,200] fs (full lines) and up to 50 fs [15,50] fs (dotted lines, identified by 'sr' in the inset), before the recurrence of the S1 wp in the FC region.

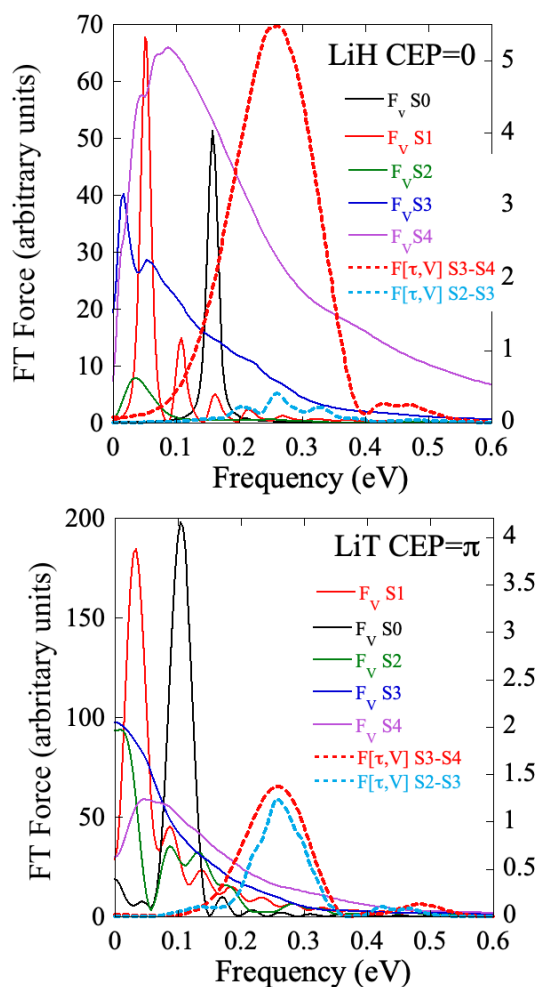


Figure S11: Spectra of the force resolved per state for the dynamics LiH CEP=0 and LiT CEP= π . Note how the S2-S3 $F_{[\tau,V]}$ term overlap with the high end of the vibrational progression for S1. In addition to the progression of the vibrational states of S1, the vibrational periods of S2 (≈ 258 fs, 0.016 eV for LiH and ≈ 344 fs, 0.012 eV for LiT) and of the fundamental of S4 (344 fs, 0.012 eV for LiH and ≈ 517 fs , 0.008 eV) are also resolved.

Reference

[1]S. van den Wildenberg, B. Mignolet, R. D. Levine, and F. Remacle, J. Chem. Phys. **151**, 134310 (2019).

Chapter 6 Efficient simulation of an ensemble of photoexcited randomly oriented molecules

Table of Contents

Chapter 6	Efficient simulation of an ensemble of photoexcited randomly oriented molecules	105
6.1	<i>Stereochemical effects in the photodynamics of an ensemble of LiH molecules</i>	105
6.1.1	Introduction to the singular value decomposition (SVD) of a matrix.....	107
6.1.2	SVD of the density matrix in an ensemble of photoexcited randomly oriented molecules.....	109
6.2	<i>Summary of contributions</i>	112
6.3	<i>References</i>	113
6.4	<i>Publication: “Electronic Coherences Excited by an UltraShort Pulse Are Robust with Respect to Averaging over Randomly Oriented Molecules as Shown by Singular Value Decomposition”</i>	113

6.1 Stereochemical effects in the photodynamics of an ensemble of LiH molecules

In Chapter 5, we considered the interaction of a single LiH molecule with the electric field of an attopulse. The molecule was oriented in the laboratory frame following the direction of the Z axis. A more realistic simulation of the quantum dynamics of LiH molecules after excitation with a short 1-2 fs optical pulse must consider an ensemble of initially randomly oriented molecules with respect to the direction of the polarization of the electric field. In such an ensemble, each molecule will interact differently with the electric field of the pulse as the dipole term used to describe the interaction with the electric field of the pulse in the Hamiltonian, Equation 2.35 in Chapter 2, depends on the dot-product $\mathbf{E}(t) \cdot \boldsymbol{\mu}(R) = (E_x\mu_x, E_y\mu_y, E_z\mu_z)$. So, even for a pulse with a fixed polarization direction $\boldsymbol{\varepsilon}$, the random nature of the initial orientations in the ensemble will cause different interaction terms in the Hamiltonian of each molecule, which results in a different vibronic dynamic. Then, an accurate description of the quantum dynamics of molecules photoexcited by short atto and few femtosecond pulses requires averaging over the initial molecular orientations with respect to the polarization direction of the exciting optical pulse.

For computational efficiency, instead of randomizing the molecule and considering a field with a fixed orientation in the laboratory frame, we analyzed the situation seen from the molecule's frame, where it is the polarization of the field that is randomized. From this point of view, each molecule in the ensemble has been aligned and oriented along the Z+ axis (Figure 6.1), and then the polarization of the field is sampled on the unit sphere.

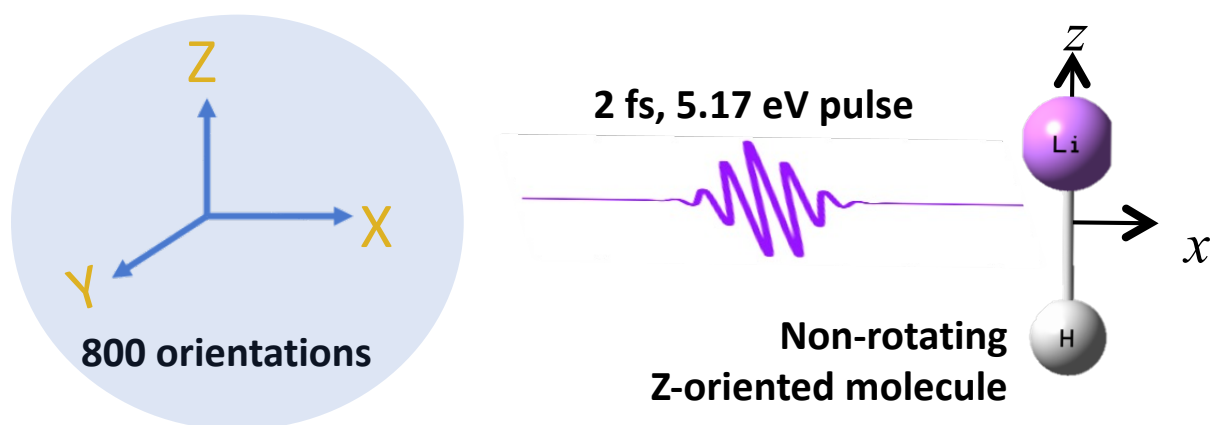


Figure 6.1. Sampling of the polarization direction of the electric field of an attosecond deep UV pulse that is used to photoexcite the molecule of LiH fixed in a non-rotating frame aligned with the Li pointed towards Z+. you need to add the electric field strength somewhere

Sampling a representative number of orientations on the sphere and integrating the TDSE for each is computationally rather costly in computer time and storage capacity. The wavefunction, even for a simple molecule like LiH, contains many coefficients: 7665 complex numbers for 15 states and 511 grid points, as considered here. And we still need to store the wavefunctions for the 800 orientations that were sampled in the sphere and for each timestep so that we can process the information later and compute the observables of interest. This generates a huge amount of data: of the order of terabytes for LiH, which poses a tremendous challenge for storing and processing. For larger molecules, such operations become unfeasible. In addition, the quantum dynamical propagation is time-consuming because it must be repeated as many times as the number of molecular orientations in the ensemble and whenever the parameters of the dynamics or of the pulse are changed. We have proposed a numerical approach for computing the ensemble dynamics that considerably lowers the computation cost and dramatically reduces the need for storage. Our approach is based on the Singular Value Decomposition (SVD) of the matrix that contains the wavefunctions associated with each molecular orientation right after interacting with the pulse. It requires numerical integration across all the orientations for a short time only: from the beginning of the propagation until the electric field drops to zero. After that, we must only propagate a few orientations defined by the dominant singular vectors. All the orientations need to be propagated during the pulse because when the pulse is relatively strong, nonlinear effects entangle the polarization directions of the field with the internal degrees of freedom of the molecule during the pulse. When the pulse is weak enough to induce single-photon transition at the maximum of the electric field, the excitation can be described in the sudden excitation or ionization approximation. In this case, the dynamics does not need to be run during the pulse. One only need to compute the transition matrix elements in the Franck-Condon region from the ground state to the excited states at the maximum of the electric field. For a sudden excitation process, one can show analytically that there are only three principal orientations in the ensemble, which correspond to the three cartesian axis of the molecular frame (I). The sudden approximation was applied to the photoionization of the CD_4 and enables the simplification of the modeling of the quantum dynamics of the cation CD_4^+ ; see Chapter 7 for more details.

6.1.1 Introduction to the singular value decomposition (SVD) of a matrix

The Singular Value Decomposition (SVD) (2) is a fundamental matrix factorization technique that plays a crucial role in many algorithms and data processing methods. It provides a numerically stable decomposition of a matrix, which not only ensures the existence of a solution but also allows for a wide range of applications across computational disciplines. As one of the most important matrix factorizations of the computational era, the SVD serves as the backbone for numerous data-driven techniques. Beyond its computational utility, the SVD also holds significant conceptual value, particularly in methods like Principal Component Analysis (PCA), where high-dimensional data is reduced into its most statistically meaningful components.(3, 4)

The singular value decomposition of an $m \times n$ complex matrix \mathbf{A} is a factorization of the form represented in Equation 6.1. Without loss of generality, we can assume that $m \geq n$.

$$\mathbf{A} = \mathbf{U}\mathbf{\Sigma}\mathbf{V}^* \tag{6.1}$$

In the compact or reduced SVD scheme, \mathbf{U} is an $m \times n$ matrix with orthonormal columns called "left singular vectors" of \mathbf{A} . The matrix $\mathbf{\Sigma}$ is an $n \times n$ diagonal matrix, with non-negative real entries called "singular values". If \mathbf{A} has full-rank n , the diagonal entries of $\mathbf{\Sigma}$ would be strictly positive real numbers. The matrix \mathbf{V} is an $n \times n$ matrix whose columns are orthonormal and are called "right singular vectors" of \mathbf{A} . Figure 6.2 illustrate the structure of the reduced SVD decomposition.

Reduced SVD ($m \geq n$)

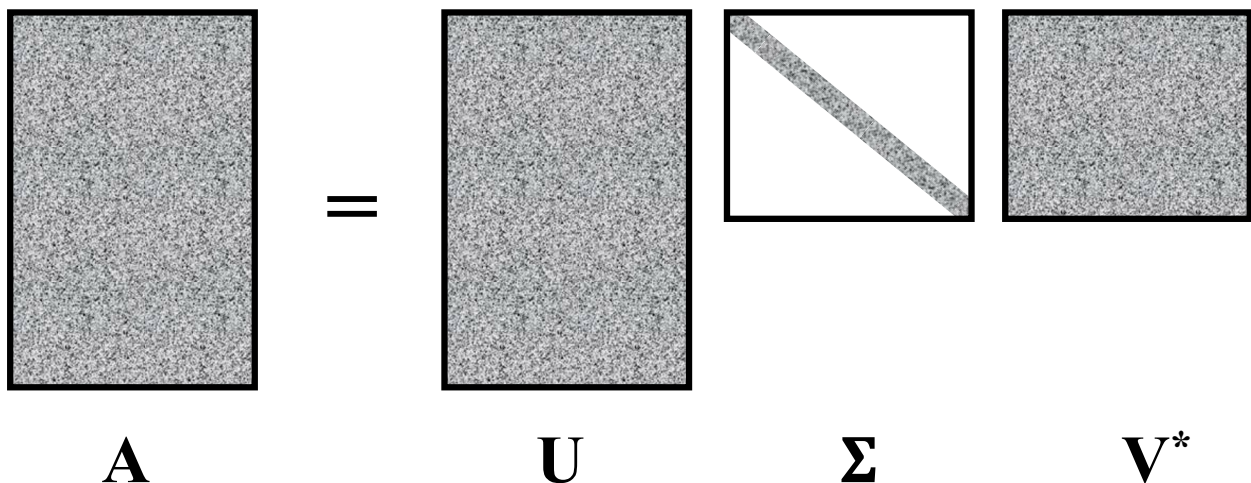


Figure 6.2: Illustration of the reduced SVD scheme. Any complex rectangular matrix can be factorized as the product of semi-unitary matrices \mathbf{U} and \mathbf{V}^* , and a diagonal matrix $\mathbf{\Sigma}$.

Although the reduced SVD scheme is the variant used in most applications, it is worth mentioning about the standard formulation called "full" SVD. In full SVD the $m \times n$ matrix \mathbf{U} is converted into

a (square) unitary matrix by adjoining an additional $m - n$ orthonormal columns. This way the columns of U can form a basis for m -dimensional space \mathbb{C}^m . This, however, has as consequence that the matrix Σ will become rectangular, containing $m - n$ extra rows consisting of zeros. The full SVD scheme is illustrated in Figure 6.3.

Full SVD ($m \geq n$)

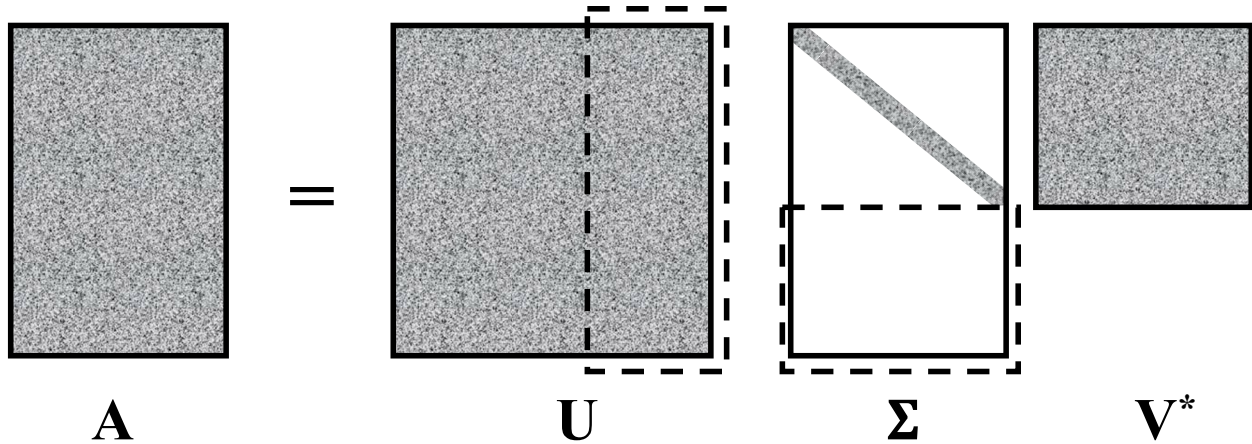


Figure 6.3: Illustration of the Full SVD scheme. This approach allows to obtain a unitary matrix U that could serve as a basis for the row-space of A . However, it is more costly computationally than the reduced scheme, especially when $m \gg n$, because it produces larger the matrices U and Σ . The latter filled with unnecessary extra rows with zero entries.

The Singular Value Decomposition (SVD) is a powerful tool once it can be computed, with applications across a wide range of problems. For example, the most effective way to determine the rank of a matrix is by counting the number of singular values greater than a carefully chosen tolerance. Additionally, the SVD provides the most accurate method for finding an orthonormal basis for the range or nullspace of a matrix. Beyond these specific applications, the SVD plays a crucial role in a variety of robust algorithms, such as those for least squares fitting, intersection of subspaces, regularization, and many other numerical problems. (4)

Some of the most important properties of the SVD (4), many of which are utilized in our work, are summarized below:

- The rank r of the matrix A is equal to the number of nonzero singular values.
- When computing the SVD, the singular values are arranged in descending order, with σ_1 being the largest. This singular value determines the 2-norm (spectral norm) of the matrix A , i.e., $\|A\|_2 = \sigma_1$
- The matrices A and Σ share the same Fröbenius norm, i.e., $\|A\|_F = \|\Sigma\|_F$. This norm can be easily obtained as: $\|A\|_F = \sqrt{\sigma_1^2 + \sigma_2^2 + \dots + \sigma_r^2}$
- The nonzero singular values of A are the square roots of the nonzero eigenvalues of A^*A or AA^* . These two matrices share the same set of nonzero eigenvalues.

- If \mathbf{A} is Hermitian ($\mathbf{A} = \mathbf{A}^*$), then the singular values of \mathbf{A} are the absolute values of its eigenvalues.
- For a square matrix $A \in \mathbb{C}^{m \times m}$, its determinant can be computed as the product of its singular values: $\det(\mathbf{A}) = \prod_{i=1}^m \sigma_i$.
- The matrix \mathbf{A} can be decomposed as the sum of r rank-one matrices, each formed from the pair of left and right singular vectors associated with the same singular value. The expansion is given by: $A = \sum_{j=1}^r \sigma_j u_j v_j^*$

6.1.2 SVD of the density matrix in an ensemble of photoexcited randomly oriented molecules

Let's define the rectangular matrix \mathbf{A} , at a given time step, whose N_o columns correspond to the number of molecular orientations and N_b rows, to the number vector of coefficients of the wavefunction associated to each orientation.

$$\mathbf{A} = [\mathbf{c}_1 \quad \mathbf{c}_2 \quad \dots \quad \mathbf{c}_{N_o}] \quad (6.2)$$

where \mathbf{c}_i represents the coefficients for the wavefunction associated to orientation i of the field and satisfy the condition $\|\mathbf{c}_i\|^2 = 1$. Notice that due to the latter condition, the Fröbenius norm $\|\mathbf{A}\|_F$ is equal to the number of orientations N_o

$$\|\mathbf{A}\|_F^2 = \sum_{i,j} |\mathbf{A}_{ij}|^2 = N_o \quad (6.3)$$

Singular value decomposition of \mathbf{A} allows the separation of the molecular degrees of freedom from the orientational ones. Through the SVD, \mathbf{A} is factorized into the product of three matrices (see Equation 6.4): the matrix \mathbf{U} is associated with the molecular degrees of freedom, while \mathbf{V} is linked to the orientational ones. The matrix $\mathbf{\Sigma}$ contains the singular values, which indicate the significance of each molecular and orientational singular vectors. Equivalently, \mathbf{A} can be expressed as a sum of outer products of the left and right singular vectors, weighted by the corresponding singular values. In our case, the number of coefficients in the wavefunction exceeds the number of electric field orientations sampled on the sphere, so $\text{rank}(\mathbf{A}) \leq N_o$.

$$\mathbf{A}(t) = \mathbf{U}\mathbf{\Sigma}\mathbf{V}^\dagger \equiv \sum_{m=1}^{N_o} \sigma_m(t) \mathbf{U}_m(t) \otimes \mathbf{V}_m^\dagger(t) \quad (6.4)$$

In Equation 6.4, the scalar $\sigma_m(t)$ represent the singular values and are ordered by decreasing values, $\mathbf{U}_m(t)$ the left (molecular) singular vectors and $\mathbf{V}_m^\dagger(t)$ the right (orientational) singular vectors.

From the rectangular matrix \mathbf{A} we can define two reduced density matrices: one with dimensions $N_b \times N_b$, representing the molecular degrees of freedom, $\rho_{mol}(t)$, and the other with dimensions $N_o \times N_o$, representing the orientational degrees of freedom $\rho_{orien}(t)$.

$$\begin{aligned}\rho_{mol}(t) &= \frac{1}{N_o} \mathbf{A} \mathbf{A}^\dagger \\ \rho_{orien}(t) &= \frac{1}{N_o} \mathbf{A}^\dagger \mathbf{A}\end{aligned}\quad (6.5)$$

where \mathbf{A}^\dagger is the Hermitian conjugate satisfying $(\mathbf{A}^\dagger)_{ij} = \mathbf{A}^*_{ij}$. The factor $\frac{1}{N_o}$ ensures that the trace of the density matrices is 1 as it should be. It arises from the fact

$$\text{Tr}(\mathbf{A} \mathbf{A}^\dagger) = \text{Tr}(\mathbf{A}^\dagger \mathbf{A}) = \|\mathbf{A}\|_F^2 = N_o \quad (6.6)$$

Substituting the expression of \mathbf{A} onto Equation 6.5 we obtain the expansions of the reduced density matrices in terms of the left and right singular vectors.

$\begin{aligned}\rho_{mol}(t) &= \frac{1}{N_o} \mathbf{A} \mathbf{A}^\dagger \\ \rho_{mol}(t) &= \frac{1}{N_o} (\mathbf{U} \Sigma \mathbf{V}^\dagger) (\mathbf{U} \Sigma \mathbf{V}^\dagger)^\dagger \\ \rho_{mol}(t) &= \frac{1}{N_o} (\mathbf{U} \Sigma \mathbf{V}^\dagger) ((\mathbf{V}^\dagger)^\dagger \Sigma^\dagger \mathbf{U}^\dagger) \\ \rho_{mol}(t) &= \frac{1}{N_o} (\mathbf{U} \Sigma \mathbf{V}^\dagger) (\mathbf{V} \Sigma \mathbf{U}^\dagger) \\ \rho_{mol}(t) &= \frac{1}{N_o} (\mathbf{U} \Sigma^2 \mathbf{U}^\dagger) \\ \rho_{mol}(t) &= \frac{1}{N_o} \sum_{m=1}^{N_o} \sigma_m^2(t) (\mathbf{U}_m \otimes \mathbf{U}_m^\dagger)\end{aligned}$	$\begin{aligned}\rho_{orien}(t) &= \frac{1}{N_o} \mathbf{A}^\dagger \mathbf{A} \\ \rho_{orien}(t) &= \frac{1}{N_o} (\mathbf{U} \Sigma \mathbf{V}^\dagger)^\dagger (\mathbf{U} \Sigma \mathbf{V}^\dagger) \\ \rho_{orien}(t) &= \frac{1}{N_o} ((\mathbf{V}^\dagger)^\dagger \Sigma^\dagger \mathbf{U}^\dagger) (\mathbf{U} \Sigma \mathbf{V}^\dagger) \\ \rho_{orien}(t) &= \frac{1}{N_o} (\mathbf{V} \Sigma \mathbf{U}^\dagger) (\mathbf{U} \Sigma \mathbf{V}^\dagger) \\ \rho_{orien}(t) &= \frac{1}{N_o} (\mathbf{V} \Sigma^2 \mathbf{V}^\dagger) \\ \rho_{orien}(t) &= \frac{1}{N_o} \sum_{m=1}^{N_o} \sigma_m^2(t) (\mathbf{V}_m \otimes \mathbf{V}_m^\dagger)\end{aligned}\quad (6.7)$
--	---

The left singular vectors \mathbf{U}_m are the eigenvectors of the molecular density matrix $\rho_{mol}(t)$, while the right singular vectors are the eigenvectors of the orientational density matrix $\rho_{orien}(t)$. Both reduced density matrices have the same set of eigenvalues λ_m which are the squares of the singular values of \mathbf{A}

$$\text{Tr}[\rho_{mol}(t)] = \text{Tr}[\rho_{orien}(t)] = \sum_{m=1}^{N_o} \lambda_m(t) = \left(\frac{1}{N_o}\right) \sum_{m=1}^{N_o} \sigma_m^2(t) = 1 \quad (6.8)$$

Observables can be computed from the reduced molecular density matrix as shown in the following equation

$$\langle \hat{O} \rangle = \text{Tr}[\rho \hat{O}] \quad (6.9)$$

Where \hat{O} is an arbitrary operator and ρ is the density matrix.

SVD can reduce considerably the number of orientations that need to be propagated in order to reproduce accurately the dynamics of the whole ensemble. We show in this thesis, that after performing SVD of the matrix \mathbf{A} containing the wavefunctions for every orientation of the field, a few singular values carry the major contribution in the expansion of Equations 6.4 and 6.7, meaning that one can define an optimal number of singular components to be retained, $N_{\min} < N_o$, to reach a given accuracy threshold :

$$\mathbf{A}(t) \approx \sum_{m=1}^{N_{\min}} \sigma_m(t) \mathbf{U}_m(t) \otimes \mathbf{V}_m^\dagger(t), N_{\min} < N_o \quad (6.10)$$

In the case of the simulation of LiH interacting with a randomly oriented electric field of the optical pulse, we show that $N_{\min} = 5$ singular values are enough to reproduce the ensemble dynamics which is much smaller than the total number of orientations (800) sampled on the sphere. This allows for a massive data compaction and reduces the number of orientations that need to be propagated beyond the interaction with the pulse. The left and right singular vectors associated with the dominant singular values are representative of the whole ensemble and carry information about the molecular state and the orientations, respectively. We show that at the end of the pulse t' , averaging over the set of dominant left singular vectors ($U_m(t')$) weighted by their corresponding singular values squared, yields a molecular density matrix (Equation 6.7) with a marginal error compared to the ‘exact’ evaluation by averaging over the whole set of orientations. Figure 5.2 outlines how the error introduced on the molecular density matrix can be decreased systematically taking more singular components in the expansion Equation 5.22 above. The error is estimated using the Fröbenius norm $\|F_m\| = \sqrt{\sum_{i,j}^{N_b} |(\rho_{mol}^{av})_{ij} - (\rho_{mol}^m)_{ij}|^2}$, where ρ_{mol}^{av} is the ‘exact’ density matrix as given by the average over all the initial orientations and ρ_{mol}^m is the density matrix considering only a few singular values (Equation 5.19 above). As we can see in the two cases shown in Figure 5.2, just considering the five largest singular values introduces an error of $\sim 10^{-5}$ on the molecular density matrix and with 15, the error drops to $\sim 10^{-12}$, which is of the order of the error arising from the numerical integration.

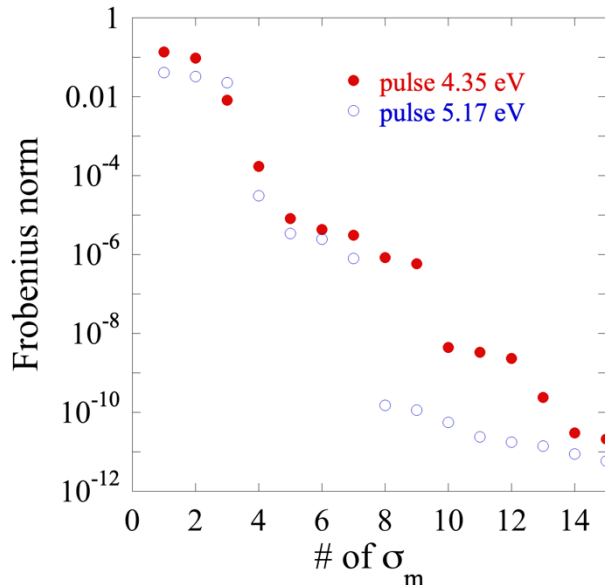


Figure 5.2 : Fröbenius measure of the difference between the density matrix averaged across the 800 initial orientations, and the density matrix recovered from the singular values after the exciting pulse is over. Two pulses with carrier frequencies of 4.35 and 5.17 eV , strength $6.71 \times 10^{12} \text{ W/cm}^2$, duration 0.8 fs and CEP = 0 are analyzed.

The massive compaction of the density matrix after SVD (Equation 6.7 above) enables an efficient propagation scheme that only requires solving the TDSE for the molecular states represented by the few, N_{min} , dominant left singular vectors, after the pulse (Equation 6.11). This is possible because the Hamiltonian is stationary after the pulse, meaning the system remains in a stationary state, which can be characterized by the same set of singular values.

$$i \frac{d\mathbf{U}_m}{dt} = \mathbf{H}\mathbf{U}_m \text{ for } t > t' \text{ and with } m = 1 \cdots N_{\text{min}} \quad (6.11)$$

Where \mathbf{H} is the same Hamiltonian used for the full-ensemble propagation, \mathbf{U}_m is each of the N_{min} largest left singular vectors that are considered for the propagation, and t' represents the time at which the pulse ends ($\|\mathbf{E}(t')\| \approx 10^{-18} \text{ au}$).

These results have been reported in a publication that has been presented at the end of this chapter and in ref. (5).

6.2 Summary of contributions

All the authors contributed to writing the manuscript, analyzing the results, and developing and refining the ideas.

Manuel Cardosa Gutierrez conducted the quantum-dynamics simulations of an ensemble of randomly oriented LiH molecules, using a Runge Kutta 4th order integrator for propagation. He sampled from the unit sphere, a set of random uniformly distributed electric field polarizations. Building on the previous work on the methane cation in the group (I) using the sudden ionization approximation, Manuel Cardosa performed the singular value decomposition on the rectangular matrix of the wavefunctions during the pulse and at the end of the pulse. He visualized and analyzed the singular vectors uncovering patterns in the dynamics of the ensemble, such as the robustness of the electronic coherences with respect to the averaging over the randomly orientated molecules. Additionally, he compared the dynamics of the full ensemble of randomly oriented molecules with those of a reduced set of singular vectors, demonstrating both the accuracy and efficiency of the method through appropriate metrics, including the Frobenius norm or the emission dipole profile.

Francoise Remacle brought her extensive expertise to guide the research and extend the previously published scheme (I) to take into account the dynamics of the interaction with the exciting pulse. Raphael Levine brought his insights about the stereodynamical aspects of the analysis of the dynamics of the ensemble.

6.3 References

1. C. E. M. Gonçalves, R. D. Levine, F. Remacle, Ultrafast geometrical reorganization of a methane cation upon sudden ionization: an isotope effect on electronic non-equilibrium quantum dynamics. *Phys. Chem. Chem. Phys.* **23**, 12051-12059 (2021).
2. G. H. Golub, C. Reinsch, in *Handbook for Automatic Computation*, F. L. Bauer *et al.*, Eds. (Springer Berlin Heidelberg, Berlin, Heidelberg, 1971), pp. 134-151.
3. S. L. Brunton, J. N. Kutz, *Data-Driven Science and Engineering: Machine Learning, Dynamical Systems, and Control*. (Cambridge University Press, ed. 1, 2019).
4. L. N. Trefethen, D. Bau, *Numerical linear algebra*. (Society for Industrial and Applied Mathematics, Philadelphia, 1997), pp. 361.
5. M. Cardosa-Gutierrez, R. D. Levine, F. Remacle, Electronic Coherences Excited by an Ultra Short Pulse Are Robust with Respect to Averaging over Randomly Oriented Molecules as Shown by Singular Value Decomposition. *J. Phys. Chem. A* **128**, 2937-2947 (2024).

6.4 Publication: “Electronic Coherences Excited by an UltraShort Pulse Are Robust with Respect to Averaging over Randomly Oriented Molecules as Shown by Singular Value Decomposition”

Electronic Coherences Excited by an Ultra Short Pulse Are Robust with Respect to Averaging over Randomly Oriented Molecules as Shown by Singular Value Decomposition

Published as part of *The Journal of Physical Chemistry A* virtual special issue "Attosecond Chemistry".

Manuel Cardosa-Gutierrez, Raphael D. Levine, and Françoise Remacle*

Cite This: <https://doi.org/10.1021/acs.jpca.3c07856>

Read Online

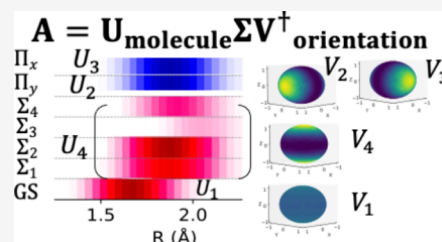
ACCESS |

Metrics & More

Article Recommendations

Supporting Information

ABSTRACT: We report a methodology for averaging quantum photoexcitation vibronic dynamics over the initial orientations of the molecules with respect to an ultrashort light pulse. We use singular value decomposition of the ensemble density matrix of the excited molecules, which allows the identification of the few dominant principal molecular orientations with respect to the polarization direction of the electric field. The principal orientations provide insights into the specific stereodynamics of the corresponding principal molecular vibronic states. The massive compaction of the vibronic density matrix of the ensemble of randomly oriented pumped molecules enables a most efficient fully quantum mechanical time propagation scheme. Two examples are discussed for the quantum dynamics of the LiH molecule in the manifolds of its electronically excited Σ and Π states. Our results show that electronic and vibrational coherences between excited states of the same symmetry are resilient to averaging over an ensemble of molecular orientations and can be selectively excited at the ensemble level by tuning the pulse parameters.



INTRODUCTION

Recent progress in attoscience^{1–3} opens the way to new avenues for controlling chemical reactivity through the selective excitation of a superposition of electronic states with the short-in-time-broad-in-energy attopulse.⁴ As pointed out very early,⁵ the orientation of the molecule with respect to the polarization direction of the pulse electric field is a very effective way to control the initial superposition built by the pulse and therefore the subsequent dynamics. Molecules can be aligned or oriented using a single or a sequence of laser pulses, enabling them to carry out field-free photoexcitation or photoionization experiments in the molecular frame.^{6–10} However, the achievable orientation is typically limited to values of $\langle \cos \theta \rangle \approx 0.7$ and $\langle \cos^2 \theta \rangle \approx 0.8$. Moreover, the proposed experimental approaches to align or orient molecules are not applicable to all types of molecules.^{11–13} Therefore, it is often the case that a realistic description of quantum dynamics of molecules photoexcited by short atto and few femtosecond pulses requires an averaging over the molecular orientations with respect to the polarization direction of the exciting optical pulse. However, averaging quantum dynamics simulations over an ensemble of molecular orientations can be computationally rather costly in computer time and storage capacity since the quantum dynamical propagation needs to be repeated as many times as the number of molecular orientations in the ensemble. This is particularly so when the pulse parameters other than the polarization direction need to be tuned to control the vibronic dynamics, which requires

repeated ensemble averaging a large number of times. While orientation averaging is manageable computationally for the vibronic quantum dynamics of diatomic molecules in a superposition of several electronic states, it becomes out of reach for a quantum dynamical simulation involving several nuclear degrees of freedom on coupled electronic states, as typical when molecules and molecular cations are excited by ultrashort, broad in energy atto pulses.^{2,14–18} Even for a diatomic molecule, tuning the pulse parameters for an ensemble of molecular orientations becomes computationally very demanding, in terms of memory capacity and computer time.

Here, we propose a numerical approach for computing the ensemble dynamics of randomly oriented molecules interacting with an ultrashort optical pulse that considerably lowers the cost of computational resources and provides insights into the orientation effects. Our approach is based on the Singular Value Decomposition (SVD)¹⁹ of the matrix built from the pure quantum states associated with each molecular orientation of the ensemble. This matrix, \mathbf{A} , is a rectangular matrix with dimension, N_b , the number of vibronic basis

Received: November 30, 2023

Revised: March 13, 2024

Accepted: March 14, 2024

functions used to expand the wave function, times the number of molecular orientations, N_o . Typically, when the pulse is over, only a few principal components suffice to obtain an accurate description of matrix \mathbf{A} . The SVD principal components identify the most important orientations that contribute to the ensemble dynamics (the singular orientation vectors) and the corresponding oriented molecular pure quantum states (the singular molecular states). Each of these molecular pure quantum states evolves in time in a specific way that it is dictated by the principal orientation to which it corresponds. One therefore gets insights into the dynamics in specific orientations whose relative weight in the ensemble can be tuned by the pulse parameters other than its polarization direction: the duration and the carrier frequency of the pulse. Valuable stereo dynamics insights are therefore gained for an ensemble of randomly oriented molecules.

In addition, we show that the SVD compaction significantly reduces the cost of computing the quantum dynamics of the ensemble since only a few singular (pure) oriented molecular quantum states need to be stored and propagated after the pulse to accurately describe the ensemble quantum dynamics. An exact description is obtained by retaining as the number of principal components the smallest dimension of \mathbf{A} matrix, which is typically the number of orientations, N_o . For an approximate description, one can adjust the number of retained principal components necessary to reach a specified accuracy threshold. We find that only a few components are required for a satisfactory semiquantitative description.

METHODS: SVD APPROACH TO COUPLED ELECTRONS-NUCLEI QUANTUM DYNAMICS AVERAGED OVER RANDOM MOLECULAR ORIENTATIONS

At time $t = 0$, the molecules of the ensemble are in their ground electronic state. The different molecules of the ensemble are distributed over their particular orientation, o , with respect to the polarization direction of the exciting pulse. Each initial orientation, o , at the time before excitation defines a pure state, $|\Psi_o(t=0)\rangle$. During and after the excitation by the atto pulse each initial state evolves into $|\Psi_o(t)\rangle$, a coherent combination represented as a Born-Huang expansion, a sum of N_b separable terms in the nuclear and electronic degrees of freedom:

$$|\Psi_o(t)\rangle = \sum_{b=1}^{N_b} c_b^o(t)|b\rangle \quad (1)$$

where $c_b^o(t)$ is the Born-Huang amplitude of the vibronic basis function $|b\rangle$ for the initial orientation, o . The index b stands for a nuclear and an electronic index that, for a pulse broad in energy, includes several coupled electronic states. In general, we expect that the number of terms in eq 1 is such that $N_b \gg N_o$, where N_o is the number of molecular orientations in the ensemble. The amplitudes $c_b^o(t)$ are computed by integrating the Time-Dependent Schrödinger Equation (TDSE), for a basis of N_g grid functions, $|g\rangle$, for the nuclear coordinates and N_e coupled adiabatic electronic states, $|i\rangle:|b\rangle = |g\rangle|i\rangle$, which leads to a total dimension $N_b = N_g \times N_e$ for the vector of the amplitudes \mathbf{c}_o :

$$i\hbar \frac{d\mathbf{c}_o}{dt} = \mathbf{H}\mathbf{c}_o \quad (2)$$

The inequality $N_b \gg N_o$ is primarily because the number N_g of grid points needs to be large. The molecular Hamiltonian, \mathbf{H} , includes the coupling to the electric field of the pulse, $\mathbf{E}(t)$, in the dipole approximation and the nonadiabatic coupling (NAC) between the electronic states driven by the nuclear motion. For a nonrotating diatomic molecule,

$$\mathbf{H} = -\frac{1}{2\mu}(\nabla_R^2 + 2\tau(R) \cdot \nabla_R + (\nabla_R \tau(R)) + \tau(R) \cdot \tau(R)) + \mathbf{V}(R) - \mathbf{E}(t) \cdot \boldsymbol{\mu} \quad (3)$$

In eq 3, the τ is the nonadiabatic coupling between electronic states, $\tau_{ij}(R) = \langle \phi_i^{\text{ele}} | \nabla_R | \phi_j^{\text{ele}} \rangle$ and $\mathbf{V}(R)$ the potential term. The last term is the dipole coupling where $\boldsymbol{\mu}$ is the total dipole operator, $\boldsymbol{\mu} = \boldsymbol{\mu}^{\text{nuc}} + \boldsymbol{\mu}^{\text{ele}}$. The electric field is given by

$$\mathbf{E}(t) = \frac{d\mathbf{A}(t)}{dt} = \hat{\mathbf{e}}|E_0| \exp\left(-\frac{(t-t_p)^2}{2\sigma_p^2}\right) \left(\cos(\omega_p(t-t_p)) - \left(\frac{t-t_p}{\omega_p\sigma_p^2}\right) \sin(\omega_p(t-t_p)) \right) \quad (4)$$

In eq 4, $|E_0|$ is the strength of the pulse. The pulse is confined in a Gaussian envelope centered at t_p , with a carrier frequency ω_p and a full width at half maximum (fwhm) given by $2\sqrt{2\ln 2}\sigma_p$. The orientation of the electric field vector, $\hat{\mathbf{e}}$, is defined in the molecular frame attached to the center of mass of the molecule. This considerably simplifies the numerical integration of the TDSE and is equivalent to defining the orientation of the molecular frame with respect to the orientation of the electric field in the laboratory frame. Note that one needs to rotate back to the laboratory frame before analyzing the angular distributions.

During the pulse, the Hamiltonian depends on time, and each polarization direction of the pulse defines specific dynamics. For an ensemble of molecular orientations, one therefore needs to average the dynamics over the ensemble. We do so by integrating the TDSE during the pulse for an ensemble of N_o orientations of $\mathbf{E}(t)$, each computed separately, obtaining N_o time-dependent pure states $|\Psi_o(t)\rangle$. These states are gathered into a rectangular, complex, $N_b \times N_o$, matrix \mathbf{A} with typically $N_o < N_b$. Singular Value Decomposition (SVD) provides an exact description of the matrix \mathbf{A} as a sum of a maximum of N_o separable terms, its principal components.¹⁹ The SVD factorization of \mathbf{A} is a sum of direct products of a left, \mathbf{U}_m , and a right, \mathbf{V}_m^\dagger , singular complex eigenvector weighted by the corresponding (real) singular value, σ_m ,

$$\mathbf{A}(t) = \sum_{m=1}^{N_o} \sigma_m(t) \mathbf{U}_m(t) \otimes \mathbf{V}_m^\dagger(t) \quad (5)$$

In each principal component, m , the right singular vector, $\mathbf{V}_m(t)$, has N_o components, $v_{om}(t)$, and depends only on the orientation index, o , and the left singular vector, $\mathbf{U}_m(t)$, has N_b components, u_{bm} , and depends only on the basis set index b . Throughout, we refer to $\mathbf{V}_m(t)$ as the orientation singular vector and $\mathbf{U}_m(t)$ as the molecular singular vector.

From the rectangular \mathbf{A} matrix, one can construct two reduced square density matrices. The $N_b \times N_b$ density matrix of the ensemble of molecules, $\rho_{\text{mol}}(t)$, is the trace over the

orientations and depends on only the molecular degrees of freedom only. It is the \mathbf{AA}^\dagger quadratic form of the matrix $\mathbf{A}(t)$:²⁰

$$\begin{aligned}\rho^{\text{mol}}(t) &= (1/N_0)\mathbf{AA}^\dagger \\ &= (1/N_0)\sum_{o=1}^{N_b}\mathbf{c}_o(t)\mathbf{c}_o^\dagger(t) \\ &= (1/N_0)\sum_{b=1}^{N_b}\sum_{b'=1}^{N_b}|b\rangle\left(\sum_{o=1}^{N_b}c_b^o(t)c_{b'}^{o*}(t)\right)\langle b'| \end{aligned} \quad (6)$$

The matrix elements of $\rho^{\text{mol}}(t)$ are the average populations and coherences between the basis set functions $|b\rangle = |g\rangle|i\rangle$. $\rho^{\text{mol}}(t)$ is a function of the molecular singular vectors only. Inserting eq 5 into eq 6, one gets

$$\begin{aligned}\rho^{\text{mol}}(t) &= (1/N_0)\sum_{m,m'}\sigma_m(t)\sigma_{m'}(t)(\mathbf{U}_m \otimes \mathbf{V}_m^\dagger \cdot \\ &\quad (\mathbf{V}_{m'} \otimes \mathbf{U}_{m'}^\dagger)) \\ &= (1/N_0)\sum_{m,m'}\sigma_m(t)\sigma_{m'}(t)(\mathbf{U}_m \otimes (\mathbf{V}_{m'}^\dagger \cdot \mathbf{V}_{m'}) \otimes \mathbf{U}_{m'}^\dagger) \\ &= (1/N_0)\sum_m\sigma_m^2(t)(\mathbf{U}_m \otimes \mathbf{U}_m^\dagger) = (1/N_0)\sum_m\sigma_m^2(t)\rho_m^{\text{mol}}(t) \end{aligned} \quad (7)$$

where the last line results from the orthogonality of the orientation singular vectors: $\mathbf{V}_m^\dagger \cdot \mathbf{V}_{m'} = \delta_{mm'}$. Each singular vector leads to a principal molecular density matrix, $\rho_m^{\text{mol}}(t)$, which in turn defines a reduced nuclear and a reduced electronic density matrix, thereby providing insights into the vibrational and electronic coherences of the principal orientations.

$$\begin{aligned}\rho_{\text{mol}}^{\text{nuc}}(t) &= \text{Tr}_{\text{ele}}(\rho^{\text{mol}}(t)) \\ &= (1/N_0)\sum_m\sigma_m^2\text{Tr}_{\text{ele}}(\rho_m^{\text{mol}}(t)) \\ &= (1/N_0)\sum_m\sigma_m^2\rho_{\text{nuc},m}^{\text{mol}}(t) \end{aligned} \quad (8)$$

whose off diagonal elements correspond to the coherences between points of the nuclear grid and its diagonal elements to the average localization of the vibronic wave packet on the grid. Tracing $\rho^{\text{mol}}(t)$ over grid points provides the reduced electronic density matrix:

$$\begin{aligned}\rho_{\text{mol}}^{\text{ele}}(t) &= \text{Tr}_g(\rho^{\text{mol}}(t)) \\ &= (1/N_0)\sum_{m=1}^{N_{\text{min}}}\sigma_m^2\text{Tr}_g(\rho_m^{\text{mol}}(t)) \\ &= (1/N_0)\sum_{m=1}^{N_{\text{min}}}\sigma_m^2\rho_{\text{ele},m}^{\text{mol}}(t) \end{aligned} \quad (9)$$

Similarly, one can define the complementary $N_o \times N_o$ reduced orientation density matrix, $\rho^{\text{orien}}(t)$, by the quadratic form $\mathbf{A}^\dagger\mathbf{A}$:

$$\rho^{\text{orien}}(t) = (1/N_0)\mathbf{A}^\dagger\mathbf{A} \quad (10)$$

with matrix elements given by

$$\rho_{oo'}^{\text{orien}}(t) = \left(\frac{1}{N_o}\right)\sum_{b=1}^{N_b}c_b^{o*}(t)c_b^o(t) = \begin{cases} (1/N_o) & \text{if } o \equiv o' \\ <(1/N_o) & \text{otherwise} \end{cases} \quad (11)$$

$\rho^{\text{orien}}(t)$ depends on the orientation of singular vectors only. Using eq 5

$$\begin{aligned}\rho^{\text{orien}}(t) &= (1/N_o)\sum_{m,m'}\sigma_m(t)\sigma_{m'}(t)(\mathbf{V}_m \otimes \mathbf{U}_m^\dagger \cdot \\ &\quad (\mathbf{U}_{m'} \otimes \mathbf{V}_{m'}^\dagger)) \\ &= (1/N_o)\sum_{m,m'}\sigma_m(t)\sigma_{m'}(t)(\mathbf{V}_m \otimes (\mathbf{U}_{m'}^\dagger \cdot \mathbf{U}_{m'}) \otimes \mathbf{V}_{m'}^\dagger) \\ &= (1/N_o)\sum_m\sigma_m^2(t)(\mathbf{V}_m \otimes \mathbf{V}_m^\dagger) = (1/N_o)\sum_m\sigma_m^2(t)\rho_m^{\text{orien}}(t) \end{aligned} \quad (12)$$

Note that the two partial traces, $\rho^{\text{mol}}(t)$ and $\rho^{\text{orien}}(t)$, have the same set of eigenvalues, which are the square of the singular values, σ_m , of the matrix \mathbf{A} :

$$\text{Tr}[\rho_{\text{mol}}(t)] = \text{Tr}[\rho_{\text{orien}}(t)] = \left(\frac{1}{N_o}\right)\sum_{m=1}^{N_b}\sigma_m^2(t) = 1 \quad (13)$$

with $\sum_{m=1}^{N_b}\sigma_m^2(t) = N_o$.

We define a set of 800 orientations on the unit sphere. Each orientation is a three-dimensional vector in the molecular frame: $\hat{\mathbf{e}}_o = x_o\hat{\mathbf{e}}_x + y_o\hat{\mathbf{e}}_y + z_o\hat{\mathbf{e}}_z$. The orientation density matrix before interacting with the molecule is defined by the scalar products between all the vectors $\hat{\mathbf{e}}_o$. Gathering the vectors $\hat{\mathbf{e}}_o$ in a $N_o \times 3$ matrix \mathbf{e} in which each row is given by the Cartesian components (x_o, y_o, z_o) of a vector $\hat{\mathbf{e}}_o$, we can write $\rho^{\text{orien}}(0) = \mathbf{e}\mathbf{e}^T$. Initially, there are at most three principal orientation vectors, one along x , one along y , and one along z . Note that the $N_o \times N_o$ matrix $\rho^{\text{orien}}(0)$ is off-diagonal. The off-diagonal elements will be large when the two orientations oo' are close to one another.

In the sudden approximation for the photoexcitation, i.e., a one photon transition at time t_p when the pulse is maximum, eq 4, and restricting the dynamics to the excited states, the initial amplitudes at each point of the nuclear grid in each excited electronic state can be factorized as the scalar product of the orientation of the electric field, $\hat{\mathbf{e}}_0$, and the transition dipole moment from the ground electronic state $\mu_{\text{T}}^{\text{GS-gi}} = (\mu_{\text{GS-gi}}^x, \mu_{\text{GS-gi}}^y, \mu_{\text{GS-gi}}^z)$:

$$c_{\text{gi}}^0 = \hat{\mathbf{e}}_0^T \cdot \mu_{\text{gi}} \quad (14)$$

We show in the SI that then $\rho^{\text{mol}}(t_p)$ is given by

$$\rho^{\text{mol}}(t_p) = \mu\mu^T \quad (15)$$

where μ is the $((N_e - 1) \times N_g) \times 3$ matrix of the Cartesian components of the transition dipole between the GS and the excited states at each grid point. $\rho^{\text{mol}}(t_p)$ is independent of the polarization direction of the electric field of the pulse for an ensemble of randomly oriented molecules. It can only have 3 principal components oriented along the three Cartesian axes of the molecular frame. We have previously used this result for describing the ultrafast vibronic Jahn–Teller structural rearrangement induced by the sudden photoionization of methane²¹ using a 3 electronic state 2 nuclear degrees of freedom model.

Here, we go beyond the sudden approximation limit and treat the case of stronger pulses that entangle the orientations and the intramolecular nuclear and electronic degrees of freedom and induce transient vibronic dynamics. The nonlinear excitation process leads to a time dependence of the singular values $\sigma_m(t)$ and of the molecular and orientation singular vectors in eq 5. When the pulse is over, the dipole coupling terms vanish, and the Hamiltonian, eq 3, becomes stationary. Then the singular values become stationary since we consider a nonrotating molecule.

The SVD of the \mathbf{A} matrix at the end of the pulse, at time t_i , therefore provides a set of orthogonal pure states, \mathbf{U}_m , that each corresponds to a specific singular orientation of the molecule as defined by the corresponding orientation singular vector \mathbf{V}_m . We show below that only a few singular values, $\sigma_m(t_i)$, $3 < N_{\min} \leq N_o$, suffice to recover accurately the molecular density matrix averaged over the molecular orientations, $\rho^{\text{mol}}(t_i)$, at the end of the pulse, t_i (eq 7). The minimum number of principal components is larger than 3 because of the transient dynamics occurring during the pulse, which entangles the nuclear and electronic molecular degrees of freedom with the orientation of the pulse electric field and the fact that the dynamics in the GS are included. One can set the maximum number of singular values, $\sigma_m(t_i)$, needed to describe the dynamics by putting a threshold on how well the norm of $\rho^{\text{mol}}(t_i)$ is recovered:

$$\Delta_{N_{\min}} = 1 - \text{Tr}[\rho_{N_{\min}}^{\text{mol}}(t_i)] = 1 - \left(\frac{1}{N_o}\right) \sum_{m=1}^{N_{\min}} \sigma_m^2(t_i) \geq 0 \quad (16)$$

Since the singular values are stationary, one can set up a very efficient propagation scheme for the density matrix of the ensemble of molecules, $\rho^{\text{mol}}(t)$, after the pulse, by propagating with the molecular Hamiltonian (eq 3) only the few, N_{\min} , \mathbf{U}_m vectors that correspond to the largest singular values:

$$i\hbar d\mathbf{U}_m/dt = \mathbf{H}\mathbf{U}_m \text{ for } t > t_i, \text{ with } \mathbf{U}_m(t_i) = \sum_{b=1}^{N_b} u_{bm}(t_i)|b\rangle \quad (17)$$

where the initial values, $u_{bm}(t_i)$, are the coefficients of the \mathbf{U}_m vectors at the time t_i (the end of the pulse).

Providing that the TDSE is integrated accurately so that the integration error is smaller than $\Delta_{N_{\min}}$, the numerical error, eq 16, which is due to the fact that we use a restricted number of principal components of the matrix \mathbf{A} , does not increase with time. Using eq 7, we get

$$\begin{aligned} \rho_{N_{\min}}^{\text{mol}}(t) &= (1/N_o) \sum_{m=1}^{N_{\min}} \sigma_m^2(t_i) \sum_b^{N_b} \sum_{b'}^{N_{b'}} u_{bm}^*(t) u_{b'm}^*(t) |b\rangle \langle b'| \\ &= (1/N_o) \sum_{m=1}^{N_{\min}} \sigma_m^2(t_i) \rho_m^{\text{mol}}(t) \\ &> t_i \end{aligned} \quad (18)$$

To summarize, our approach requires propagation of all of the initial states defined by a sampling of the molecular orientations until the pulse is over. Since we consider excitation by short atto or few, 1–2, fs pulses, this propagation time is short, on the order of 20 fs for a pulse with a fwhm of 2 fs. Then when the Hamiltonian is stationary, one performs an SVD analysis of the matrix \mathbf{A} (eq 5) and retains the N_{\min}

largest principal components necessary to reach a specified accuracy threshold. Only these fewer components need to be propagated after the pulse by using the TDSE as long as the molecular Hamiltonian remains stationary. This approach reduces the computer time needed to compute quantum molecular dynamics averaged over molecular orientations by at least 2 orders of magnitude for the dynamics of a diatomic molecule taking place on several electronic states. The gain is even larger when the molecule has several nuclear degrees of freedom. It is also storage efficient because it allows compacting the information on dynamics of the randomly oriented initial states into a few singular components. Using our approach, one does not need to store and analyze the dynamics of all of the randomly orientated initial states. Each of the principal molecular vectors provides the vibronic stereodynamics corresponding to a specific principal molecular orientation of the ensemble.

RESULTS AND DISCUSSION

SVD Approach to the Dynamics of Randomly Oriented LiH Molecules. We apply our scheme to the nonrotating LiH molecule excited by two deep UV few cycles pulses of different carrier frequencies and with the same fwhm of 2 fs (fwhm bandwidth in energy of 1.82 eV), eq 4. Such pulses are ideally suited to excite neutral polyatomic molecules by one-photon excitation and their generation has recently been reported.^{22–24} LiH has a rotational period of 4.4 ps, which justifies the fact that there is no coupling to rotations during the pulse and for the next 200 fs of the dynamics. In the Franck–Condon (FC) region, $R_{\text{eq}} = 1.6\text{\AA}$ (see Figure S2a), the transition dipole moment from the GS to the lowest Σ state, Σ_1 , along z is smaller than the transition dipole along x or y to the lowest Π state, Π_1 , and to the higher Σ and Π states. We report on the dynamics induced using pulses with two different carrier frequencies, ω_p , tuned to access different combinations of the Σ and Π states. The first pulse has a carrier frequency of 4.35 eV so that both the lowest Σ_1 and Π_1 states fall within the pulse energy bandwidth. However, because of the difference in the transition dipole moments, for random orientations, it is the Π_1 state that is accessed, with only very low populations in Π_3 , in Σ_1 , and in the entire Σ manifold. The second pulse has a higher carrier frequency of 5.17 eV which allows accessing the higher Σ and $i\hbar \frac{dc_o}{dt} = \mathbf{H}c_o$ states with similar probabilities. The strength of the electric field, $|E_0|$ is 0.01 au ($3.51 \cdot 10^{12}$ W/cm²) for both pulses. A field strength of $\approx 10^{12}$ W/cm² is at the higher end of the range of currently available 1–2 fs DUV pulses.^{22–24} It is also low enough to avoid photoionization by two-photon absorption. As discussed below, this field strength is large enough to induce nonlinear effects and transient population dynamics during the excitation process and entangle the orientations with the intramolecular degrees of freedom.

The dynamics induced by the first pulse is used for benchmarking the SVD approach for random initial molecular orientations. Excitation by the 4.35 eV pulse yields very different populations: the population of the Π_1 state is 1–2 orders of magnitude larger than that of the Σ and Π_3 states. To benchmark our approach, we computed the time evolution by solving the TDSE for 800 random initial orientations using eq 2 for 200 fs. The electronic structure parameters (potential energy, transition dipole, and NAC curves) are those reported in ref 25 and plotted in the SI (Figures S1, S2a–d, and S3a–c).

The NAC terms couple electronic states of the same symmetry, Σ or Π . Electric fields oriented along the molecular axis (the z axis in the molecular frame (see inset of Figure S1)) can access only excited Σ states since the ground state is of Σ symmetry. However, as soon as the electric field has components along x or y in the molecular frame, a linear combination of Σ and Π states is excited. Since the transition dipole to the Π_1 state is larger than that to the Σ states and to the other Π states, the averaged populations in its two components are much larger than that of the other states. The populations in the electronic states averaged over 800 random molecular orientations are plotted in Figure 1a for the Π_1 state and in Figure 1b for the Σ manifold and the Π_3 state.

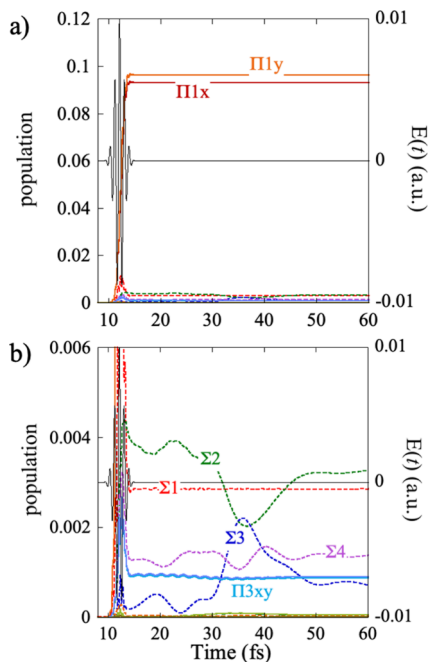


Figure 1. Populations averaged over 800 molecular orientations in the Π_1 state (a) and (b) in the Σ manifold (Σ_2 , Σ_3 and Σ_4) and the Π_3 state computed for an excitation by the deep UV 2 fs pulse of 4.35 eV. The reason why the two components of the Π_1 state are not exactly equal is because only 800 orientations are included in the averaging procedure. After the pulse, the population of the Π_1 state is essentially stationary. The long time behavior is given in Figure S4.

The electronic states within each manifold are coupled by the NAC terms. As can be seen from Figure 1b, the population transfers are far larger within the states of the Σ manifold than those for the Π ones. This is mainly due to the fact that the energy difference between the two lowest Π states is much larger. For the same reason, the population transfers between the Σ_1 state and the higher Σ states are also small.

Our SVD approach to the ensemble dynamics begins by building the matrix A (eq 5) from the 800 randomly oriented c_v vectors and computes its principal components by SVD at every time step during the excitation by the pulse. The singular values are arranged in order of decreasing magnitude, with σ_1 being the largest. The square of the 8 largest singular values, σ_m^2 , normalized by N_0 , the number of initial random orientations, are plotted in Figure 2a as a function of time on a log scale to emphasize how fast they decrease in magnitude with increasing order m . As discussed above, after the pulse, the Hamiltonian is stationary, and the singular values are constant in time. The

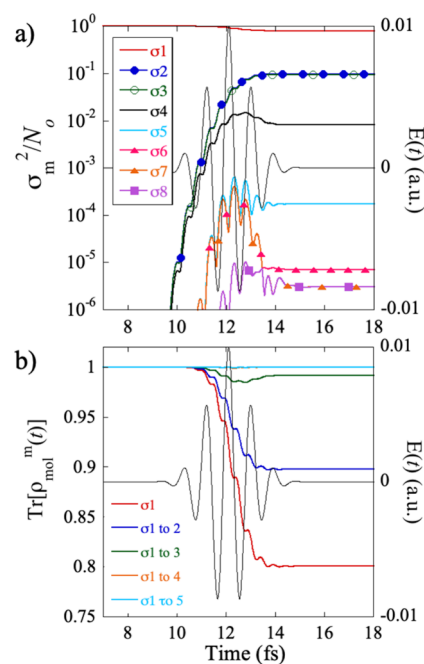


Figure 2. (a) Time evolution of the 8 largest normalized singular values, σ_m^2/N_0 , during and after the pulse. The singular values of that correspond to molecular singular vectors U_m localized on the two components of Π states and are plotted with markers so as to better identify them. The two pairs of degenerate singular values localize on the Π states, σ_2 and σ_3 on Π_1 (blue diamonds for Π_{1x} and green ones for Π_{1y}) and σ_6 (red triangles) and σ_7 (orange-filled triangles) during the pulse and σ_7 and σ_8 (filled squares) after the pulse on Π_3 . (b) The cumulative trace recovered with an increasing number of singular values, from 1 to 5.

normalized singular value σ_1 is unity before excitation and remains close to one after the pulse. It can be correlated with the ground electronic state, as we discuss below (Figure 4). σ_2 and σ_3 are degenerate during and after the pulse, while σ_6 and σ_7 that are degenerate during the pulse but after the pulse, it is the pair σ_7 , σ_8 that are equal. As shown in Figure 4 below, these two pairs of singular values are localized on the two Π states Π_1 and Π_3 . One can also see in Figure 2a that a larger number of singular values are important during the pulse than after the pulse, which is due to the entanglement between the orientations and the molecular degrees of freedom during the pulse. The populations of the higher Σ states that are involved in the transient dynamics during the pulse go back to zero when the pulse is over. Figure 2b shows how much of the trace of the density matrix, $\text{Tr}[\rho_{N_{\text{min}}}^{\text{mol}}(t)]$ (eq 16) is recovered for an increasing number of singular values, σ_m , $m = 1$ to 5. Five singular values suffice to recover the trace of the density matrix of the ensemble of 800 randomly oriented molecules with a precision better than that of 10^{-3} during the pulse and that of 10^{-5} after it is over; see Figure 3a. In Figure 3b, we plot on a log scale the set of the 25 largest singular values at the maximum of the pulse (12.3 fs) and after the pulse when the Hamiltonian and therefore the singular values are stationary (18 fs). One can see that indeed the entanglement between orientation and intramolecular degrees of freedom is larger during the transient dynamics induced by the pulse; a sixth singular value would be needed to get an accuracy of 10^{-5} during the pulse. Figure 3b also shows that with 15 eigenvalues, the SVD fit reaches error values of $\approx 10^{-13}$

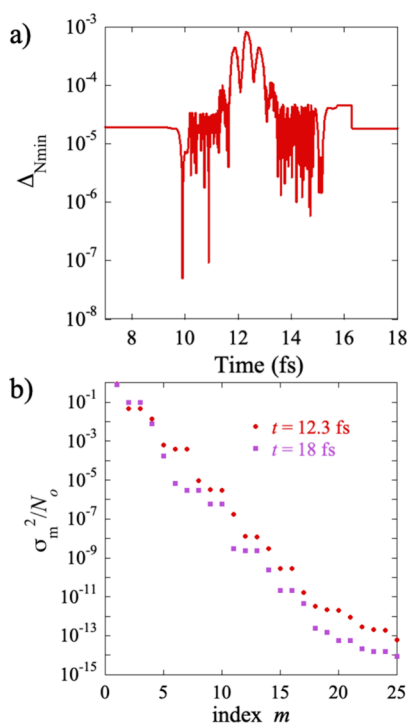


Figure 3. (a) $\Delta_{N_{\min}}$ (eq 16) the absolute value on the error on the trace computed by including 5 singular values in the trace of the density matrix, $\text{Tr}[\rho_{N=5}^{\text{mol}}(t)]$. (b) 25 largest normalized singular values computed at the maximum of the pulse (violet squares) and after the pulse, when their values are constant (red dots) at 18 fs. The doublets of degenerate singular values correlate with the two components of the Π states.

(numerically zero), which corresponds to the accuracy of the numerical integration of the TDSE.

In Figure 4, we show the localization of the molecular (left) singular vectors, \mathbf{U}_m , on the electronic states and along the R

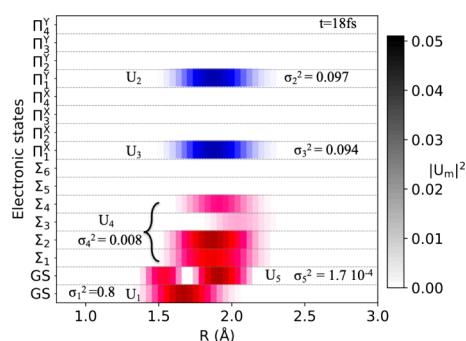


Figure 4. Localization of the molecular singular vectors \mathbf{U}_m on the grid for the 5 largest singular values. Computed for the excitation by the 2 fs 4.35 eV pulse.

coordinate, at 18 fs, after the pulse is over. \mathbf{U}_1 , which corresponds to the largest singular value, is localized on the ground electronic state and corresponds to the ground vibrational state (the initial state). \mathbf{U}_2 and \mathbf{U}_3 are localized on the Π_1 state (on the y and x components respectively) with essentially equal values of σ_2 and σ_3 . \mathbf{U}_4 is localized on the manifold of excited Σ states (Σ_1 , Σ_2 , Σ_3 , Σ_4) with a σ_4 value an order of magnitude smaller than σ_2 and σ_3 . \mathbf{U}_5 is localized on

the GS but corresponds to excited vibrational states, with an even smaller value of σ_5 .

The corresponding singular orientation vectors are shown in Figure 5a–d. \mathbf{V}_1 (panel a) is distributed uniformly on the sphere, corresponding to the initial distribution of orientations, in agreement with the localization of \mathbf{U}_1 on $v = 0$ of the ground electronic state (see Figure 4). \mathbf{V}_2 (panel c) and \mathbf{V}_3 (panel d) are localized along the y and the x -axis respectively since \mathbf{U}_2 and \mathbf{U}_3 are localized in the y and x components of the Π_1 state. \mathbf{V}_4 (panel b) is localized along the z axis since it corresponds to excited Σ states. \mathbf{V}_5 (Figure S5) is a much smaller component and corresponds to the excited vibrational state of the GS and is localized on z . We therefore see that the localization of the singular vectors is dictated by the symmetry of the electronic states, which is conserved after the pulse since the NAC terms can only couple states of the same symmetry. The carrier frequency of the pulse induces one photon transition, which means that during the pulse, the GS of Σ symmetry is coupled to the Π states, which breaks the Σ – Π symmetry, and couples in second order the Π states with the excited Σ states. This explains the higher degree of entanglement between orientations and the intramolecular degrees of freedom during the pulse discussed above. The effect here remains limited because the excited Σ and Π are populated by one photon transitions and the pulse remains relatively weak.

Since the Hamiltonian is stationary after the pulse, the left eigenvectors, \mathbf{U}_m , which are localized on the grid and on the electronic states, can be used to compute the quantum dynamics of the ensemble. We do so using eq 10 by propagating numerically the 5 \mathbf{U}_m vectors that correspond to the five largest singular values, σ_m , starting at the end of the pulse, $t_i = 18$ fs. Since the numerical precision of the integration is on the order of 10^{-12} for the 200 fs of the propagation time, the error that we make by retaining the 5 largest principal components (10^{-5} relative error on the trace of the density matrix $\rho^{\text{mol}}(t)$) does not increase. In parallel, as a benchmark, we propagated the 800 initial states separately for 200 fs using the TDSE and performed the averaging over these 800 $|\Psi_o(t)\rangle$.

The agreement between the “exact” and the ‘SVD’ ensemble averaging computations is excellent for the populations of electronic states, electronic coherences, and for observables such as the time-dependent dipole moment, which depends on both the populations and the coherences between electronic states and grid points. This is true not only for the states with a large population, like the two components of the Π_1 state and the GS plotted in Figure 1a, but also for the populations of the Σ states (Figure 1b), which have populations of a few tenths of percent only; see SI and Figures S6–S8 for details.

In Figure 6a, we show the full time-dependent emission dipole, $\mu(t)$ which is an observable very sensitive to the electronic and vibrational coherences.

$$\mu(t) = \text{Tr}[\mu\rho^{\text{mol}}(t)] = \frac{1}{N_o} \sum_{o=1}^{N_o} \sum_{g=1}^{N_g} \sum_{i,j} c_{gi}^{o*}(t) c_{gj}^o(t) \mu_{gt,gi} \quad (19)$$

Using eq 18, $\mu(t)$ can be written in terms of N_{\min} the principal components

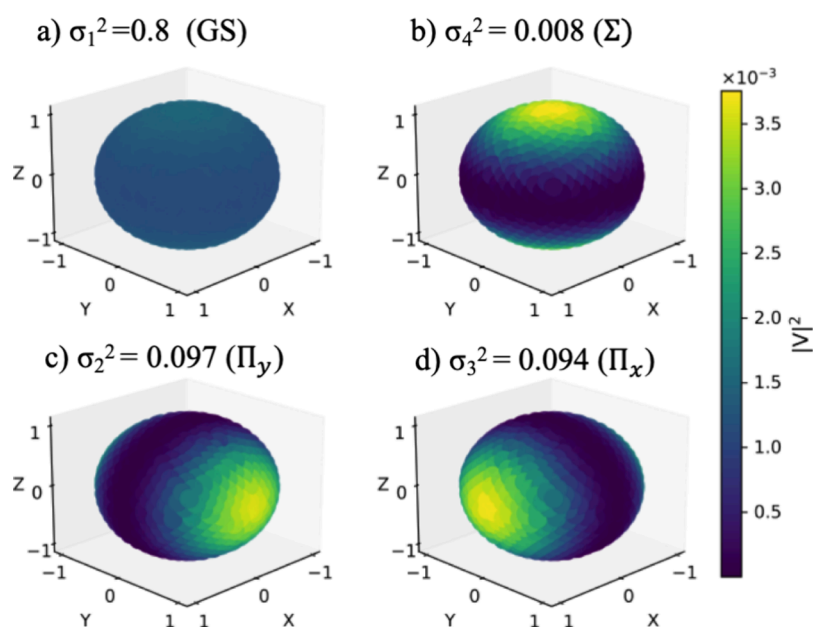


Figure 5. Orientation distribution on the unit sphere of the square modulus of the V vectors of the 4 largest principal components. V_1 (a) is uniformly distributed over all orientations. V_2 (c) and V_3 (d) are oriented along y and x respectively to account for the excitation of the Π states while V_4 (b) is oriented along z and accounts for the excitation of the Σ excited states. The color code on the rhs is common to V_2 , V_3 , and V_4 . The V vectors are normalized to 1. V_3 , which is oriented along z as well, corresponds to a more minor principal component. It is shown in Figure S5.

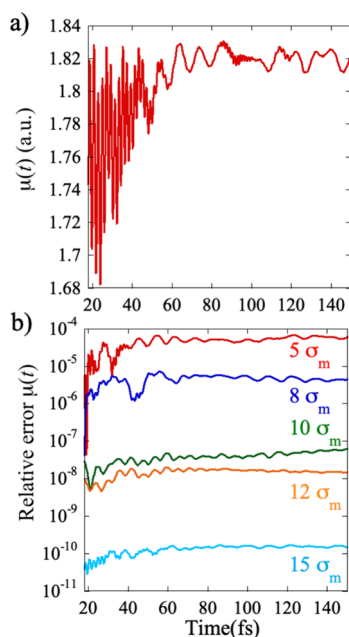


Figure 6. (a) Absolute value of the emission dipole moment, $|\mu(t)|$, computed for the exact averaging over 800 random orientation for the exciting 2 fs deep UV (4.35 eV) pulse. (b) Relative error on $\mu(t)$ computed for an increasing number of principal components as indicated.

$$\begin{aligned} \mu(t) &= \text{Tr}[\mu\rho^{\text{mol}}(t)] \\ &= \frac{1}{N_o} \sum_{m=1}^{N_{\text{min}}} \sigma_m^2(t_i) \sum_{g=1}^{N_g} \sum_{i,j} u_{gi}^{m*}(t) u_{gi}^m(t) \mu_{gi,gj} \end{aligned} \quad (20)$$

From eq 20, one sees that beatings of the emission dipole correspond to electronic coherences between Π states or between excited Σ states since the molecular singular vectors

project electronic states of a given symmetry (see Figure 4 above). The fast ≈ 2 fs periods are the beatings between the Π_1 and the Π_3 states and those between Σ_1 and Σ_2 . The longer beatings with a ≈ 10 fs period correspond to the beatings of the electronic coherences between the higher Σ excited states. Note that the amplitudes of the beatings of $\mu(t)$ decrease in time because while the GS and Σ_1 are bound, all the other excited states, including Π_1 , are dissociative and the electronic coherences fade away. The revival of the fast period at ≈ 80 fs corresponds to the revival of the Σ_1 – Σ_2 coherence when the wave packet on Σ_1 recurs to the FC region where a small fraction of the population is trapped in Σ_2 . The relative error in the emission dipole computed for an increasing number of principal components is plotted in Figure 6b. One can see that 5 principal components give a relative error of 10^{-5} – 10^{-4} , similar to that computed for the populations of the electronic states while already for 10 components, an error of 10^{-8} is reached. As for the populations, the largest error is made in the first 50 fs when the NAC between the Σ states is strong. Figure 6a shows that the electronic and vibrational coherences are robust with respect to averaging over random molecular orientations, and we come back to this point in the following section.

The results reported in Figures 6b, S6a,b, S7a,b, and S8 of the SI show that one can accurately describe the dynamics of the ensemble after the pulse is over by numerically solving the TDSE for the 5 molecular singular vectors, U_m , instead of the 800 needed for an averaging over the initial random orientations. This represents a considerable saving of computer time and storage. One only needs to propagate and store these 800 random oriented initial vectors during the pulse, for a dozen of femtoseconds or so. The accuracy of the SVD propagation can be set by fixing a threshold for the recovery. For a threshold of the order of the accuracy of the numerical integration of the TDSE, one gets essentially ‘exact’ results, as seen already in Figure 6b. Setting a larger threshold inevitably

introduces small errors in the populations of the electronic states. Another measure of the error is to use the Frobenius distance between the ‘exact’ density matrix obtained from averaging over 800 random initial orientations and the one recovered by propagating a small number of U_m vectors. The Frobenius distance provides a measure of the error for the entire density matrix, and not only for its diagonal matrix elements as is provided by the difference in the trace, $\Delta_{N_{\min}}$ (eq 16). The Frobenius distance is plotted in Figure S9 on a log scale at $t = 18$ fs for an increasing number of principal components. Its distance is of the same order of magnitude as $\Delta_{N_{\min}}$ (eq 16) (Figure 3a) and of the error of on time-dependent dipole, $\mu(t)$, (Figure 6a) and decreases in a similar way with increasing the number of principal components included to recover the density matrix.

The expansion in terms of principal components, eq 18, is exact when all of the N_o principal components are included. Otherwise, the SVD theorem¹⁹ states that including more singular values in the expansion will improve the fit or, at worst, not change it. Therefore, in the absence of a benchmark as in the example discussed above, one can readily determine the desired accuracy threshold by increasing the number of singular components used for propagating the TSDE after the pulse, based on the analysis of the magnitude of the singular values and the error on the trace of the ensemble (Figures 3b, S8, and S9) at the end of the pulse, here at 18 fs.

To illustrate further the power of the method, we now discuss the results for a second exciting pulse, with a slightly higher carrier frequency (5.17 eV) so that the higher Σ and Π states are accessed with similar weights. In this case, we only ran the dynamics for the 800 initial random molecular orientations until 18 fs, when the pulse is over. After the pulse was over, the propagation was carried out by integrating the TDSE using a few principal molecular singular vectors, U_m , eq 17.

We illustrate the convergence process of using an increasing number of principal components for the propagation of the pulse after 18 fs in Figure S10a,b (normalized σ_m^2 singular values and errors on the populations), and S9 (Frobenius distance) of the SI. Similarly to the previous example, $N_{\min} = 5$ σ_m^2 suffice to converge the SVD description of the ensemble dynamics.

The localization of the U_m vectors on the grid and on the electronic states at 18 fs is shown in Figure S11. As in the example for the pulse with a lower carrier frequency (Figure 4), U_1 is localized on the GS. For the higher carrier frequency, U_2 is localized on the manifold of excited Σ states, $\Sigma_2, \Sigma_3, \Sigma_4$, and U_3 and U_4 on the x and y components of Π_1 and Π_3 respectively. Correspondingly, V_1 is uniform, V_2 is localized along z , and V_3 and V_4 are localized along y and x , respectively; see Figure S12a–d. Note how for this exciting pulse, σ_2, σ_3 , and σ_4 are essentially equal. The small fifth singular component is localized on the excited vibrational states of GS (U_5) and oriented along z (V_5).

The dynamics of the population transfer as well as the total emission dipole, $\mu(t)$, computed by propagating the U_m vectors, are plotted in Figure 7 for 5 σ_m values and compared to the exact average over 800 orientations until 24 fs. We give in Figure S13 the differences between the values of the dipole computed for 5 σ_m , 10 σ_m , and 15 σ_m . One can see that the value is essentially converged for the range of 5 σ_m . In Figure 7a, one sees a small population transfer between the Π_2 and the Π_3 states, which are coupled by NAC at the exit of the FC

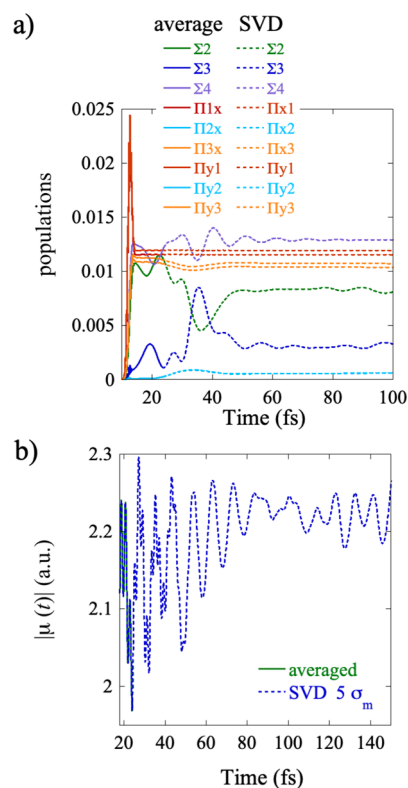


Figure 7. Populations (a) and emission dipole, $|\mu(t)|$, eq 20, (b), computed for the excitation by the 2 fs deep UV 5.17 eV pulse. In panel (a), the exact averaging over 800 initial random orientations is plotted in full lines up to 24 fs. For later times, the approximate values computed by the propagation of 5 U_m vectors using the TDSE (eq 17) are shown as dotted lines, starting at 18 fs. In panel b, the same is done for the full time-dependent dipole, $|\mu(t)|$.

region, while there is extensive population transfer between the states of the Σ manifold. Note how the time dependence of the emission dipole (Figure 7b) is different from that shown in Figure 6a for a 2 fs pulse with a different carrier frequency. The fast oscillations with a period of ≈ 2 fs are those of the electronic coherences between Π_1 and the Π_3 states (quasi-degenerate with the Π_2 in the FC region). However here, they are modulated by the slower ones (≈ 10 fs) which correspond to the electronic coherences between the excited Σ manifold.

Dynamics of the Vibrational and Electronic Coherences of the Ensemble. Figures 6a and 7b show that the total emission dipole $\mu(t)$ averaged over an ensemble of molecular orientations oscillates with the periods of the electronic and vibrational coherences. However, not all types of electronic coherences survive the orientation averaging. Eqs 7 and 9 show that only the electronic coherences between electronic states that contribute to the same molecular singular vector, U_m , survive the orientation averaging. This means that there will not be electronic coherences between Σ and Π states in an ensemble of randomly oriented molecules, unlike when a superposition of Σ and Π states is built by exciting oriented LiH molecules with a pulse that has a polarization direction in the (x, z) and in the (x, y) plane of the molecular frame,^{5,26} see Figure S14a–c. In the ensemble of randomly oriented molecules, the Σ – Π coherences average out: only the Π – Π and Σ – Σ electronic coherences are present. They are plotted in Figure 8a,b respectively for the dynamics induced by the low 4.35 eV frequency 2 fs exciting pulse (see Figures 1, 4, 5, and 6

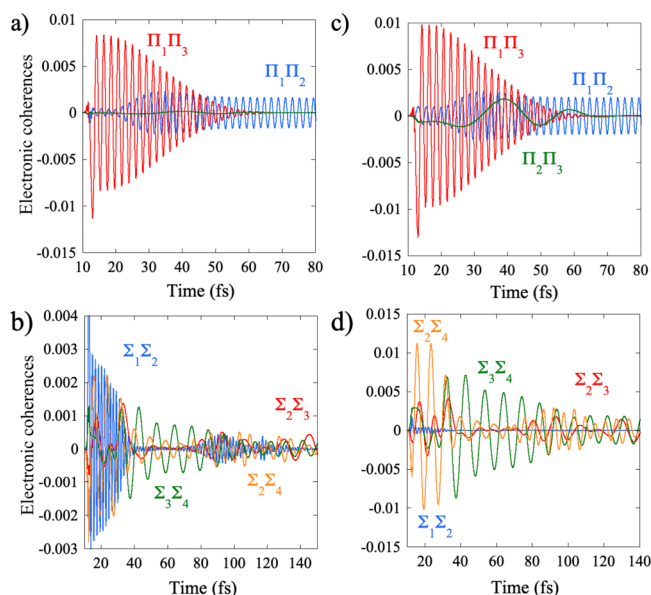


Figure 8. Time-dependence of the electronic coherences for the ensemble of randomly oriented molecules. (a, b) Dynamics induced by the lower frequency 4.35 eV exciting pulse. (c, d) Dynamics induced by the higher frequency 5.17 eV exciting pulse.

above) and in Figure 8c,d for the higher frequency one (see Figures 7, S11, and S12 of the SI). There is a rich dynamics of the Σ – Σ coherences that is modulated by the NAC coupling, with electronic coherences between specific electronic states dominating the dynamics over different time ranges. The Π – Π coherences are much more regular since there is only a weak

NAC coupling between the Π_3 and the Π_2 states. The Π_3 – Π_2 NAC leads to a small population transfer to Π_2 in the 20–50 fs time range and a Π_2 – Π_1 electronic coherence that does not vanish because the wave packets are moving on very similar dissociative potentials. The Π_3 – Π_1 vanishes at around 50 fs because Π_3 is bound (see Figure S1) but Π_1 is dissociative. A slow beating Π_3 – Π_2 electronic coherence is clearly visible in Figure 8c which also vanishes because Π_1 is dissociative. The Σ – Σ and Π – Π electronic coherences govern the emission dipole (eq 20) which does not exhibit periods corresponding to Σ – Π coherences after the pulse; see Figures 6a and 7b.

Vibrational coherences are also robust with respect to molecular averaging as can be seen from Figure 9a–h, where plots of heatmaps of the reduced nuclear density matrix, $\rho_{\text{nuc},m}^{\text{mol}}(t)$, eq 8, that correspond to the largest three principal components, $m = 1, 2, 3$, are shown for the lower frequency, 4.35 eV, exciting pulse. Two times are shown, the time $t = 18$ fs, at which the SVD analysis is carried out after the pulse and $t = 50$ fs at the end of the region of strong NAC interactions between the Σ states (see Figure 1b for the population dynamics and Figure 4 for the localization of the largest principal components), which induces more complex patterns in the heatmap (Figure 9f) of the third principal components localized on Σ states than on the second principal component localized on Π states, see Figure 4 above.

The same overall behavior is recovered for the higher frequency exciting 2 fs pulse; see Figure S15a–j. The difference is that one can identify the effect of the Π_3 – Π_2 NAC coupling in the heatmap of the $\rho_{\text{nuc},m}^{\text{mol}}(t)$ for the third principal component.

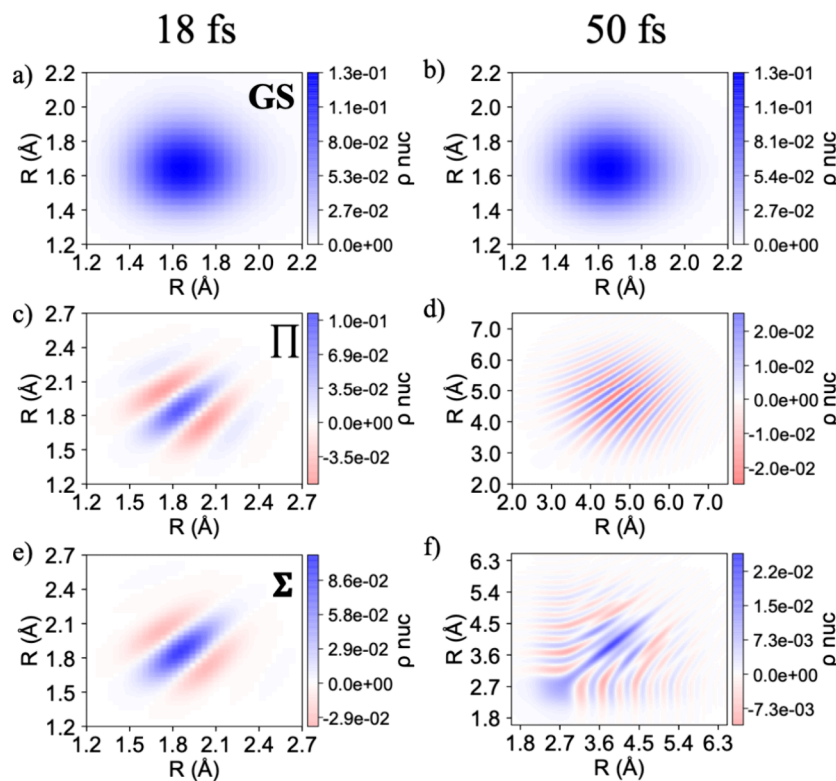


Figure 9. Heat maps of the real part of the reduced nuclear density, $\rho_{\text{nuc},m}^{\text{mol}}(t)$ $m = 1, 2, 3$, eq 8, computed at 18 fs (left column) and 50 fs (right column) for the lower carrier frequency (4.35 eV) exciting pulse. (a, b): Largest principal component, $m = 1$, that is localized on the GS. (c, d): second largest, $m = 2$, localized on the Π_1 state. (e, f) third largest, $m = 3$, localized on the Σ states (see Figure 4).

CONCLUSIONS

Our SVD-based method allows for accurately describing the dynamics of the coherent excitation of an ensemble of randomly oriented molecules by a broad, energy ultrashort pulse that encompasses several electronic states. It shows that rather few singular vectors are sufficient to represent the ensemble of orientations of attosecond excited molecules. For excitations by the reasonably strong 2 fs pulses used in the numerical examples ($3.51 \times 10^{12} \text{ W/cm}^2$) the number of singular orientations is nevertheless larger than the 3 Cartesian orientations expected in the linear regime. Equally noteworthy is that fewer than the expected singular vectors are sufficient to represent the ensemble of excited electronic states. Even beyond that, note the stereodynamics: there is a 1:1 correspondence between the two sets of singular vectors. Each dominant orientation is thereby associated with its own coherent set of excited electronic states. Our derivation and numerical examples show that electronic coherences within the coherent state associated with a specific molecular orientation of the ensemble are robust with respect to orientation averaging, while those between electronic states belonging to coherent states that correspond to different principal orientations are washed out by the orientation averaging. From a numerical point of view, the SVD provides a storage and computer time-efficient approach for studying the dynamics of coherently excited randomly oriented molecules. Future work will address multiphoton photoexcitation by stronger (with peak intensity in the range 10^{13} – 10^{14} W/cm^2) few-cycle NIR pulses as well as the excitation of nonlinear molecules for which it is expected that a few additional principal orientations will be required for describing the dynamics of an ensemble of initially randomly oriented molecules.

ASSOCIATED CONTENT

Supporting Information

The Supporting Information is available free of charge at <https://pubs.acs.org/doi/10.1021/acs.jpca.3c07856>.

Supplemental figures and a detailed derivation of the SVD approach for a sudden photoexcitation process (PDF)

AUTHOR INFORMATION

Corresponding Author

Francoise Remacle – Theoretical Physical Chemistry, UR MOLSYS, University of Liege, Liege B-4000, Belgium; Fritz Haber Center, Institute of Chemistry, The Hebrew University of Jerusalem, Jerusalem 91904, Israel; orcid.org/0000-0001-7434-5245; Email: fremacle@uliege.be

Authors

Manuel Cardoso-Gutierrez – Theoretical Physical Chemistry, UR MOLSYS, University of Liege, Liege B-4000, Belgium
Raphael D. Levine – Fritz Haber Center, Institute of Chemistry, The Hebrew University of Jerusalem, Jerusalem 91904, Israel; Department of Molecular and Medical Pharmacology, David Geffen School of Medicine, Los Angeles, California 90095, United States; Department of Chemistry and Biochemistry, University of California, Los Angeles, California 90095, United States; orcid.org/0000-0001-5423-1582

Complete contact information is available at:

<https://pubs.acs.org/10.1021/acs.jpca.3c07856>

Notes

The authors declare no competing financial interest.

ACKNOWLEDGMENTS

F.R. and M.C.G. acknowledge the support of the Fonds National de la Recherche (F.R.S.-FNRS, Belgium), #T0205.20, and of the action of concerted research MECHANOCHEM (ARC 19/23-20, ULiege). Computational resources have been provided by the Consortium des Equipements de Calcul Intensif (CECI), funded by the F.R.S.-FNRS under Grant # 2.5020.11. The authors thank the COST action ATTOCHEM (CA18222).

REFERENCES

- (1) Vrakking, M. J. J.; Lepine, F. *Attosecond Molecular Dynamics*; The Royal Society of Chemistry: Cambridge, 2019; pp. P001-P500.
- (2) Nisoli, M.; Decleva, P.; Calegari, F.; Palacios, A.; Martin, F. Attosecond Electron Dynamics in Molecules. *Chem. Rev.* **2017**, *117*, 10760–10825.
- (3) Merritt, I. C. D.; Jacquemin, D.; Vacher, M. Attochemistry: Is Controlling Electrons the Future of Photochemistry? *J. Phys. Chem. Lett.* **2021**, *12*, 8404–8415.
- (4) Remacle, F.; Levine, R. D. An Electronic Time Scale for Chemistry. *Proc. Natl. Acad. Sci. USA* **2006**, *103*, 6793–6798.
- (5) Remacle, F.; Nest, M.; Levine, R. D. Laser Steered Ultrafast Quantum Dynamics of Electrons in Lih. *Phys. Rev. Lett.* **2007**, *99*, No. 183902.
- (6) Stapelfeldt, H.; Seideman, T. Colloquium: Aligning Molecules with Strong Laser Pulses. *Rev. Mod. Phys.* **2003**, *75*, 543–557.
- (7) Gordon, R. J.; Zhu, L.; Seideman, T. Coherent Control of Chemical Reactions. *Acc. Chem. Res.* **1999**, *32*, 1007–1016.
- (8) Ghafur, O.; Rouzee, A.; Gijbetsen, A.; Siu, W. K.; Stolte, S.; Vrakking, M. J. J. Impulsive Orientation and Alignment of Quantum-State-Selected No Molecules. *Nature Physics* **2009**, *5*, 289–293.
- (9) Kraus, P. M.; Baykusheva, D.; Wörner, H. J. Two-Pulse Field-Free Orientation Reveals Anisotropy of Molecular Shape Resonance. *Phys. Rev. Lett.* **2014**, *113*, No. 023001.
- (10) Fleischer, S.; Zhou, Y.; Field, R. W.; Nelson, K. A. Molecular Orientation and Alignment by Intense Single-Cycle Thz Pulses. *Phys. Rev. Lett.* **2011**, *107*, No. 163603.
- (11) Zare, R. N. *Angular Momentum, Understanding Spatial Aspects in Chemistry and Physics*; Wiley: New York, 1991.
- (12) Bernstein, R. B. *Chemical Dynamics Via Molecular Beam and Laser Techniques*; Oxford University Press: Oxford, 1992.
- (13) Bernstein, R. B.; Herschbach, D. R.; Levine, R. D. Dynamical Aspects of Stereochemistry. *J. Phys. Chem.* **1987**, *91*, 5365–5377.
- (14) Calegari, F.; et al. Ultrafast Electron Dynamics in Phenylalanine Initiated by Attosecond Pulses. *Science* **2014**, *346*, 336–339.
- (15) Kraus, P. M.; et al. Measurement and Laser Control of Attosecond Charge Migration in Ionized Iodoacetylene. *Science* **2015**, *350*, 790–795.
- (16) Valentini, A.; van den Wildenberg, S.; Remacle, F. Selective Bond Formation Triggered by Short Optical Pulses: Quantum Dynamics of a Four-Center Ring Closure. *Phys. Chem. Chem. Phys.* **2020**, *22*, 22302–22313.
- (17) Månsson, E. P.; et al. Real-Time Observation of a Correlation-Driven Sub 3 Fs Charge Migration in Ionised Adenine. *Commun. Chem.* **2021**, *4*, 73.
- (18) Schwickert, D.; et al. Electronic Quantum Coherence in Glycine Molecules Probed with Ultrashort X-Ray Pulses in Real Time. *Sci. Adv.* **2022**, *8*, No. eabn6848.
- (19) Golub, G. H.; Reinsch, C. Singular Value Decomposition and Least Squares Solutions. In *Linear Algebra*, Wilkinson, J. H.; Reinsch, C.; Bauer, F. L., Eds.; Springer: Berlin Heidelberg: Berlin, Heidelberg, 1971; pp. 134-151.

- (20) Jaynes, E. T. Information Theory and Statistical Mechanics. *II*. *Phys. Rev.* **1957**, *108*, 171–190.
- (21) Gonçalves, C. E. M.; Levine, R. D.; Remacle, F. Ultrafast Geometrical Reorganization of a Methane Cation Upon Sudden Ionization: An Isotope Effect on Electronic Non-Equilibrium Quantum Dynamics. *Phys. Chem. Chem. Phys.* **2021**, *23*, 12051–12059.
- (22) Galli, M.; et al. Generation of Deep Ultraviolet Sub-2-Fs Pulses. *Opt. Lett.* **2019**, *44*, 1308–1311.
- (23) Wanie, V.; et al. Ultraviolet Supercontinuum Generation Using a Differentially-Pumped Integrated Glass Chip. *Journal of Physics: Photonics* **2024**, *6*, No. 025005.
- (24) Brahms, C.; Travers, J. C. Efficient and Compact Source of Tuneable Ultrafast Deep Ultraviolet Laser Pulses at 50 KHz Repetition Rate. *Opt. Lett.* **2023**, *48*, 151–154.
- (25) van den Wildenberg, S.; Mignolet, B.; Levine, R. D.; Remacle, F. Temporal and Spatially Resolved Imaging of the Correlated Nuclear-Electronic Dynamics and of the Ionized Photoelectron in a Coherently Electronically Highly Excited Vibrating Lih Molecule. *J. Chem. Phys.* **2019**, *151*, 134310.
- (26) Nikodem, A.; Levine, R. D.; Remacle, F. Spatial and Temporal Control of Populations, Branching Ratios, and Electronic Coherences in Lih by a Single One-Cycle Infrared Pulse. *Phys. Rev. A* **2017**, *95*, No. 053404.

Electronic coherences excited by an ultra short pulse are robust with respect to averaging over randomly oriented molecules as shown by singular value decomposition

Manuel Cardosa Gutierrez¹, R. D. Levine^{2,3,4}, F. Remacle^{1,2*}

¹Theoretical Physical Chemistry, UR MOLSYS, University of Liege, Belgium

²Fritz Haber Center, Institute of Chemistry, The Hebrew University of Jerusalem, Jerusalem 91904, Israel

³ Department of Molecular and Medical Pharmacology, David Geffen School of Medicine and

⁴Department of Chemistry and Biochemistry, University of California, Los Angeles, CA 90095, USA

Supplementary Information

Section S1: Singular value decomposition of the density matrix in the sudden approximation

Supplemental figures

Figure S1: Potential energy curves of the 7 lowest Σ states and 3 lowest Π states of the LiH molecule.

Figure S2: Selected electronic dipole curves.

Figure S3: Selected non adiabatic coupling (NAC curves) within the Σ manifold and the Π manifold.

Figure S4: Long time population dynamics for Π states for the 4.35 eV exciting pulse.

Figure S5: Orientation singular vector, \mathbf{V}_5 , computed at 18 fs for the dynamics induced by the 4.35 eV – 2fs pulse.

Figure S6: Relative errors on the populations of the electronic states computed by averaging of 800 initial random orientations and by the approximate SVD propagation scheme including the 5 largest principal components for the 4.35 eV – 2fs pulse.

Figure S7: Comparison between the time evolution of the populations of the electronic states computed by averaging of 800 initial random orientations and by the approximate SVD propagation scheme for the 4.35 eV – 2fs pulse.

Figure S8: Relative errors on the populations computed at 18 fs with 5, 8, 10, 12 and 15 σ_m for the 4.35 eV – 2fs pulse.

Figure S9: Frobenius distance between the density matrix averaged of 800 initial random orientations and the one approximated with 5 σ_m computed at 18 fs for the 4.35 eV – 2fs pulse and the 5.17 eV one.

Figure S10: Principal values, error on the norm, Δ_{Nmin} , and errors on the populations in the electronic states computed with 5 σ_m for the dynamics induced by the 2f 5.17 eV pulse.

Figure S9: Heatmaps of the orientation singular vectors corresponding to the 5 largest σ_m computed at 18 fs for the 5.17 eV – 2fs pulse.

Figure S11: Localization of the principal molecular vectors on the nuclear grid and on the adiabatic electronic states for the 5.17 eV – 2fs pulse.

Figure S12: Localization of the principal orientation vectors on the unit sphere for the 5.17 eV – 2fs pulse

Figure S13: Convergence of the emission dipole moment computed with 5 and 10 principal values for the 5.17 eV – 2fs pulse.

Figure S14: Real part of the electronic coherences for a 2fs- 4.35 eV pulse polarized in the (x,z) plane for a LiH molecule oriented as in Figure S1.

Figure S15: Heatmaps of the real part of the reduced nuclear density matrix computed for a 2fs- 5.17 eV pulse.

*Corresponding author: fremacle@uliege.be

Section S1: Singular value decomposition of the density matrix in the sudden approximation

In the sudden approximation for the photoexcitation, i.e. a one photon transition at t_p when the pulse is maximum, Eq. (4) of the main text, and restricting the dynamics to the excited states, the initial amplitudes at each point of the nuclear grid in each excited state can be factorized as the scalar product of the orientation of the electric field, $\hat{\mathbf{e}}_o$, and the transition dipole moment from the ground electronic state $\boldsymbol{\mu}_{GS-gi}^T = (\mu_{GS-gi}^x, \mu_{GS-gi}^y, \mu_{GS-gi}^z)$:

$$c_{gi}^0 = \hat{\mathbf{e}}_o^T \boldsymbol{\mu}_{GS-gi} \quad (\text{S1})$$

Then each element of $\rho^{mol}(t_p)$ are given

$$\begin{aligned} \rho_{gi,g'j}^{mol}(t_p) &= (1/N_o) \sum_o^{N_o} \left(\hat{\mathbf{e}}_o^T \boldsymbol{\mu}_{GS-gi} \right) \left(\hat{\mathbf{e}}_o^T \boldsymbol{\mu}_{GS-g'j} \right)^\dagger = \sum_o \left(\boldsymbol{\mu}_{GS-g'j}^T \cdot \hat{\mathbf{e}}_o \right) \left(\hat{\mathbf{e}}_o^T \boldsymbol{\mu}_{GS-gi} \right) \\ &= \boldsymbol{\mu}_{GS-g'j}^T \left(\sum_o \hat{\mathbf{e}}_o \hat{\mathbf{e}}_o^T \right) \boldsymbol{\mu}_{GS-gi} \end{aligned}$$

where $\sum_o^{N_o} \mathbf{e}_o^T \mathbf{e}_o = \begin{pmatrix} 1 & 0 & 0 \\ 0 & 1 & 0 \\ 0 & 0 & 1 \end{pmatrix}$ for an ensemble of random orientations. In that particular case,

$\rho^{mol}(t_p)$ is given by

$$\rho^{mol}(t_p) = \boldsymbol{\mu} \boldsymbol{\mu}^T \quad (\text{S2})$$

where the $((N_e-1) \times N_g) \times 3$ matrix $\rho^{mol}(t)$ is the matrix of the cartesian components of transition dipole between the GS and the excited states at each grid point. $\rho^{mol}(t_p)$ is independent of the polarization direction of the electric field of the pulse for an ensemble of randomly oriented molecules. It can only have 3 principal components oriented along the three cartesian axis of the molecular frame.

In the case of a sudden process, the matrix $\rho^{orien}(t_p) = \mathbf{A}^\dagger \mathbf{A}$ also takes a factorizable simple form. A matrix element of $\rho^{orien}(t_p)$ is given by

$$\begin{aligned}
\rho_{oo'}^{orien}(t_{exc}) &= \sum_{gi=1}^{Ne-1Ng} (c_{gi}^o)^* c_{gi}^{o'} = \sum_{gi=1}^{Ne-1Ng} (\hat{\mathbf{e}}_o^T \cdot \boldsymbol{\mu}_{GS-gi})^T (\hat{\mathbf{e}}_{o'}^T \cdot \boldsymbol{\mu}_{GS-gi}) \\
&= \sum_{gi=1}^{Ne-1Ng} \boldsymbol{\mu}_{GS-gi}^T \mathbf{e}_o \mathbf{e}_{o'}^T \boldsymbol{\mu}_{GS-gi} = \mathbf{e}_o \mathbf{e}_{o'}^T \sum_{gi=1}^{Ne-1Ng} \boldsymbol{\mu}_{GS-gi}^T \boldsymbol{\mu}_{GS-gi}
\end{aligned} \tag{S3}$$

each matrix element of $\rho^{orien}(t_{exc})$ will be multiplied by the same number which is the total oscillator strength. Using the $N_o \times 3$ matrix \mathbf{e} of the Cartesian components of the orientations $\hat{\mathbf{e}}_o$, defined above

$$\rho^{orien}(t_p) = \left(\sum_{gi}^{Ne-1Ng} \mu_{GS-gi}^2 \right) \mathbf{e} \mathbf{e}^T \tag{S4}$$

$\rho^{orien}(t_p)$ will therefore have 3 principal components oriented along the three cartesian axis.

It is not diagonal because the scalar product $\hat{\mathbf{e}}_o \hat{\mathbf{e}}_{o'}^T$ can be very close to 1.

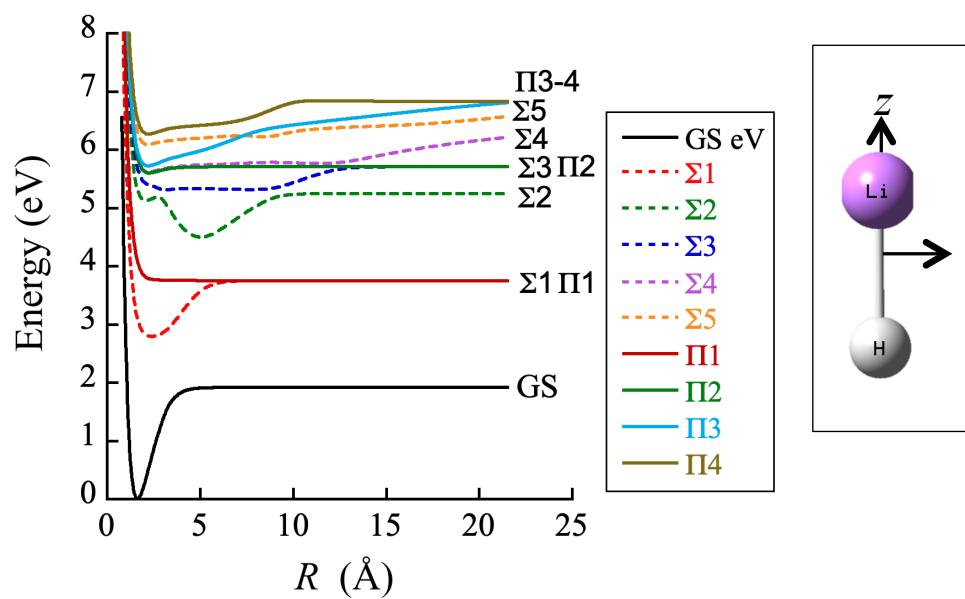


Figure S1: Potential energy curves of the 6 lowest Σ and the 4 lowest Π electronic states, adapted from ref [1]. Right: Orientation of the LiH molecule in the Cartesian molecular frame.

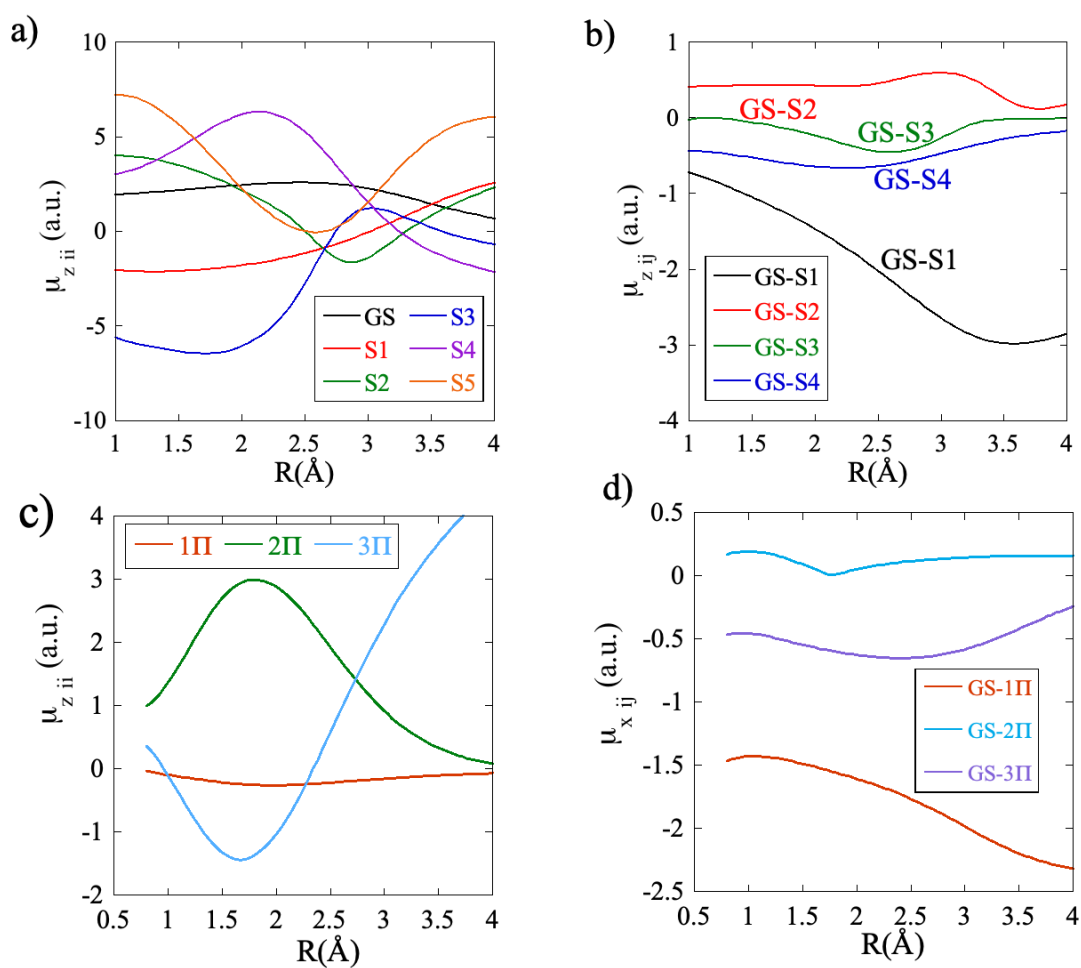


Figure S2: Selected electronic dipole curves for the Σ manifold (along z) a) permanent b) transition, c) and d) Π manifold permanent (along z) and transition (along x) respectively, adapted from ref. [1]. The values for the y components of the Π are identical.

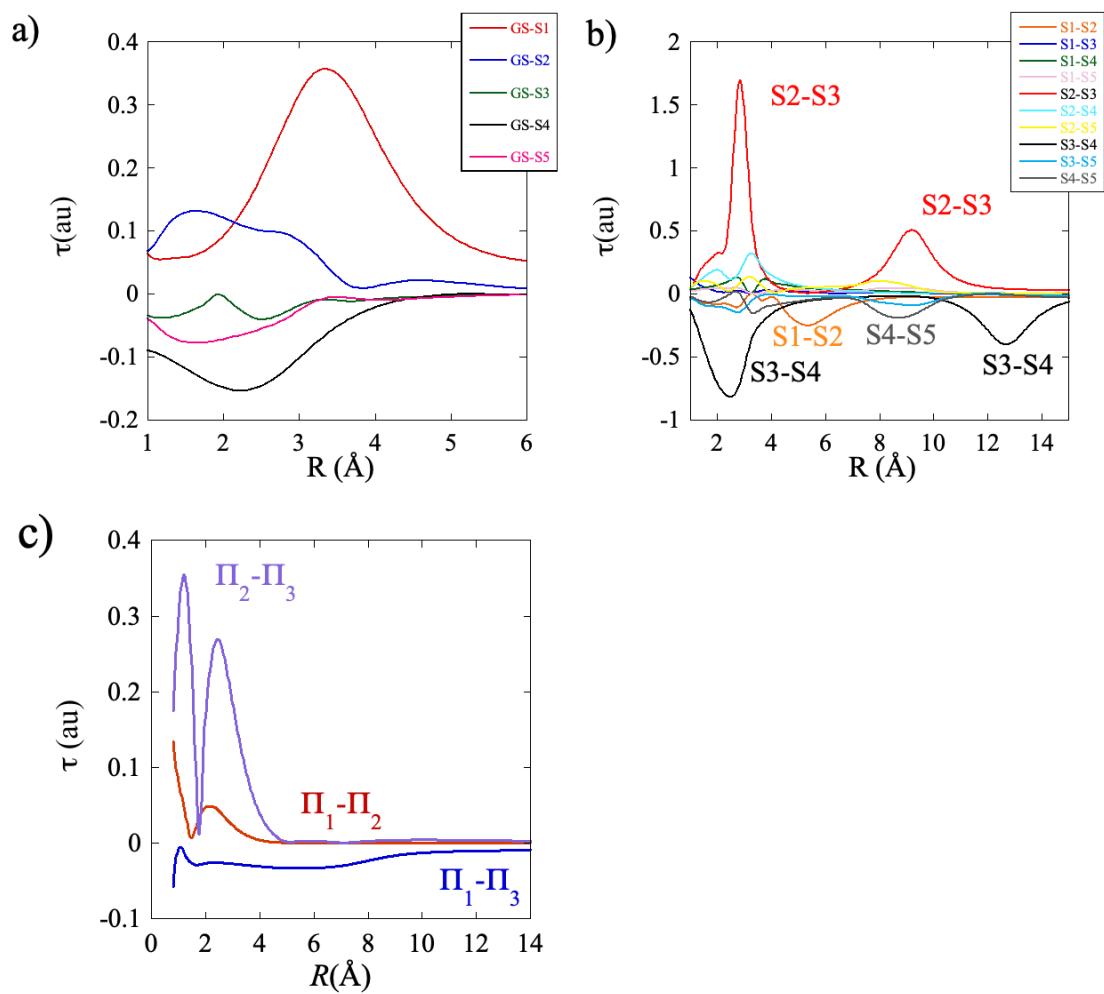


Figure S3 : Selected NAC curves a) Ground state to Σ excited states at short distance. b) Between Σ excited states, c) Between Π excited states, adapted from ref.[1].

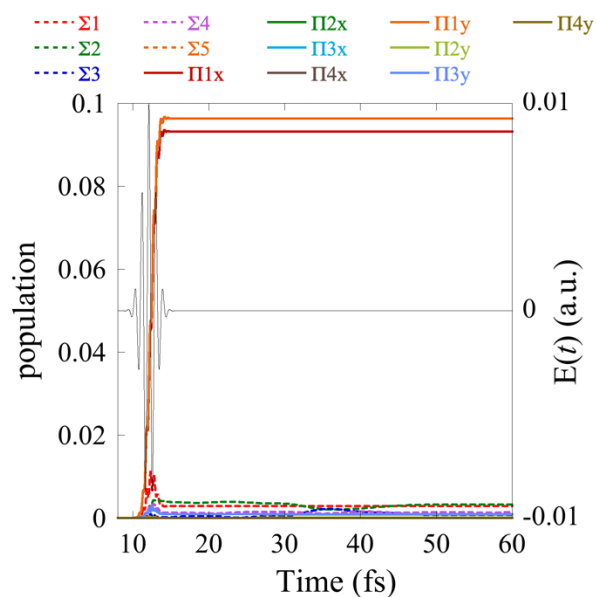


Figure S4. Long time dynamics in LiH for the two components of the Π_1 state computed for the 4.35eV-2fs exciting pulse, average over 800 initial random orientations. See Figure 1b for the details of the population in the Σ excited states.

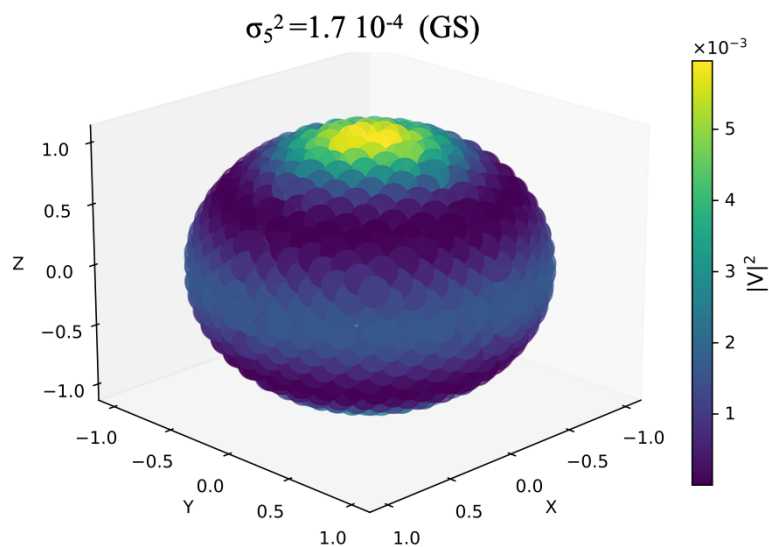


Figure S5. Localization of the \mathbf{V}_5 orientation on the sphere. It is oriented along z and localized on excited state of the GS (see Figure 4). Computed at 18 fs for the 4.35 eV – 2fs exciting pulse.

The relative error for the population of the GS and of the Π_1 state computed as an exact average over the 800 orientations or by the SVD propagation of the 5 largest principal components is of the order 10^{-4} percent (Figure S6a), which can be understood from the fact that 4 among the 5 principal values retained for the SVD propagation localize on these states. For the manifold of Σ_1 , Σ_2 , Σ_3 and Σ_4 (Figure S6b), the error is larger, of the order of a tenth of percent, which again can be understood from the fact that the population in those states is only ≈ 100 times larger than the threshold (10^{-5}) fixed to recover the trace of the ensemble density matrix and that only one singular component, the fourth one, accounts for the dynamics of the populations in the excited Σ manifold. The largest error is made when the non adiabatic coupling is strong between the excited Σ states. For completeness, we show in Figure S7 that the populations computed by the two methods cannot be distinguished to reading accuracy.

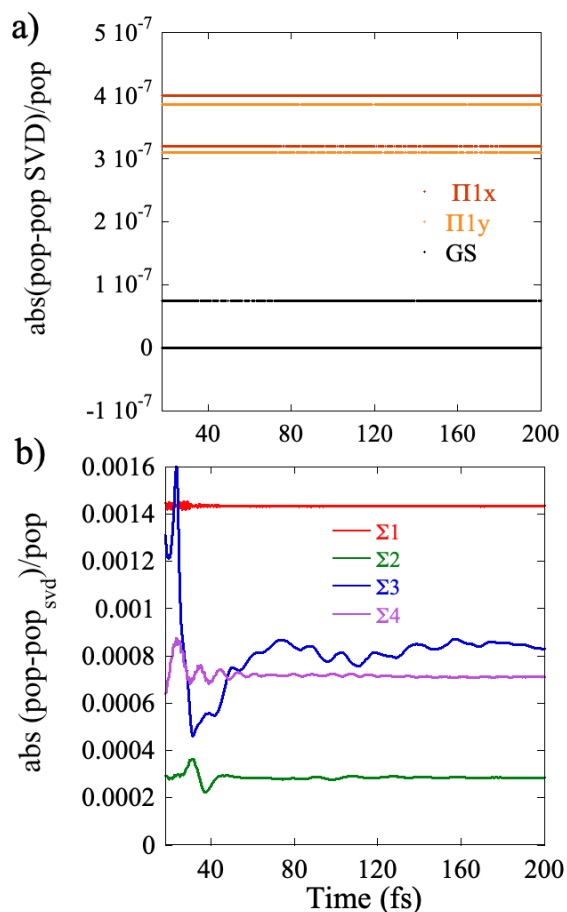


Figure S6. Relative errors on the populations of the GS and Π_1 states computed as an exact averaging over 800 initial orientations or by propagating the \mathbf{U}_m vectors of the 5 largest principal components. The plot of the populations is shown in Figure S6. Figure S7 of the SI shows the error on the populations at 18 fs computed for 5, 8, 10, 12 and 15 σ_m respectively.

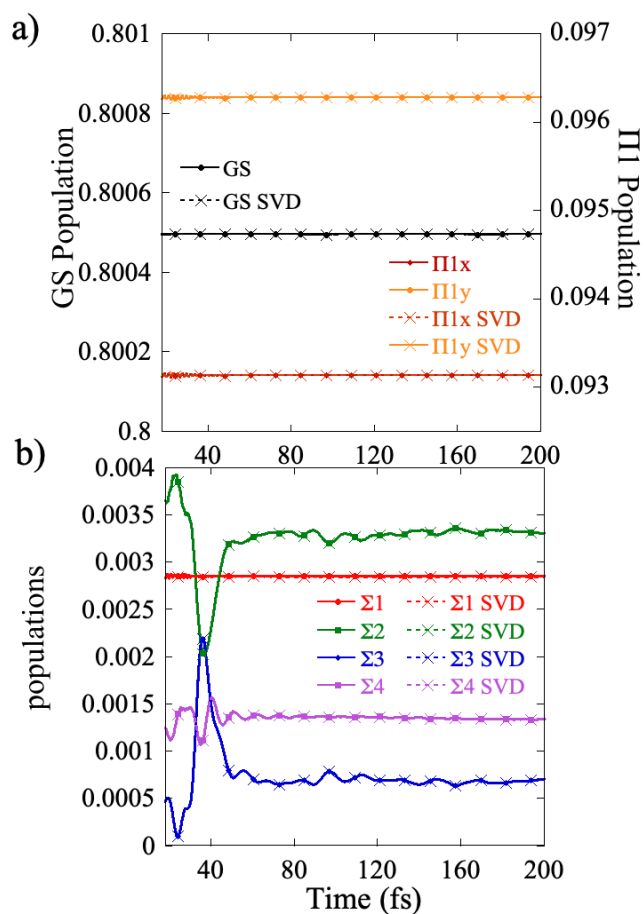


Figure S7. Comparison of the population in the electronic states for the excitation by the 4.35 eV – 2fs pulse, obtained by averaging the 800 randomly oriented initial states (full lines-full circles) and those computed using the five largest principal components of the SVD analysis (dotted lines, crosses). a) population in the two components of the Π_1 state and the GS. b) population in the manifold of Σ excited states.

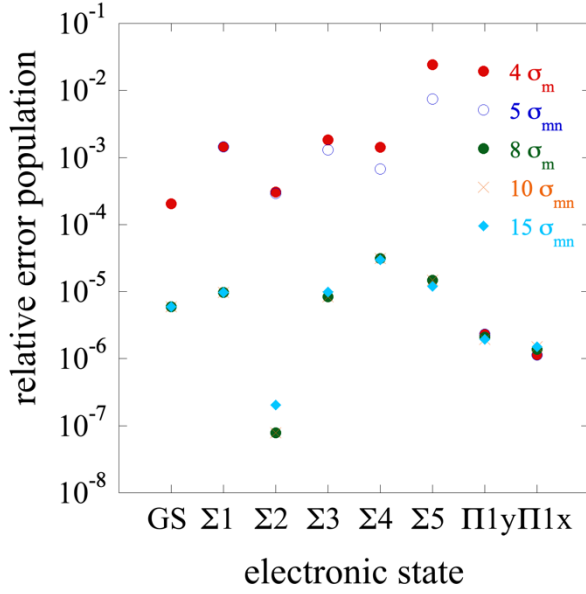


Figure S8: Error on the populations in the excited electronic states for excitation by the 4.35 eV- 2fs pulse computed at 18fs for an increasing number of principal components as indicated.

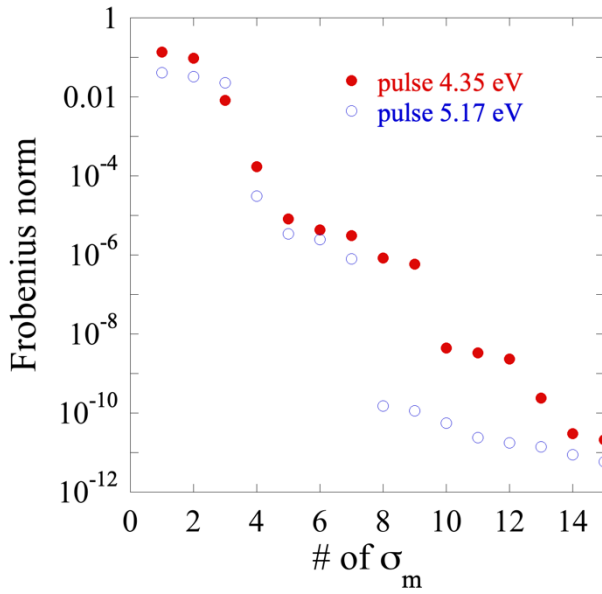


Figure S9 : Frobenius measure of the difference between the density matrix average of 800 initial orientations and the density matrix recovered with in increasing number of singular values computed at 18 fs, after the exciting pulse is over, for the two 2fs pulse used here with carrier frequencies of 4.35 and 5. 17 eV respectively. The Frobenius distance drops faster for the 5.17 eV pulse, with a gap at σ_8 . This pulse excites more commensurate populations in the excited Π and Σ manifolds. The Frobenius distance is computed as

$$\|F_m\| = \sqrt{\sum_{i=1}^N \sum_{j=1}^N \left| (\rho_{mol}^{av})_{ij} - (\rho_{mol}^m)_{ij} \right|^2} .$$

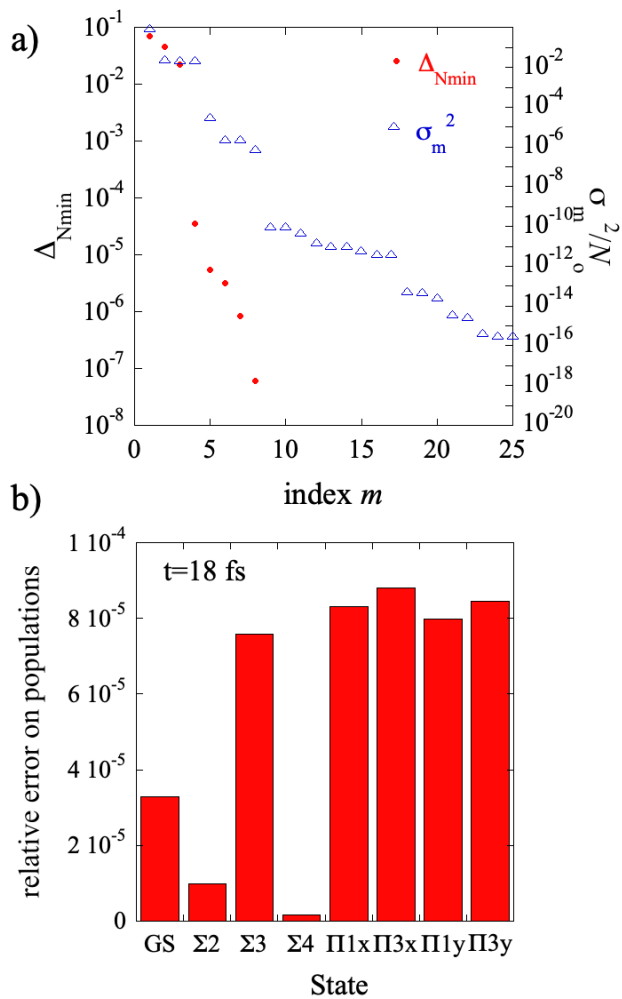
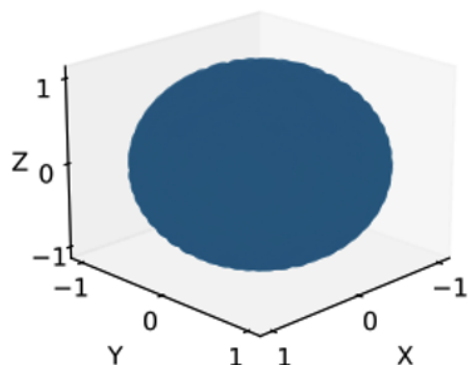
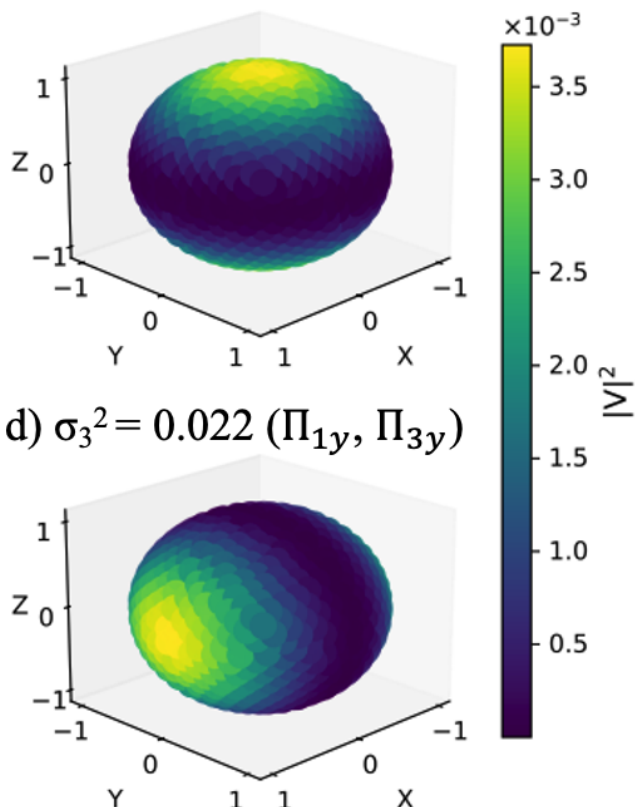


Figure S10. a) The normalized singular values, σ_m^2/N_0 , (right y axis) and Δ_{Nmin} (right axis) at $t=18$ fs, computed for the excitation of LiH by a 2fs deep UV pulse with a carrier frequency of 5.17 eV. Note the two breaks in the magnitude of the singular values, one between $m=4$ and $m=5$ and one between $m=8$ and $m=9$. The same break is obtained for the Frobenius distance shown in Figure S9. b) Relative error on the populations computed for 5 σ_m .

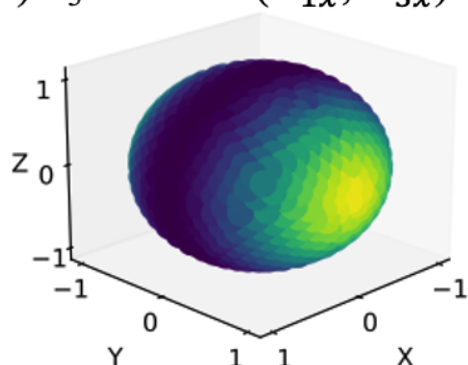
a) $\sigma_1^2=0.93$ (GS)



b) $\sigma_2^2=0.025$ (Σ excited states)



c) $\sigma_3^2=0.023$ (Π_{1x}, Π_{3x})



d) $\sigma_3^2=0.022$ (Π_{1y}, Π_{3y})

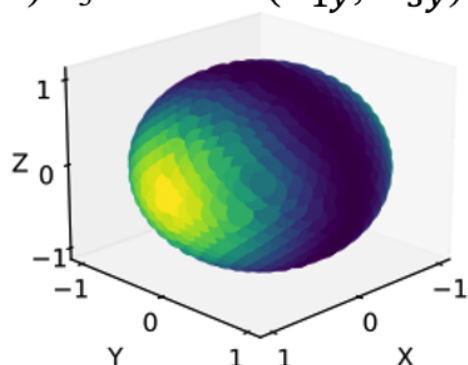


Figure S12. Heat map of the square modulus of the V_m orientation singular vectors that correspond to the four largest singular values computed at 18fs for an excitation by the 5.17 eV.

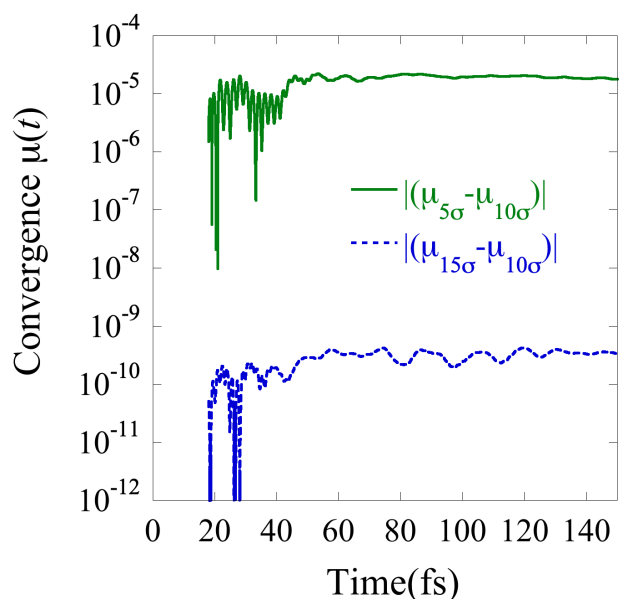


Figure S13. Convergence of the value of the time-dependent dipole, $\mu(t)$, for increasing number of principal components included in the propagation as indicated.

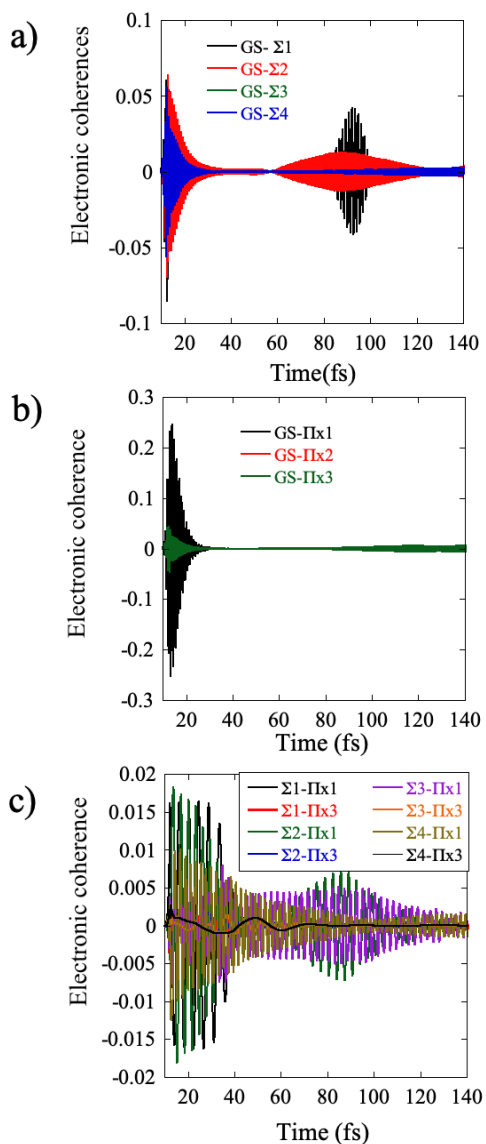


Figure S14. The Σ – Π electronic coherences that appear when the polarization direction of the pulse is in the (x,z) plane of the molecular frame for oriented molecules as shown in Figure S1. a) Electronic coherences between the GS of Σ symmetry and the excited Σ states. b) electronic coherences between the GS and the Π states. c) Electronic coherences between excited Σ and Π states. Not shown are the coherences within the manifold of excited Σ states and within the manifold of the excited Π states.

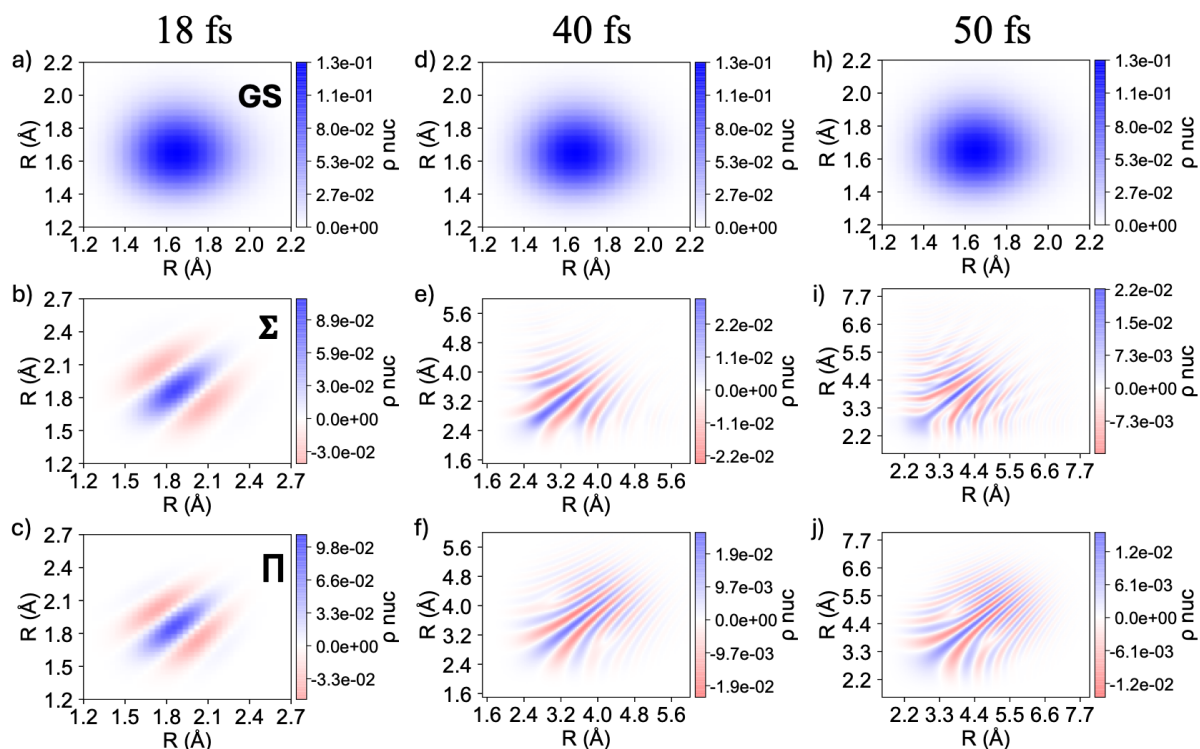


Figure S15: Heatmaps of the reduced nuclear density matrix, $\rho_{nuc,m}^{mol}(t)$ (Eq. (8) of the main text), for the 3 largest principal components of the ensemble dynamics induced by the higher frequency (5.17 eV) exciting pulse, computed at 18 fs (when the pulse is over), and 40 fs and 50 fs where there is a strong NAC coupling between the Π and the Σ states. Top row, $m=1$, localized on the GS, panels a),d),h). Medium row $m=2$, localized on excited Σ states, panels b), e), i). Bottom row, $m=3$, localized in Π states, panels c), f) and j). See figure S11 above. Note the effect of the NAC on the vibrational coherences of the third principal component, localized on Π states, at 40 and 50 fs.

Reference

[1]S. van den Wildenberg, B. Mignolet, R. D. Levine, and F. Remacle, J. Chem. Phys. **151**, 134310 (2019).

Chapter 7 Perspectives

Table of Contents

Chapter 7	Perspectives	114
7.1	<i>Perspectives on the modeling of mechanochemistry</i>	114
7.2	<i>Perspectives on modeling attochemistry</i>	120
7.2.1	Forces arising in an ensemble of initially randomly oriented photoexcited molecules.	121
7.2.2	Forces mediating the ultrafast stereo dynamics in the Jahn-Teller rearrangement of CD_4^+	124
7.3	<i>References</i>	130

7.1 Perspectives on the modeling of mechanochemistry

At the time we leave the MECHANOCHEM project, there is still much to do, and that can be achieved. First, we expect to publish a joint experimental-modeling paper with the findings obtained by our partners from the NANOCHEM group with whom we worked closely. We have theoretically characterized the response of the furan/maleimide adducts to the external force and reported a switch of mechanism from the thermal concerted to a sequential one with a diradical intermediate (*I*). In the lab, they have also advanced greatly regarding the chemistry of the polymers used to embed the mechanophore and the chemistry of its anchoring to the tip and the surface. They have also obtained experimental results on the rupture under force.

From the theoretical point of view, we complemented our published study with *ab initio* steered molecular dynamics (AISMD) simulations that allow us to assess the dynamics of the response of the polymer to a constant external force applied from fixed pulling points in the lab frame. As we explained in Chapter 3 Section 3.1, this approach of simulating the external force has the advantage that the force is not constrained to the pulling direction between the edges of the polymer. Instead, it can be defined from two arbitrary points in space, thereby reflecting more accurately the action of the tip of the AFM cantilever when it grabs the polymers attached to the surface, closer to the experimental set-up. Moreover, this approach allows probing the effect of the force on the overall rotational motion of the system, to which a significant part of the energy coming from the force can be funneled. Such a dynamical approach turns out to be very promising to elucidate the change of mechanisms that can be induced by the force and nonstatistical effects. (2)

However, methods to simulate the dynamics on realistic timescales comparable to the experiments need to be developed. I summarize below the findings obtained in both directions.

Preliminary studies (Figure 7.1) suggest that the forces needed to observe the breaking of furan/maleimide adducts can be reduced by ~ 1 nN compared to what we report with the CoGEF and EFEI static methodologies. This is understandable since the latter considers the reaction path where the system is always at its equilibrium position, which means the kinetic energy is zero. In reality, the molecules vibrate around the equilibrium position, so rather than a single geometry and

a single reaction path, we should consider an ensemble of trajectories, each starting with different velocities and geometries to account for the statistical nature of a sample at room temperature. AISMD allows the simulation of the time evolution of the polymer in the presence of a constant external force applied between the cantilever and the surface, much like force-clamp experiments in SMFS. These simulations require careful selection of initial conditions to ensure they reflect the Boltzmann distribution of velocities at the given temperature of the system, see Chapter 2, Section 2.2.2.

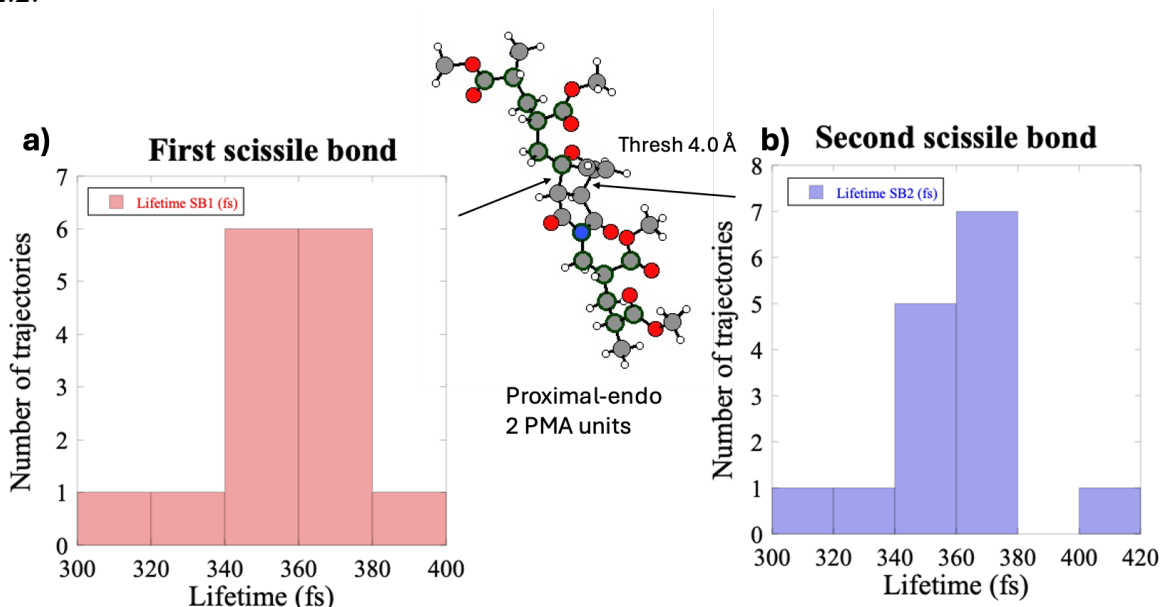


Figure 7.1. Simulated dynamics of a proximal-endo polymer with 5 PMA units on each side, subjected to a 3.0 nN external force using AISMD. The polymer, initially in its globular equilibrium conformation, was stretched in CoGEF until it unfolded with a distance between the methyl carbon atoms at the end of the chain equal to 13.2 Å. The lifetimes for both rupture events correspond to the time it takes for the molecule to dissociate when the bond distance exceeds 4.0 Å. Therefore, these lifetimes by no means reflect the lifetime expected for the molecule to dissociate in the experiments, which we give an estimate in our previous publication. (1) Panel a) shows the time it takes to break the first scissile bond, and panel b) shows it for the second scissile bond. The two rupture events occur very close together, which challenges the experimental ability to resolve the sequential rupture events.

In Figure 7.1, one sees that the rupture mechanism is also sequential in the dynamical simulation. The second bond rupture follows the first one very rapidly, making the two events very difficult to separate experimentally. Alternatively, an enhanced sampling approach (2) can be employed to observe rare events. This enables the identification and tracking of trajectories that are most likely to exhibit specific chemical outcomes, such as dissociation or conformational changes. Enhanced sampling is particularly useful for verifying experimentally observed phenomena that occur with very low probability, and which require sampling a great deal of initial conditions from the Boltzmann distribution to be captured in the simulation. By using enhanced sampling techniques to filter and select initial conditions that are more likely to evolve toward the desired event, for example, those with an activated local mode of interest, we can reduce the number of trajectories that need to be computed and analyzed, thus improving the efficiency of the simulation. Enhanced

sampling could turn out to be very valuable in providing an understanding of the latest experimental SMFS results obtained by our collaborators.

In addition, we propose to scale the computations that we reported in our paper(1) to include an increasing number of units of PMA ligands. This will allow us to assess the effect of the chain on the reaction and to characterize the mechanism of force transduction (3) from the AFM cantilever to the ligand and from the ligand to the mechanophore. To successfully implement this step, it is, however, necessary to simplify the electronic structure computations: it is not feasible with the actual computational resources to treat accurately quantum mechanically large systems such as the polymers bearing the mechanophore in the center. We have carried out preliminary studies to benchmark several computational methodologies that would allow us to scale the computations of the furan/maleimide system to include the PMA chains. From this work, we could reproduce the force response measure with CASSCF and UDFT levels using the semiempirical DFTB built-in Amber (4-6) and semiempirical xTB (7, 8) that is implemented in TeraChem (9). Both software are currently available in the group. However, at this level, there is still a limit to the polymer size that can be treated in the computer. To simulate very large systems that could be potentially closer to the reality of the SMFS experiments, one would need to employ a force field such as those that have been developed in molecular biology that allows the study of the dynamics of macromolecules like proteins, lipids, and complex membranes. The AMBER (10, 11), CHARM (12, 13), and GROMOS (14, 15) force fields are some of the most used, and applications are extensively reported in the literature. This MD approach was used in our group in the work of Barbara Fresh *et al.* (16), who studied the interaction between DNA fragments and small binders, highlighting the important influence of dynamical changes in the DNA double-helix on the thermodynamics of the molecular recognition process, already in collaboration with the NanoChem group.

A force field description of the potential energy surface will significantly reduce the computational cost since it bypasses electronic computation at each time step and uses a parametrized potential energy surface. However, bond breaking cannot be described accurately with a force field potential, which limits the range of force values that can be applied. The MD approach using force fields presumably allows reaching the nanosecond time scale in the simulations, which is more realistic when compared to experimental results. In addition, we could also include explicitly solvation effects by creating a cubic or octahedral solvent box and equilibrating the polymers inside. Figure 7.2 shows a proximal-endo mechanophore with 5 units of PMA on each side that has been equilibrated in a box of N-dimethylformamide, the solvent used in the SMFS experiments. As we can see, the whole system is quite large (23123 atoms), and using Amber, we can run molecular dynamics simulations in a reasonable amount of time, especially since this software is heavily optimized to work on graphics processing units and many of its critical modules support MPI parallelization.

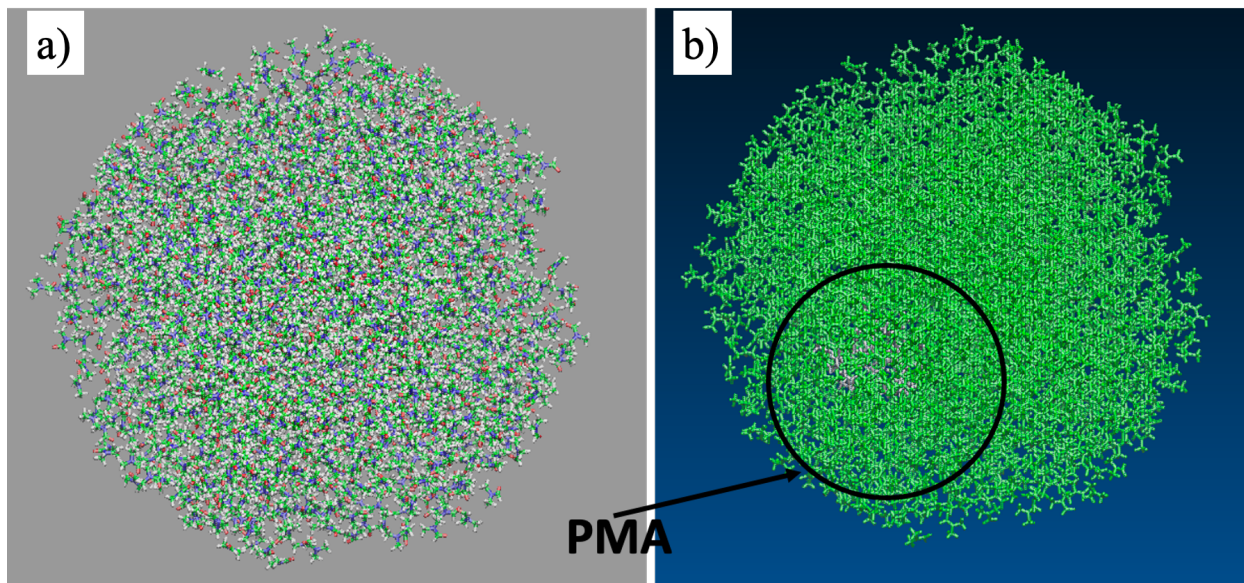


Figure 7.2: System of a 5-units PMA polymer with the proximal-endo mechanophore in the middle, equilibrated in a DMF solvent box using the Amber molecular dynamics package. Panel a) shows the whole system, highlighting the atomic composition. The polymer is located at the center of the box but is not clearly visualized. Panel b) displays each solvent molecule in green, helping to distinguish the polymer, which is shown in gray and highlighted within the black circle.

The effect of the external force can be simulated in Amber using the Steered Molecular Dynamics (SMD) approach, where the external force is applied through a virtual damped harmonic spring to one terminus of the polymer while the opposing end is fixed in space. The force is time-dependent and can be correlated to conformational changes in the system. SMD can be used to simulate constant-velocity pulling of the polymer, which is commonly done in SMFS and will allow us to obtain force-extension profiles that are closer to the experimental measurements. The non-equilibrium work performed on the system during the SMD simulation can be related to the potential of mean force (PMF), which describes how the free energy changes with respect to the pulling coordinate. The PMF is computed from the exponential-Boltzmann-weighted average (17, 18) of the non-equilibrium work performed on the system when transitioning from state A to state B :

$$PMF = G_B - G_A = -\frac{1}{\beta} \ln \langle e^{-\beta W_{A \rightarrow B}} \rangle_A \quad (7.1)$$

In Equation 7.1, PMF is the potential of mean force. G_B and G_A are the free energies of the final state (B) and the initial state (A), respectively. The factor $\beta = 1/k_B T$ where k_B is the Boltzmann constant, and T the temperature. $W_{A \rightarrow B}$ is the work performed from a given path γ from A to B.

We have already benchmarked the SMD method by carrying out two simulations of pulling the Pendo polymer at different speeds of the cantilever (see Figure 7.3). In these simulations, we stretch the polymer but the forces that are developed cannot induce the bond rupture. The scissile bonds are stretched up to $\sim 1.7 \text{ \AA}$ in both cases as can be seen from the histograms in Figure 7.4. However, we observe an effect of the rate of pulling on the response of the polymer. Namely, the

trend is that the slower the pulling rate is, the more time the system has to relax the energy transferred by the force, which leads to a more adiabatic process. In such circumstances, other effects might come into play; for example, interactions with solvent and other external molecules can affect the course of the furan/maleimide reaction. As we increase the pulling speed (100 Ang/ns), there is less chance for the system to relax, and it will be kept out of equilibrium as the force is maintained continuously. This does not necessarily mean that the force will do a better job at targeting the scissile bonds. Figure 7.3b shows that the potential of mean force (PMF) is relatively high at a pulling rate of 100 Ang/ns compared to the slower speed. This suggests that the system has to overcome a significant energy barrier to change the configuration, which can be thought of as a sign of stiffness or resistance to deformation. This behavior can be understood since the higher rate means the system has less time to explore all possible, stable configurations during the relaxation phase. Figure 7.4 shows the histograms of the bond lengths for the two pulling rates. One sees that they are very similar, which can be explained by the fact that, in the simulations, the forces are insufficient to excite or activate the bonds significantly. Instead, the polymer undergoes unfolding while the bonds in the carbon skeleton oscillate around their equilibrium distances, as governed by the equilibrium distribution of bond lengths.

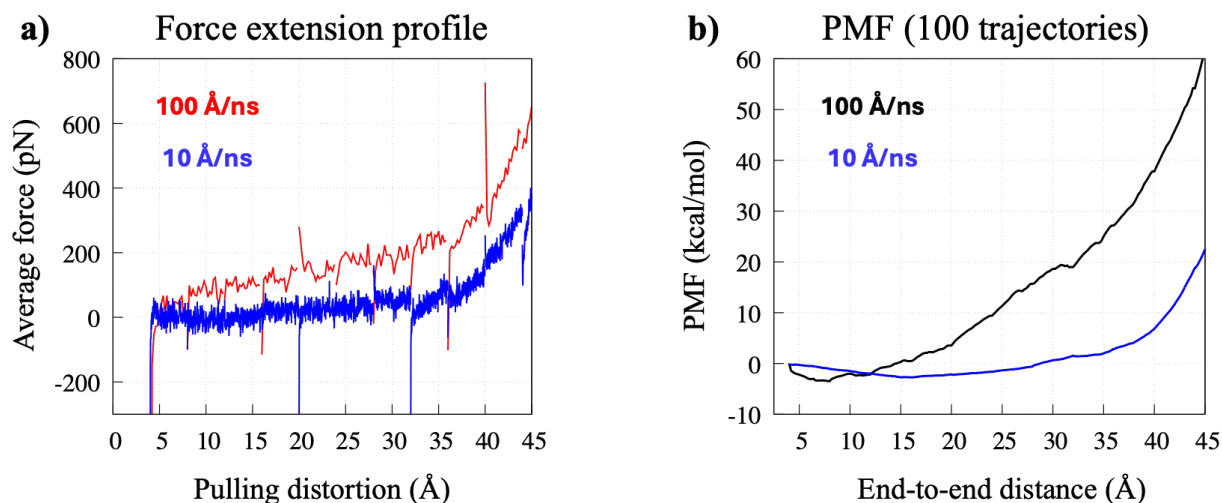


Figure 7.3: Constant velocity pulling simulations done with Amber using the SMD protocol. We observe an effect of the pulling rate in the force and free energy profile profiles, which can impact the chemistry developed during the stretching of the polymer. The slower the rate, the more adiabatic the pulling becomes, and the system has a longer time to relax and respond to the external force.

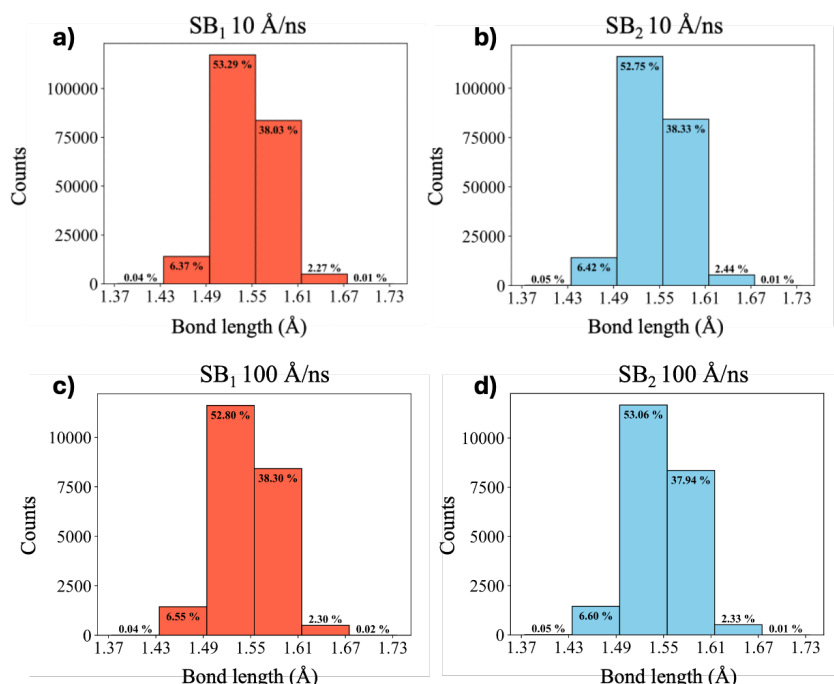


Figure 7.4: Distribution of the bond lengths of the scissile bonds for the 10 Å/ns simulation and for the 100 Å/ns simulation. Panels a) and b) correspond to the first and second scissile bonds for the slow simulation at 10 Å/ns. Panels c) and d) show the distributions for the faster simulation at 100 Å/ns. The 10 Å/ns simulation has a higher sampling because it has a larger number of time steps compared to the faster 100 Å/ns simulation; this explains the difference in the counts.

Relying exclusively on force fields for the theoretical treatment of the molecule has the great disadvantage that the bond breaking cannot be modeled. This problem can be solved using a combined QM/MM methodology (4), which treats the mechanophore quantum mechanically while the rest of the polymer and the solvent (if present) are treated classically. This, however, is challenging as we need to define carefully the interface between the quantum and classical regions. As evidence of the usefulness of this approach, we show in Figure 7.5 a simulation of two proximal-endo polymers at a given pulling rate. One of the polymers has the mechanophore symmetrically located in the middle of the chain, while the other has more PMA units on one side of the mechanophore than on the other, and thus, it is referred to as asymmetric.

The forces that we observe near the rupture (jump in the curve) are consistent with the values we obtain in CoGEF and AISMD. In addition, we observe a difference in the rupture forces for the asymmetric and symmetric polymers, which suggests a potential effect of the position of the mechanophore within the chain on the mechanical properties of the polymer.

Constant speed pulling 80 Å/ns

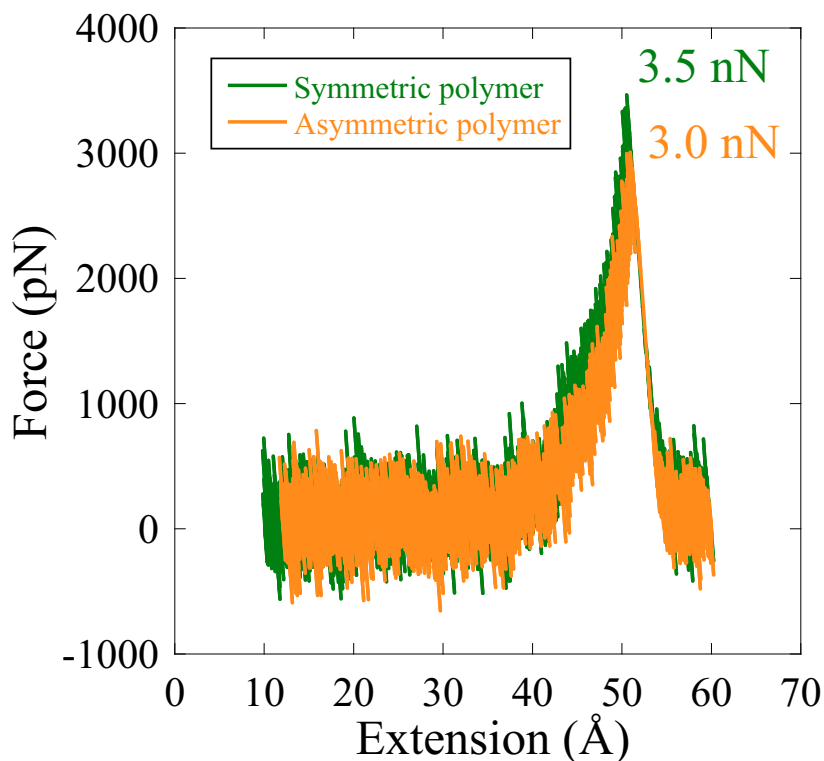


Figure 7.5: Force extension profiles extracted from SMD simulations using Amber with a QM/MM approach. The mechanophore is treated at the DFTB level, while the rest of the polymer is modeled with the Amber GAFF force field. This allows us to observe the bond breaking, and it is a powerful method that can be used in future studies. All atoms of the proximal-endo furan/maleimide mechanophore and the methyl group connecting the mechanophore to the PMA chains are included in the QM part.

7.2 Perspectives on modeling attochemistry

Electronic coherences are now reliably observed experimentally using pump-probe techniques, which track ultrafast dynamics and resolve the time evolution of electronic states in molecular systems. Common techniques include Transient Absorption Spectroscopy and Time-Resolved Photoelectron Spectroscopy. For that reason, we are working to extend the methodology of the vibronic force discussed in Chapter 5 to the analysis of molecular systems with large number of dimensions. In this section, we present our most recent findings, where we applied this formalism to study an ensemble of randomly oriented LiH molecules, increasing the number of molecular orientations taken into account and the CD_4^+ cation, increasing the number of nuclear degrees of freedom. The latter is a polyatomic molecule with several nuclear degrees of freedom, whose quantum dynamics was modeled in a 2D grid.

7.2.1 Forces arising in an ensemble of initially randomly oriented photoexcited molecules.

In the work discussed in Chapter 5, we have delved into the nature of the intramolecular forces that control the motion of the wavepacket in a manifold of coupled potential energy surfaces considering an oriented molecule with a fixed direction of the electric field: LiH in Section 5.1.1. But we can extend our approach to analyze an ensemble of initially randomly oriented LiH molecules. The dynamics can be efficiently simulated with the SVD methodology that we reported in Chapter 6. From there, one can obtain the molecular density matrix of the ensemble, Equation 6.5, by averaging over the few dominant principal orientations at every time step with negligible errors. The forces can then be evaluated afterward using the methodology presented in Chapter 5. Figure 7.6 shows the populations and the forces computed for each of the contributing principal orientations derived from the SVD analysis of the ensemble of initially randomly oriented LiH molecules discussed in our paper (19); see Chapter 6.

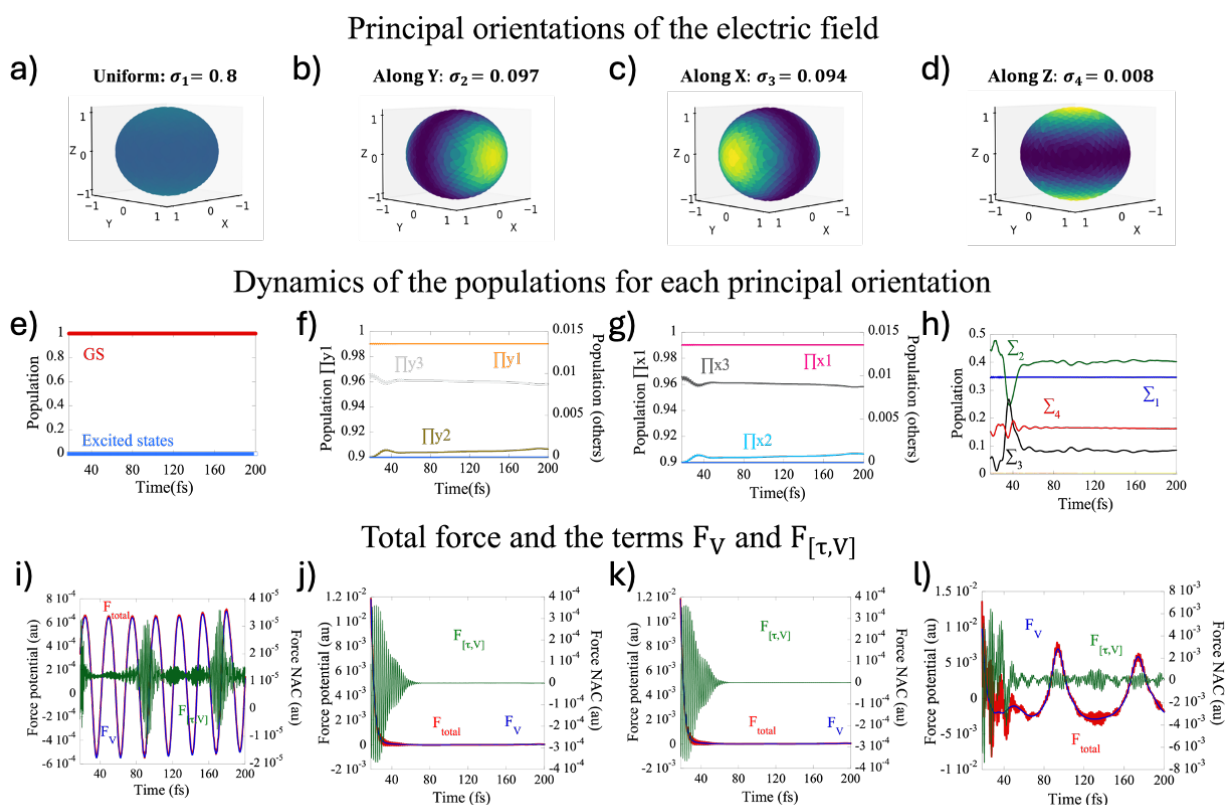


Figure 7.6: Analysis of the forces in an ensemble of randomly oriented LiH molecules, studied using our SVD scheme. The applied pulse had a carrier frequency of 4.35 eV, strength of $6.71 \times 10^{12} \text{ W/cm}^2$, duration of 0.8 fs, and CEP = 0. The top row (panels a, b, c, d) depicts the localization of dominant orientations on the unit sphere, corresponding to the four largest principal orientations (\mathbf{V}_i). The σ values are the singular values squared and normalized by the number of orientations, and they represent the contribution of each principal component to the ensemble average. The middle row (panels e, f, g, h) displays the time-dependent populations computed after propagating the dominant molecular singular vectors (\mathbf{U}_i). These must be scaled by their respective σ values to compute the ensemble average. The bottom row (panels i, j, k, l)

shows the total force and its components (F_V and $F_{[\tau,V]}$) along the $\mathbf{U}_i(\mathbf{t})$ vectors. Panels a, e and I correspond to the first principal orientation; b, f, and j to the second; c, g, and k to the third; and d, h, and l to the fourth.

To carry out the SVD, a rectangular matrix $\mathbf{A} = [\mathbf{c}_1 \ \mathbf{c}_2 \ \dots \ \mathbf{c}_{800}]$ is built. It is composed of the coefficients of the wavefunctions at the end of the pulse, corresponding to each orientation sampled on the unit sphere; see Equation 5.14 above. The SVD leads to four principal directions of the field, which are linear combinations of the whole set of orientations and carry $\sim 99.9\%$ of the information on the state of the ensemble. The first principal component is uniformly distributed over all orientations on the sphere resulting in a zero net electric field on average and thus corresponds to almost no excitation of the molecules. The only state that is populated is the GS, although there is very little population ($\sim 10^{-6}$) in the other Σ states because the number of points sampled on the sphere is finite. Thus, the first principal orientation essentially captures the motion of the wavepacket on the ground state. It can be seen from the forces that the major contribution comes from the force term F_V , which oscillates with a period of ~ 25 fs caused by the beatings of the wavepacket in the well of the GS (see Figure 5.4). The force term $F_{[\tau,V]}$ is due to coherences between the wave packets on the excited states, particularly $\Sigma 1$, and the GS. It revives every 80 fs, which is the fingerprint of the period of the beatings of the WP on the well of $\Sigma 1$.

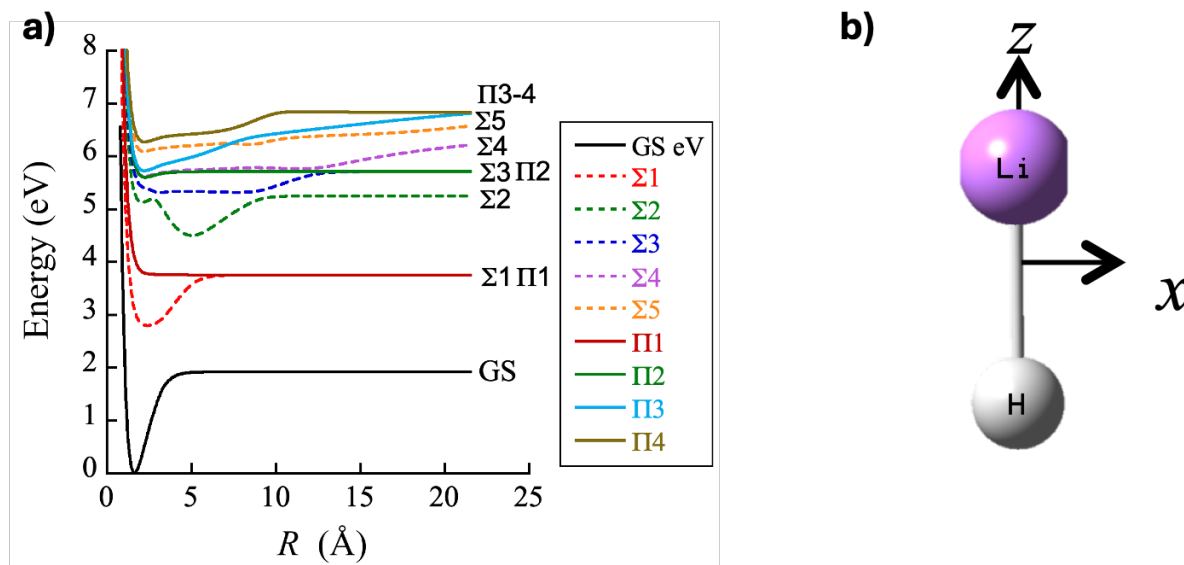


Figure 7.7: a) Electronic potential energy surfaces for the LiH molecule reported in (20). The Σ states are shown with continuous lines, while the Π states are shown with discontinuous lines. b) LiH in a system of coordinates with the origin at the center of mass. The molecule is oriented along the Z axis, with the Li atom pointing towards Z+.

The second and third principal orientations in Figure 7.6 have very low and degenerate singular values. This is because, for these pulse parameters, the excitation to the excited states is very weak, which results in a low population. The 2nd and the 3rd principal orientations correspond to orientations along the Y and X axes, which favor transitions to the excited states that localize the electron density in the excited Π electronic states in regions that do not include the internuclear axis in LiH. The Π states are doubly degenerate and have two components: the Π_y states are selectively excited with pulses oriented along Y that are accounted by the second principal

component. In contrast, the Π_x states are accessed with pulses polarized along the X axis, as indicated by the third principal component. The lowest state Π_1 carries $\sim 99\%$ of the excited population in the π manifold. Π_2 and Π_3 have little population and interact by NAC in the FC region. The Π states are not bound; when they are populated, the wavepacket tends to spread and evolve towards larger internuclear distances. Consequently, the force term F_V decays as soon as the wavepacket departs from the FC region because the potential energy surface becomes essentially flat (no gradient) in the case of states Π_1 and Π_2 . In the case of state Π_3 , it can be seen from Figure 5.4 that it has a more pronounced well, but this state is coupled by NAC to Π_2 , so the population will be transferred to Π_2 , favoring the dissociation mechanism. The term $F_{[\tau,V]}$ is nonzero only at the beginning of the dynamics and due to the non-adiabatic interactions and coherences between Π_2 and Π_3 states. Finally, the fourth principal direction corresponds to an electric field oriented along the Z axis of the molecule, which coincides with the internuclear distance axis. Therefore, it describes the excitation to the excited states of Σ symmetry. This principal component also has a very low contribution to the whole dynamics of the ensemble, as signaled by the small weight. The populations show the rich nonadiabatic dynamics among this manifold of excited states. The most populated states are Σ_2 , Σ_1 , Σ_4 , and Σ_3 , in that order. The states Σ_2 , Σ_3 , and Σ_4 are coupled by NAC in the FC region; this can be observed in the dynamics as they exchange population in the 40 fs that follow the end of the pulse. There are strong $F_{[\tau,V]}$ forces when these nonadiabatic interactions take place, and the F_V force shows the beatings of the wavepacket on the wells of Σ_1 and Σ_2 .

The electronic states are grouped per symmetry in the SVD representation, with the manifold of Σ states associated with an orientation of the field parallel to the Z axis and orientations along X and Y that correspond to the excitation to Π_x and Π_y states, respectively. Consequently, the electronic coherences among states of different symmetry (Π vs Σ) are washed out after the averaging over the principal orientations and only those that arise between electronic states that contribute to a given principal orientation are robust. Figure 7.8 shows the electronic coherences among Π - Π and Σ - Σ states as a function of time.

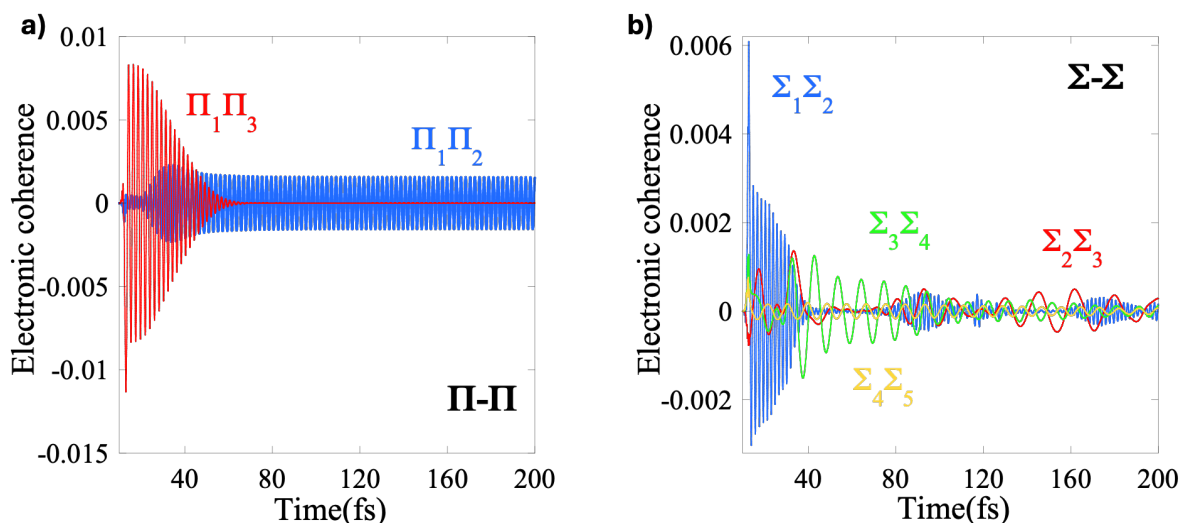


Figure 7.8: Electronic coherences that are robust to the orientational averaging are those established among the electronic states that contribute to a given dominant principal component

of the orientations. A) Electronic coherences among the Π manifold and B) among the Σ excited states.

Figure 7.8a shows there is a significant electronic coherence among Π 1 and Π 3 states at the beginning but they vanish rather quickly as the wavepacket moves away from the FC region after the interaction with the pulse. The coherences between Π 1 and Π 2 states follow a different trend, being very small at the beginning but rising at around 20 fs and remaining constant afterward, reflecting the role of the NAC coupling that leads to a transfer from Π 3 to Π 2. The coherences between the Σ excited states similarly reflect the role of the NAC between excited Σ states and exhibit a more complex behavior in time, as shown in Figure 7.8b. They have a larger magnitude during the first 40 fs, particularly the coherence Σ 1 Σ 2 (blue curve), which also shows the 80-fs period due to the revival of the population in the well of Σ 1.

The next section discusses how this approach can be extended to a more complex multidimensional molecule, such as the methane cation.

7.2.2 Forces mediating the ultrafast stereo dynamics in the Jahn-Teller rearrangement of CD_4^+

The neutral methane molecule has a T_d equilibrium geometry. Sudden ionization of the neutral methane molecule produces a cation in the T_d geometry, but the latter is unstable for the cation and gets distorted quickly, within 5 fs, due to the Jahn-Teller effect. This ultrafast rearrangement of the cation is modulated by strong nonadiabatic couplings in the FC region of the T_d geometry, where the three lowest electronic states of the cation are degenerate.

Broad-in-energy attosecond XUV pulses can photoionize the neutral molecule CD_4^+ from its ground electronic state to a coherent superposition of the three lowest electronic states of the cation. The non-equilibrium electronic density resulting from the photoionization is the driving force behind the Jahn-Teller rearrangement of the molecule.

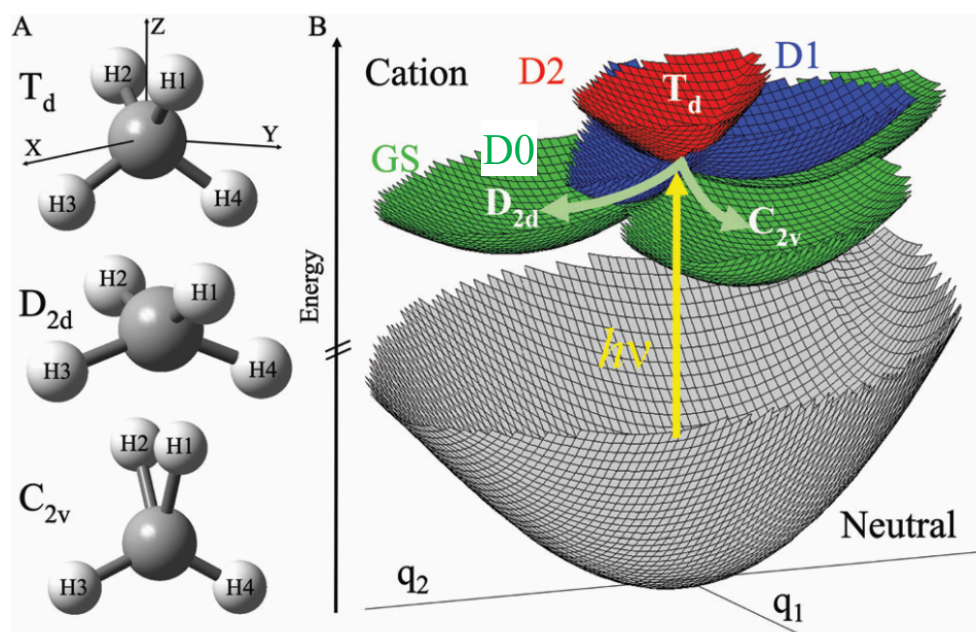


Figure 7.9: Adapted from (21). 2-dimensional potential energy surfaces in the FC region of the neutral T_d molecule. The cation undergoes Jahn-Teller distortion to lift the triple degeneracy of its three lowest electronic states, thereby stabilizing the molecule. With a broad XUV pulse, a coherent superposition wave packet of the cation is obtained.

At the T_d geometry, the three electronic states D_0 , D_1 , and D_2 of the cation are degenerate. The potential energy surfaces around the T_d singularity are plotted in Figure 7.9 for the two nuclear coordinates defined to describe the first 50 fs dynamics.(21) In D_0 the cation is stable either in a C_{2v} or D_{2d} configurations, which are the minima that define the wells in the green surface of Figure 7.9, with C_{2v} being the equilibrium geometry. The two relaxation pathways compete. In addition, a seam of C_{3v} conical intersection D_0/D_1 is localized in the vicinity of the T_d configuration. In D_1 , there are three minima localized close to the D_0/D_1 seams. In D_2 , the potential has a parabolic shape and a minimum around the T_d geometry; this state transfers its population to the lowest states due to strong non-adiabatic couplings. These features of the potentials explain the rich vibronic wave packet dynamics once it is created in the unstable T_d configuration of the cation by photoionization from the neutral GS.

We investigated the ultrafast, non-adiabatic dynamics of the coherent wavepacket of the deuterated CD_4^+ cation formed after sudden photoionization of the neutral molecule to a superposition of the three lowest states of the cation. The attopulses used in the experiments correspond to the 13th harmonic (~ 800 nm) of the IR laser pulse used to produce the high harmonics.

To simulate the quantum dynamics, we use a grid-based discrete variable representation of the wavefunction as in the case of LiH. But, because methane is a polyatomic molecule with six nuclear degrees of freedom, it is necessary to reduce the number of nuclear dimensions to a more manageable 2D case. This was done in the work of Goncalves *et al* (21) where the potential energy surfaces, dipoles, and non-adiabatic couplings were precomputed in a grid of two nuclear

coordinates q_1 and q_2 which are linear combinations of cartesian displacements. $-q_1 + q_2$ points to the C_{2v} minimum of the GS cation while $q_1 - q_2$ points to the D_{2d} minimum.

The expression of the Hamiltonian for the CD_4^+ cation is given below

$$\mathbf{H}_{i_g,j_{g'}} = -\frac{1}{2\mu} \mathbf{T}_{i_g,j_{g'}} \delta_{ij} + \mathbf{V}_{i_g,j_{g'}} \delta_{ij} \delta_{gg'} + \left(\frac{1}{i} \boldsymbol{\tau}_{i_g,j_{g'}} \delta_{gg'} \right) \cdot \mathbf{p}_{j_{gg'}} \quad (7.2)$$

In Equation 7.2, the indices i, j run over the three lowest electronic adiabatic states, D_0 , D_1 , and D_2 , while the indices g, g' span the nuclear coordinates. $\mathbf{T}_{i_g,j_{g'}}$ and $\mathbf{V}_{i_g,j_{g'}}$ are the matrix elements of the nuclear kinetic energy and the electronic potential, respectively. μ is the reduced mass of the system. δ_{ij} is the Kronecker delta function, which helps to capture the correct form of the matrices. The kinetic energy is represented using finite differences, which leads to a band matrix, diagonal in electronic states (δ_{ij}). The potential energy is diagonal in both electronic (δ_{ij}) and nuclear coordinates ($\delta_{gg'}$). The third term accounts for the entanglement between electrons and nuclei due to nuclear motion: $\boldsymbol{\tau}_{i_g,j_{g'}}$ represents the matrix elements of the non-adiabatic coupling matrix, which is diagonal on nuclear coordinates and off-diagonal in electronic coordinates. $\mathbf{p}_{j_{gg'}} = -i\nabla_{j_{gg'}}$ is the momentum operator expressed in matrix form using finite differences.

The Hamiltonian (Equation 7.2) describes the dynamics after a sudden photoionization process. This approximation is justified by the short duration of the XUV pulse and the fact that it is weak, allowing the absorption of a single photon only. It assumes that the photoionization is instantaneous and occurs at the maximum of the electric field of the XUV pulse. In these conditions, the amplitudes of the initial wave packet on each state, D_0 , D_1 , and D_2 , of the cation are given by the computed photoionization matrix elements from the ground vibrational state of the neutral, which defines the Franck-Condon region to the excited states, see ref. (21) and Chapter 2, Section 2.2.3.3 for the Franck-Condon approximation. Our approach, which is different from using a Wigner distribution (Chapter 2, Section 2.3.2), provides the amplitudes of the initial wave packet on each excited electronic state of the cation. It allows us to build a coherent superposition of electronic states, thereby accounting for the electron-nuclei entanglement in the initial state of the cation.

In addition, the random orientations in the ensemble of molecules were captured by SVD analysis in a similar way as outlined in Chapter 6 for LiH. To account for this effect, the quantum dynamics is averaged over an ensemble of random orientations of the electric field.

As opposed to the ethylene cation simulation (Chapter 4), in CD_4^+ , the initial state is not represented by a Wigner distribution. Instead, it is directly determined by the photoionization amplitudes. To define the initial quantum state, the theoretical photoionization amplitudes for the range of molecules falling on the FC region on the 2D grid were computed. Then, the amplitudes of the initial state of the cation are obtained by weighting the amplitudes of the neutral GS wavefunction with the photoionization cross sections and renormalizing. The photoionization amplitudes are defined for each point of the 2D grid, g , in the electronic state i , and for each orientation of the field m as follows

$$c_{ig}^m = c_{GS,g}^{neut} \sqrt{\rho(\epsilon)} \hat{\mathbf{e}}_m \cdot \mathbf{d}_{i,g}^\epsilon \quad (7.3)$$

Where $c_{GS,g}^{neut}$ are the amplitudes of the neutral vibrational ground state, $\rho(\epsilon)$ represents the density of photoelectron states for a given kinetic energy of the photoelectron computed at grid point ig , and $\hat{\mathbf{e}}_m = \mathbf{E}_m/|\mathbf{E}_m|$ is the polarization of the electric field of the ionizing pulse. Finally, $\mathbf{d}_{i,g}^\epsilon$ is the computed transition dipole from the GS of the neutral to the continuum of the i^{th} electronic state at grid point g integrated over the solid angle $\hat{\Omega}$. It is expressed more clearly in Equation 7.4.

$$\mathbf{d}_{i,g}^\epsilon = \sqrt{2} \int d\hat{\Omega} \int d\mathbf{r} \phi_{GS-ig}^{Dyson}(\mathbf{r}) \mathbf{r} \phi_{\epsilon,\hat{\Omega}}^{photoel}(\mathbf{r}) \quad (7.4)$$

In Equation 7.4, ϕ_{GS-ig}^{Dyson} is the effective one-particle Dyson orbital describing the ionization transition from the neutral N electrons wavefunction to the cation with $N-1$ electrons. The norm of the Dyson orbital is a qualitative measure of the ionization probability to a given channel. \mathbf{r} is the electronic coordinate and $\phi_{\epsilon,\hat{\Omega}}^{photoel}$ is a plane wave representing the state of the photoelectron.

In the study of the methane cation non-adiabatic dynamics, a mixture of 8000 initial states was generated, each corresponding to the ionization of the neutral molecule with the electric field of the pulse polarized along a different orientation $\hat{\mathbf{e}}_m$. The 8000 orientations are sampled randomly and uniformly on the unit sphere, as we explained in Chapter 6. The same SVD methodology that we used before to study the ensemble of randomly oriented LiH molecules can be applied to determining the principal orientations of the electric field of the ionizing pulse in the methane case. The rectangular matrix \mathbf{A} contains the initial states \mathbf{c}^m computed for each orientation m according to Equation 6.2. However, when performing SVD, only three principal orientations are found. This result can be proved analytically and is a consequence of the sudden approximation made for the interaction of the molecule with the pulse, which prevents any coupling between the molecular and orientational degrees of freedom during the pulse as we saw in the case of LiH where the full interaction term was included explicitly in the Hamiltonian.

The three vectors U_1 , U_2 , and U_3 that correspond to the three orientations are propagated using the TDSE and allow for computing accurately the density matrix of the ensemble, avoiding the propagation of the TDSE for all the 8000 orientations, which would have been very time-consuming. Figure 7.10a shows the composition of the singular vectors in the ensemble of initial states of the CD_4^+ cation created with the H13 XUV pulse. The last row shows the composition of the wavepacket after averaging each singular vector with the corresponding weights w_i , which are the singular values squared and divided by the number of orientations. The temporal dynamics of the populations in each electronic state are shown in Figure 7.10b. The wavepacket at time 0 fs is in the T_d region, where it experiences strong forces due to the Jahn-Teller effect. This drives it away from the T_d geometry, favoring relaxations to C_{2v} and D_{2d} in D_0 . But in D_2 , due to the steep parabolic shape of the well of the potential energy surface around the T_d form, the wavepacket essentially relaxes to the lower states thanks to strong nonadiabatic coupling effects. This explains the rapid and continuous decay of the population on D_2 , which was the largest population among all the states at the beginning of the dynamics, right after ionization. Figure 7.10c shows that the strongest electronic coherences appear during the first 5 fs of the dynamics when the wavepacket

is localized in the T_d form; later they decrease due to dephasing once the WP moves differently on each potential energy surface.

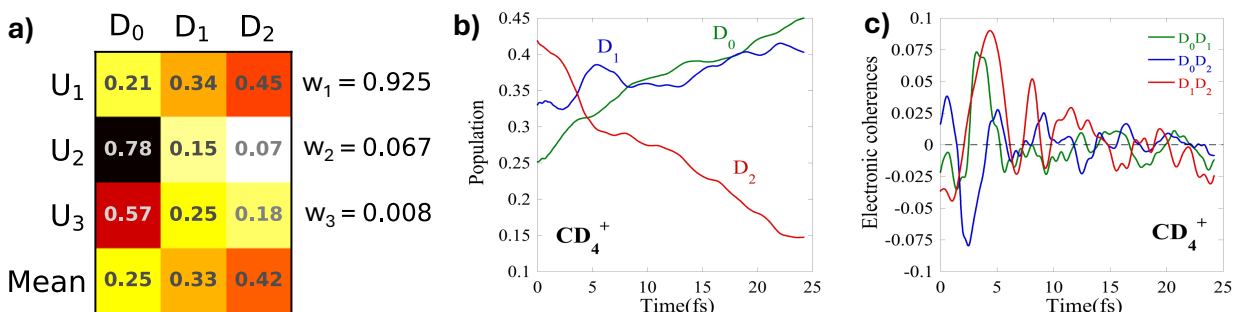


Figure 7.10 a) Composition of the three singular vectors in terms of the electronic states of the cation. b) Populations per electronic state. The rapid decay from D_2 is due to the fact that the steep parabolic potential traps the wavepacket in the T_d region where the NAC is the strongest. c) Coherences among the pair of electronic states. They are particularly large at the beginning of the dynamics because the wavepacket is localized in the FC region of the unstable T_d geometry and overlaps.

There is a rich interplay between the electronic potential and non-adiabatic couplings in determining the wavepacket's motion in the methane cation. This can be summarized as a competition between the populations dependent force F_V and the coherence-dependent force $F_{[\tau,V]}$. Because the coherence amplitudes, see Figure 7.10c, are much smaller than the populations and dephase as the dynamics proceeds, the dominant term of the force is F_V and defined by the gradients of each potential. The force F_V is responsible for trapping the WP in the T_d well in D_2 and in the C_{2v} and D_{2d} wells for the lower D_0 . As the WP is driven away rather quickly from the FC of the T_d form, the nonadiabatic forces $F_{[\tau,V]}$ are less pronounced, yet they play a crucial role in the decay of the D_2 state.

The force in CD_4^+ , contrary to LiH, will have two components, one in the direction of q_1 and the other along q_2 . Because, during the dynamics, there is no electric field, the force has only terms determined by the electronic potentials. In Figure 7.11 the forces and populations are shown. The population trapped on the well of D_2 around T_d , is transferred quickly to the states D_1 and D_0 due to the strong non-adiabatic couplings (Figure 7.11a). The wavepacket relaxing on D_0 follows on the grid two main pathways: one that leads to the C_{2v} minimum in the direction $-\mathbf{q}_1 + \mathbf{q}_2$, and the other to the D_{2d} minimum, in the direction $\mathbf{q}_1 - \mathbf{q}_2$. Therefore, when the first component of force $\mathbf{F}q_1$ is negative while the second component $\mathbf{F}q_2$ is positive, the wavepacket will be driven to the C_{2v} region. When $\mathbf{F}q_1$ is positive and $\mathbf{F}q_2$ is negative, the wavepacket will be steered onto the D_{2d} region. Figures 7.11d and 7.11e show the force term F_V projected on the states D_0 and D_1 , respectively, and both components are plotted. Initially, both components of the force are positive, which suggests that the wavepacket is being sent in the direction $\mathbf{q}_1 + \mathbf{q}_2$, but around 5 fs we observe that one component becomes negative: $\mathbf{F}q_2$ in the case of D_0 and $\mathbf{F}q_1$ in the case of D_1 .

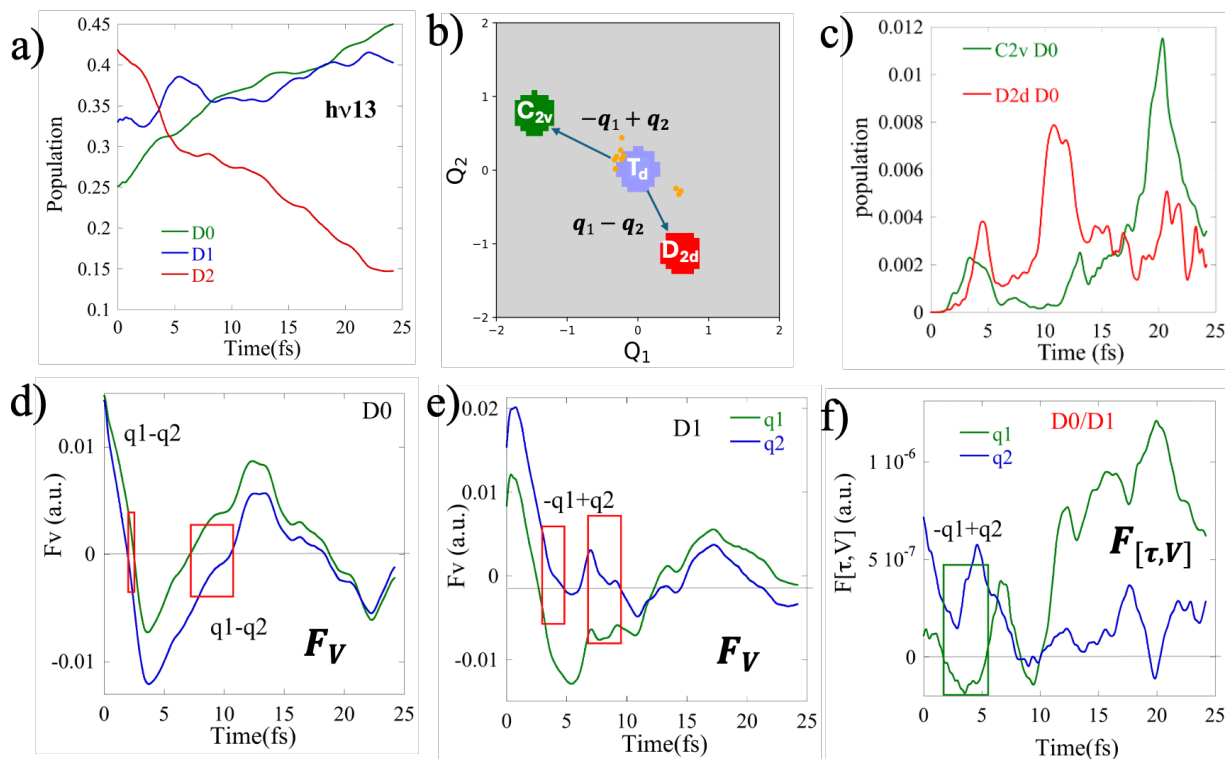


Figure 7.11: Forces controlling the stereodynamics in the ensemble of initial random orientations. Panel a) shows the populations per electronic state. b) shows the regions on the grid of approximate C_{2v} symmetry in green, T_d in violet, D_{2d} in red. The yellow spots correspond to localizations of the C_{3v} conical intersections. Panel c) shows the population of the C_{2v} and D_{2d} during the dynamics. The panels d)-f) are showing the forces involving the electronic states D_0 and D_1 .

Consequently, the force in D_0 points in the D_{2d} direction, while in D_1 it points in opposite direction. This correlates with what is observed from the motion of the wavepacket in these two states (Figure 7.12). The force determined by the NAC between D_0/D_1 states is much smaller than the F_V terms because the WP tends to move quickly out of the Franck Condon region, and the coherences become weaker.

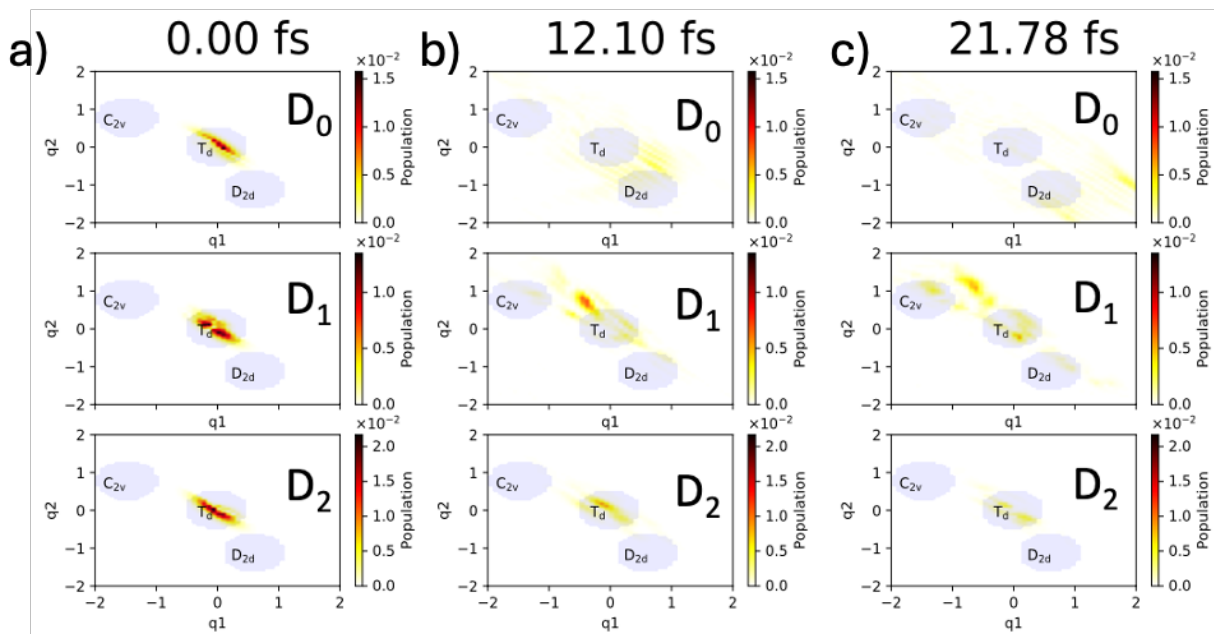


Figure 7.12: Localization of the CD_4^+ wavepacket on each electronic state as a function of time. Selected time steps are shown: a) at the beginning of the dynamics (0 fs), b) at ~ 12 fs, and c) at ~ 22 fs. As predicted from the analysis of the force direction, the wavepacket in state D_0 is steered more toward the D_{2d} region (see D_0 in panel c). In contrast, in state D_1 , it moves toward the C_{2v} region (see D_1 in panel c), which is unstable in the D_1 state and located close to the D_1/D_0 conical intersection seams. In D_2 , the wavepacket remains localized on the T_d region and the population tends to decrease due to NAC coupling to D_0 and D_1 .

7.3 References

1. M. Cardosa-Gutierrez, G. De Bo, A.-S. Duwez, F. Remacle, Bond breaking of furan–maleimide adducts *via* a diradical sequential mechanism under an external mechanical force. *Chemical Science* **14**, 1263-1271 (2023).
2. Y. Liu *et al.*, Flyby reaction trajectories: Chemical dynamics under extrinsic force. *Science* **373**, 208-212 (2021).
3. J. Ribas-Arino, M. Shiga, D. Marx, Mechanochemical Transduction of Externally Applied Forces to Mechanophores. *J. Am. Chem. Soc.* **132**, 10609-10614 (2010).
4. V. W. D. Cruzeiro, M. Manathunga, K. M. Merz, A. W. Götz, Open-Source Multi-GPU-Accelerated QM/MM Simulations with AMBER and QUICK. *J. Chem. Inf. Model.* **61**, 2109-2115 (2021).
5. G. D. M. Seabra, R. C. Walker, M. Elstner, D. A. Case, A. E. Roitberg, Implementation of the SCC-DFTB Method for Hybrid QM/MM Simulations within the Amber Molecular Dynamics Package. *J. Phys. Chem. A* **111**, 5655-5664 (2007).
6. D. A. Pearlman *et al.*, AMBER, a package of computer programs for applying molecular mechanics, normal mode analysis, molecular dynamics and free energy calculations to simulate the structural and energetic properties of molecules. *Computer Physics Communications* **91**, 1-41 (1995).
7. C. Bannwarth, S. Ehlert, S. Grimme, GFN2-xTB—An Accurate and Broadly Parametrized Self-Consistent Tight-Binding Quantum Chemical Method with Multipole Electrostatics

- and Density-Dependent Dispersion Contributions. *J. Chem. Theory Comput.* **15**, 1652-1671 (2019).
8. S. Grimme, C. Bannwarth, P. Shushkov, A Robust and Accurate Tight-Binding Quantum Chemical Method for Structures, Vibrational Frequencies, and Noncovalent Interactions of Large Molecular Systems Parametrized for All spd-Block Elements ($Z = 1-86$). *J. Chem. Theory Comput.* **13**, 1989-2009 (2017).
 9. I. S. Ufimtsev, T. J. Martinez, Quantum Chemistry on Graphical Processing Units. 3. Analytical Energy Gradients, Geometry Optimization, and First Principles Molecular Dynamics. *J. Chem. Theory Comput.* **5**, 2619-2628 (2009).
 10. W. D. Cornell *et al.*, A Second Generation Force Field for the Simulation of Proteins, Nucleic Acids, and Organic Molecules. *J. Am. Chem. Soc.* **117**, 5179-5197 (1995).
 11. J. Wang, R. M. Wolf, J. W. Caldwell, P. A. Kollman, D. A. Case, Development and testing of a general amber force field. *J Comput Chem* **25**, 1157-1174 (2004).
 12. B. R. Brooks *et al.*, CHARMM: A program for macromolecular energy, minimization, and dynamics calculations. *J Comput Chem* **4**, 187-217 (1983).
 13. X. Zhu, P. E. M. Lopes, A. D. MacKerell, Recent developments and applications of the CHARMM force fields. *WIREs Comput Mol Sci* **2**, 167-185 (2012).
 14. D. Poger, W. F. Van Gunsteren, A. E. Mark, A new force field for simulating phosphatidylcholine bilayers. *J Comput Chem* **31**, 1117-1125 (2010).
 15. N. Schmid *et al.*, Definition and testing of the GROMOS force-field versions 54A7 and 54B7. *Eur Biophys J* **40**, 843-856 (2011).
 16. B. Fresch, F. Remacle, Atomistic account of structural and dynamical changes induced by small binders in the double helix of a short DNA. *Phys. Chem. Chem. Phys.* **16**, 14070-14082 (2014).
 17. C. Jarzynski, Nonequilibrium Equality for Free Energy Differences. *Phys. Rev. Lett.* **78**, 2690-2693 (1997).
 18. B. Roux, The calculation of the potential of mean force using computer simulations. *Computer Physics Communications* **91**, 275-282 (1995).
 19. M. Cardosa-Gutierrez, R. D. Levine, F. Remacle, Electronic Coherences Excited by an Ultra Short Pulse Are Robust with Respect to Averaging over Randomly Oriented Molecules as Shown by Singular Value Decomposition. *J. Phys. Chem. A* **128**, 2937-2947 (2024).
 20. S. van den Wildenberg, B. Mignolet, R. D. Levine, F. Remacle, Temporal and spatially resolved imaging of the correlated nuclear-electronic dynamics and of the ionized photoelectron in a coherently electronically highly excited vibrating LiH molecule. *The Journal of Chemical Physics* **151**, 134310 (2019).
 21. C. E. M. Gonçalves, R. D. Levine, F. Remacle, Ultrafast geometrical reorganization of a methane cation upon sudden ionization: an isotope effect on electronic non-equilibrium quantum dynamics. *Phys. Chem. Chem. Phys.* **23**, 12051-12059 (2021).

Chapter 8 Conclusions

In this thesis, we investigated how mechanical forces and electric fields from ultrafast light pulses influence chemical reactions. The mechanical forces applied in Single-Molecule Force Spectroscopy (SMFS) experiments act directly on the nuclei of a single molecule in its ground electronic state. On the other hand, attosecond pulses, which have extremely short durations and correspondingly broad energy bandwidths, can excite a single molecule to a superposition of multiple electronic states, creating a quantum state where both nuclear and electronic motions are entangled and out of equilibrium. Due to this entanglement, the nuclei experience complex forces arising from the vibronic wavepacket, and the molecule's reactivity is no longer confined to the pathways within the ground electronic state but extends across the manifold of states populated by the pulse.

In Chapter 3, we reported a shift from the thermal, concerted mechanism to a sequential reaction pathway in the [4+2] retro-Diels-Alder reaction of furan/maleimide adducts when subjected to mechanical stress.⁽¹⁾ Furan/maleimide adducts are commonly used as mechanophores embedded in polymers because of their weak covalent bonds, which preferentially break when a bulk polymer sample is sonicated or when a single polymer chain is stretched, as in SMFS experiments.

In both cases, the polymer is subjected to an external mechanical force, and the direction of this force determines the degree to which the target bonds in the molecule are activated. When the force is aligned with the scissile bonds of the adduct, bond rupture is enhanced compared to normal thermal conditions. Conversely, if the force does not project well in the bond direction, it has no action and instead distorts the potential, increasing the energy barrier for the rupture, which, in turn, makes the polymer more resistant to mechanical stress. Furthermore, if the force direction has a larger overlap with one of the two scissile bonds than the other, as we demonstrated in our study ⁽¹⁾, the reaction shifts from a concerted mechanism to a sequential rupture, leading to diradical intermediates and transition states. These diradical species, which we identified and characterized, are reported for the first time in the dissociation of furan/maleimide adducts under force. Our study suggests that when attempting to steer the rupture of a bond in a molecule using a mechanical force, it is not the nominal value of the force itself that matters but rather how much energy the force transfers to the molecule, particularly to the target bonds. Since the timescale on which the force acts is much longer than the vibrational relaxation time, which occurs on a picosecond time scale, the efficiency of the force is largely determined by the molecule's response to the excitation and how the energy is redistributed. This redistribution can either effectively activate the target bonds or fail to do so. Moreover, since the force is transmitted through the polymer to the mechanophore, it is crucial to consider the couplings among internal coordinates as they articulate the molecular response and can help direct the excitation into neighboring modes or dissipate the energy.

In addition, we have characterized the diradical species formed during the intermediate state of the sequential pathway and shown that the lowest triplet state becomes degenerate with the singlet ground state, which could lead to strong spin-orbit coupling, especially if heavy atom substituents are present. This finding raises awareness within the polymer chemistry community about the

complex electronic structure of the species, which can be formed during the relaxation of the polymer under stress. Diradicals are highly correlated species, and their electronic structure can only be fully understood theoretically using multireference quantum chemistry methods. This presents a challenge, as many modern tools used to model large polymers, such as classical mechanics, semiempirical methods, and restricted DFT, are not suitable for accurately assessing the chemistry of diradicaloid species. We explained how diradicals and other strongly correlated systems can be studied using the CASSCF and UDFT methods, and we identified key properties that can be used to probe and characterize these species. For example, properties like the permanent dipole moment, atomic charges, CASSCF configurations, and spin-orbit couplings are valuable indicators.

Furthermore, we have revealed stereochemical effects between endo/exo configurations in the furan/maleimide reaction under force, which supports experimental findings (2). Our computations allowed us to estimate the free energies of activation for the reaction at various force values, from which we derived the lifetimes of the scissile bonds. This proved to be a useful tool for interpreting experimental data, as it provides a way to estimate observables, such as bond lifetimes, that can be measured in the lab. We described the full procedure we followed to obtain these lifetimes from theoretical calculations using state-of-the-art software.

The ideas developed in this thesis pave the way for the rational design of mechanophores with mechanoresponsive properties, with applications in materials science, including the development of self-healing materials and smart devices powered by external forces. By controlling the direction of the applied external force, it is possible to guide chemical reactions along different pathways, leading to distinct mechanisms and novel products. Our results also suggest that the magnitude of the force can influence the rDA reaction of furan/maleimide, either enhancing or inhibiting it. This could enable the use of the molecule as a logical switch.

Chapters 4, 5, and 6 were devoted to photoactivation. We studied the control of chemical reactivity in reactions driven by ultrafast laser pulses in the context of the emerging field of attochemistry. In Chapter 4, using a semiclassical surface hopping method, we analyzed observations from pump-probe experiments studying the relaxation of the ethylene cation formed after sudden ionization of the neutral molecule by an ultrashort pulse. This work has been recently submitted to the *J. Phys. Chem. Lett.* journal. We highlighted the critical role of the network of conical intersections (CIs) in funneling the relaxation pathways of the cation. Our results confirm that isotopic substitution can enhance the dissociation via H_2/D_2 loss or H/D loss by slowing down the motion of the wavepacket in the heavier isotopomer. This affects the filtering process at the CIs, which are pivotal for the relaxation pathways. We demonstrate how Fourier transforms can be employed to identify important vibrational modes, their couplings, and reactive coordinates by analyzing the relevant frequencies in the time-dependent signals generated by the simulations.

Towards the control of chemical reactivity with attopulses, we introduced a theoretical method (3) (see Chapter 5) that calculates the forces exerted on the nuclei by the vibronic wavepacket in a superposition of many electronic states. This allows us to explore the interplay between vibrational effects coming from motion on each potential energy surface and electronic effects arising from non-diabatic couplings. We extended an approach originally developed by Felix T. Smith (4) to describe the forces arising from the interaction between the electric field of the attopulse and the

molecular dipole. The method relies on solving the time-dependent Schrödinger equation (TDSE) for the nuclei, with a Hamiltonian that includes the potential, kinetic, and coupling terms. The representation of the wavefunction and the Hamiltonian, and the quantum-dynamical propagation is the main computational bottleneck. Once the time-dependent wavefunctions are obtained, the forces on the nuclei can be calculated and analyzed. For example, we determined the forces for the LiH molecule, which has a single nuclear degree of freedom, represented in a grid-based discrete variable representation. By tuning the pulse parameters, we show how these forces can be controlled and, in turn, alter nuclear motion, ultimately leading to different reaction pathways. Particularly, we report a significant effect on the populations of the excited states with a carrier-envelope phase of the pulse of π compared to 0 for an essentially one-cycle ultrashort IR pulse.⁽³⁾ The CEP controls which half-cycle of the electric field of the pulse, negative or positive, interacts with the dipole of the molecule and whether the electrons are pumped toward the Li or H atom, generating distinct forces on the nuclei. The CEP is a useful experimental parameter to control the composition of the initial superposition wavepacket created by the attopulse, indirectly determining the forces that will drive the nuclei during the relaxation phase. We also applied this force formalism to analyze more complex scenarios (see Chapter 7), such as the dynamics of an ensemble of randomly oriented LiH molecules and the Jahn-Teller rearrangement of CD_4^+ cation upon sudden ionization of the neutral T_d molecule. The latter system was modeled in a two-dimensional grid, demonstrating that the method can be extended to larger dimensions when a well-defined Hamiltonian and propagation scheme are available.

Additionally, to study the ensemble of randomly oriented LiH molecules, we developed a computational scheme (5) based on the singular value decomposition (SVD) of the matrix of wavefunctions for each electric field orientation sampled on the unit sphere. From the SVD, we obtained a minimal set of four or five principal polarizations of the field instead of the original several hundreds of orientations necessary to uniformly sample the unit sphere, allowing for significant computational savings in time and memory while still accurately simulating the dynamics of the entire ensemble. This method replaces traditional averaging over all orientations during the timespan of the TDSE propagation by focusing on the principal orientations determined by the SVD after the pulse is over. Each of the principal orientations is a linear combination of all the initial set of polarizations of the fields and thus encapsulates all the critical information concerning the dynamics of the ensemble. Using this compact representation of the ensemble of randomly oriented LiH molecules, we uncovered correlations among the excited states in the superposition wavepacket. For example, after the pulse, we observe a clear separation between the ground state and the manifolds of Σ and Π excited states, which have different stereodynamical properties. Each group of states was associated with a singular vector, with the Π states appearing at two degenerate singular vectors corresponding to orientations along X and Y and the Σ states appearing at another singular vector corresponding to orientations along the Z axis. While electronic coherences between Σ and Π electronic states were washed out by averaging over random orientations, coherences within the Σ or Π manifolds were robust and persisted throughout the ensemble.

In summary, this thesis discussed the potential for steering chemical reactions using either an external mechanical force and the electric force of ultrashort attosecond or femtosecond optical pulses. While controlling the forces in the nuclei remains challenging in both cases, experimental

conditions could be fine-tuned to guide nuclear relaxation along desired pathways, facilitating the selective outcome of chemical reactions.

References

1. M. Cardosa-Gutierrez, G. De Bo, A.-S. Duwez, F. Remacle, Bond breaking of furan–maleimide adducts *via* a diradical sequential mechanism under an external mechanical force. *Chemical Science* **14**, 1263-1271 (2023).
2. Z. Wang, S. L. Craig, Stereochemical effects on the mechanochemical scission of furan–maleimide Diels–Alder adducts. *Chemical Communications* **55**, 12263-12266 (2019).
3. M. Cardosa-Gutierrez, R. D. Levine, F. Remacle, Electronic coherences built by an attopulse control the forces on the nuclei. *J. Phys. B: At. Mol. Opt. Phys.*, (2024).
4. F. T. Smith, Diabatic and Adiabatic Representations for Atomic Collision Problems. *Phys. Rev.* **179**, 111-123 (1969).
5. M. Cardosa-Gutierrez, R. D. Levine, F. Remacle, Electronic Coherences Excited by an Ultra Short Pulse Are Robust with Respect to Averaging over Randomly Oriented Molecules as Shown by Singular Value Decomposition. *J. Phys. Chem. A* **128**, 2937-2947 (2024).